Microstructures and anisotropy of pyrolite in the Earth's lower mantle : insights from high pressure/temperature deformation and phase transformation experiments

Jeffrey Gay

Université de Lille
Laboratoire Unité Matériaux Et Transformation

Ecole doctorale n°104:
Sciences de la Matiére, du rayonnement et de l'environnement

Thèse de doctorat
Spécialité: Milieux denses, matériaux et composants

Microstructures and anisotropy of pyrolite in the Earth's lower mantle: insights from high pressure/temperature deformation and phase transformation experiments

Microstructures et anisotropie de la pyrolite dans le manteau inférieur : expériences de déformation et de transformations de phase sous hautes pressions et températures

---

Thèse préparée et soutenue publiquement par
Jeffrey Gay
pour obtenir le grade de Docteur

Dirigée par
Sébastien Merkel

Présentée et soutenue le 24 Novembre 2022 devant un jury composé de:

Pr Motohiko Murakami	ETH Zürich	Rapporteur
Pr Denis Andrault	Univ. Clermont Auvergne	Rapporteur
Pr Ana Ferreira	Univ. College London	Examinateur
Dr Angelika Rosa	European Synchrotron Radiation Facility	Examinateur
Pr Hugues Leroux	Univ. Lille	Président de jury
Pr Sébastien Merkel	Univ. Lille	Directeur de thèse

Octobre 2018 - Novembre 2022

Contents

Abstract

Microstructures in mantle rocks impact the way seismic waves travel through the Earth and are dependent on the pressure, temperature, and deformation applied to the rock. At approximately 660 km depth, an increase in seismic wave velocities mark a distinct boundary that separates the upper and lower mantle. Another boundary is found at approximately 2700 km depth and marks the beginning of the D" layer. Furthermore, observations of seismic anisotropy at these discontinuities have been made. These boundaries are largely believed to be related to phase transitions from ringwoodite [$(Mg,Fe)_2SiO_4$, space group $Fd\bar{3}m$] to bridgmanite [$(Mg,Fe)SiO_3$, space group $Pbnm$] to post-perovskite [$(Mg,Fe)SiO_3$, space group $Cmcm$]. In order to make interpretations of these seismic observations, however, a sound understanding of what generates these microstructures is required.

Here, we approach this problem through high pressure and high temperature experiments. We identify microstructures in polycrysalline mantle minerals resulting from in-situ transformation and deformation using radial and multigrain X-ray diffraction in the diamond anvil cell. In the first study we transform a bridgmanite analogue, $NaCoF_3$, from a perovskite to post-perovskite structure. The following two studies investigate the transformation of an average mantle composition, pyrolite, at conditions relevant to the 660 km discontinuity and further deformation at pressures and temperatures corresponding to depths between 500 and 2400 km. In the final study, we test an aluminum rich 'pyrolite' composition (pyrolite minus olivine) in order to compare transformation and deformation microstructures to those observed in experiments on pure pyrolite.

Results from radial diffraction experiments show the transformation from perovskite to post-perovskite in $NaCoF_3$ are reconstructive in nature and for which we identify the orientation relationships. Major takeaways from the multigrain X-ray diffraction experiments are as follows: i) the decomposition from (ringwoodite + garnet) to (bridgmanite + davemaoite + ferropericlase) result in non-reconstructive 001 transformation textures in bridgmanite, 101 and 111 textures in davemaoite, and no preferred orientation in ferropericlase. ii) With further deformation, bridgmanite changes to 100 and 010 orientations with no change in either davemaoite or ferropericlase. iii) Textures in bridgmanite and davemaoite in pyrolite minus olivine are similar to those observed in our experiments on

pure pyrolite.

Finally, we use the results of these experiments to build a model for S and P-wave seismic anisotropy within a subducting slab and the surrounding mantle for multiple scenarios and compare our results to those of the literature. This interplay between experiments and seismic models are important in order to provide constraints on deformation, dynamics, and history of the Earth's interior.

Résumé

Les microstructures des roches du manteau affectent la propagation des ondes sismiques dans la Terre. Elles dépendent de la pression, de la température et de la déformation appliquées à la roche. À environ 660 km de profondeur, un saut de vitesses des ondes sismiques marque la frontière qui sépare le manteau supérieur du manteau inférieur. Une autre frontière se trouve à environ 2 700 km de profondeur et marque le début de la couche D". Ces frontières sont communément associées à des transformations de phase de la ringwoodite [$(Mg,Fe)_2SiO_4$, groupe d'espace $Fd\bar{3}m$] à la bridgmanite [$(Mg,Fe)SiO_3$, groupe d'espace $Pbnm$] puis la post-perovskite [$(Mg,Fe)SiO_3$, groupe d'espace $Cmcm$]. Cependant, une bonne compréhension de ce qui génère les microstructures associées à la déformation ou les transformations de phase est nécessaire pour interpréter les observations sismiques et les associer aux processus dynamiques dans le manteau.

Ici, nous abordons cette question par le biais d'expériences à haute pression et à haute température en cellule à enclume de diamant. Nous identifions des microstructures résultant de transformations de phase ou de déformation dans des matériaux polycristallins pertinent pour le manteau, in situ, à l'aide de la diffraction des rayons X radiale ou multi-grains. Dans la première étude, nous transformons un analogue de bridgmanite, $NaCoF_3$, d'une structure pérovskite à une structure post-pérovskite. Les deux études suivantes se concentrent sur la transformation d'une composition moyenne du manteau, la pyrolite, dans des conditions pertinentes pour la discontinuité à 660 km et une déformation supplémentaire à des pressions et des températures correspondant à des profondeurs comprises entre 500 et 2400 km. Dans le dernier chapitre, nous testons une composition 'pyrolite' riche en aluminium (pyrolite-minus-olivine) afin de comparer les microstructures de transformation et de déformation à celles observées expérimentalement sur la pyrolite pure.

Les résultats d'expériences de diffraction radiale montrent que la transformation de pérovskite en post-pérovskite dans $NaCoF_3$ est de nature reconstructive et nous identifions les relations d'orientation qui entrent en jeu. Les principales conclusions des expériences de diffraction des rayons X multigrains sont les suivantes : i) la décomposition de (ringwoodite + grenat) en (bridgmanite + davemaoite + ferropériclase) donne des textures

de transformation non reconstructives 001 dans la bridgmanite, 101 et 111 dans la davemaoite, et aucune orientation préférentielle dans la ferro-périclase. ii) Avec une déformation supplémentaire, la bridgmanite passe à des orientations de type 100 puis 010 sans changement de texture observé, ni dans la davemaoite, ni dans la ferro-périclase. iii) Les textures de la bridgmanite et de la davemaoite dans la composition pyrolite-minus-olivine sont similaires à celles observées dans nos expériences sur la pyrolite pure.

Enfin, nous utilisons les résultats de ces expériences pour construire un modèle d'anisotropie sismique des ondes S et P dans une plaque en subduction et dans le manteau environnant pour plusieurs scénarios et comparons nos résultats à ceux de la littérature. Cette combinaison entre les expériences et les modèles sismiques est importante pour fournir des contraintes sur la déformation, la dynamique et l'histoire de l'intérieur de la Terre.

Plain Language Summary

The Earth's interior has been gradually cooling through heat exchange from the core to the surface, which leads to many of the physical processes observed on the surface of the planet including plate tectonics and the underlying mantle convection. Seismic observations provide a mean to observe structures within the Earth's interior through features such as anisotropy or the detection of boundaries through changes in wave velocity. At the rock scale, seismic waves are sensitive to microstructures (i.e. grain size, shape, and orientation) created by ongoing deformation or mineralogical transformations. Here, we implement experimental transformation and deformation experiments at the conditions of the upper and lower mantle on rocks in a pyrolitic composition. We quantify how these microstructures are developed and the deformation mechanisms that may be active in dominant mantle minerals such as bridgmanite, providing an avenue to constrain mantle processes from observations.

Résumé grand public

L'intérieur de la Terre se refroidit gâce aux échanges de chaleur du noyau vers la surface, ce qui se manifeste par des processus tels que la tectonique des plaques et la convection sous-jacente du manteau. Les observations sismiques (vitesses de propagation d'onde, anisotropie, ou discontinuités de vitesses) permettent de sonder les structures à l'intérieur de la Terre. À l'échelle de la roche, les ondes sismiques sont sensibles aux microstructures (la taille, la forme et l'orientation des grains) générées par la déformation ou les transformations minéralogiques. Ici, nous utilisons des expériences de transformation et de déformation aux conditions de pression et température du manteau sur une composition pyrolitique. Nous quantifions la façon dont ces microstructures se développent et les mécanismes de déformation sous-jacents dans des minéraux tels que la bridgmanite, fournissant ainsi les données nécessaires pour contraindre les processus mantelliques à partir des observations.

General Introduction

Dynamic processes within the Earth's mantle are responsible for much of the geologic activity we can observe on the surface including plate tectonics, earthquakes, volcanoes, or the magnetic field. These surface processes have been attributed to the transportation of heat and material within the mantle or core through convective processes. The mechanisms that drive this phenomena, however, are poorly understood, motivating geoscientists to probe for answers about the structure and composition of the Earth's interior.

One of the most effective methods to probe the interior is by using seismic wave propagation, as direct observations are limited. Seismologists have successfully used seismic waves to effectively map the Earth's interior, through observations of wave velocity changes, which mark layered boundaries, referred to as discontinuities. Although these boundaries are not seen everywhere, velocity variations within the mantle have been documented at 410, 520, and 660 km depth and linked to compositional and structural variations. In the case of the 660 km discontinuity ('660'), changes in seismic velocity are attributed to a phase transformation of ringwoodite ($(Mg,Fe)_2SiO_4$) to bridgmanite ($(Mg,Fe)SiO_3$).

Reports of seismic anisotropy, the directional dependence of velocity on propagating waves, in the upper mantle are commonplace and are often attributed to preferred orientation, or texture, of olivine due to plastic deformation. Within the mantle transition zone and lower mantle, however, observations of anisotropy are not made everywhere and their cause is largely debated. An understanding of microstructures generated by phase transformation and deformation in bridgmanite (the most abundant mineral in the Earth's mantle) is necessary in order to interpret seismic anisotropy. This is why mineral physicists use experimental tools in order to investigate mineralogical microstructures at high pressures and temperatures, quantify their impact on mantle flow processes, and provide constraints on deformation within the mantle.

To accomplish this, we rely on modern experimental techniques to recreate the conditions of the mantle transition zone and lower mantle while tracking the development and evolution of these microstructures in-situ. In this work we implement a high pressure device paired with a X-ray source to actively monitor the onset of transformation and deformation of a pyrolitic material in a controlled environment. We aim to characterize the resulting microstructures, whether caused by transformation or deformation, and determine the specific mechanisms responsible for observed seismic anisotropy below the mantle transition zone. The resulting experimental microstructures are then used to model seismic anisotropy and compared to real world measurements.

In the first chapter of this thesis I discuss the different layers of the Earth's interior. Dynamic processes within the mantle will also be discussed, along with seismological observations and their microscopic origins. This will also include a review of experimental and numerical techniques used to investigate the sources of these microstructures within mantle materials. The second chapter will cover the methods used complete the experiments and data processing. Starting with an overview of our high pressure experiments, how the data was collected, and different X-ray diffraction techniques; then briefly discussing data processing tools used to interpret our results. Chapter 3 will present a published study on the perovskite analogue $NaCoF_3$ which covers the deformation, transformation to post-perovskite, and resulting textures of $NaCoF_3$ using radial diffraction techniques in the diamond anvil cell. Chapter 4 details the transformation microstructures induced in pyrolite at conditions of the 660 km discontinuity using multigrain X-ray diffraction techniques. Seismic anisotropy is also calculated, using these experimental results, before and after transformation while presenting simple scenarios based on our predicted amplitudes and those of other geodynamic models presented in literature. Chapter 5 builds on the experiments performed in Chapter 4 by investigating further deformation of three pyrolitic samples after transformation and the resulting textures generated by plastic deformation. This includes a discussion and comparison of deformation mechanisms responsible for the observed textures. A mantle convection model is also presented, using our texture results, that predicts seismic anisotropy below '660' to depths of 2400 km. Chapter 6 presents transformation texture results from multigrain X-ray diffraction experiments on two py-

rolite minus olivine compositions, meant to represent an extreme case and highlight the impact aluminum has on the phase transformations and deformation of bridgmanite. Finally, this thesis will conclude with general implications of this research on the field of geophysics.

Chapter 1

Mineral Microstructures and Their Impact on Mantle Dynamics

1.1 The Interior of the Earth

1.1.1 Layers of the Earth

The Earth's interior, on a rudimentary level, can be divided into 4 concentric layers: the crust, mantle, inner core, and outer core. Although direct sampling can be made within the crustal and uppermost portions of the mantle (through exhumation from volcanic vents), investigation of the deeper interior requires indirect measurements from seismic tomography. Seismic waves are used to determine physical properties of the materials it interacts with. Two commonly used elastic body waves that can measure the physical properties of the deep earth are primary/pressure waves (P-wave) and secondary/shear waves (S-waves). P-waves are compressional waves that can be transmitted through solids, liquids, or gas and have polarization parallel to the direction of propagation. They are the fastest traveling body waves and hence are the first to reach the seismic receiver. Secondary waves, on the other hand, can only be transmitted through solids or liquids with high viscosity, and have polarization directions that are orthogonal to propagation. These waves arrive at seismic receivers after P-waves as they travel more slowly through solids.

Physical properties such as density and elastic properties impact the velocity of propagating P and S waves, which can be represented as:

$$V_P = \sqrt{\frac{4\mu/3 + K}{\rho}} \text{ and } V_S = \sqrt{\frac{\mu}{\rho}} \tag{1.1}$$

where V_P is the P-wave velocity, V_S is the S-wave velocity, and μ, K, and ρ are the shear modulus, bulk modulus, and density of the material, respectively. The PREM (Preliminary Reference Earth Model), proposed by Dziewonski and Anderson [1981], was one of the first seismological models constructed using V_P and V_S variations in order to calculate the average radial physical properties of the Earth (Figure 1.1). Increases in seismic wave velocities mark changes in the elastic properties or density of the material they pass through, allowing for the identification of layers within the Earth.

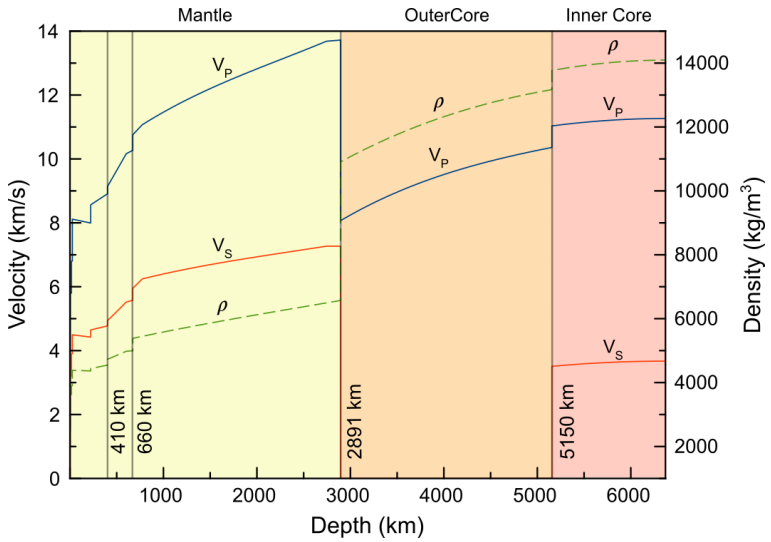

Figure 1.1: Average seismic velocity and density profile of V_P, V_S, and ρ modified from Dziewonski and Anderson [1981] to clearly show seismic boundary layers.

These layers interact with one another through the exchange of heat and material (Figure 1.2). The inner core is composed of solid iron-nickel alloy, while the outer core is in the liquid state. The mantle is composed of slowly moving ductile rock and acts as the conduit for which heat efficiently escapes to the surface. Cold material, such as subducting oceanic slabs, are drawn down into the mantle where it is eventually recycled, while hot material from the outer core rises via magma plumes. This process is responsible for what is known as mantle convection and manifests in the more brittle crustal and upper mantle layers as observable geologic surface processes such as plate tectonics, earthquakes, volcanoes, tsunamis etc.

The interaction of Earth's layers are complex however, and in the case of the mantle not homogeneous. Seismic boundaries, or discontinuities, can be clearly seen from seismic tomography data and further divide the mantle into a upper and lower parts (Figure 1.2),

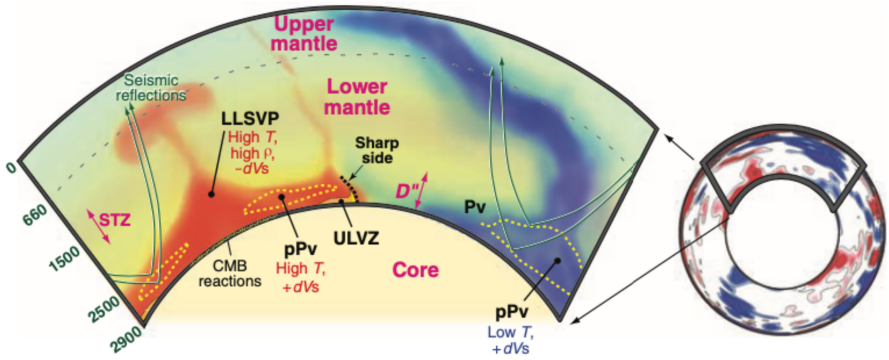

Figure 1.2: Seismic tomography profile of the upper and lower mantle and associated structures from Garnero and McNamara [2008].

which are separated by the mantle transition zone (MTZ). The upper mantle extends to a depth of 410 km, followed by the MTZ which exists down to 660 km, and then the lower mantle which reaches a depth of approximately 2900 km. The chemical composition between these boundaries does not vary however, so marked increases of wave velocities are attributed to structural changes within the mineralogy in the form of phase transformations, which are a result of the pressures and temperatures they are subjected to [Birch, 1952].

1.1.2 Mineralogy of Pyrolite

A model composition of the mantle, called pyrolite, was proposed by Ringwood [1962a], consisting of 1 part basalt and 4 parts dunite. Although pyrolite is a theoretical composition, the primitive material is defined by fractional melting of basaltic magma and residual dunite or peridotite [Ringwood, 1962a]. Additionally, the properties of a pyrolitic material match well with what is observed in seismic velocity and density data within the transition zone [Weidner, 1985, Ita and Stixrude, 1992]. Mineral assemblages and the expected transformation conditions at temperature and pressure were first provided by Ringwood [1991], although improved phase diagrams have been constructed more recently using experimental multianvil data [Ishii et al., 2018] (Figure 1.3).

The composition of pyrolite varies at three observable seismic discontinuities within the mantle. Immediately above the first major discontinuity at 410 km depth, pyrolite is composed of approximately 60% olivine, 20% pyroxenes, and 20% garnet by volume [Ringwood, 1991]. Beyond this depth, however, a polymorphic transformation of olivine $(Mg,Fe)_2SiO_4$

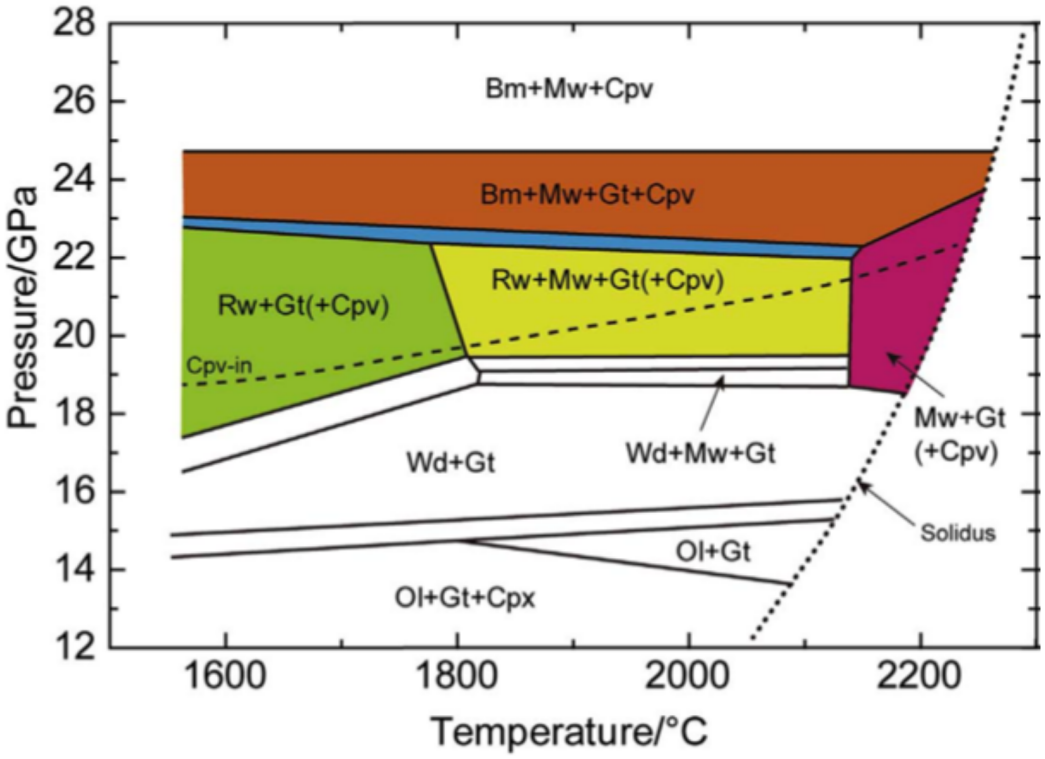

Figure 1.3: Phase diagram of pyrolite in the MTZ as a function of pressure and temperature from Ishii et al. [2018]. Acronyms in figure are as follows: olivine (Ol), garnet (Gt), clinopyroxene (Cpx), wadsleyite (Wd), magnesiowüstite (Mw), ringwoodite (Rw) calcium perovskite (Cpv), bridgmanite (Bm).

to wadsleyite occurs, which marks the beginning of the MTZ. An intermediate discontinuity exists at 520 km depth and is characterized by another polymorphic transformation, where wadsleyite transitions to ringwoodite and pyroxene phases dissociates to form garnet. Beyond this boundary a final polymorphic transformation of wadsleyite to ringwoodite occurs and the mineralogy of pyrolite becomes approximately 60% ringwoodite and 40% garnet [Ringwood, 1991]. The final major discontinuity exists at 660 km depth and marks the end of the MTZ or the beginning of the lower mantle. Here, ringwoodite disassociates to form bridgmanite $(Mg,Fe)SiO_3$ and ferropericlase $(Mg,Fe)O_3$ with the presence davemaoite $CaSiO_3$. At these depths pyrolite is composed of 80% bridgmanite, 15% ferropericlase, and 5% davemaoite [Ringwood, 1991]. This composition remains homogeneous to a depth of approximately 2600 km (Figure 1.4), which marks the base of the mantle and the beginning of a 200 km thick boundary known as the D", which separates the mantle from the outer core.

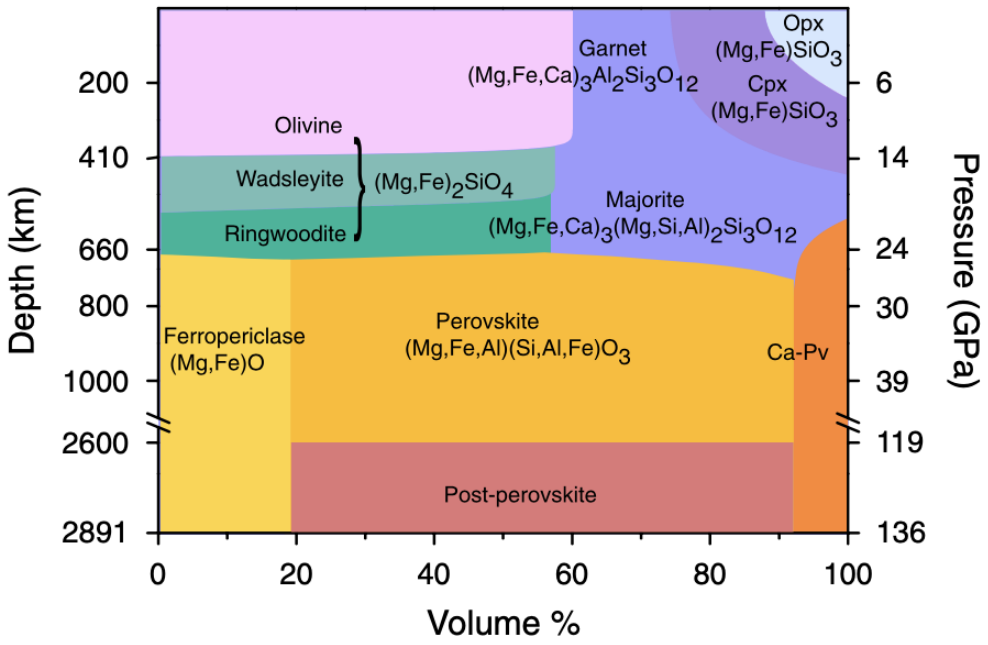

Figure 1.4: Composition of pyrolite as a function of depth (km) and pressure (GPa) down to the core mantle boundary from Lin et al. [2013].

1.2 Mantle Dynamics

1.2.1 Mantle Convection

Slab subduction is a major driving mechanism of plate tectonics as cold slabs sink into the Earth's mantle and interact with the hotter surrounding material. Subducting slabs are more dense than the surrounding mantle and might eventually reach the core mantle boundary (CMB) [van Der Hilst et al., 1997]. It is believed that these slabs end up piling near the CMB and result in the upwelling of hot mantle plumes [Garnero et al., 2016] (Figure 1.5). It is the exchange of heat from the interior to the surface of the Earth that drives mantle convection, with subduction controlling the downward component of movement and plumes the rising component. Plumes, like oceanic slabs, can also be detected using seismic waves, resulting in lowered shear wave velocities (V_S) generally located under surface regions of hotspot volcanism [Garnero and McNamara, 2008]. These low velocity zones are not detected everywhere, however, and are separated by areas of faster than average V_S related to the subducted oceanic lithosphere [Lekic et al., 2012], eluding to compositional variations in the lower mantle [McNamara et al., 2010].

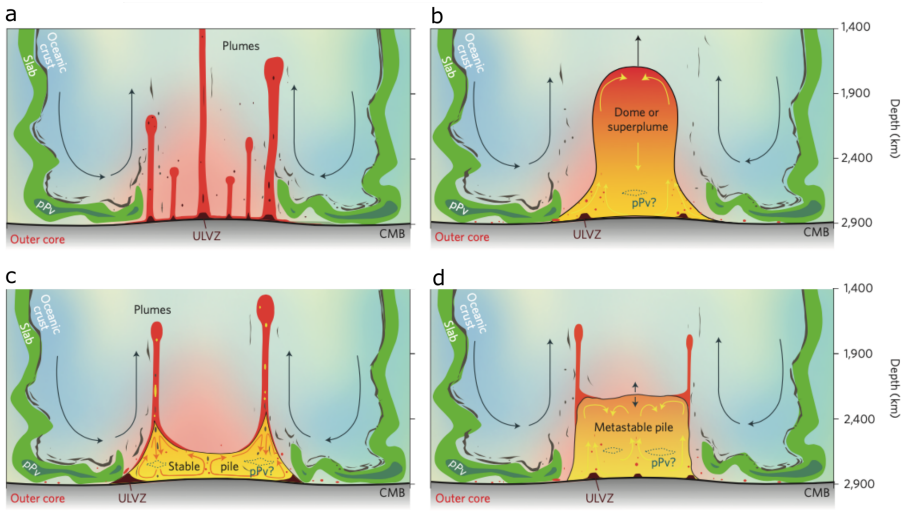

Figure 1.5: Possible scenarios of rising mantle plumes driven by the interaction of subducting slabs with the core mantle boundary (CMB) in the deep mantle. a) Plume cluster. b) Thermochemical superplume. c) Stable thermochemical pile. d) Metastable thermochemical pile. ULVZs; ultralow velocity zones. Figure from Garnero et al. [2016].

1.2.2 Seismic Anisotropy

Seismic anisotropy, or the directional dependence of wave velocity, can be generated several ways including the structure of crystals, crystallographic preferred orientation (CPO) or texture, grain shape preferred orientation (SPO), or the presence of fluids. There are two components of seismic anisotropy; variations in propagation velocity with respect to azimuth (P-wave and S-waves) and the difference in propagation speed of two polarized waves (S-waves). While surface waves in upper mantle regimes provide large-scale information on azimuthal anisotropy [Beller and Chevrot, 2020], shear wave splitting measurements are more commonly used in sampling the deep mantle due to the straight forward measurement process [Long and Becker, 2010]. When shear waves interact with an isotropic material, the initial linearly polarized wave splits into two perpendicular components. One is polarized parallel to the fast direction and the other parallel to the slow direction. Each component accumulates a time delay as it travels through the material that can be measured on a seismograph (Figure 1.6).

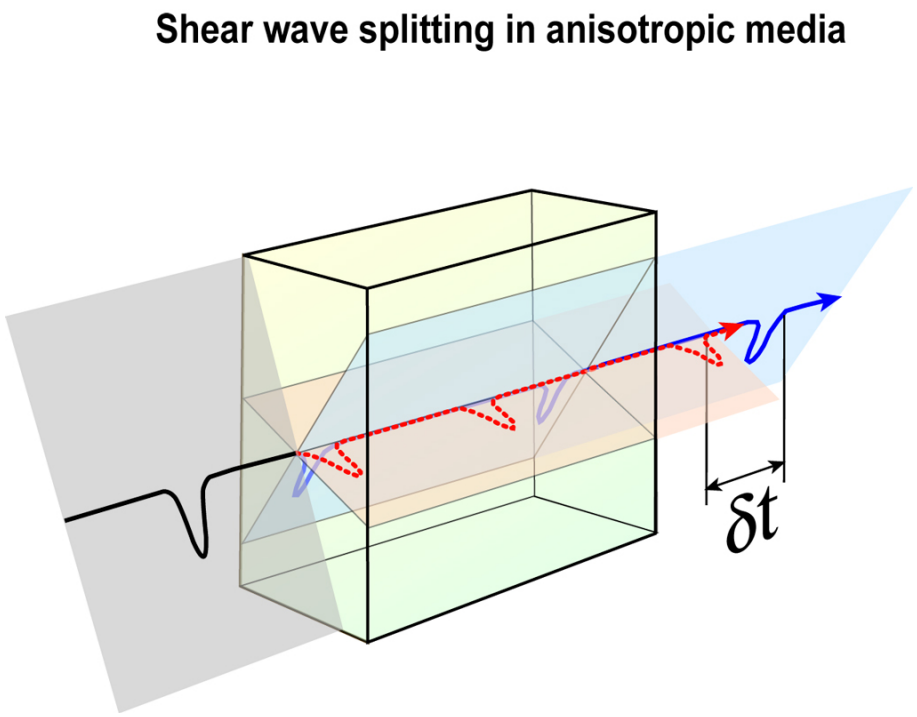

Figure 1.6: Schematic of shear wave splitting from Garnero (http://garnero.asu.edu/research_images/images_anisotropy.html), modified from Crampin [1981]. Fast polarization direction in blue and slow direction in red. Measured time difference between the two waves represented by δt.

1.2.3 Observations of Seismic Anisotropy

Observations of seismic anisotropy, or the directional dependence of wave velocity, can give information about direction of mantle flow patterns. By measuring the difference in travel time of the vertical and horizontal components of S-waves, observations of vertical flow in the upper mantle have been made near spreading centers with observations of horizontal flow beneath the lithosphere [Panning and Romanowicz, 2006a]. These convective processes cause deformation of the underlying mantle caused by the interaction with the lithospheric plates above [Billen, 2008, Long and Becker, 2010, Faccenda and Capitanio, 2012, Lynner and Long, 2015, Yoshida, 2017]. In the case of horizontal flow, plastic deformation in the upper mantle generates the preferential alignment of olivine crystals [Jung et al., 2009, Tommasi et al., 2009] which is considered to be the source of anisotropy in this region. While the cause of anisotropy in the upper mantle is fairly well resolved, microstructures within the MTZ and lower mantle are less understood and require further investigation in order to interpret observations seismic anisotropy in these regions [Long, 2013].

The upper mantle as a whole is largely seismically anisotropic due to the abundance of olivine and its intrinsic anisotropy. Within the MTZ, anisotropy is also observed [Montagner and Kennett, 1996, Trampert and van Heijst, 2002, Yuan and Beghein, 2013], however, it is less pronounced [Panning and Romanowicz, 2006a]. Observations of anisotropy within the MTZ are often made near regions of slab subduction [Chen and Brudzinski, 2003, Long and Silver, 2008, Nowacki et al., 2015, Huang et al., 2019] and thought to be a result of crystallographic preferred orientation in wadsleyite [Kawazoe et al., 2013]. In these regions, subducting plates carry water into the MTZ, which could in turn impact the mechanical properties of rocks and contribute to observations of anisotropy [Nowacki et al., 2015]. Deeper within the MTZ, however, observations of anisotropy decrease in strength [Huang et al., 2019], which is attributed to isotropic properties of ringwoodite at these conditions [Li et al., 2006a].

Seismic anisotropy below the MTZ is largely debated as observations have been made below the '660' locally [Wookey et al., 2002, Ferreira et al., 2019, Agrawal et al., 2020, Montagner et al., 2021], but are absent in other more global models [Meade et al., 1995, Panning and Romanowicz, 2006a, Panning et al., 2010]. Additionally, there are altering suggestions on the exact location of these observations with some suggesting anisotropy is developed mostly around rigid subducting slabs due to high induced strain in the surrounding hot mantle [Ferreira et al., 2019] and others arguing anisotropy is strongest within the slabs where they are most contorted; as the surrounding mantle is largely isotropic [Agrawal et al., 2020].

Although observations of anisotropy below the '660' are generally confined to depths between 600-1200 km [Ferreira et al., 2019], the amplitude of azimuthal anisotropy varies with depth in the mantle [Panning and Romanowicz, 2006a] (Figure 1.7). Within the upper mantle, shear wave splitting amplitudes (V_S) are on the order of 3%, dropping to zero at depths of 1000-2500 km. Beyond 2500 km, however, V_S anisotropy can again be observed at amplitudes of 1-2%. Further characterization of these observations can be made using radial anisotropy by investigating polarization directions of S-waves, which also varies with depth. Polarization directions of S-waves switch from horizontally polarized S-waves (V_{SH}) leading vertically polarized S-waves (V_{SV}) in the upper mantle and MTZ,

to vertically polarized S-wave leading horizontally polarized S-wave ($V_{SV} > V_{SH}$) at the '660', then reverse again ($V_{SH} > V_{SV}$) at D" [Mainprice et al., 2000].

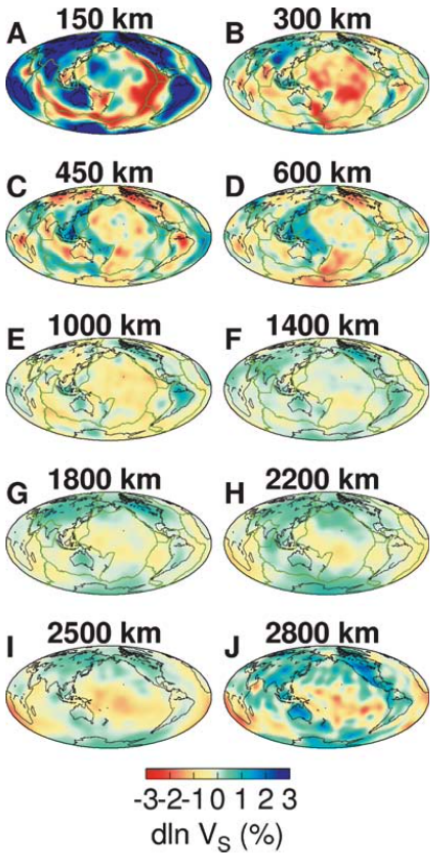

Figure 1.7: Variations in azimuthal S-wave anisotropy (V_S) with depth from Panning and Romanowicz [2006a].

The study of seismic anisotropy is largely motivated by providing constraints on deformation within the Earth's interior and interpreting mantle flow processes. Interpretations of observed anisotropy in the mantle, however, require an understanding of mineralogical microstructures and how they manifest.

1.3 Microstructures in Mantle Minerals

1.3.1 Microscopic Origins of Anisotropy

Anisotropy observed in the mantle is a direct result of microstructures within a polyphase aggregate. The interaction of individual grains within a polycrystal dictates the bulk properties of an aggregate such as grain size, grain shape, texture, shape preferred orientation, and spatial relationship between grains. Although most mantle minerals are strongly

anisotropic [Mainprice, 2015], their microstructures depend on the pressure, temperature, and deformation applied to the material. Individual randomly oriented anisotropic minerals within an aggregate are not enough to produce seismic anisotropy within the bulk material; however, if these grains undergo plastic deformation or a phase transformation that leads to the preferential alignment of each grain, their anisotropic properties would compound and result in seismic anisotropy. P-wave velocity will differ depending on the direction of propagation through the aggregate and S-waves will have differing propagation speeds between their vertically (V_{SV}) and horizontally (V_{SH}) polarized components. Understanding microstructures in the mantle and how they develop, hence gives direct insight to the mechanisms that produce them.

1.3.2 Plastic Deformation

Plastic deformation is non-reversible deformation that is a result of an applied force on a material. It can occur through series of different mechanisms including diffusion, dislocations, or grain boundary sliding. These mechanisms are a result of defects within a crystalline lattice either at a point, a line, or plane that allows the movement of individual atoms. In mantle rocks, plastic deformation requires stress and high temperatures. Texture development is a result of plastic deformation; however, some mechanisms are more likely to produce textures than others. In the following sections, an overview of deformation mechanisms at play in our experiments will be provided.

Dislocation

Dislocation involves linear crystallographic defects in which movement of atoms slide or glide across one another due to an applied stress. The movement of dislocations can be characterized by the plane they slip along and the direction of slip, or Burgers vector. The burgers vector describes the magnitude and direction of the lattice movement due to dislocation and is normal to the slip plane. There are two general types of dislocations; sessile, or dislocations that are immobile, and glissile, which are dislocations that are mobile. Glissile dislocations can further be subdivided into two categories know as edge and screw dislocations. Edge dislocations contain a Burgers vector that is perpendicular to the dislocation line (meaning there is only one plane in which the dislocation can slip),

whereas for a screw dislocation the Burgers vector is parallel to the dislocation line. In some cases dislocations can contain Burgers vectors that are neither perpendicular nor parallel to the dislocation line, meaning there is a combination of edge and screw dislocations and are referred to as mixed dislocations.

The movement of a dislocation is generally restricted to a slip plane and a specific direction called a slip system. For a slip plane to be active, the applied shear stress must exceed the critical resolved shear stress (CRSS) value. Slip systems with the lowest CRSS will activate first, with the possibility of multiple slip systems being active simultaneously as deformation continues. Stresses applied to the entire crystal is accommodated by plastic deformation through these dislocations. Dislocations within a polycrystalline material can often lead to texture development, or lattice preferred orientations [Wenk and Houtte, 2004, Carrez et al., 2007, Tsujino et al., 2016] in addition to distortions of the lattices within the crystal.

Diffusion

Plastic deformation can also be accommodated by diffusion. Diffusion creep involves the migration of crystal defects through the movement of interstitial atoms or gaps. Point defects in the crystal lattice can be caused by an extra atom that occupies space between atoms in their normal sites (interstitial defect) or due to the absence of an atom at its normal site (gap defect). In order for an atom to fill a vacancy in the lattice, chemical bonds must be broken and reformed, which requires a specific activation energy. The activation energy is more easily reached at higher temperatures, making diffusion more sensitive to temperature that other deformation mechanisms [Poirier, 1985]. The rate of diffusion largely depends on the path of which the atoms move. Diffusion is hence less efficient across larger distances than it is for shorter paths. Grain size has a large control on diffusion creep with smaller grain sizes being more efficient than larger sizes [Poirier, 1985].

There are two types of diffusion creep; Nabarro-Herring and Coble creep. Nabarro-Herring creep involves the movement of vacancies through the crystal lattice, whereas Coble creep the vacancies migrate along the grain boundaries. When the crystal is subjected to compression, both forms of creep involve the movement of interstitial atom to-

wards the direction of extension with gaps moving towards the direction of compression. The accommodation of deformation by diffusion creep generally does not result in microstructures with crystallographic preferred orientations [Karato, 1988]; however, has led to grain growth in $MgSiO_3$ perovskite at lower mantle conditions [Yamazaki et al., 1996, Fei et al., 2021].

Summary

Microstructures within crystalline materials have an impact on deformation mechanisms. For large grain sizes plastic deformation is generally accommodated by movement of dislocations, whereas with smaller grains sizes diffusion processes are more likely at play; although the activation of dislocation or diffusion creep can also depend on external parameters such as temperature, pressure, or strain rate. Both of these deformation mechanisms directly effect the development of microstructures including texture, grain elongation, grain growth, etc. These microstructures develop and evolve with the onset of plastic deformation with dislocation glide generally responsible for generating crystallographic preferred orientations, diffusion leading to grain growth, with or without preferred orientation, and recrystallization leading to homogeneous structures. Microstructures therefore provide direct information on the dominant deformation mechanisms in the polycrystalline material and can be used to characterize plastic deformation and the flow history of material.

In chapter 5 we will delve further into the deformation mechanism of bridgmanite. We observe 001 transformation textures with the development of 100 orientations upon further deformation of bridgmanite in our experiments. These 100 orientations reorient themselves to 010 once pressures exceed 50 GPa. We assign the 100 textures to dominant (100)[001] slip with minor contributions from (010)[001] and (001)[010] and 010 textures to dominant (010)[100] and (010)[001] slip.

1.3.3 Phase Transformation

In this thesis we investigate phase transformations in pyrolite (ringwoodite + garnet ⇒ bridgmanite + davemaoite + ferropericlase) and the transformation from the perovskite structure to the post-perovskite structure in the analogue material $NaCoF_3$. Phase transformations require the application of pressure and temperature; and result in the change of

crystal structure. In some cases, these transformations lead to the development of texture. Transformations can be categorized as displacive, where atoms within the material move in a homogeneous fashion, or reconstructive, which involves the movement of atoms through long range diffusion. In a displacive or diffusionless transformation, orientation relationships between the initial (parent) and resulting (daughter) phase can be defined. They are sometimes referred to as martensitic [Christian et al., 1995]. Conversely, reconstructive transformations do lead to clear orientation relationships.

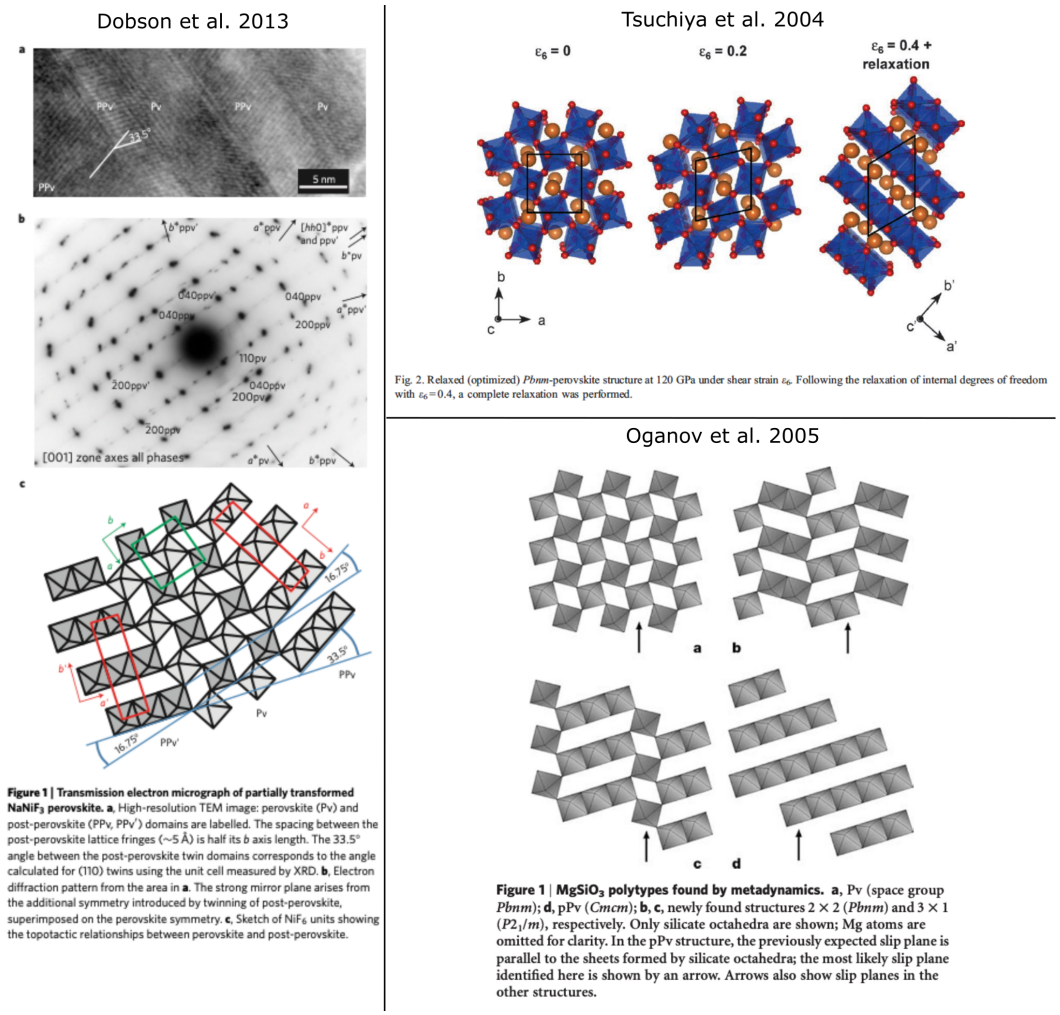

Figure 1.8: Figures from Dobson et al. [2013], Tsuchiya et al. [2004], and Oganov et al. [2005] illustrating the orientation relationships between perovskite and post-perovskite proposed in each work.

Displacive transformations are rapid and requires less energy compared to reconstructive transformations. Simulations have been used in the past in order to investigate the transformation from perovskite to post-perovskite [Tsuchiya et al., 2004, Oganov et al.,

2005] in addition to experimental efforts [Dobson et al., 2013]. The orientation relationships presented in Tsuchiya et al. [2004] suggest that $[1\bar{1}0]$, [110], and [001] in $MgSiO_3$ perovskite are parallel to [100], [010], and [001] in post-perovskite, respectively (Figure 1.8). Contrarily, simulations in Oganov et al. [2005] indicate slip along {010} in perovskite and {110} in post-perovskite would be more likely from an energy stand point, which involve the formation of stacking faults as the most favourable pathway for the phase transition. No specific orientation relationships are suggested in Oganov et al. [2005], however, and orientation relationships are only considered along the c direction (Figure 1.8). High pressure experiments and electron microscopy on the recovered $NaNiF_3$ samples in Dobson et al. [2013], show that the c-axis of the perovskite phase is preserved during the transformation to post-perovskite. Additionally, they observe the b-axis of the perovskite is perpendicular to the plane family $\langle 110 \rangle$ in post-perovskite, suggesting a martensitic relationship between the two phases. The relationship between the perovskite and post-perovskite structure in Dobson et al. [2013] is a 36° rotation around the common c axis after inversion of the a and b axes (Figure 1.8). We later test these transformation mechanisms in Chapter 3 on an $NaCoF_3$ analogue. Reconstructive transformations do not display clear orientation relationships between the parent and daughter phase. Atomic bonds are broken, destroying the original crystal structure, then growth of the resulting phase takes place through diffusive processes. Diffusive growth requires an abundance of defects in order for the grains to nucleate, which in turn has a direct impact on nucleation rate [Zahn, 2013]. An example of this process is presented in Zahn [2013], where molecular simulations at temperatures and pressures of the Earth's lower mantle, simulate the perovskite to post-perovskite transformation in $MgSiO_3$. The nucleation process requires a high activation energy, however, if reached allows for rapid oriented growth of post-perovskite grains. Interestingly enough, the transition speed ($10^3 - 10^4$ m/s) is on the same order of magnitude as shear and compressional wave velocities (7.26 and 13.7 km/s respectively) in the D" layer.

An example of a non-reconstructive transformation in bridgmanite is presented in Chapter 4 when transformed from ringwoodite + garnet. Nevertheless, we observe strong 001 transformation textures in bridgmanite due to oriented growth under stress rather than deformation.

1.3.4 Experimental Approach to Deep Earth Mineralogy

Interpretations of seismic anisotropy observed in the mantle requires the understanding of mineralogical microstructures and how they develop. Furthermore, these interpretations are needed in order to refine geodynamic models that aim to quantify flow and constrain deformation in the mantle. This requires experimental mineralogical data, which can provide a wealth of information, including measurements of texture, grain size, phase occurrence, etc. Textures generated during deformation experiments in polycrystalline pyrolite, for instance can be used to calculate seismic anisotropy and directly compared to observations of seismic anisotropy in the mantle. Deformation and transformation mechanisms responsible for these produced textures can later be determined through modeling. Unlike the upper mantle, where it is generally accepted that anisotropy is a result of preferred orientation in olivine, microstructures in the MTZ and lower mantle are not as well resolved. Here I will discuss a few of the most common experimental approaches used to study mantle microstructures in the lower mantle and hence bolster our knowledge of deep earth processes.

There are several deformation devices that are able to generate pressures and temperatures relevant to the conditions of the mantle. One such device is the rotational Drickamer apparatus, which allows for shear deformation and has been used to investigate strain weakening in bridgmanite and resulting shear localization in the lower mantle [Girard et al., 2016]. Another device that allows for simultaneous compression and heating is the deformation DIA (D-DIA), which has been used to perform viscosity measurements of bridgmanite in the dislocation creep regime [Tsujino et al., 2022] at temperatures between 1473 to 1673 K and pressures of 23 to 27 GPa. A particular advantage of the D-DIA is its ability to control strain rate and confining stresses, while also providing direct strain measurements using radiography images. The D-DIA is limited, however, in its ability to generate pressures relevant to the lower mantle. For this, the most common device used to deform samples in-situ is the diamond anvil cell (DAC).

The DAC has been used extensively in the high pressure community to perform deformation experiments that allow for the investigation of deformation and transformation microstructures in the lower mantle [Merkel et al., 2003, Komabayashi et al., 2007, Mu-

rakami et al., 2007, Miyagi et al., 2009, Miyagi and Wenk, 2016, Chandler et al., 2018]. When paired with a synchrotron energy source, X-ray diffraction images can be collected which provide information on the mineralogy of the sample including phases present, relative grain size, unit cell parameters, and texture. This data can then be applied to study the plasticity of mantle minerals [Miyagi et al., 2010] by identifying the specific deformation mechanisms responsible for the resulting microstructures. Furthermore, numerical modeling can implement these deformation mechanisms in order to study the effect of chemistry and strain rate of minerals such as bridgmanite [Carrez et al., 2007, Ferré et al., 2007, Mainprice et al., 2008, Boioli et al., 2017, Carrez et al., 2017], which are unable to be directly measured using current experimental techniques.

All of the experiments conducted in this thesis involve the application of pressure and temperature through the DAC paired with a monochromatic X-ray beam from a synchroton source to collect diffraction images. Details on radial diffraction and multigrain X-ray diffraction experiments, along with their data processing techniques are presented in Chapter 2.

1.4 A Focus on the Lower Mantle

In this next section I will provide a brief overview of the minerals that make up pyrolite below the '660'. This will include a list of identified slip systems and textures generated through transformation and deformation in past experiments. The first part will focus on (Mg,Fe)SiO_3 bridgmanite as it is the most abundant mineral in the mantle, followed by $CaSiO_3$ davemaoite and (Mg,Fe)O ferropericlase. Finally, a discussion on the transformation of bridgmanite to post-perovskite will be covered.

1.4.1 Bridgmanite

Deformation textures and associated slip systems in bridgmanite have been investigated using a series of experimental techniques. Radial diffraction experiments in the DAC performed by Merkel et al. [2003], Wenk et al. [2004b], Miyagi and Wenk [2016], Couper et al. [2020] all report 100 textures perpendicular to compression in bridgmanite upon deformation. In Miyagi and Wenk [2016] the transformation to pure bridgmanite from enstatite at 31 GPa results in a 001 transformation texture which remains through the

compression up to 56 GPa. In the same study bridgmanite + ferropericlase transformed from olivine at 33 GPa also results in a weak 001 transformation texture, however, this maximum slowly shifts to 100 at 61 GPa. Ringwoodite to bridgmanite + ferropericlase in Miyagi and Wenk [2016] results in a weak 100 transformation texture that grows in strength at 51 GPa. Bridgmanite transformed from olivine in Wenk et al. [2004b] also produces the same 100 transformation texture, but at 25 GPa with orientations remaining up to 43 GPa. In in an aggregate composed of bridgmanite, ferropericlase, ringwoodite, and stishovite, 100 orientations are observed as well at pressures of 37 to 39 GPa and 1000 K [Couper et al., 2020].

These deformation textures have also been modeled using visco-plastic self-consistent (VPSC) calculations, presented in Chapter 2. Slip systems responsible for the initial 001 orientations seen in bridgmanite + ferropericlase in Miyagi and Wenk [2016] are attributed to [100], [010], and ⟨110⟩ along (001) planes which are most active at pressures below 55 GPa; however at pressures above 55 GPa they see slip activity shift to [100], [010], and ⟨110⟩ along (100). This is consistent with textures observed in Wenk et al. [2004b] who suggest the initial (100) transformation texture is likely a result of mechanical {110} twinning and nucleation in orientations that minimize elastic strain energy. Textures observed in the mineral assemblage of Couper et al. [2020] are assigned to dominant slip in [010](100) with the remaining activity split between [001](100) and ⟨011⟩(100). Textures from uniaxial deformation experiments using the D-DIA in a study by Tsujino et al. [2016] are also compatible with dominant slip on [001](100). Studies by Cordier et al. [2004] show that dislocation creep is active at uppermost lower-mantle conditions in $MgSiO_3$, with slip along ⟨100⟩ possibly due to dislocation climb. Additionally, [100](010) slip in bridgmanite is modeled to show creep is dominated by dislocation pure climb [Boioli et al., 2017]. Furthermore, this mechanism does not produce texture, which is consistent with reports that seismic anisotropy is weak in the Earth's lower mantle.

Table 1.1: Most active slip systems in bridgmanite depending on pressure and temperature. All compositions of bridgmanite are pure $MgSiO_3$ with the exception of studies by Miyagi and Wenk [2016], Couper et al. [2020], and Tsujino et al. [2016] who use compositions $MgSiO_3$ + MgO, $MgSiO_3$ + Mg_2SiO_4 + MgO, and $(Mg_{0.97},Fe_{0.03})SiO_3$, respectively.

	Proposed Slip Systems in Bridgmanite		
Study	Slip or Twin System	P/T	Method
Wenk et al. [2004b]	{110} twinning	43 GPa/300K	DAC
Miyagi and Wenk [2016]	<55 GPa: [100],[010], ⟨110⟩(100) >55 GPa: [100],[010], ⟨110⟩(010)	65 GPa/300 K	DAC
Couper et al. [2020]	[010](100), [001](100), ⟨011⟩(100)	39 GPa/1000 K	DAC
Tsujino et al. [2016]	[001](100)	25 GPa/1837 K	D-DIA (Shear)
Mainprice et al. [2008]	[010](100)	30 GPa/300 K	First-principal calculations + VPSC
Ferré et al. [2007]	[100](001)	30 GPa/300 K	First-principal calculations
Hirel et al. [2014]	[010](100)	30-50 GPa/300 K	Peierls–Nabarro model
Kraych et al. [2016]	[010](100) [100](010)	30 GPa/2000 K 60 GPa/2000 K	Numerical modeling
Cordier et al. [2004]	[100]	25 GPa/1673 K	Multianvil + numerical calculations
Boioli et al. [2017]	[001](010)	25-26 GPa/1973-2273 K	Numerical modeling

Numerical modeling methods have been used to deduce information about slip systems in bridgmanite. First-principle calculations by Mainprice et al. [2008] indicate (100)[010] to be the most active slip system at all pressures in $MgSiO_3$ bridgmanite, while Ferré et al. [2007] suggest the [100](001) slip system as the easiest to activate in bridgmanite caused by dislocation glide. Modeling of dislocations in $MgSiO_3$ bridgmanite by Hirel et al. [2014], determine [010](100) edge dislocations are most mobile at between pressures of 30 and 50 GPa. Slip activities in bridgmanite have also been shown to vary depending on the pressures it is subjected to. Modeling dislocation glide in [100](010) and [010](100) at 30 and 60 GPa show a change in CRSS depending on what pressure is used; with CRSS values of [010](100) being much lower at 30 GPa and 2000 K than [100](010) at the same temperature [Kraych et al., 2016]. At 60 GPa the CRSS values of [010](100) becomes larger than [100](010), allowing easier slip along (010) planes. Table 1.1 provides a summary of proposed slip systems from other experimental and modeling studies in bridgmanite.

1.4.2 Other Mantle Minerals

In this section we will briefly overview two other major minerals observed in our experiments; $CaSiO_3$ davemaoite and (Mg,Fe)O ferropericlase. Textures in davemaoite have been documented in past DAC experiments, with observations of 001 orientations at pressures between 25.5 and 49.3 GPa and ambient temperatures [Miyagi et al., 2009]. Radial diffraction experiments in the DAC by Immoor et al. [2022] also report textures in 001 planes perpendicular to compression with texture strength increasing from 31.1 to 52.5 GPa at 1150 K. It has been suggested by Miyagi et al. [2006] that this texture is a result of $\{110\}\langle 1\bar{1}0\rangle$. We do not model slip systems of davemaoite in this work as it is considered a minor phase, around 6% by volume, in pyrolite.

Resistive heated DAC experiments on ferropericlase by Immoor et al. [2018] have reported strong textures in both 001 and 101 orientations at pressures between 20-80 GPa and 1400 K. Room temperature radial diffraction experiments in Merkel et al. [2002] also show 001 orientations perpendicular to compression in MgO starting at 5.3 GPa and increasing in strength until 35.4 GPa. These textures are a result of $\{110\}\langle 1\bar{1}0\rangle$ slip based on comparisons of the experimental textures to results from polycrystal plasticity [Merkel et al., 2002]. In contrast, other experiments in the DAC on bridgmanite + ferroperi-

clase aggregates have shown little to no texture in the ferropericlase phase [Miyagi and Wenk, 2016] when compressed between 33-61 GPa. In agreement, the radial diffraction DAC experiments of Couper et al. [2020] also observe random textures in ferropericlase between 28 and 39 GPa at 1000 K. Much like bridgmanite, observed textures have the potential to be impacted by the phases they coexist with. Numerical modeling by Reali et al. [2017] on MgO indicate dislocation glide is dominant at low ($\leq$ (600) K) and intermediate ($\leq$ (1000) K) temperatures; however, contributions from dislocation climb must be considered to model creep at higher temperatures ($1500 \leq T \leq 1800$ K). Additionally, slip systems modeled in Amodeo et al. [2012] using the Peierls–Nabarro model, find that there is an switch of active slip system between 30 and 60 GPa. CRSS values of $1/2\langle 110\rangle\{110\}$ are lower at pressures between 0 and 30 GPa, but increase at pressures between 60 and 100 GPa where $1/2\langle 110\rangle\{100\}$ becomes the easiest slip system to activate [Amodeo et al., 2012].

Experimental transformation textures in both davemaoite and ferropericlase are discussed in Chapter 4, with further calculations of anisotropy in single and polycrystal davemaoite. Although we do not observe transformation textures in ferropericlase, we do observe 010 and 111 orientations in davemaoite upon transformation. Further deformation and resulting textures of these two phases are also discussed in Chapter 5, however, orientations remain much the same.

1.4.3 Transition to Post-perovskite

Phase transformations in $MgSiO_3$ bridgmanite have been observed during high pressure and temperature DAC experiments; corresponding to depths of 2700 km near the base of the mantle [Murakami et al., 2004]. The transition involves a change of crystal structure in $MgSiO_3$ from orthorhombic perovskite (Pbnm setting) to orthorhombic post-perovskite (Cmcm setting). Transformation conditions of $MgSiO_3$ post-perovskite (between 119 and 125 GPa) coincide with the conditions of the D" layer, where there is a large contrast in physical properties including density, elastic moduli, and electrical conductivity [Murakami et al., 2007]. Hence, the D" layer is of great interest to mineral physicist and seismologist alike, as it marks a boundary through which a large amount of thermal energy is transferred and could contribute to dynamic and thermal evolution of the mantle.

Lattice preferred orientations in post-perovskite (pPv) when transformed from perovskite (Pv) are observed immediately upon transformation in deformation experiments. Results of these experiments vary, however, as textures observed depend on the starting material. Additionally, some pPv phases, like $MgSiO_3$ and $MgGeO_3$, are not stable at ambient pressures, making microscopy analysis on recovered samples impossible. The use of structural analogues such as $CaIrO_3$ and $NaCoF_3$ (both stable at ambient conditions) allow for postmortem analysis and require lower pressures and temperatures to induce a transformation, making quantitative deformation experiments less challenging.

Numerous experimental studies have observed transformation and deformation textures in natural composition $MgSiO_3$ post-perovskite [Merkel et al., 2007, Miyagi et al., 2010, Miyagi and Wenk, 2016, Xu et al., 2022] as well as in several analogues [Merkel et al., 2006, Niwa et al., 2007b, Yamazaki et al., 2006, Miyajima and Walte, 2009, Okada et al., 2010, Miyagi et al., 2011, Dobson et al., 2013, Hunt et al., 2016]. Many of these aforementioned studies also implement VPSC modeling to determine which slip systems are responsible for the produced textures. Furthermore, numerical modeling of dislocation cores based on the Peierls–Nabarro model have also been used to predict slip systems in $MgSiO_3$ and analogue pPv materials [Carrez et al., 2007, Metsue et al., 2009, Goryaeva et al., 2015a,b, 2017]. Details on the slip systems of pPv are not covered in this thesis, however, in which we focus on the transformation mechanisms of Pv to pPv structured materials.

Radial diffraction experiments performed in the DAC on the analogue $NaCoF_3$ is presented in Chapter 3 of this thesis. Here we induce a transformation from the Pv to pPv structure. We test various proposed orientation relationships in order to match a transformation model with our experimental observations and conclude on orientation relationships between Pv and pPv.

Chapter 2

Methods

2.1 High pressure experiments

Multiple synchrotron X-ray diffraction experiments were conducted using a laser-heated diamond anvil cell (DAC). Experiments were performed on beamline P02.2 of the PETRA III facility at the Deutsches Elektronen Synchrotron (DESY) in Hamburg, Germany. We use this beamline for both radial x-ray diffraction at high temperature and the collection of multigrain diffraction images, allowing the user to track individual grains, their composition, orientation, and size at relevant mantle conditions. Most of what is described here will focus on the multigrain diffraction experiments, even though one chapter of this thesis involves radial diffraction. Radial diffraction involves slightly different procedures which will be discussed separately. The data were collected over the course of four separate sessions at PETRA III which will be described later in this chapter.

2.1.1 Diamond anvil cell

The DAC is a device that allows its user to apply high pressure through uniaxial compression. The DAC can achieve pressures exceeding 750 GPa at ambient temperature [Dubrovinsky et al., 2015] and temperatures of 4700 K at 340 GPa [Tateno et al., 2012], which allows for the in-situ study of earth materials at relevant mantle and core conditions. These high pressures are generated due to the relationship between force (F) and area (A) where pressure is defined as $P = F/A$. The culet of the diamonds used are on the order of 100-300 μm and only requires a force of approximately 100 bars to generate 100 GPa of pressure to the sample. Diamonds are a favorable material for the application of high pressure experiments due to their mechanical properties (it is the hardest know material

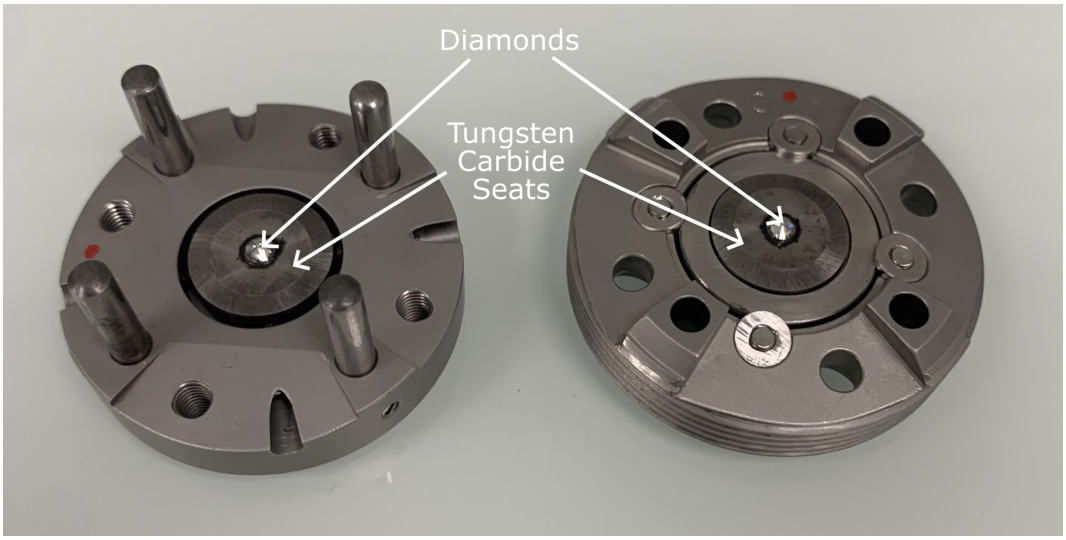

Figure 2.1: Open DAC with diamonds glued to tungsten carbide seats.

in existence) and the fact that they are transparent to X-rays and light. For most of the experiments detailed in this manuscript, a membrane diamond anvil cell (MDAC) from the company BETSA is used. The DAC itself is composed of two external steel pieces, generally a sliding piston and a stationary cylinder, that house the internal assembly (Figure 2.1). Within the DAC there are two tungsten carbide seats, one that sits inside a cup and the other flat, which allows for parallel and lateral alignment respectively between the diamond culets. The diamonds are glued to the seat using an epoxy and sit directly in the bevel of the seat which is aligned to the center of the DAC apparatus. Both the seats and external housing of the assembly have a wide angle window to allow the access and diffraction of the X-ray beam (Figure 2.2). In order to increase pressure in the DAC remotely, a gas pressure membrane is inserted on the piston side of the DAC that pushes on the back of the assembly; closing the distance between the diamond tips (Figure 2.2). This also allows for more precise control of pressure and ability to increase it in small increments.

The diamonds used for these experiments had culet sizes ranging from 100 μm to 250 μm in diameter. Diamonds with 100 μm culet size were beveled in order to prevent cupping of the diamond tips during higher pressure compression. In order to contain the sample placed between the two diamonds, a gasket made of rhenium must be indented and drilled. Rhenium is chosen as the gasket material due to its resistance to elastic

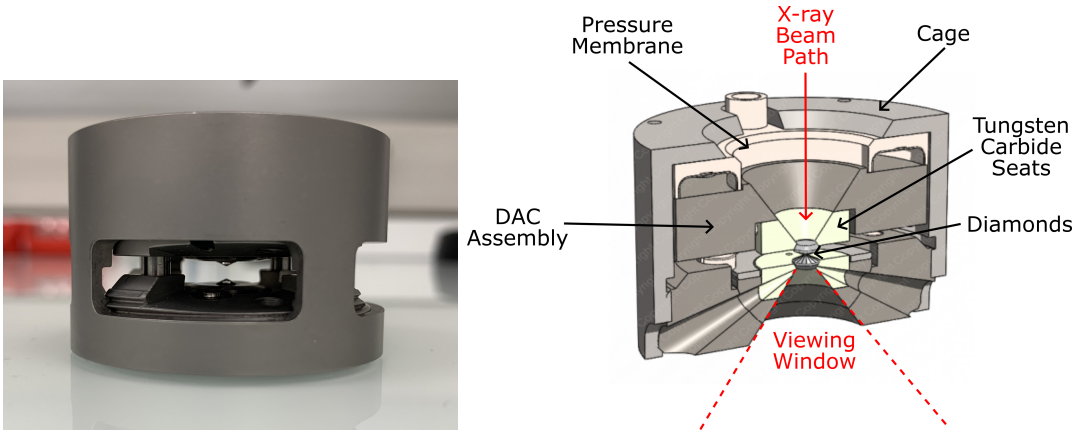

Figure 2.2: Left: Closed DAC assembly inside cage with pressure membrane inserted. Right: Cross section schematic of MDAC assembly from BETSA, with aligned diamonds glued to tungsten carbide seats, screwed into cage with pressure membrane. X-ray viewing window allows for 56° of rotation based on seats used in our multigrain diffraction experiments. Modified from https://www.betsa.fr/membrane-diamond-anvil-cell.html.

and plastic deformation between the diamonds. The gasket is first indented between the two aligned diamonds to a thickness between 25 μm and 30 μm by hand tightening four assembly screws. A hole is then drilled to serve as a sample chamber. It is important for the hole to be directly in the center of the gasket indentation in order to prevent the hole from extruding over the side of the culet during compression. The hole is made using a motorized electric discharge machine (EDM) or laser cutting machine and is generally 1/3 the diameter of the diamond culet. For our experiments we drilled 50, 100, and 150 μm holes depending on diamond culet size. For further details on the DAC assembly and its use refer to Jayaraman [1983].

2.1.2 Choice of pressure medium

A pressure medium is necessary in order to compress the sample as hydrostatically as possible and act as a thermal insulator while laser heating. Pressure mediums vary in composition and state depending on the conditions of the experiment. Liquid pressure mediums including alcohol mixtures such as methanol-ethanol mixed with H_2O, are hydrostatic up to 14.5 GPa at ambient conditions [Jayaraman, 1983]. Argon, nitrogen, neon, and helium gasses are also commonly used as pressure media. Argon, for instance, is both abundant and easy to load with; however, at pressures beyond 1.4 GPa at 300 K it solidifies [Klotz et al., 2009]. Helium becomes solid at 12.1 GPa at 300 K and also has a

well resolved equation of state in its solid state, giving it a clear advantage over the other gasses [Klotz et al., 2009].

For the experiments performed in this manuscript, KCl and MgO were chosen due to the high pressure and tempertures required. Both of these pressure mediums have several advantages including a well resolved high pressure equation of state [Speziale et al., 2001, Tateno et al., 2019], that allows for pressure calibration, and cubic crystallographic structure which limits the number of peaks in the diffraction patterns. An advantage of KCl is its ability to thermally insulate the sample due to its high melting point [Boehler et al., 1996] and lower thermal pressures, which can be as low as 10 GPa at 3000 K [Tateno et al., 2019]. This is useful in experiments where laser heating is used to induce a phase transformation or relax any shear stresses caused by the solid pressure medium. MgO has an even higher melting temperature than that of KCl [Boehler et al., 1997]. KCl and MgO grains were compressed between two tungsten carbide seats into small platelets using a hydraulic press and later loaded into the gasket inside the DAC assembly.

2.1.3 Pressure calibrant

The ability to extract accurate pressure readings exerted on the sample is necessary during high pressure experiments. This can be challenging for several reasons. Not only is there a difference between the force applied on the piston and the pressure exerted on the sample itself, but pressure gradients also exist within the DAC assembly across the diamond culets. Diamonds experience large elastic deformation in the region of the sample and vary greatly as pressure increases [Merkel et al.]. An internal pressure indicator is critical for accurate pressure readings of the sample.

Internal pressure indicators (or pressure gauges) such as ruby fluorescence luminescence [Mao et al., 1986, Datchi et al., 1997] and X-ray gauges [Anderson et al., 1989, Holmes et al., 1989] have been used in the past to accurately determine pressures within a DAC. X-ray gauges are used by measuring changes of volume within a material that has a well resolved equation of state [Dewaele et al., 2004]. Metals including platinum, tantalum, aluminum, copper, tungsten, and gold have been calibrated as pressure standards [Dewaele et al., 2004, Fei et al., 2007] as well as alkali halides [Dewaele et al., 2012, Tateno et al., 2019]. The advantage of using alkali halides is that they can be used as a pressure transmitting

medium and pressure calibrants. This allows for pressure measurements on the sample and pressure standard and the same diffraction location simultaneously, which reduces issues of pressure gradients within the DAC.

At ambient conditions, KCl takes a cubic B1 structure; however, once pressure exceeds 2 GPa it undergoes a phase transition to cesium-chloride B2 structure. This transition can be observed in all potassium halides when subjected to increasing pressures and the pressure at which the B1 B2 transition occurs depends on the material and varies greatly [Boehler et al., 1997]. With the transition to KCl B2, the K-Cl bond lengths increase making the bonds more compliant and thus thermally expandable [Walker et al., 2002]. As a result, the melting temperature of KCl increases significantly at higher pressures, which ensures the pressure medium will not melt during the laser heating process. As with all pressure gauges, pressures during the experiment are calculated by measuring the unit cell parameters in-situ and using an equation of state that relate pressure to changes in volume of the material. These equations of state are also determined experimentally, using single crystal X-ray diffraction and another pressure standard as a reference. For this series of experiments, both KCl and MgO are used as internal pressure indicators. The volumes were determined using unit cell values provided by X-ray diffraction throughout the experiments. For KCl, pressures were calculated using the equation of state from Tateno et al. [2019], which fits P-V-T data to the Vinet equation of state with the Mie-Grüneisen-Debye model for thermal pressure. For MgO, a third-order Birch-Murnaghan-Debye thermal equation of state from Speziale et al. [2001] was used.

2.1.4 Equations of state

An equation of state is a thermodynamic equation used to quantify the relationship between pressure, temperature, and volumetric change in a material. As such, there are several representations of these equations, each with different assumptions and mathematical derivations The Birch-Murnaghan equation of state is a finite strain equation of state and is expressed as a Taylor series in the finite Eulerian strain f_E, where $f_E = \frac{1}{2}\left[\left(\frac{V_0}{V}\right)^{2/3} - 1\right]$ [Angel, 2000]. The third-order form of the equation is written as follows:

$$P(V, 300K) = \frac{3}{2}K_0\left[\left(\frac{V_0}{V}\right)^{7/3} - \left(\frac{V_0}{V}\right)^{5/3}\right]\left\{1 + \frac{3}{4}\left(K_0' - 4\right)\left[\left(\frac{V_0}{V}\right)^{2/3} - 1\right]\right\} \quad (2.1)$$

Where V is volume and V_0 and K_0 represent the volume and bulk modulus at room temperature and zero pressure respectively. K_0' is the pressure derivative of the bulk modulus with respect to pressure at P = 0 GPa. The Vinet equation of state can also be used as a better representation of materials at higher compression and is written as follows [Vinet et al., 1987]:

$$P(V,T_0) = 3K_0\left(\frac{V}{V_0}\right)^{-2/3}\left[1-\left(\frac{V}{V_0}\right)^{1/3}\right]\exp\left\{\frac{3}{2}\left(K_0'-4\right)\left[1-\left(\frac{V}{V_0}\right)^{1/3}\right]\right\} \tag{2.2}$$

V, V_0, K_0, and K_0' are the same quantities as in the Birch-Murnaghan equation of state.

There is also the added effect of temperature on pressure which needs to be accounted for [Andrault et al., 1998]. To account for this a thermal equation of state is needed where volume depends on both pressure and temperature and describes the material's behavior at high temperatures. Pressure at a reference temperature, 300 K isotherm $P\left(V,300K\right)$, and thermal pressure with increasing temperature along isochors $P_{th}\left(V,T\right)$ are required. Pressure at any given temperature is represented by the following equation:

$$P(V,T) = P(V,300K) + P_{TH}(V,T) \tag{2.3}$$

To calculate thermal pressure, P_{TH}, the Mie Grüneisen Debye (MGD) model is used:

$$E(T,\theta_D) = 9nRT\left(\frac{T}{\theta_D}\right)^3\int_0^{\frac{\theta_D}{T}}\frac{t^3dt}{e^t-1} \tag{2.4}$$

where n is the number of atoms per formula unit, R is the gas constant, and θ_D is the Debye temperature. The Debye temperature is calculated using the following equation:

$$\theta_D = \theta_0\, exp\left[\frac{(\gamma_o-\gamma(V))}{q}\right] \tag{2.5}$$

where θ_0 and γ_0 are the is the Debye temperature and Grüneisen parameter at ambient conditions, q is an adjustment constant, and $\gamma(V)$ is the Grüneisen parameter at a given volume. Both θ_D and $\gamma(V)$ depend on the variation of volume with pressure and temperature. The Grüneisen parameter (γ) given by:

$$\gamma(V) = \gamma_0 \left(\frac{V}{V_0}\right)^q \tag{2.6}$$

where γ_0 is again the Grüneisen parameter at ambient conditions, q a constant, and V_0 the initial volume.

Thermal pressure can then be defined by:

$$P_{th} = \frac{\gamma(V)}{V} \left[E(T, \theta_D) - E_c(T_c, \theta_D)\right] \tag{2.7}$$

where E_c and T_c are energy and temperature at reference conditions. The thermal state of the system is therefore controlled by the three parameters: Debye temperature (θ_D), the thermal Grüneisen parameter (γ), and the constant q [Angel et al., 2018].

These equations of state along with the thermal parameters were used for pressure calculations of our pressure mediums KCl and MgO, in addition to the phases investigated within the samples [Tarrida and Richet, 1989, Andrault et al., 2001, Speziale et al., 2001, Nishihara et al., 2005, Wolf et al., 2015, Tateno et al., 2019].

2.2 Sample preparation

Multigrain Diffraction

Two different compositions were used during these series of experiments. The first is a pyrolite composition, which is largely considered representative of the average mantle [Ringwood, 1962a,b, Green and Ringwood, 1963]. It is made up of a mixture of minerals including 66.9% olivine, 12.5% diopside, 11.3% enstatite, and 9.3% garnet by weight. The second composition is referred to as a pyrolite-minus-olivine and consists as a mixture of 37.6% diopside, 34.1% enstatite, and 28.2% garnet by weight. Many of the proposed mantle compositions contain olivine content between 49-62% [Frost, 2008], including those based on chondritic ratios with lower olivine content and those based on mantle samples with higher olivine values. Two pyrolite-minus-olivine compositions have been proposed before. In Irifune [1987] pyrolite-minus-olivine contains between 44.5% and 46.2% SiO_2, while in Irifune and Ringwood [1987] SiO_2 content is 51.78%. The pyrolite-minus-olivine samples used in our experiments contain no olivine and are representative of an extreme case, which seeks to highlight the impact aluminum has on the phase transformations and

Table 2.1: Starting compositions for pyrolite and pyrolite-minus-olivine given by mixed mineral proportions in weight %. Below a list of sample names used in experiments that include the corresponding sample composition, maximum pressure achieved, pressure medium, and phases indexed.

Starting Composition	Olivine (wt.%)	Diopside (wt.%)	Enstatite (wt.%)	Garnet (wt.%)
Pyrolite	66.9%	12.5%	11.3%	9.3%
Pyrolite-minus-olivine	0%	37.6%	34.1%	28.2%
Sample	**Composition**	**Max P (GPa)**	**P Med.**	**Phases Indexed**
Pyr01	Pyrolite	108	MgO	Bm
Pyr02	Pyrolite	33	KCl	Rw, Gt, Bm, Dm, Fp
Pyr05	Pyrolite	50	KCl	Rw, Gt, Bm, Dm, Fp
Pyr07	Pyrolite	57.5	KCl	Rw, Gt, Bm, Dm, Fp
Pyr-Ol-1	Pyrolite-minus-olivine	25	KCl	Bm, Dm
Pyr-Ol-2	Pyrolite-minus-olivine	28	MgO	Bm, Dm

deformation of bridgmanite. Table 2.1 gives each samples composition in terms of mineral weight percentage, along with an overview of the sample names and information for the experiments ran at beamline P02.2.

To create these samples olivine, diopside, enstatite, and pyrope were ground into powders using a mortar and pestle with a target grain size of 1-2μm and then weighed and mixed. A piston-cylinder press was then used to sinter the samples at 2 GPa and 1000 °C for 30 minutes. The sample was then cut into individual disks using a diamond wire saw in order to be polished to the desired thickness. The polishing was carried out using a series of diamond polishing papers, starting at a 15μm grit, incrementally reducing the grit until 1μm. Afterwards diamond paste was used to polish at 1/4μm grit until the sample reached a thickness of 10μm. Throughout the process we check for scouring using an optical microscope until there are no marks left from abrasion (Figure 2.4a). Both sides of the sample are then coated with 500 nm of platinum using a GATAN 682 Precision Etching and Coating System (PECS). This allows the sample to couple during the laser heating process of the experiment and compensates for heterogeneous optical absorption of lasers by the crystals in the sample during phase changes. Afterwards, the coated samples were cut into smaller disks of 20μm in diameter using the laser machining apparatus equipped with a laser with femtosecond pulses at IMPMC, Sorbonne University, Paris.

For the sample to be analyzed in the scanning electron microscope (SEM), we had to perform an additional stage of ion polishing using a 1061 SEM Mill from Fischione Instruments. Using a Hitachi SU 5000 SEM, we collected a band contrast image and

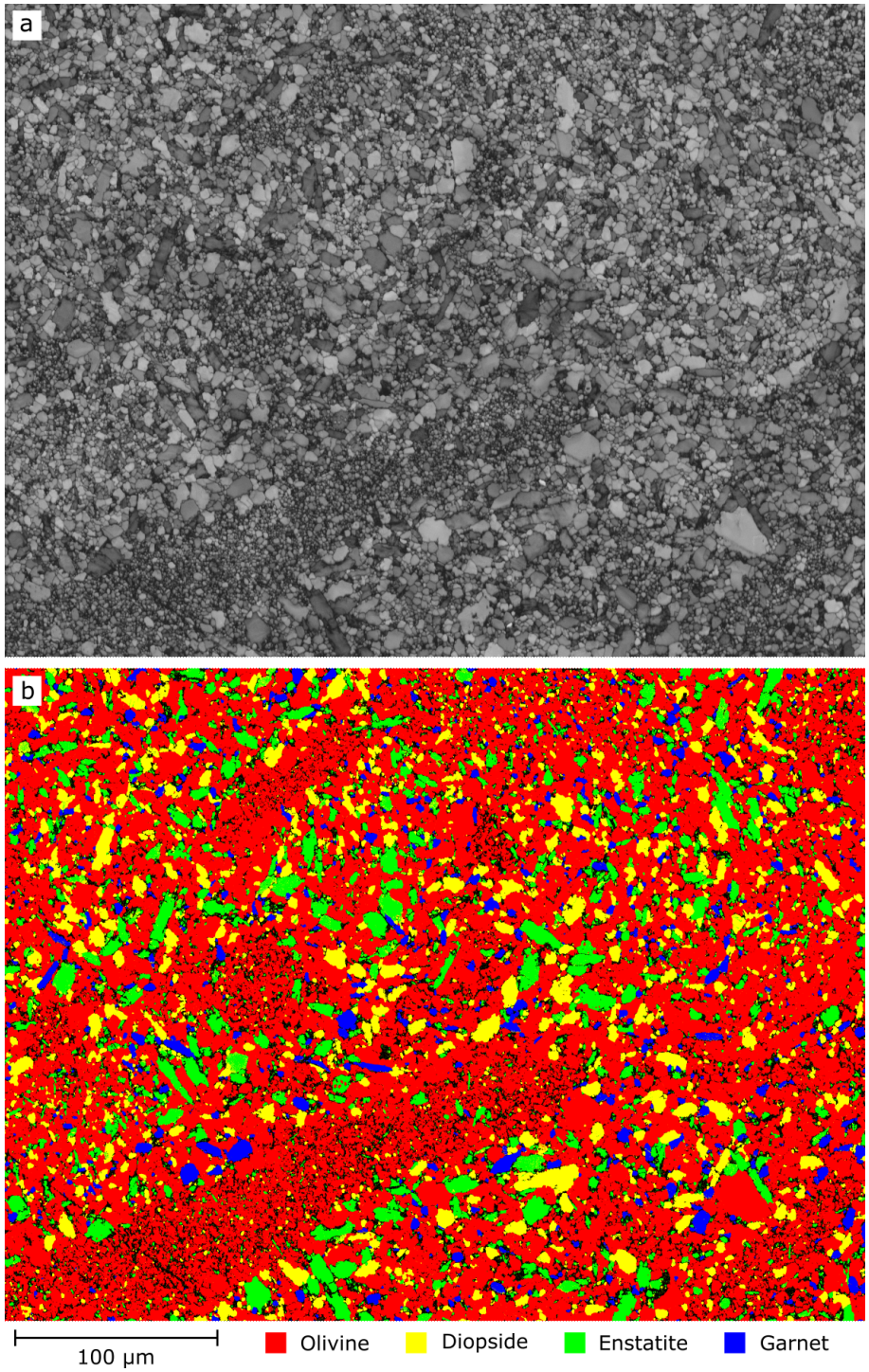

Figure 2.3: a) Band contrast image from scanning electron microscope of pyrolite sample. b) Phase map of same area. Red grains are olivine, yellow diopside, green enstatite, and blue garnet. Area proportions in fraction percent are as follows: olivine (61%), diopside (11.8%), enstatite (10.2%), garnet (4%), and not indexed (13%).

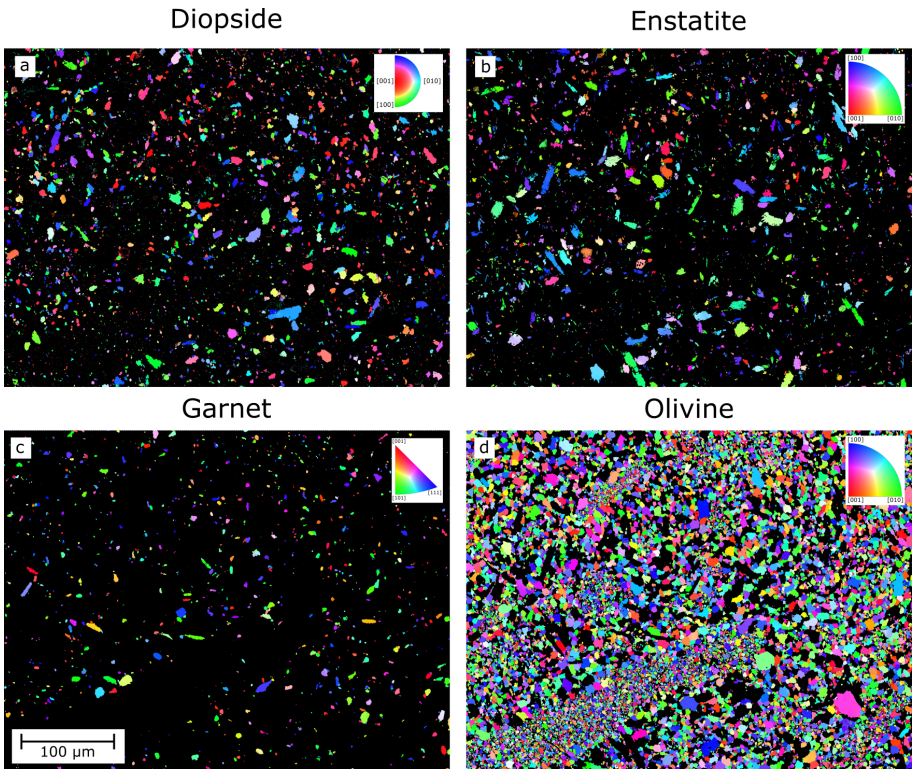

Figure 2.4: EBSD orientation map of the starting material. All grain orientations are random upon synthesis. a) Diopside b) Enstatite c) Garnet d) Olivine.

constructed a phase map of our sample in order to identify phases, their grain sizes, and distribution 2.3. We then collected electron backscattered diffraction images, which show our starting material was randomly orientated (Figure 2.4). Although grains of our starting material range from 1-10 μm after sintering in the piston cylinder press, they will synthesize at smaller sizes, on the order of 1 μm, upon transformation to ringwoodite (the starting point of our multigrain experiments).

A chemical map was also collected of our pyrolite sample using the SEM in order to confirm the phases presents after synthesis (Figure 2.5). In the EDS image, a variety of grains can be distinguished from differences in contrast. The chemical map allows us to determine what mineral each grain of the sample is. A 5μm grain of garnet can be seen in the EDS image, for instance, which is evidenced by its high aluminum content. This is further confirmed through electron microprobe analysis, which was performed to determine the exact sample chemistry, shown in Table 2.2. Garnet therefore contains the majority of the aluminum within our pyrolite.

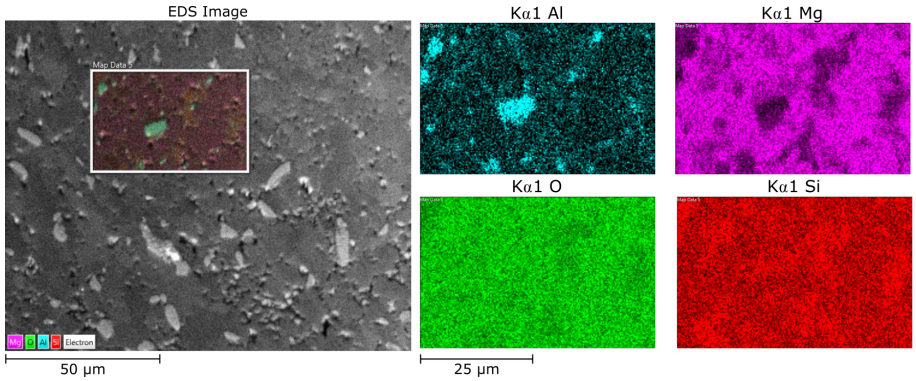

Figure 2.5: Chemical map of area selected on the energy dispersive spectroscopy image.

Table 2.2: Results from electron microprobe analysis of pyrolite sample. Oxides in each phase (olivine, pyroxene, and garnet) are reported in mass percent.

Oxide	Olivine (mass %)	Pyroxene (mass %)	Garnet (mass %)
SiO_2	41.091	58.556	38.163
Al_2O_3	0.008	0.114	21.625
CaO	0.010	0.152	0.756
TiO_2	0.005	0.042	0.011
Cr_2O_3	0.010	0.000	0.005
MnO	0.165	0.226	3.505
FeO	11.292	6.117	30.838
Na_2O	0.010	0.041	0.009
MgO	47.601	35.203	5.985
Total	100.192	100.451	100.897

Radial Diffraction

Sample preparation of powdered $NaCoF_3$ perovskite used in this experiment was performed by Dobson et al. [2011]. Finely ground stoichiometric mixtures of NaF and CoF_2 were packed into cylindrical Aluminum (Platinum) capsules 2.5 (1.2) mm in diameter and 2 (1.3) mm in length; then loaded into the MgO insulating sleeves. The samples were then synthesized in a Re-foil furnace with temperatures measured using W/Re thermocouples. Cold compression was carried out to the desired end-load followed by rapid heating, about 20 minutes, to 600°C. The temperature was maintained for 15 hours, then experiments were terminated by cutting power to the furnace and slow decompression over a period of 15 hours. The recovered samples were gently broken apart, placed on microscope slide coverslips, and dispersed using using propanol.

After the propanol is evaporated, the powdered $NaCoF_3$ perovskite was loaded into an X-ray transparent boron epoxy gasket with an 80 μm diameter hole. A platinum flake was

also loaded to be used as a pressure marker, using the thermal equation of state parameters of Zha et al. [2008] to calculate pressure.

2.2.1 Loading conditions

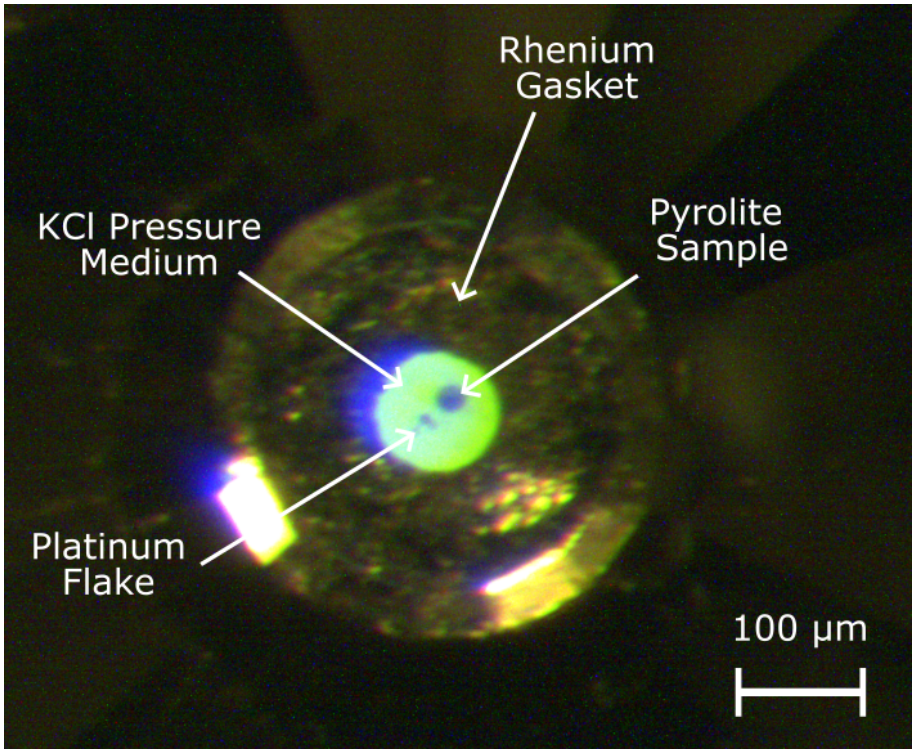

Figure 2.6: Loaded DAC viewed through an optical microscope.

Samples and pressure mediums were loaded using a micro manipulator from Micro Support under an optical microscope. First small platelets of KCl are loaded into the gasket hole ensuring the diamond is completely covered. After the sample and a flake of platinum are carefully loaded in the center in order to prevent any contact of the sample with the gasket. Finally, a few more platelets of KCl are loaded on top to cover the surface of the other diamond. An example of a loaded DAC as view from an optical microscope is shown in Figure 2.6. A gas bag was attached around the microscope in order to load in a controlled atmosphere of argon gas and prevent any hydration of the KCl or MgO (Figure 2.7).

Figure 2.7: Loading setup including micro manipulator and gas bag.

2.3 In situ measurements at the synchrotron

2.3.1 Characterization using X-ray diffraction

X-rays are a form of high-energy electromagnetic radiation with wavelengths ranging from 10 pm to 10 nm and energies between 124 eV and 124 keV. These properties make X-rays ideal for interactions with electrons at interatomic distances within crystallographic materials. Given the size of our samples, we use a synchrotron source that generates a bright monochromatic beam capable of small beam sizes. This allows for rapid image collection of about a second, which is essential for multigrain X-ray diffraction experiments and most DAC experiments.

In a crystal, atoms are repeated in an identical manner at regular intervals in three dimensions. These atoms create lattice planes which can be defined by their Miller indices (h,k,l). Diffraction of a X-ray beam is caused by the elastic scattering of photons when X-rays interact with the periodic arrangement of atoms within a crystal. Constructive interference causes the scattered X-rays to diffract a maximum intensities, resulting in conditions that satisfy Bragg's Law [Bragg, 1912]:

$$2d_{hkl} \sin\theta = n\lambda \tag{2.8}$$

Where d_{hkl} is the distance between atomic lattice planes, λ is the wavelength of the incident X-ray beam, 2θ is the angle between the diffracted beam and incident X-ray, and n is an integer. In our experiments λ is fixed along with d at a given pressure. This allows for the resulting diffraction pattern to be analyzed (Fig. 2.8), giving direct information on the structural properties of the sample including identification of phases, lattice parameters,

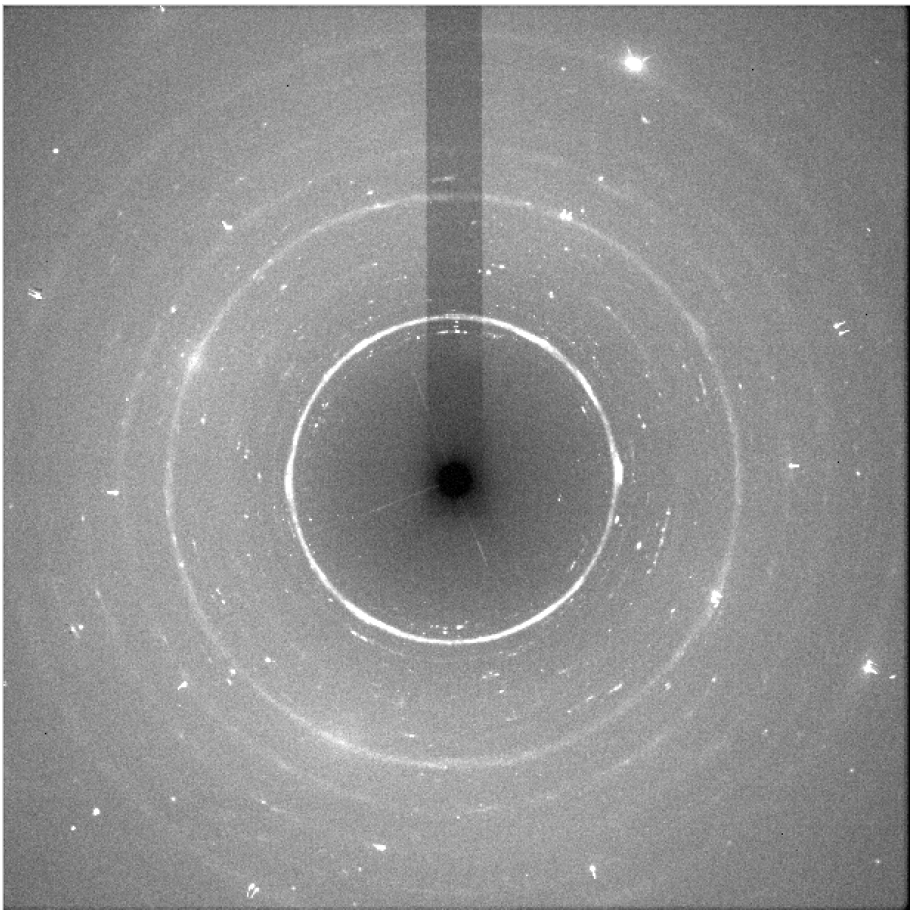

Figure 2.8: Multigrain diffraction image. Small bright spots are individual grains of the sample with powder parts and pressure medium diffracting as continuous concentric rings.

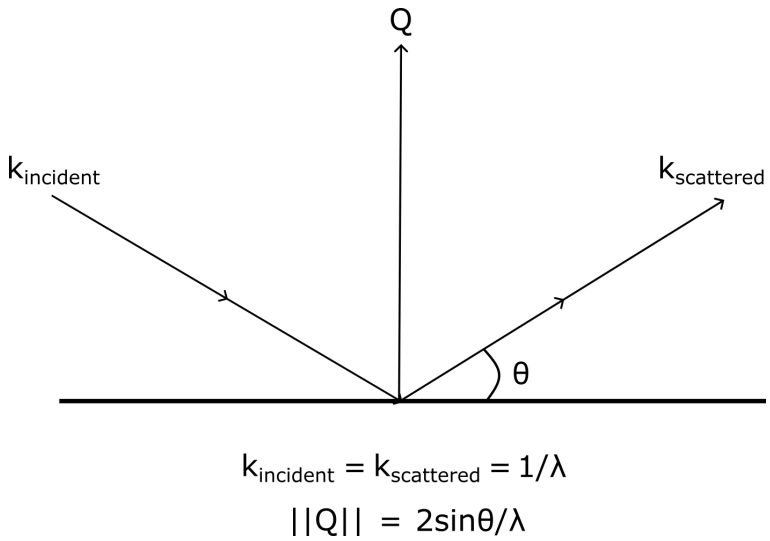

Figure 2.9: Laue condition for diffraction results in a general scattering vector $\mathbf{Q}$ that is equivalent to $\mathbf{G_{hkl}}$; the vector of the reciprocal lattice of the crystal whose norm is $1/d$.

strain, grain size, symmetry, and preferred orientation of grains.

Bragg's law expresses the condition for diffraction in a polycrystal; however, diffraction can also be described in terms of reciprocal space with a general scattering vector $\mathbf{Q}$. First described by Max von Laue, the scattering vector is defined as the difference in incident and scattered wave vectors of the X-ray beam, expressed as follows:

$$\mathbf{Q} = \mathbf{k_{scattered}} - \mathbf{k_{incident}} \tag{2.9}$$

where $\mathbf{k_{incident}}$ is the incoming wave vector and $\mathbf{k_{scattered}}$ is the diffracted wave vector. In diffraction, the interaction of X-rays with the crystal results in elastic scattering and both vectors' norm is $1/\lambda$. This results in $\|\mathbf{Q}\| = 2\sin\theta/\lambda$ (Figure 2.9). The Laue condition for diffraction is when $\mathbf{Q}$ equals $\mathbf{G_{hkl}}$, where $\mathbf{G_{hkl}}$ is a vector of the reciprocal lattice of the crystal:

$$\mathbf{G_{hkl}} = \mathbf{k_{scattered}} - \mathbf{k_{incident}} = \mathbf{Q} \tag{2.10}$$

$\mathbf{G_{hkl}}$ is referred to as the g-vector and a series of these are used to assign diffraction peaks to individual grains within the sample using multigrain X-ray diffraction techniques discussed later.

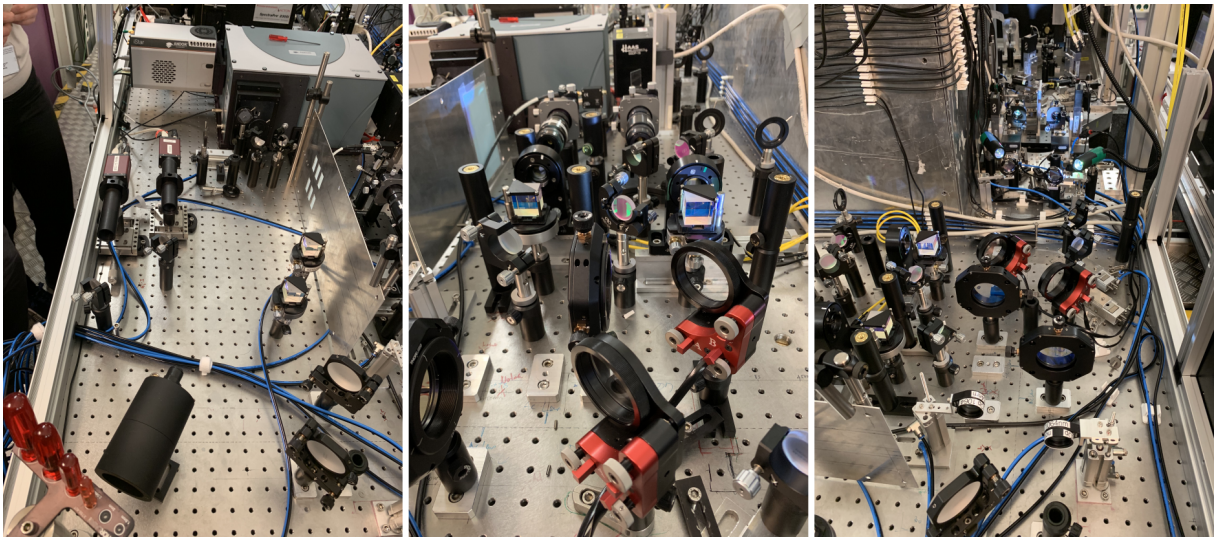

Figure 2.10: Laser heating system inside the hutch at beamline P02.2. Series of mirrors and focusing lenses direct the laser towards the sample and allows for temperature measurement using spectroradiometry [Konôpková et al., 2021].

2.3.2 Heating in the DAC

Resistive heating radial diffraction

Heating the sample within a DAC can be achieved using two methods, each with their own particular applications. The first method is to use a resistive-heated DAC as implemented in Liermann et al. [2009]. This method allows for homogeneous heating of the sample using an externally placed graphite sleeve, which reduces temperature gradients that are associated with laser heating methods. Restive heating is generally used for lower pressure experiments as degradation of the graphite heater occurs at higher pressures. Additionally, the graphite sleeve can cause oxidation of the cell and diamonds at higher temperatures. A modified version of the resistive heated DAC is used for experiments presented in Chapter 3, which implements a water-cooled vacuum chamber [Immoor et al., 2020]. The water cooling prevents the pistons of the DAC assembly from expanding, which reduces the friction between the piston and cylinder interface. The vacuum chamber also prevents the oxidation of the cell and diamonds.

Laser-heated multi-grain X-ray diffraction

The second method used for heating is performed externally using infrared lasers. Laser heating is used in order to achieve higher temperatures ($> 3000\ K$) during in-situ X-ray

diffraction experiments [Andrault and Fiquet, 2001]. Laser heating is more stable compared to heating using a graphite sleeve, because it does not require delicate components to be situated around the sample chamber. It does, however, have its share of disadvantages.

Laser heating requires the X-ray beam path to be in perfect alignment with the heating area, with the added challenge of keeping the optics aligned for temperature measurements. If the DAC is heated at higher temperatures, over time it can cause a shift of the heating area in relation to where X-ray measurements are being collected. This makes it difficult to get accurate temperature readings if not meticulously monitored. Additionally, the laser needs to be absorbed by the sample during the laser heating process. Samples containing silica are more difficult to heat than metals, as they do not couple as readily. To remedy this in our experiments, we powder coat the samples with a thin layer of platinum.

Diamonds also need to be insulated from the sample as laser heating is not as homogeneous as resistive heating techniques. If the sample comes in contact with the diamonds, the heat generated by the lasers will dissipate through the diamonds due to their high thermal conductivity. Here we use KCl or MgO as a pressure medium in order to prevent this. All of our experiments, implemented double-sided laser heating, using a series mirrors and optical focusing lenses at beamline P02.2 of the PETRA III (Fig. 2.10). Double-sided laser heating significantly reduces the temperature gradient within the sample.

2.3.3 Beamline parameters

Multigrain X-ray diffraction and radial diffraction data were collected during four separate sessions at beamline P02.2. As such, each of these experiments have a different series of experimental parameters. Here we will give an overview of the four sessions, separating them by date.

May 2016

Prior to the star of this thesis, a series of deformation experiments in the DAC were performed, with the resulting data being processed and published in 2021. A graphite resistive-heated radial DAC was used to perform a uniaxial compression experiment on a polycrystalline sample of $NaCoF_3$. An incident monochromatic X-ray beam focused to 5.8 x 3.2 μm^2 and Perkin-Elmer XRD1621 detector with 200 μm x 200 μm pixel size were used

to capture the diffraction images. A CeO_2 standard from National Institute of Standards and Technology (NIST; 674b) was used for calibration in order to correct for detector tilt and calculate a sample to detector distance of 438.35 mm. Wavelength was fixed at 0.4908 Å.

March 2019

Samples Pyr02, Pyr05, and Pyr07 were ran using an incident monochromatic X-ray beam focused to 1.4 μm x 1.9 μm. A PerkinElmer XRD 1621 detector with 200 μm x 200 μm pixel size was used to capture the diffraction images. A CeO_2 standard from the National Institute of Standards and Technology (NIST; 674b) was used for calibration in order to correct for detector tilt, beam center, and calculate a sample to detector distance of 551.5828 mm. The wavelength for these experiment was fixed at 0.2898 Å.

December 2019

Sample Pyr-Ol-1 was ran using an incident monochromatic X-ray beam focused to 1.9 μm x 1.9 μm paired with a PerkinElmer XRD 1621 detector with 200 μm x 200 μm pixel size. A CeO_2 standard from the National Institute of Standards and Technology (NIST; 674b) was used for calibration in order to correct for detector tilt, beam center, and calculate a sample to detector distance of 404.5133 mm. The wavelength for this experiment was fixed at 0.2891 Å.

October 2020

Samples Pyr01 and Pyr-Ol-2 were ran using an incident monochromatic X-ray beam focused to 1.2 μm x 1.9 μm paired with a PerkinElmer XRD 1621 detector with 200 μm x 200 μm pixel size. A CeO_2 standard from the National Institute of Standards and Technology (NIST; 674b) was used for calibration in order to correct for detector tilt, beam center, and calculate a sample to detector distance of 403.4252 mm. The wavelength for this experiment was fixed at 0.2904 Å.

2.3.4 Radial X-ray diffraction

Crystalline materials can be studies numerous ways using X-ray diffraction techniques. One of the more commonly used techniques for deformation experiments in the DAC is radial

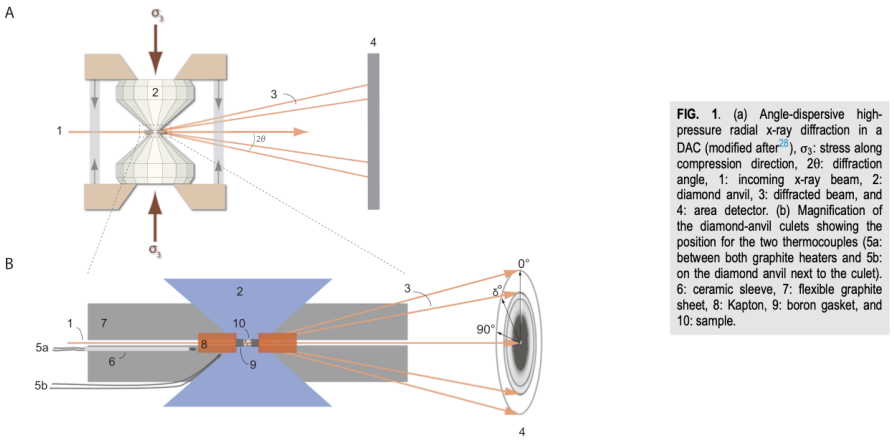

FIG. 1. (a) Angle-dispersive high-pressure radial x-ray diffraction in a DAC (modified after[28]), σ_3: stress along compression direction, 2θ: diffraction angle, 1: incoming x-ray beam, 2: diamond anvil, 3: diffracted beam, and 4: area detector. (b) Magnification of the diamond-anvil culets showing the position for the two thermocouples (5a: between both graphite heaters and 5b: on the diamond anvil next to the culet). 6: ceramic sleeve, 7: flexible graphite sheet, 8: Kapton, 9: boron gasket, and 10: sample.

Figure 2.11: Experimental setup of radial X-ray diffraction from Immoor et al. [2020]. X-ray beam passes through the boron gasket material and sample in the radial direction. Concentric diffraction rings from powder sample.

diffraction [Merkel et al., 2002, 2003, 2004, 2006, Wenk et al., 2006, Merkel et al., 2007, Niwa et al., 2007a, Liermann et al., 2009, Miyagi et al., 2009, Hirose et al., 2010, Miyagi et al., 2013, Immoor et al., 2020, Gay et al., 2021]. Radial diffraction experiments generally use powdered samples where many individual grains are loaded into a gasket and essentially allows all (hkl) planes of the sample to be detected when in contact with the incident X-ray beam in the form of concentric circles referred to as Debye rings (Figure 2.11).

During the deformation or phase transformation of a material, these individual grains can orient themselves in specific preferred orientations. This is referred to as crystallographic preferred orientation (CPO) or texture. In the case of texture development, the Debye rings will vary in intensity along δ, in Figure 2.11, with higher intensities among diffracting planes that are preferentially oriented and weaker intensities among grains that are not in favorable orientations.

X-ray diffraction can be utilized in order to extract information about the sample including the structural properties of the sample, phases present, lattice parameters, stress, strain, grain size, symmetry, and preferred orientation of grains. To achieve this we use the software MAUD [Lutterotti et al., 1997], which uses the diffracted peak positions, their intensities, and a series of experimental parameters to perform a Rietveld refinement [Rietveld, 1969]. This refinement uses a least squares method to fit a calculated diffraction profile to the one collected during the experiment. After the refinement process is completed, we are able to extract detailed information on the phases present in our sample

including phase identification, the unit cell values (used to calculate pressure using an equation of state), stress, crystallite size, which (hkl) planes are responsible to intense peaks, and more. The Rietveld refinement process use in MAUD is described in more detail in the 2.4 section of this chapter.

In a powder diffraction images, however, the parameters extracted are averages of the overall diffracted volume of the sample. If one wants to extract information about individual grains within a polycrytalline sample, multigrain X-ray diffraction (MGC) is required.

2.3.5 Multigrain X-ray diffraction

Multigrain X-ray diffraction allows for extraction of individual grains, their orientations, and grain size distributions. We are able to monitor phase transformations and study deformation microstructures in-situ. The pyrolite samples contain a mixture of different phases and grain sizes including both powder and larger grains on the order of $< 1\mu$m - 2μm. In the 3DXRD images, the powder portion of the sample will diffract as continuous rings which are weak in intensity, whereas the larger grains in the sample will generate more intense diffraction peaks in the form of spots on the detector (Figure 2.12). The idea behind this technique is to extract the individual diffraction peaks from the images and assign them to individual grains within the sample. This technique requires intensive data processing, which will be explained in the following section of this chapter.

In these multigrain X-ray diffraction experiments compression and heating of the sample are conducted simultaneously to monitor transformations and deformation in situ. Pressures and occurrence of corresponding phases are identified during the experiment using powder diffraction images collected in situ at high P/T and analyzed in the software Dioptas [Prescher and Prakapenka, 2015]. Quenching the sample to ambient temperature is required to collect MGC data with the layout used in this work. During the data collection process, the DAC, which is fixed to a stage, is rotated in ω in incremental steps perpendicular to the X-ray beam with diffraction spots being captured on a detector (Figure 2.12). It is necessary to collect many images in order to improve data coverage and generate as many diffraction peaks as possible. Image collections are acquired as close to the transformation conditions as possible in order to observe microstructures immediately

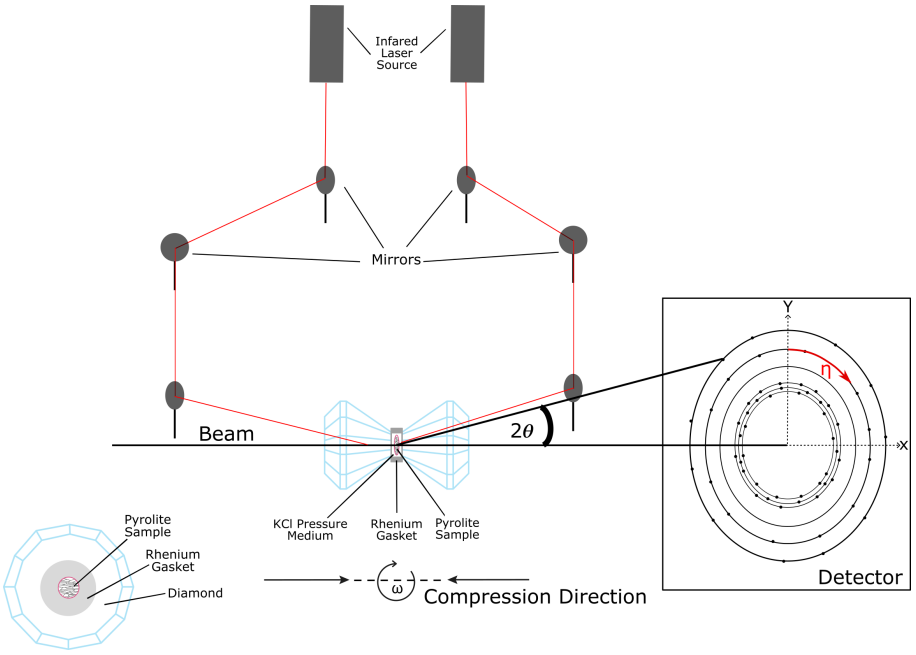

Figure 2.12: Experimental setup of multigrain X-ray diffraction as viewed from above. X-ray beam passes through the diamonds and sample in the axial direction. Cell assembly is rotated in ω from $-28°$ to $28°$ with images collected every $0.5°$ step. Concentric diffraction rings from powder part of the sample and pressure medium with spots from individually diffracting grains of sample material. Artifacts such as diamond reflection spots and shadows cast from the gaskets during rotation at high angles are removed in the data processing stage before diffraction peaks can be extracted. Bottom left is a view of the sample inside the gasket as viewed in the direction of the X-ray beam.

before and after the transition. The MGC experiments presented in the following chapters investigate both transformation and deformation microstructures in pyrolitic materials at pressure and temperature ranges of 17-108 GPa and 1500-2000 K, respectively.

2.4 Data processing

2.4.1 Radial diffraction

Radial diffraction data analysis is performed using the program MAUD (Material Analysis Using Diffraction) [Lutterotti et al., 1997] following the general refinement procedure outlined in Wenk et al. [2014]. Refinements rely on a Rietveld least-squares fitting method by fitting diffraction peak intensities to the data.

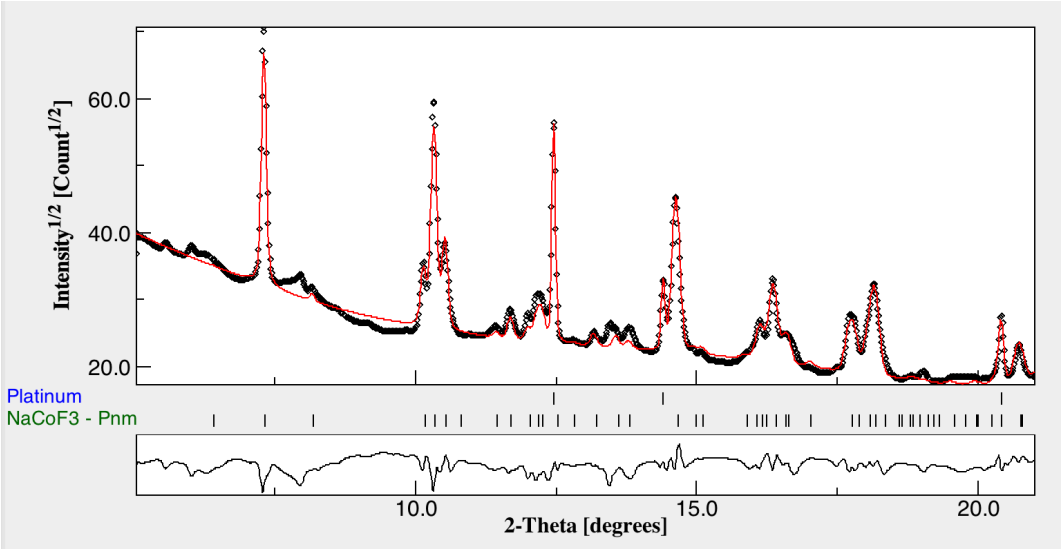

Figure 2.13: Powder diffraction profile of $NaCoF_3$ perovskite at 1.1 GPa and 868 K. Diffraction intensity vs 2θ. Black line is the data and red line the fit to the data after Rietveld refinement.

The first step is to refine the instrument parameters within MAUD including sample to detector distance, detector tilt, and beam center by using a well know standard such as CeO_2 standard from NIST (674b). The wavelength of the X-ray beam must also be provided. After this step, the powder diffraction images are imported and integrated over 5° azimuthal arcs into 72 spectra. A profile of the diffraction peaks can then be viewed as intensity vs 2θ (Figure 2.13). Individual phases that make up the sample are then imported in the form of crystallographic information files (.cif), which contain information including the unit cell parameters, space group, associated symmetry operations, and atomic

positions within the unit cell. Background and lattice parameters are first refined before proceeding with the refinements of microstructures and texture.

In the case of a sample with multiple phases, MAUD can refine sample proportions by volume fraction. To do this, the beam intensity and each phase is provided a scale factor which are optimized during the refinement process. The refined scale factors are then used to compute the volume fractions of the phases. In the case of our radial diffraction experiments presented in a subsequent chapter, we only analyze a single phase, thus it is not necessary for our study.

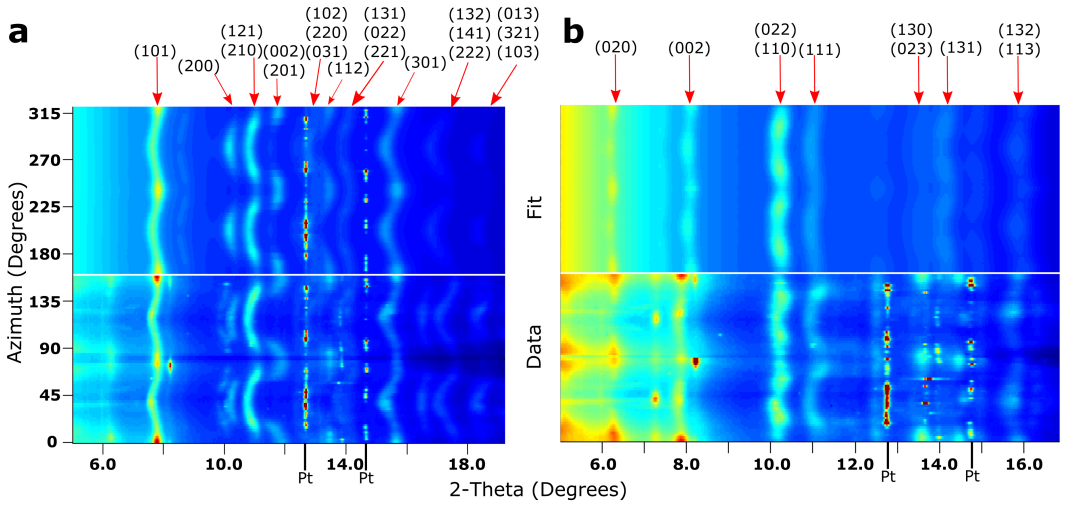

Figure 2.14: a) Unrolled diffraction image of $NaCoF_3$ perovskite at 20.1 GPa and 997 K, immediately before transformation to post-perovskite. Below: measured diffraction (labeled data). Above: diffraction image recalculated by MAUD (labeled fit). Diffraction peaks of perovskite are labeled by their Miller indices and platinum peaks are indicated by Pt. b) Diffraction and fit for post-perovskite phase at 26.1 GPa and 1013 K.

Microstructural information such as crystallite size and microstrains are determined from peak line broadening. Differential stress can also be calculated by providing elastic properties of the phases of interest and performing a fit according to the displacements of peak positions with orientations. To determine texture of the sample an orientation distribution function (ODF) is calculated. The ODF is a probability distribution function to find an orientation, which is normalized over the entire sample. An ODF with a multiple of random distribution (m.r.d) of one indicates a random texture. Values greater or smaller than one indicate texture within an aggregate of grains. Texture is expressed in the azimuthal intensity variations. Diffraction images can be viewed as an unrolled

diffraction image plotted as 2θ vs. azimuth (Figure 2.14), where families of diffracted hkl can be identified after Rietveld refinement is performed. Diffraction lines vary in position and intensity as a result of stress and texture as a result of compression. At the end of the refinement process we extract lattice parameters, normalized stress, and crystallite size measured in the experiment.

2.4.2 Multigrain diffraction

An overview of the data processing techniques will be given below; however, extensive reviews of MGC techniques have been published by Oddershede et al. [2010], Sørensen et al. [2012], Rosa et al. [2015], and Langrand et al. [2017]. After the multigrain images are collected, they need to be processed in order to extract diffraction peaks and assign them to individual grains within the sample (Figure 2.15). To do this we we use the open source software package FABLE-3DXRD, which is available at https://github.com/FABLE-MGC and other tools developed as a part of the TIMEleSS project: https://github.com/FABLE-3DXRD/TIMEleSS. A manual describing these data processing techniques can be found at: http://multigrain.texture.rocks/doku.php.

We begin this process by creating a median image of all the images collected and subtracting it from each individual image in the series. This eliminates the background noise, pressure medium, and any other artifacts (Figure 2.16b). From there it is necessary to mask the diamond reflections which have high intensities and are generally present across large regions of the detector (Figure 2.16c). Once this is accomplished, we perform a peak search using a script, which will select peaks based on a user set intensity threshold; where everything above the set threshold will be identified as a peak, and those below ignored (Figure 2.16d).

The extracted peaks can then be plotted as a histogram as the number of diffraction spots in counts, which allows for the peaks to be easily identified (Figure 2.17). Prior knowledge of which phases might be present in our sample are needed in order to extract the necessary unit cell parameters. Only then, after the phases in the sample are identified can we carry on with the refinement and grain indexing processes. During the experiment we use Dioptas to check for the expected phases in our sample, which also provides a rough estimate of the unit cell parameters of each phase. We use the EoSFit program [Gonzalez-

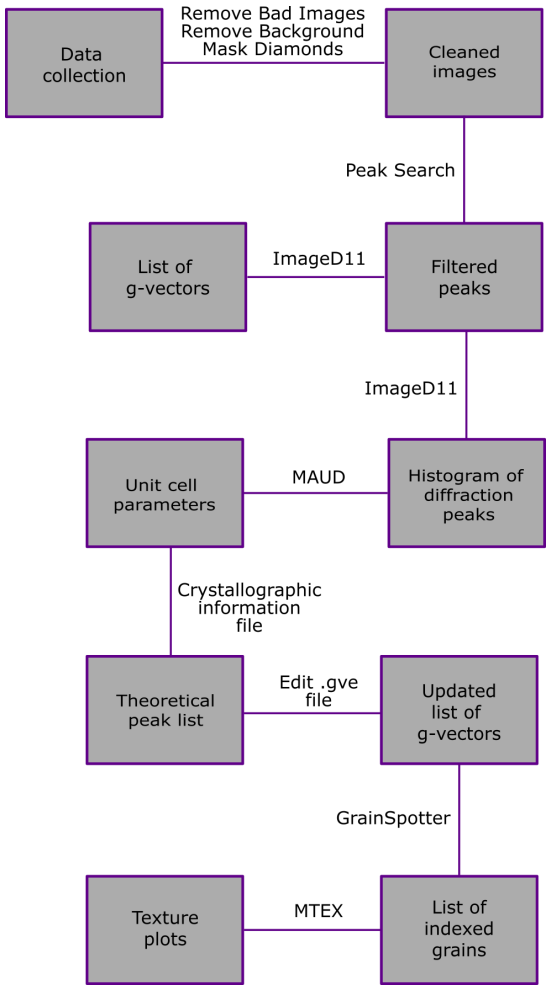

Figure 2.15: Flow chart of data processing steps for multigrain crystallography data.

Platas et al., 2016] in order to provide a better estimation of unit cell parameters, which are further refined in MAUD. The histogram is loaded into MAUD, where a least squares fit is performed in order to obtain our final unit cell values (Figure 2.17). The analysis of this spectrum is not a true Rietveld refinement, however, because the data in the histogram is a number of single grain peaks rather than a true peak intensity.

Once the peaks are extracted and phases identified, the peaks are imported into ImageD11, providing the experimental conditions (wavelength, sample to detector distance, detector tilt, etc.), and their detector coordinates are converted into 2θ, ω, and η angles. Here we are able to compute a list of diffraction vectors, which are normal to the crystallographic planes responsible for the generated diffraction peaks. These vectors, called g-vectors (ghkl), are represented in reciprocal space with a length $ghkl = 1/dhkl$, where dhkl distance is the diffracted set of hkl planes.

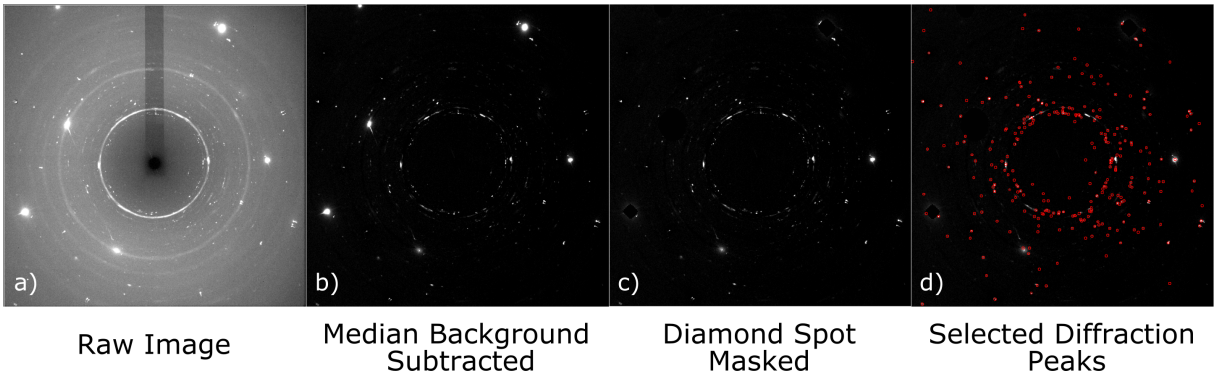

Figure 2.16: Image cleaning process of real data. a) Single raw diffraction image collected during 3DXRD b) Diffraction image with median background subtracted. c) Diffraction image with diamond spots masked. d) Red circles are peaks selected based on intensity after background subtraction and diamond spot masking.

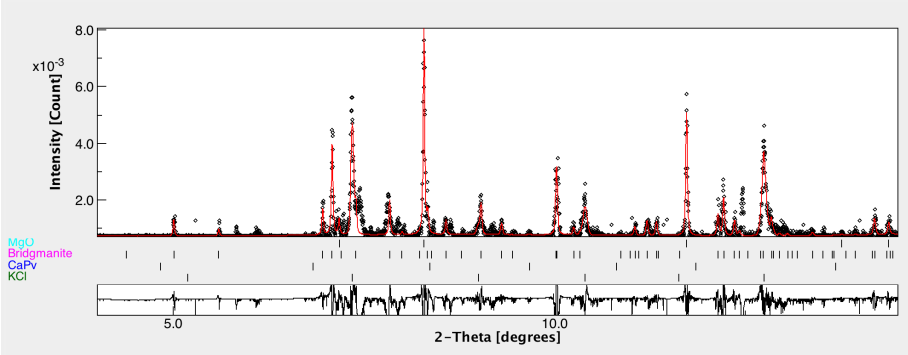

Figure 2.17: Histogram of selected peaks from peak search loaded into the software MAUD. Black line is the number of extracted single-grain diffraction peaks vs. 2θ and the red line is a fit.

To improve the accuracy of our grain indexing in the final stages of processing, we calculate theoretical peak positions using a crystallographic information files for each phase present, and experimental conditions such as wavelength, sample to detector distance, and detector tilt. Providing the script with the crystal structure contained in the file, a new set of *dhkl* and theoretical intensities are generated. Implementing Bragg's Law, the script also calculates the associated 2θ position of the diffraction peaks, which we use to update the existing list of g-vectors generated by ImageD11.

The final step involves the use of the GrainSpotter software [Schmidt, 2014]. GrainSpotter calculates a list of hypothetical g-vectors from randomly oriented grains of the phase being searched for based on provided experimental parameters, crystal symmetry, and refined lattice parameters. It then attempts to match these theoretical g-vectors to the experimental values in orientation space using a series of thresholds set by the user. These

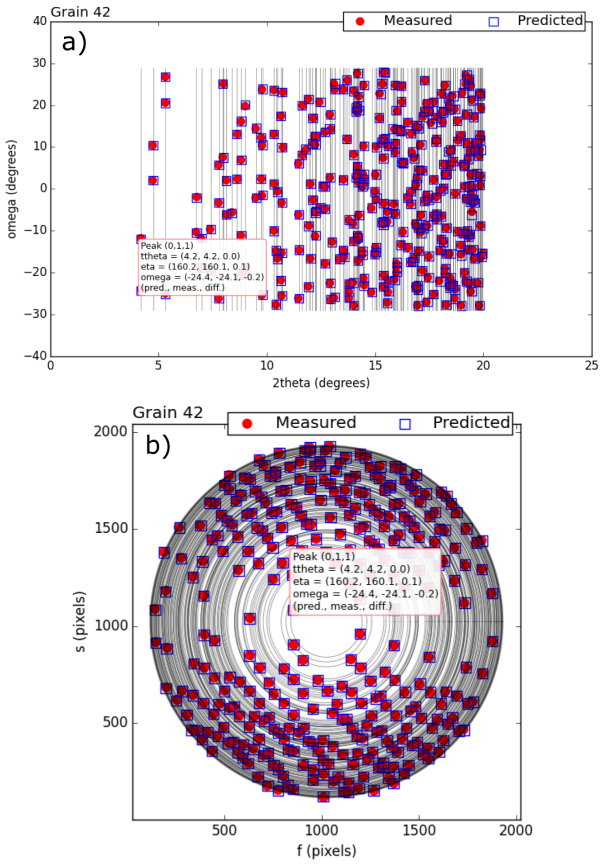

Figure 2.18: Single grain of bridgmanite. a) Measured diffraction peaks of bridgmanite marked as red dots with predicted locations indicated as blue boxes plotted as 2θ vs. ω. b) Same grain of bridgmanite plotted along XY coordinates as Debye rings.

thresholds include angular tolerances of 2θ, ω, and η as well as a minimum completeness ratio. Minimum completeness describes what percentage of expected g-vectors must match a given grain orientation in order to be assigned to that grain. For example, if a crystal should have 10 peaks measured in an experiment, and the completeness is set to 70%, 7 of the 10 theoretical g-vectors would be required to match the experimental g-vector locations in order for a grain to be considered indexed.

GrainSpotter is used in a loop in order to index multiple phases simultaneously, as opposed to indexing a single phase each time it is ran. Searching for multiple phases requires a unique list of theoretical g-vectors for each phase, in order to prevent any overlap that might cause redundant peak assignment to the same grain. Uncertainties are also set individually for each phase, with stricter tolerances set at the beginning of the loop that eventually become more broad with each iteration in order to assign as many g-vectors to

grains as possible. This becomes increasingly difficult when phases of similar symmetry are present. At the end of each loop, any g-vectors that were assigned to grains are then removed from the list of unassigned g-vectors in order not to assign the same g-vector to a grain multiple times. This process alternates between each phase before each loop is completed.

GrainSpotter provides information on the number of grains indexed for each phase, the list of assigned diffraction peaks (g-vectors) to each grain, and what percentage of the total theoretical g-vectors were assigned. Figure 2.18 shows an example of predicted g-vectors matched to the measured for a single bridgmanite grain within the sample. After this process is completed, we obtain a series of individual grain orientations, for which orientations can then be plotted as inverse pole figures.

2.5 Data interpretation

2.5.1 Texture modeling with VPSC

Texture development in a polycrystaline material can be generated by dislocations, which are a result of crystallographic defects or other irregularities within the crystal structure, caused by plastic deformation. Other factors including deformation geometry, total strain, and starting texture also impact the development of texture. Slip can occur on multiple different lattice planes within the crystal during deformation; however, determining which slip systems are responsible for the observed preferred orientations is not always clear. Interpretation of experimental textures requires the application of numerical modeling, which we apply to bridgmanite in chapters 3-5.

Here we apply a visco-plastic self-consistent (VPSC) model, using code developed by R. Lebensohn and C.N. Tomé at Los Alamos, to determine which slip systems are responsible for observed experimental textures in our DAC samples. VPSC allows for deformation of a virtual polycrystal in small increments, at which point the orientation of the grains are calculated at each step of deformation. This code has been used in multiple studies in high pressure research [Mainprice et al., 2008, Miyagi and Wenk, 2016, Kaercher et al., 2016]. In our simulations each grain is treated as an ellipsoidal inclusion within a homogeneous matrix, accounting for individual grain shape. As plastic deformation is generated, indi-

vidual grains rotate with the flow field and assume distorted shapes and aspect ratios. As such, properties of the polycrystal matrix is calculated as an average of the properties of each grain.

In order to run the deformation simulation, the code requires a file describing the crystallography of the phase of interest; containing a list of possible slip systems, in addition to an input file that generates a number of, generally 3000, orientations (either random or orientations from a previously generated texture). Increments of deformation are set by the user with orientations of grains and slip system activity being calculated at the end of each step. The output files provide information on the activity of each slip system and their direction at each stage of deformation as well as a texture output file that is generated as a result of the deformation.

VPSC simulations require an input file which contains information about the crystal including crystal symmetry, possible slip systems and their equivalent slip planes, and critical resolved shear stress (CRSS) values for each slip plane. The texture files provided at the end of the simulation depend on the choice of slip system and CRSS values, which are threshold values of stress. Once the CRSS value is exceeded, slip will occur along the plane in the specified direction. A low CRSS value will not require as much stress as a high value to generate slip, for instance. An example of such file is shown in Figure 2.20 and 2.21.

Here we will demonstrate how changing CRSS values impact the resulting textures generated during VPSC simulations. We will use an example directly from Chapter 5 where we model experimental deformation textures in bridgmanite under uniaxial compression. We use MTEX to plot the inverse pole figures by providing the output texture files from the simulation. In this example, bridgmanite begins from a 001 transformation texture (Figure 5.6a).

In our example file, lines 17-72 in Figure 2.20 provide VPSC with the modes of slip for a given plane and direction that are to be tested. The CRSS values for each individual slip system can be found in Figure 2.21. For example, the (100)[001] slip system has a CRSS value of 1, as indicated by the first integer in Figure 2.21 line 83. Slip systems that allow slip along (100) and (010) planes, i.e. lines 77, 81, 85, 93, and 97, have low CRSS

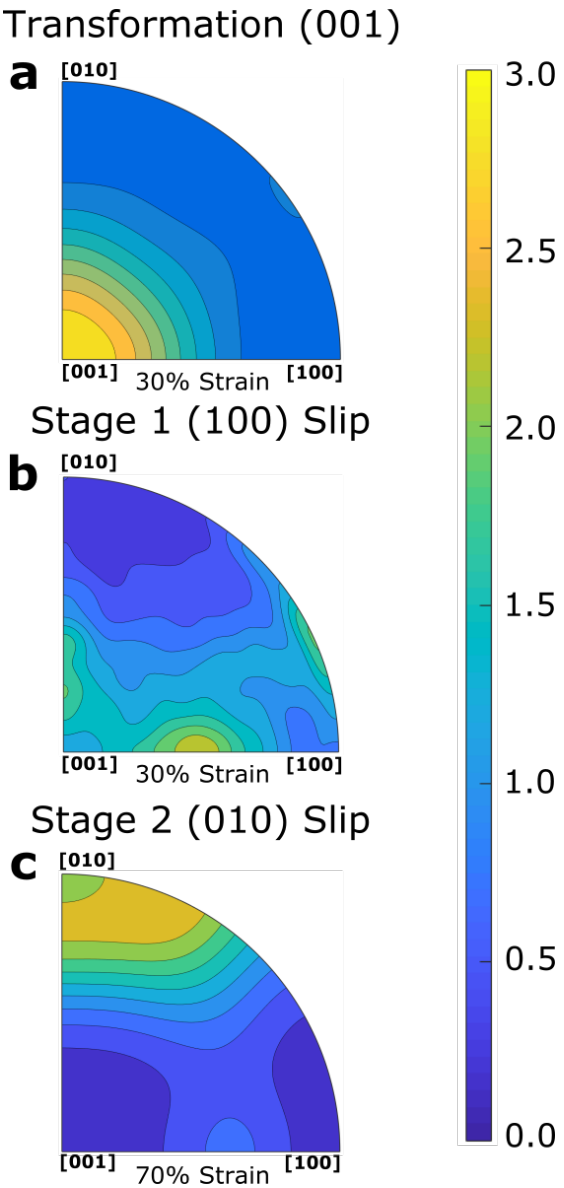

Figure 2.19: Inverse pole figures (a, b, c) of axial compression in VPSC simulation. Starting from transformation texture (a) applying 30% axial strain and allowing dominant slip on (100) planes generates (Fig. 5.6b). Second stage of deformation (c) starting from (Fig. 5.6b), allowing 70% strain with dominant slip along (010) planes.

values compared to slip systems involving (001) planes (lines 101, 105, and 109). This allows for the gradual depletion of 001 orientations in the starting texture and a shift of orientations towards maximums in 100 and 010 shown in Figure 5.6b. A second stage of compression must be simulated in order to generate the 010 maximum we observe in our experimental textures. Here we keep CRSS values low for (010) planes, and increase the CRSS on (001) and (100) planes in order for bridgmanite orientations to converge on a 010 maximum (Figure 5.6c).

Besides this quick example, VPSC modeling can be used to investigate the mechanisms responsible for development of texture as a result of deformation and further examples of its implementation on real datasets are presented in chapters 3-5.

2.5.2 Wave propagation models with MTEX

MTEX is used to calculate and plot amplitudes of P and S-wave seismic anisotropy based on our experimental results. Seismic anisotropy can be a result of crystal structure, crystallographic preferred orientation (CPO), grain shape preferred orientation (SPO), or even the presence of fluids. In our work, we investigate the impact of texture (CPO) in a pyrolitic subducting slab under compressive stresses, focusing on regions both above and below the '660'.

Calculating seismic anisotropy requires the input of single crystal elastic constants of the phases that make up the material. Polycrystal elastic properties must be calculated in order to investigate wave velocities within the polycrystalline aggregate. For each phase, we use a texture that matches what we observe in our experiments. The corresponding polycrystal elastic properties and seismic velocities can then be calculated for each phase. To calculate seismic velocities for the overall aggregate, we calculate a weighted average of the polycrystalline elastic tensors of each phase based on their volumetric proportions in the aggregate. More specifically, we calculate a Voigt average by summing the polycrystalline elastic stiffness of each phase, then calculate a Reuss average by summing the polycrystalline elastic compliance of each phase, and finally calculate an average of those two averages, which provides us with a Hill average.

We use this Hill average to calculate seismic velocities and construct all of our seismic anisotropy plots. S-wave splitting and P-wave anisotropy are plotted as upper hemisphere

projections in MTEX. S-wave splitting (ΔV_S) is plotted as the difference in velocity between the fast and slow propagation either in km/s or as a percentage. P-wave anisotropy (V_P) is plotted as a function of orientation. A fiber symmetry is imposed in the seismic plots as our experiments are performed under uniaxial compression, which would result in a fiber symmetry along the compression axis. Chapter 4 shows the resulting anisotropy plots and provides further details on experimental data. An example of the MTEX script used is provided below (Figure2.22).

```
*Material: (Mg,Fe)SiO3 perovskite Jeff 24 June 2020
orthorhombic                crysym
   4.64    4.8    6.66    90.    90.    90.    unit cell axes and angles
Elastic stiffness (single crystal [GPa]; dummy, not used in VPSC)
 205.0    138.0    138.0    000.0    000.0    000.0
 138.0    205.0    138.0    000.0    000.0    000.0
 138.0    138.0    205.0    000.0    000.0    000.0
 000.0    000.0    000.0    126.0    000.0    000.0
 000.0    000.0    000.0    000.0    126.0    000.0
 000.0    000.0    000.0    000.0    000.0    126.0
*Thermal expansion coefficients (single crystal in crystal axis) not used for
     perovskite:
  0.0e-6   0.0e-6  0.0e-6   0.0e0   0.0e0   0.0e0
*Info about slip & twinning modes in this file:
  12            nmodesx     (total # of modes listed in file)
  12            nmodes      (# of modes to be used in the calculation)
  1 2 3 4 5 6 7 8 9 10 11 12              mode(i)    (label of the modes to be
      used)
(100) [010] SLIP
  1  1  1   0                          modex,nsmx,iopsysx,itwtypex
    1  0  0        0  1  0              slip (n & b)
(100) [001] SLIP
  2  1  1   0                          modex,nsmx,iopsysx,itwtypex
    1  0  0        0  0  1              slip (n & b)
(100) <011> SLIP
  3  2  1   0                          modex,nsmx,iopsysx,itwtypex
    1  0  0        0  1  1              slip (n & b)
    1  0  0        0 -1  1
(010) [100] SLIP
  4  1  1   0                          modex,nsmx,iopsysx,itwtypex
    0  1  0        1  0  0              slip (n & b)
(010) [001] SLIP
  5  1  1   0                          modex,nsmx,iopsysx,itwtypex
    0  1  0        0  0  1              slip (n & b)
(010) <101> SLIP
  6  2  1   0                          modex,nsmx,iopsysx,itwtypex
    0  1  0        1  0  1              slip (n & b)
    0  1  0        1  0 -1
(001) [100] SLIP
  7  1  1   0                          modex,nsmx,iopsysx,itwtypex
    0  0  1        1  0  0              slip (n & b)
(001) [010] SLIP
  8  1  1   0                          modex,nsmx,iopsysx,itwtypex
    0  0  1        0  1  0              slip (n & b)
(001) <110> SLIP
  9  2  1   0                          modex,nsmx,iopsysx,itwtypex
    0  0  1        1  1  0              slip (n & b)
    0  0  1        1 -1  0
  fake {111}<110> SLIP for Von Mises criteria
  10  12  1   0                          modex,nsmx,iopsysx,itwtypex
   1  1  1        0  1 -1              slip (n & b)
   1  1  1        1  0 -1
   1  1  1        1 -1  0
  -1  1  1        0  1 -1
  -1  1  1        1  0  1
  -1  1  1        1  1  0
  -1 -1  1        0  1  1
  -1 -1  1        1  0  1
  -1 -1  1        1 -1  0
   1 -1  1        0  1  1
   1 -1  1        1  0 -1
   1 -1  1        1  1  0
  {110}<1-10> TWIN
 11  2  0   2                          modex,nsmx,isensex,itwtypex
 0.0737                                 twshx
    1  1  0        1 -1  0
   -1  1  0       -1 -1  0
  {112}<111> TWIN
  12  4  0  2                          modex,nsmx,isensex,itwtypex
  -0.20737                               twshx
     1  1 -2        1  1  1
    -1  1 -2       -1  1  1
    -1 -1 -2       -1 -1  1
     1 -1 -2        1 -1  1
```

Figure 2.20: Example input file describing crystal symmetry, slip modes, equivalent slip planes, and CRSS values used in VPSC simulations.

```
*Constitutive law
   0        Voce=0, MTS=1
   1        iratesens (0:rate insensitive, 1:rate sensitive)
   50       grsze --> grain size only matters if HPfactor is non-zero
  (100)[010] SLIP ------------------------------------------------
   3                                        nrsx
   2.0    0.0    0.0    0.0   0.           tau0x,tau1x,thet0,thet1, hpfac
   1.0     1.0     1.0     1.0     1.0     1.0     1.0     1.0     1.0     1.0     1.0
          1.0   hlatex(1,im),im=1,nmodes
  (100)[001] SLIP ------------------------------------------------
   3                                        nrsx
   1.0    0.0    0.0    0.0   0.           tau0x,tau1x,thet0,thet1, hpfac
   1.0     1.0     1.0     1.0     1.0     1.0     1.0     1.0     1.0     1.0     1.0
          1.0   hlatex(1,im),im=1,nmodes
  (100)<011> SLIP ------------------------------------------------
   3                                        nrsx
   3.0    0.0    0.0    0.0   0.           tau0x,tau1x,thet0,thet1, hpfac
   1.0     1.0     1.0     1.0     1.0     1.0     1.0     1.0     1.0     1.0     1.0
          1.0   hlatex(1,im),im=1,nmodes
  (010)[100] SLIP ------------------------------------------------
   3                                        nrsx
   4.0    0.0    0.0    0.0   0.           tau0x,tau1x,thet0,thet1, hpfac
   1.0     1.0     1.0     1.0     1.0     1.0     1.0     1.0     1.0     1.0     1.0
          1.0   hlatex(1,im),im=1,nmodes
  (010)[001] SLIP ------------------------------------------------
   3                                        nrsx
   2.0    0.0    0.0    0.0   0.           tau0x,tau1x,thet0,thet1, hpfac
   1.0     1.0     1.0     1.0     1.0     1.0     1.0     1.0     1.0     1.0     1.0
           1.0   hlatex(1,im),im=1,nmodes
  (010)<101> SLIP ------------------------------------------------
   3                                        nrsx
   3.0    0.0    0.0    0.0   0.           tau0x,tau1x,thet0,thet1, hpfac
   1.0     1.0     1.0     1.0     1.0     1.0     1.0     1.0     1.0     1.0     1.0
          1.0   hlatex(1,im),im=1,nmodes
  (001)[100] SLIP ------------------------------------------------
   3                                        nrsx
   4.0    0.0    0.0    0.0   0.           tau0x,tau1x,thet0,thet1, hpfac
   1.0     1.0     1.0     1.0     1.0     1.0     1.0     1.0     1.0     1.0     1.0
          1.0   hlatex(1,im),im=1,nmodes
  (001)[010] SLIP ------------------------------------------------
   3                                        nrsx
   4.0    0.0    0.0    0.0   0.           tau0x,tau1x,thet0,thet1, hpfac
   1.0     1.0     1.0     1.0     1.0     1.0     1.0     1.0     1.0     1.0     1.0
          1.0   hlatex(1,im),im=1,nmodes
  (001)<110> SLIP ------------------------------------------------
   3                                        nrsx
   5.0    0.0    0.0    0.0   0.           tau0x,tau1x,thet0,thet1, hpfac
   1.0     1.0     1.0     1.0     1.0     1.0     1.0     1.0     1.0     1.0     1.0
          1.0   hlatex(1,im),im=1,nmodes
 {111}<110> SLIP ------------------------------------------------
  3                                        nrsx
  30.0    0.0    0.0    0.0   0.           tau0x,tau1x,thet0,thet1, hpfac
  1.0     1.0     1.0     1.0     1.0     1.0     1.0     1.0     1.0     1.0     1.0
         1.0   hlatex(1,im),im=1,nmodes
  {110}<1-10> TWIN -----------------------------------------------
  3                                        nrsx
  100.0    0.0     0.     0.     0.          tau0x,tau1x,thet0,thet1, hpfac
  1.0     1.0     1.0     1.0     1.0     1.0     1.0     1.0     1.0     1.0     1.0
         1.0   hlatex(1,im),im=1,nmodes
  0       0.05    0.50                     isectw, thres1,thres2
  {112}<111> TWIN ------------------------------------------------
  3                                        nrsx
  100.0    0.0     0.     0.     0.          tau0x,tau1x,thet0,thet1, hpfac
  1.0     1.0     1.0     1.0     1.0     1.0     1.0     1.0     1.0     1.0     1.0
         1.0   hlatex(1,im),im=1,nmodes
  0       0.05    0.50                     isectw, thres1,thres2
```

Figure 2.21: Continued from Figure 2.20.

```
%Bridgmanite @ 27 GPa & 1900K - 741.8 km depth
clear all
% Define crystal and sample symmetry
%cs_pnma = crystalSymmetry('Pnma',[4.796952 6.6631093 4.6442945])
cs_pbnm = crystalSymmetry('Pbnm',[4.6442945 4.796952 6.6631093])
ss = specimenSymmetry()
rho_Bgm = 4.493
Cij = [[540.43 200.20 188.70 0      0      0];...
       [ 200.20 610.79 208.20 0      0      0];...
       [ 188.70 208.20 548.32 0      0      0];...
       [ 0      0      0      208.87 0      0];...
       [ 0      0      0      0      177.94 0];...
       [ 0      0      0      0      0      161.13]];

%Defining tensor for elastic properties of bridgmanite
CBgm = stiffnessTensor(Cij, cs_pbnm, 'density', rho_Bgm)

% Plotting convention
plotx2east

%%
%Create fiber ODF for bridgmanite
h = Miller({0,0,1}, cs_pbnm)
r = vector3d(0, 1, 0);
odf_bgm = fibreODF(h, r, 'halfwidth', 30*degree)

%%
fprintf('Elastic constants of bridgmanite single crystal\n')
odf_bgm

%%
plotPDF(odf_bgm,Miller({1,0,0},{0,1,0},{0,0,1},odf_bgm.CS))

%%
%Plot IPF for bridgmanite
plotIPDF(odf_bgm, yvector)

%%
%Shows strength of ODF
textureindex(odf_bgm)

%%
%Compute Tensors for poly crystal for bridgmanite
[CVoigt_bgm, CReuss_bgm, CHill_bgm] = calcTensor(odf_bgm, CBgm);

%%
%Plot Vs Anisotropy
plotvs_anisotropy(CHill_bgm,0,0.3)

%%
% Plot Vp
plotvp(CHill_bgm, 11.0, 11.4)

%%
%Davemaoite @ 27 GPa/1900 K - 741.8 km depth
% Define crystal and sample symmetry. Unit cell from experiments
% Pyr05_940-1051
cs_CaPv = crystalSymmetry('Pm-3m',[3.457113 3.457113 3.457113])
%Calculated in HeFESTo
rho_CaPv = 4.4646
%Interpolationio of Cij from Li et al. (2006) PEPI
Cij = [[423.22   217.09   217.09   0       0       0];...
       [ 217.09   423.22   217.09   0       0       0];...
       [ 217.09   217.09   423.22   0       0       0];...
       [ 0        0        0        201.28  0       0];...
       [ 0        0        0        0       201.28  0];...
       [ 0        0        0        0       0       201.28]];

%Defining tensor for elastic properties of CaPv
CCaPv = stiffnessTensor(Cij, cs_CaPv, 'density', rho_CaPv)

%%
```

Figure 2.22: Example MTEX script for calculating and plotting seismic anisotropy in pyrolite at conditions of 27 GPa and 1900 K.

```
%Create fiber ODF for CaPv
h = Miller({0,1,1}, cs_CaPv)
r = vector3d(0, 1, 0);
odf_CaPv_1 = fibreODF(h, r, 'halfwidth', 10*degree)

h = Miller({1,1,1}, cs_CaPv)
r = vector3d(0, 1, 0);
odf_CaPv_2 = fibreODF(h, r, 'halfwidth', 15*degree)

odf_CaPv = 0.5*(odf_CaPv_1+odf_CaPv_2)

%%
plotPDF(odf_CaPv,Miller({1,1,1},{0,1,1},{0,0,1},odf_CaPv.CS))

%%
%Plot IPF for davemaoite
plotIPDF(odf_CaPv, yvector)

%%
%Compute Tensors for poly crystal for davemaoite
[CVoigt_capv, CReuss_capv, CHill_capv] = calcTensor(odf_CaPv, CCaPv);

%%
%Plot Vs Anisotropy of davemaoite
plotvs_anisotropy(CHill_capv,0,0.3)

%%
%Plot Vp
plotvp(CHill_capv, 10.4, 10.8)

%%
%Mw @ 27 GPa/1900 K - 741.8 km depth
% Define crystal and sample symmetry. Unit cell from experiments
% Pyr05_940-1051
cs_Mw = crystalSymmetry('Fm-3m',[4.0323825 4.0323825 4.0323825])
%Calculated in HeFESTo
rho_Mw = 4.4296
K = 227.6
G = 128.5
Cij = [[K+4*G/3  K-2*G/3  K-2*G/3  0  0  0];...
       [ K-2*G/3  K+4*G/3  K-2*G/3  0  0  0];...
       [ K-2*G/3  K-2*G/3  K+4*G/3  0  0  0];...
       [ 0        0        0        G  0  0];...
       [ 0        0        0        0  G  0];...
       [ 0        0        0        0  0  G]];

%Defining tensor for elastic properties of MgO
CMw = stiffnessTensor(Cij, cs_Mw, 'density', rho_Mw)

%%
%Plot Vs Anisotropy
plotvs_anisotropy(CMw,0,1)

%%
% Plot Vp
plotvp(CMw)

%%
%Average for pyrolite composition
Cij_Voigt_pyrolite = 0.7715*CHill_bgm + 0.059*CHill_capv + 0.1686*CMw

Sij_Reuss_pyrolite = 0.7715*inv(CHill_bgm) + 0.059*inv(CHill_capv) + 0.1686*
    inv(CMw)
inv(Sij_Reuss_pyrolite)

Cij_Hill_pyrolite = 0.5*(Cij_Voigt_pyrolite + inv(Sij_Reuss_pyrolite))

%%
%Plot Vs Anisotropy of pyrolite
plotvs_anisotropy(Cij_Hill_pyrolite,0,0.1)

%%
%Plot Vp
plotvp(Cij_Hill_pyrolite)
```

Figure 2.23: Continued from Figure 2.22.

Chapter 3

Deformation and Phase Transformation in $NaCoF_3$

3.1 Introduction

A phase transition in (Mg,Fe)SiO_3 Bridgmanite is thought to occur in the vicinity of the D" layer in the Earth's lower mantle [Murakami et al., 2004, Hernlund et al., 2005, Koelemeijer et al., 2018]. This transformation involves a structural change from perovskite (Pbnm setting) to post-perovskite (Cmcm setting) [Murakami et al., 2004, Oganov and Ono, 2004]. It also coincides with strong observable seismic anisotropy in the same region [Garnero et al., 2004, Panning and Romanowicz, 2006b, Wookey and Kendall, 2007] which is attributed to the anisotropic properties of bridgmanite and ferropericlase, which increase with depth [Chen et al., 1998, Mainprice et al., 2000]. Although, studies show that the effect of post-perovskite is observable in seismic data [Nowacki et al., 2013, Koelemeijer et al., 2018, Pisconti et al., 2019], the details of the transformation between bridgmanite and post-perovskite have an impact on the observed data [Pisconti et al., 2019, Walker et al., 2018] and require further experimental characterization.

In addition, the Earth's lower mantle is believed to be composed predominantly of bridgmanite in the perovskite structure [Tschauner et al., 2014]. This motivates experimental studies aiming to gain insight on plastic behavior, deformation processes, and the mechanisms responsible for the transformations of bridgmanite at relevant conditions. Past experimental studies on bridgmanite have investigated the development of crystallographic preferred orientation (texture) and the deformation mechanisms responsible [e.g. Wang et al., 1992, Merkel et al., 2003, Wenk et al., 2004a, Cordier et al., 2004, Wenk et al.,

2006, Ferré et al., 2007, Mainprice et al., 2008, Miyagi and Wenk, 2016, Kraych et al., 2016, Boioli et al., 2017]. One experimental device commonly used to deform crystalline samples is the diamond anvil cell (DAC) [Wenk et al., 2004b, Miyagi and Wenk, 2016], which allows the user to reach lower mantle pressures and temperatures. These experiments are challenging to perform, however, due to the large pressures and temperatures required.

Structural analogues of (Mg,Fe)SiO_3, such as $NaCoF_3$, can also undergo perovskite to post-perovskite phase transitions, but require lower pressures and temperatures making quantitative deformation experiments less challenging. Several experiments on analogues have resulted in perovskite/post-perovskite deformation and transformation textures [Niwa et al., 2007b, Okada et al., 2010, Dobson et al., 2011, Miyagi et al., 2011, Dobson et al., 2013]. Furthermore, deformation experiments on analogues can be used to gain insight on the plasticity of perovskite phases and can be compared to the behavior of (Mg,Fe)SiO_3 at mantle conditions.

In the following study we compare compression textures, deformation mechanisms, and phase transformation mechanisms in $NaCoF_3$ perovskite and post-perovskite to natural samples in order to determine if $NaCoF_3$ is a relevant experimental analogue to (Mg,Fe)SiO_3. We used a resistive-heated radial diamond anvil cell (DAC) combined with synchrotron radiation in the radial X-ray diffraction geometry at pressures and temperatures between 1.1 and 29.6 GPa and 300 and 1013 K, respectively. In-situ texture development and phase change from a perovskite to a post-perovskite structure in $NaCoF_3$ was observed. We then used the data to model plastic deformation and deformation mechanisms in perovskite along with experimental texture measurements to model orientation relationships and transformation mechanisms between perovskites and post-perovskites.

This study is published in the European Journal of Mineralogy [Gay et al., 2021]. The following section will provide an overview of the results and conclusions made in the study. The full publication is included at the end of this chapter, providing a more detailed background and information on the parameters of the experiment.

3.2 Methods

Experiments were performed on beamline P02.2 of the PETRA III facility at Deutsches Elektronen Synchrotron (DESY) in Hamburg, Germany. A graphite resistive-heated radial DAC was used in order to perform a uniaxial compression experiment on a polycrystalline sample of $NaCoF_3$. The setup used is identical to that of Immoor et al. [2020]. Further details on the experimental setup can be found there. Using this technique the stress state and texture of the sample can be analyzed in-situ at high pressure and temperature.

Processing of the diffraction data was completed using the program MAUD (Material Analysis Using Diffraction) [Lutterotti et al., 1997] following the general refinement procedure outlined in Wenk et al. [2014]. MAUD can extract phase proportions, unit cell parameters, texture, and identify phases. Differential stress in $NaCoF_3$ was also fit in MAUD using a model that relies on the elastic theory of Singh et al. [1998], which assumes isotropic elastic properties and fits a value for the differential stress according to displacement of peak positions with orientations. In order to perform this fit, MAUD requires an input value of the shear modulus, which is unknown for $NaCoF_3$ perovskite and post-perovskite at high temperature. To address this, we use a constant shear modulus value of 44 GPa, which was extracted from first-principles calculations on a cubic $NaCoF_3$ perovskite at zero pressure and temperature [Chenine et al., 2018]. This choice of numerical value for the shear modulus has no impact on the final results (see below).

At the end of the refinement procedure we are able to extract normalized stress, unit cell parameters, pressure, and texture. Pressure was evaluated using the thermal equation of state parameters of platinum from Zha et al. [2008]. Two type-R thermocouples were used in order to monitor temperatures during resistive heating.

3.3 Summary of Results

The transformation of $NaCoF_3$ perovskite to post-perovskite took place between 20.1 and 26.1 GPa at temperatures of $\sim$ 1000 K. We used the program EoSFit [Gonzalez-Platas et al., 2016] to fit a second order Birch-Murnaghan equation of state trend for perovskite between 1.1 GPa and 868 K and 20.1 GPa and 997 K for all post-perovskite data (Figure 3.1). Considering the small ranges in temperature for the measurements, temperature

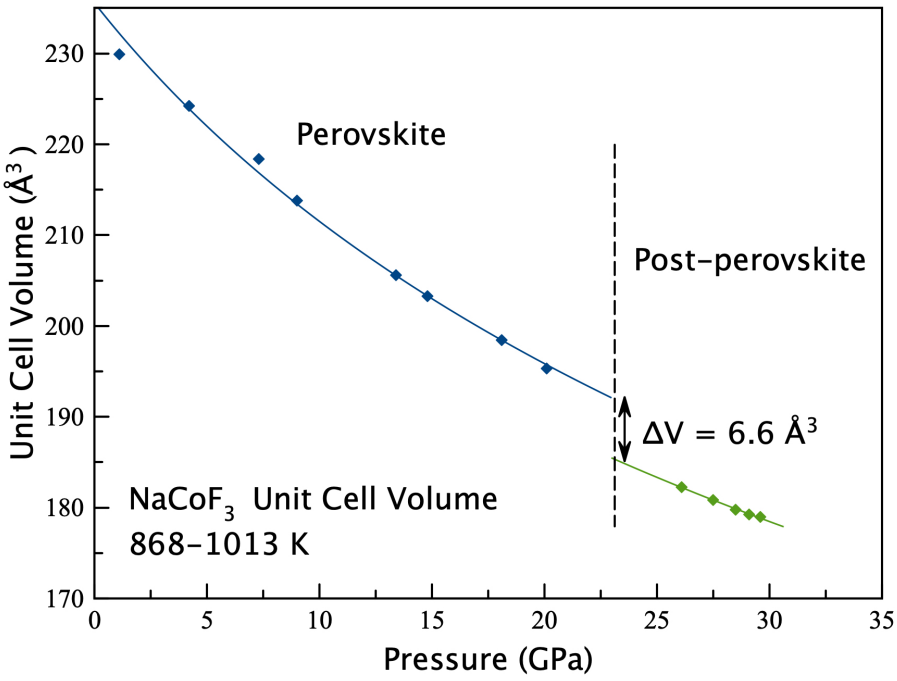

Figure 3.1: Unit cell volumes of $NaCoF_3$ perovskite and post-perovskite plotted vs. pressure. Lines are second order Birch-Murnaghan equation of state fit for each phase assuming constant temperature used to illustrate compression behavior vs. experimental values.

effects were ignored. The resulting bulk modulus for perovskite and post-perovskite in the 868-1013 K range are 74.9 and 85.9 GPa respectively. From the fit, we are able to estimate the the reduction in unit cell volume due to the transformation, which is 6.6 $Å^3$.

3.3.1 Stress

Stresses for $NaCoF_3$ were reported in terms of normalized stress t/G, which recalculated from the fitted t and the fixed G value, and has been used in past studies to compare materials to each other [Duffy, 2007, Miyagi et al., 2009, Dorfman et al., 2015]. Normalized stress in $NaCoF_3$ perovskite increased from 0.010 to 0.054 at pressures and temperatures between 1.1 to 18.1 GPa and 868 and 929 K, respectively (Figure 3.2). Before the onset of transformation to post-perovskite, a decrease in normalized stress to 0.048 at 997 K was observed. This decrease in stress was likely due to relaxation as the transition is initiated. t/G dropped to 0.016 as post-perovskite was formed at 26.1 GPa and 1013 K. Upon further compression to 29.6 GPa at 1003 K, t/G in post-perovskite increased to 0.020.

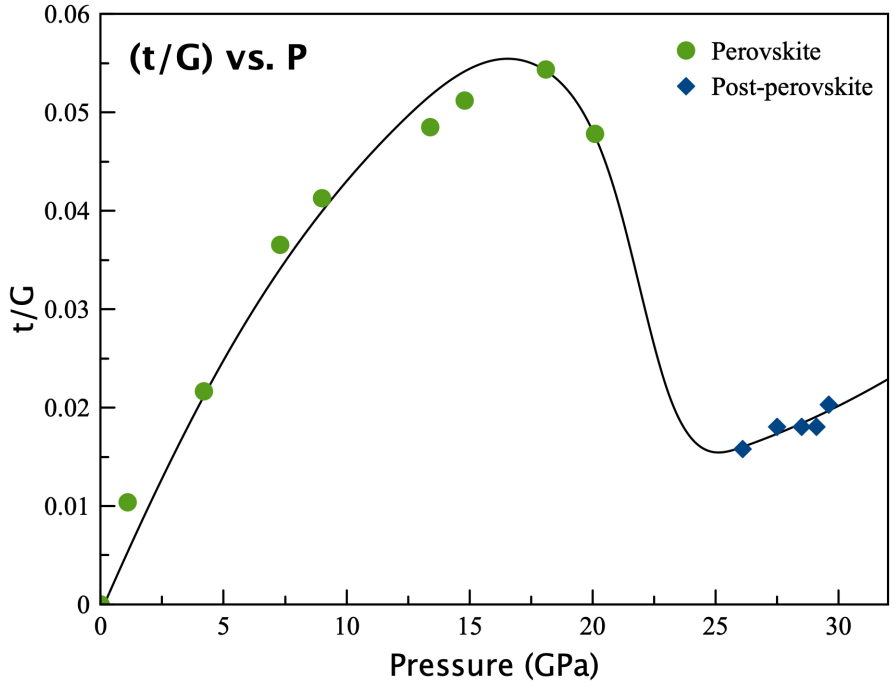

Figure 3.2: Normalized stress t/G in $NaCoF_3$ perovskite (green circles) and post-perovskite (blue diamonds) as a function of pressure. Solid line is a visual guide through the experimental data. Perovskite to post-perovskite transition occurs between 20.1 GPa and 26.1 GPa.

3.3.2 Deformation Textures

Texture development during the experiment is shown as inverse pole figures of the compression direction (Fig. 3.3). In the perovskite phase we observed a weak maximum at 100 (2.2 m.r.d.) after the closure of the sample chamber (Fig. 3.3a). As compression of $NaCoF_3$ continued the maximum at 100 strengthened to an m.r.d. value of 4.2 at 7.3 GPa (Fig. 3.3b). Upon further compression to 13.4 GPa, a weak secondary maximum appeared at 001 (Fig. 3.3c). This texture weakened before transitioning to post-perovskite at 26.1 GPa (Fig. 3.3f). This is likely a feature of the transformation. In all cases, there was a clear minimum at 010 in the perovskite phase.

At 26.1 GPa $NaCoF_3$ transforms to a post-perovskite structure and weak preferred orientation can be observed at 010 (Fig. 3.3f). This texture strengthens upon compression to 29.6 GPa with m.r.d values never exceeding 3. Additionally, a clear minimum at 001 develops upon compression of the post-perovskite phase as well as a small shift of 010 towards 001 (Fig. 3.3g).

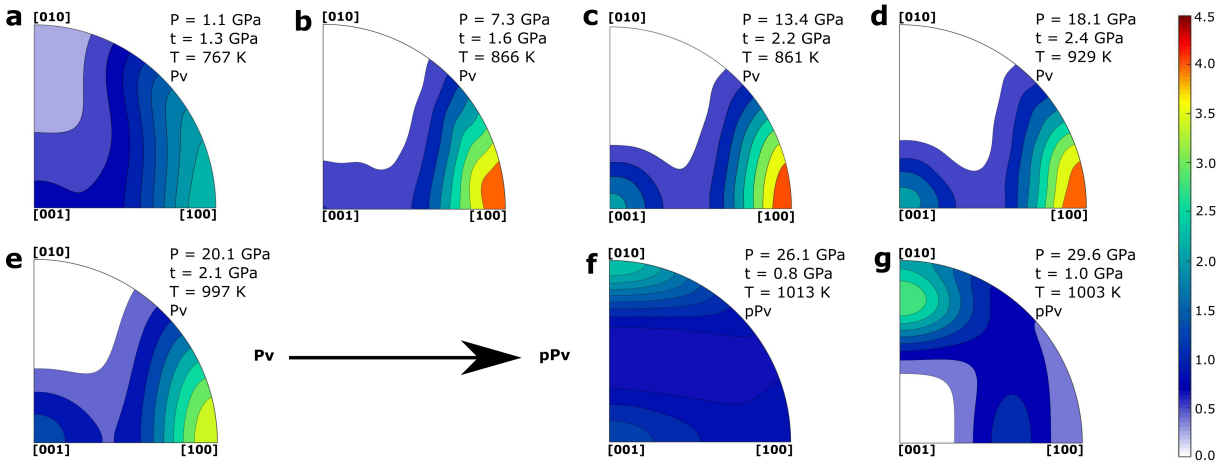

Figure 3.3: Inverse pole figures in the compression direction of $NaCoF_3$ at various stages of compression. (a, b, c, d, e), perovskite structure (Pbmn setting). (f, g) post-perovskite structure. Equal area projection. Color scale in multiples of random distribution (m.r.d.).

3.3.3 Discussion

Texture Evolution in the Perovskite Phase

We observed a 100 compression texture very early in the compression in the perovskite structure (Fig. 3.3a) which strengthened with further compression to 18.1 GPa (Fig. 3.3d). This increase of the 100 texture maximum was accompanied by a decrease of intensity at 010. At 13.4 GPa, we observed the appearance of a secondary maximum at 001. The 100 maximum induced by the first stage of compression compares favorably with experiments on bridgmanite [Merkel et al., 2003, Wenk et al., 2004b, Miyagi and Wenk, 2016] in which it was assigned to a likely contribution of {110} mechanical twinning as identified in early TEM studies [Wang et al., 1992]. Slip along (100) planes would also lead to 100 maximums; however, twinning is an efficient mode for inducing fast grain re-orientations without producing a gradual texture shift, which is not observed here. This same 100 texture maximum was also observed in compressed $NaMgF_3$ [Kaercher et al., 2016]. The secondary 001 maximum observed later in compression was also observed in D-DIA deformation experiments on $NaMgF_3$ [Kaercher et al., 2016] and was reported in the study of Miyagi and Wenk [2016] on brigmanite at pressures below 55 GPa in which it was assigned to slip along (001). Based on texture measurements, $NaCoF_3$ is a good analogue for constraining the plasticity of bridgmanite as both maxima at 100 and 001 are observed in both

phases in compression experiments. The interpretation of which deformation mechanisms are responsible for experimental texture, however, requires a comparison with polycrystal plasticity simulations.

VPSC Modeling

Texture development depends on a number of factors including deformation geometry, total strain, starting texture, and plastic deformation mechanism activity. Interpretations were made by using a Visco-Plastic Self-Consistent (VPSC) model, which simulates the plastic deformation of polycrystalline aggregates depending on deformation mechanisms and loading conditions [Wenk, 1999]. We were able to generate a strong 100 texture while depleting 010 and maintaining orientations at 001 by applying 25% strain in axial compression with dominant slip on (100) and a significant contribution of {110} twins. It was necessary to include {110} twins in order to deplete the 010 direction while maintaining orientations at 001. Indeed, dominant slip on (100) only results in the depletion of both 010 and 001 [Kaercher et al., 2016] and is not consistent with our experimental results.

We were not able to obtain orientations on the secondary 001 maximum while preserving the initial 100 texture as measured in the experiment above 13.4 GPa (Fig. 3.3c). Among the proposed deformation mechanisms, slip on (001) can indeed move orientations from 100 to 001, but such simulations generated a slow movement of orientations from 100 to 001. In our experimental textures we did not observe any intermediate orientations between 100 and 001. Twinning is an efficient mode for inducing fast grain re-orientations without producing a gradual texture shift. The fast reorientation of grains from 100 to 001 hence alludes to a potential contribution of an unknown twinning mode. Despite all our attempts, we were unable to characterize the observed 001 maximum based on twinning laws reported for perovskites.

Transformation Mechanism from Perovskite to Post-perovskite

Due to the restricted pressure range in which post-perovskite was compressed and the limited texture evolution observed; textures were interpreted to arise primarily from transformation. Interpretation based on deformation mechanisms would have been biased, so we focused on the perovskite to post-perovskite transformation mechanism instead. Many

questions have arisen regarding the transformation of perovskite to post-perovskite, including the transformation mechanism itself [Tsuchiya et al., 2004, Oganov et al., 2005, Dobson et al., 2013], its effect on lattice preferred orientations [Okada et al., 2010, Miyagi et al., 2011], stress [Hunt et al., 2009, Dobson et al., 2012], and anisotropy in the Earth's lower mantle [Dobson et al., 2013, Walker et al., 2018].

Phase transformations change crystal structures, but also induce a change in texture of materials. Transformations can be diffusionless in nature, meaning the atoms within the material move in a homogeneous fashion or they can be reconstructive in nature and move by means of long-range diffusion. Diffusionless transformations involve orientation relationships between the parent and daughter phase, and are sometimes referred to as martensitic [Christian et al., 1995]. Diffusive transformation, on the other hand, do not imply orientation relationships between the parent and daughter phase.

We tested three different transformation models from Tsuchiya et al. [2004], Oganov et al. [2005], and Dobson et al. [2013]. In the end, we were able to simulate a post-perovskite texture that matches our experimental results by implementing orientations relationships suggested by Dobson et al. [2013] [e.g. Figure 3.4], where the vector $hh0$ (normal to (110) in post-perovskite) is parallel to [010] in perovskite and [001] in post-perovskite is parallel to [001] in perovskite. In both the experimental and simulated textures, we observes a maximum at 010 and the strength of the texture was consistent between experiments and simulations. Based on the above reasoning, we concluded that the transformation from perovskite to post-perovskite in $NaCoF_3$ involves orientation relationships and falls within the group of displacive phase transformations. Furthermore, these relationships fit the model of Dobson et al. [2013], based on experiments performed on $NaNiF_3$, which supports the idea that this mechanism could apply to natural perovskite phases.

3.4 Conclusions

This work presented experimental results of $NaCoF_3$ compressed inside a resistive-heated radial diffraction DAC at pressures of 1.1 to 29.6 GPa and temperatures between 300 and 1013 K. A phase transformation from $NaCoF_3$ perovskite to post-perovskite was observed between 20.1 and 26.1 GPa. Deformation of $NaCoF_3$ perovskite initially results in a strong

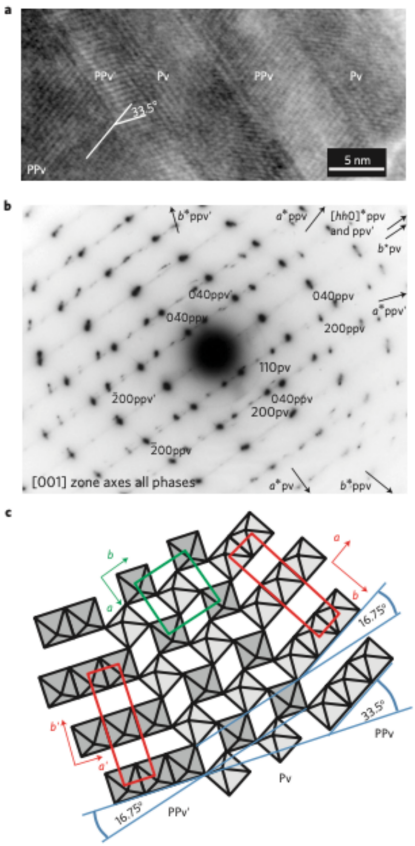

Figure 1 | Transmission electron micrograph of partially transformed $NaNiF_3$ perovskite. a, High-resolution TEM image: perovskite (Pv) and post-perovskite (PPv, PPv') domains are labelled. The spacing between the post-perovskite lattice fringes (~5 Å) is half its *b* axis length. The 33.5° angle between the post-perovskite twin domains corresponds to the angle calculated for (110) twins using the unit cell measured by XRD. **b**, Electron diffraction pattern from the area in **a**. The strong mirror plane arises from the additional symmetry introduced by twinning of post-perovskite, superimposed on the perovskite symmetry. **c**, Sketch of NiF_6 units showing the topotactic relationships between perovskite and post-perovskite.

Figure 3.4: Taken from Dobson et al. [2013].

100 maximum when the sample is at 7.3 GPa. VPSC simulations show that this texture is formed by slip along (100) paired with important contributions from {110} twins. Later in the deformation process we observe a weak secondary 001 maximum appearing at 13.4 GPa. These deformation textures compare well with those of $NaMgF_3$ shown in Kaercher et al. [2016]. Direct comparison to $MgSiO_3$ deformation textures are made difficult because of the effect of starting material on the $MgSiO_3$ transformation textures [Miyagi and Wenk, 2016]. Nevertheless, both the 100 and 001 compression textures observed in $NaCoF_3$ have been observed in natural compositions [Merkel et al., 2003, Wenk et al., 2004b, Miyagi and Wenk, 2016, Couper et al., 2020]. $NaCoF_3$ hence appears as a good analogue for plasticity studies relevant for the Earth's mantle. Transformation plasticity or transient weakening

is likely responsible for a normalized strength drop from 0.054 to 0.016 resulting from the phase transition from perovskite to post-perovskite. Additionally, transformation of $NaCoF_3$ perovskite to post-perovskite is martensitic in nature, as we are able to reproduce our data using the orientation relationships proposed in Dobson et al. [2013].

Perovskite analogues continue to provide valuable insight to the behavior of materials at extreme pressures and temperatures relevant for planetary mantles. For Earth's mantle materials, it is important to understand the effect of temperature on deformation mechanisms which may be different from what is observed at 300 K. Analogues such as $NaCoF_3$, allow studies at lower pressures. A general understanding of plasticity in perovskite/post-perovskite will help with improving the interpretation of seismic models in terms of mantle dynamics such as heat transfer through convection. For more details about this study, the full paper published in the European Journal of Mineralogy is attached below.

Eur. J. Mineral., 33, 591–603, 2021
https://doi.org/10.5194/ejm-33-591-2021

European Journal of Mineralogy
Open Access

Deformation of $NaCoF_3$ perovskite and post-perovskite up to 30 GPa and 1013 K: implications for plastic deformation and transformation mechanism

Jeffrey P. Gay[1], Lowell Miyagi[2], Samantha Couper[2], Christopher Langrand[1], David P. Dobson[3], Hanns-Peter Liermann[4], and Sébastien Merkel[1]

[1]Univ. Lille, CNRS, INRA, ENSCL, UMR 8207 - UMET - Unité Matériaux et Transformations, 59000 Lille, France
[2]Department of Geology and Geophysics, University of Utah, Salt Lake City, UT 84108, USA
[3]Department of Earth Sciences, University College London, Gower Street, London WC1E 6BT, UK
[4]Deutsches Elektronen-Synchrotron (DESY), 22607 Hamburg, Germany

Correspondence: Jeffrey P. Gay (jeffrey-phillip.gay@univ-lille.fr) and Sébastien Merkel (sebastien.merkel@univ-lille.fr)

Received: 11 May 2021 – Revised: 9 August 2021 – Accepted: 19 August 2021 – Published: 30 September 2021

Abstract. Texture, plastic deformation, and phase transformation mechanisms in perovskite and post-perovskite are of general interest for our understanding of the Earth's mantle. Here, the perovskite analogue $NaCoF_3$ is deformed in a resistive-heated diamond anvil cell (DAC) up to 30 GPa and 1013 K. The in situ state of the sample, including crystal structure, stress, and texture, is monitored using X-ray diffraction. A phase transformation from a perovskite to a post-perovskite structure is observed between 20.1 and 26.1 GPa. Normalized stress drops by a factor of 3 during transformation as a result of transient weakening during the transformation. The perovskite phase initially develops a texture with a maximum at 100 and a strong 010 minimum in the inverse pole figure of the compression direction. Additionally, a secondary weaker 001 maximum is observed later during compression. Texture simulations indicate that the initial deformation of perovskite requires slip along (100) planes with significant contributions of {110} twins. Following the phase transition to post-perovskite, we observe a 010 maximum, which later evolves with compression. The transformation follows orientation relationships previously suggested where the c axis is preserved between phases and $hh0$ vectors in reciprocal space of post-perovskite are parallel to [010] in perovskite, which indicates a martensitic-like transition mechanism. A comparison between past experiments on bridgmanite and current results indicates that $NaCoF_3$ is a good analogue to understand the development of microstructures within the Earth's mantle.

1 Introduction

Earth's lower mantle is believed to be composed predominantly of bridgmanite, i.e., $(Mg,Fe)SiO_3$ in the perovskite structure (Tschauner et al., 2014). At deep-lower-mantle conditions, this composition transforms from the perovskite to the post-perovskite structure (Murakami et al., 2004; Oganov and Ono, 2004). The deformation and transformation of perovskite and post-perovskite phases are important for a number of processes in the deep Earth (Čížková et al., 2010; Nakagawa and Tackley, 2011; Tackley, 2012), including the development of crystallographic preferred orientation (Yamazaki and Karato, 2007; McCormack et al., 2011; Hunt et al., 2016), also known as texture, which can lead to seismic anisotropy (Cobden et al., 2015; Walker et al., 2018b). Texture development can also be studied experimentally (Wenk et al., 2006; Merkel et al., 2007; Miyagi et al., 2010) and is thought to be a reasonable approximation for seismic anisotropy observed within the mantle (Wookey et al., 2002; Nowacki et al., 2010; Ferreira et al., 2019).

Seismic anisotropy within the Earth's deep mantle is commonly measured using shear wave splitting. This shear wave

Published by Copernicus Publications on behalf of the European mineralogical societies DMG, SEM, SIMP & SFMC.

splitting can be used to characterize mantle strain fields, which in turn allows for mantle structures to be observed (Savage, 1999). There are many regions within the lower mantle, past 1000 km, that are seismically isotropic (Panning and Romanowicz, 2006; Beghein et al., 2006) even though numerous experimental studies demonstrate lower-mantle phases of bridgmanite and ferropericlase are highly anisotropic and even increase in anisotropy with depth (Chen et al., 1998; Mainprice et al., 2000). In the case of the D″ region, where a phase transformation from perovskite to post-perovskite could take place (Murakami et al., 2004; Hernlund et al., 2005; Koelemeijer et al., 2018), strong anisotropy is observed (Garnero et al., 2004; Panning and Romanowicz, 2006; Wookey and Kendall, 2007). It is difficult, however, to determine the physical origin of anisotropy (i.e., crystallographic preferred orientation or periodic layering) due to poor azimuthal sampling of D″ (Romanowicz and Wenk, 2017). Recent studies (Nowacki et al., 2013; Koelemeijer et al., 2018; Pisconti et al., 2019) show that the effect of post-perovskite is observable in seismic data, but the details of the transformation between bridgmanite and post-perovskite have an impact on the observed data (Pisconti et al., 2019; Walker et al., 2018a) and require further experimental characterization. In order to characterize how bridgmanite and post-perovskite deform within the lower mantle and what mechanisms are responsible for the transformations of bridgmanite to post-perovskite, it is necessary to utilize experimental mineral physics.

The study of the transition of perovskite to post-perovskite requires the application of pressure (P). Several experimental methods can be used to study deformation and phase transformation in situ at high pressure, such as the diamond anvil cell (DAC) (Wenk et al., 2004b; Miyagi and Wenk, 2016), the multi-anvil press (Cordier et al., 2004; Walte et al., 2009; Wang et al., 2013; Tsujino et al., 2016; Hunt et al., 2016), and the rotational Drickamer apparatus (Girard et al., 2016). For many years, deformation experiments in the DAC were limited to ambient temperatures (T). Recent developments, however, allow for the combined application of pressure and temperatures up to 1900 K (Liermann et al., 2009; Miyagi et al., 2013; Immoor et al., 2020), which we will use here. In addition, structural analogues of $(Mg,Fe)SiO_3$ can undergo perovskite to post-perovskite phase transitions at lower pressures and temperatures, making quantitative deformation experiments less challenging. Several experiments on analogues have resulted in perovskite and/or post-perovskite deformation and transformation textures (Niwa et al., 2007; Okada et al., 2010; Dobson et al., 2011; Miyagi et al., 2011; Dobson et al., 2013). Furthermore, deformation experiments on analogues can be used to gain insight on the plasticity of perovskite phases and can be compared to the behavior of $(Mg,Fe)SiO_3$ at mantle conditions (e.g., Fig. 10 in Wang et al., 2013). Not all analogues behave in the same manner, however. Deformation textures in $CaIrO_3$ post-perovskite, for instance, are known to be different from those measured in $(Mg,Fe)SiO_3$ or $MgGeO_3$ (Miyagi et al., 2008). Numerical modeling has also been implemented in order to investigate deformation mechanisms in perovskite and post-perovskite (e.g., Ferré et al., 2007; Carrez et al., 2007; Mainprice et al., 2008; Metsue et al., 2009; Boioli et al., 2017; Carrez et al., 2017). This allows for the study of not only the effect of chemistry, pressure, and temperature but also the effects of strain rate on perovskite and post-perovskite deformation, which can not be measured in experiments using current experimental techniques.

Questions remain regarding compression textures, deformation mechanisms, and phase transformation mechanisms in perovskites and post-perovskites. The comparison of $NaCoF_3$ to $(Mg,Fe)SiO_3$ in deformation experiments is essential in order to determine if $NaCoF_3$ is a relevant experimental analogue. Additionally, understanding how transformation mechanisms vary between analogues and natural compositions, including their effects on deformation and transformation textures, can inform us on the validity of analogues and their ability to predict the behavior of natural samples when direct studies of $(Mg,Fe)SiO_3$ cannot be performed. Here we use a resistive-heated radial DAC combined with synchrotron radiation at pressures and temperatures between 1.1 and 29.6 GPa and 300 and 1013 K, respectively, to observe in situ texture development and phase change from a perovskite to a post-perovskite structure in $NaCoF_3$. We use these data to model plastic deformation and deformation mechanisms in perovskite. We find $(100)\langle 011\rangle$ slip and $\{110\}\langle 1\bar{1}0\rangle$ twins to be the most active deformation mechanisms during initial deformation of the perovskite phase. Texture measurements in these experiments are used to model orientation relationships and transformation mechanisms between perovskites and post-perovskites. We determine that the transformation of $NaCoF_3$ perovskite to post-perovskite is martensitic in nature, with orientation relationships matching those of $NaNiF_3$ outlined in Dobson et al. (2013). Normalized stress measurements also demonstrate a stronger perovskite phase than post-perovskite phase in $NaCoF_3$. Overall, these results can help us to better understand the deformation and phase transformation in perovskite and post-perovskite phases and will lead to greater knowledge of deep mantle dynamics.

2 Experimental details

2.1 High-P–T experiments

In this study, we use a graphite resistive-heated radial DAC apparatus to perform a uniaxial compression experiment on a polycrystalline sample of $NaCoF_3$. Experiments were performed on beamline P02.2 of the PETRA III facility at the Deutsches Elektronen Synchrotron (DESY) in Hamburg, Germany. By utilizing synchrotron X-ray diffraction in radial geometry, the stress state and texture of the sample can

be analyzed in situ at high pressure and temperature. An incident monochromatic X-ray beam focused to 5.8 µm × 3.2 µm and PerkinElmer XRD 1621 detector with 200 µm × 200 µm pixel size were used to capture the diffraction images. A CeO_2 standard from the National Institute of Standards and Technology (NIST; 674b) was used for calibration in order to correct for detector tilt and calculate a sample to detector distance of 438.35 mm. Wavelength was fixed at 0.4908 Å.

Powdered $NaCoF_3$ perovskite from the study of Dobson et al. (2011) was loaded into an X-ray transparent boron epoxy gasket with an 80 µm diameter hole. A platinum flake was also loaded to be used as a pressure marker, using the thermal equation of state parameters of Zha et al. (2008) and the EosFit program (Gonzalez-Platas et al., 2016).

Details on the synchrotron beamline setup and DAC can be found in Liermann et al. (2015) and Immoor et al. (2020). The diamonds we used had a 300 µm culet size. Two thin graphite layers in contact with the anvils and surrounding the diamond tips were used for a restive heater, while two type-R thermocouples were used to monitor temperature. One of the thermocouples is located between both graphite heaters and the second on the diamond anvil next to the culet. Reported temperatures are the average between both thermocouple measurements. The graphite sheets contained a small window that was carved out of the graphite in order to allow the X-rays to pass through the heater. The DAC assembly was placed within a vacuum chamber maintaining a pressure of 10^{-3} mbar in order to prevent oxidation during heating. A water cooling system kept at low temperatures was used to prevent the assembly from overheating. The sample was compressed using a gas membrane system, while radial diffraction images were simultaneously collected.

The sample was pre-compressed up to 3.4 GPa at ambient temperature to close the sample chamber. Temperature was then increased to 873 K over the course of 3 h. $NaCoF_3$ was compressed to a maximum pressure of 30.8 GPa and heated at temperatures ranging from 861 to 1013 K (Table 1, Fig. 1). Diamonds broke at 30.8 GPa, marking the end of the experiment. We observe the transformation of $NaCoF_3$ perovskite to a post-perovskite structure (e.g., Fig. 1) between 20.1 and 26.1 GPa. During the first stage of compression from 1.1 GPa to 14.8 GPa temperatures are held constant between 861 and 868 K. Thereafter, temperature is increased to 997 K at 20.1 GPa just before the transition. The post-perovskite phase is then visible in the diffraction pattern at 26.1 GPa and 1013 K, although some perovskite may still be visible. Data files used can be found online (Gay et al., 2021).

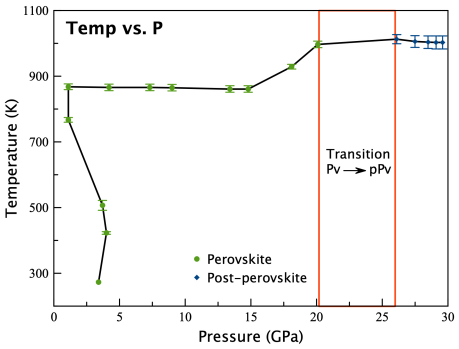

Figure 1. Pressure–temperature path during the experiment. Start of high-temperature compression is at 1.1 GPa and 868 K. Perovskite to post-perovskite transformation is observed between 20.1 and 26.1 GPa.

2.2 Data analysis

Diffraction images were integrated over 5° azimuthal arcs into 72 spectra and analyzed using the program MAUD (material analysis using diffraction) (Lutterotti et al., 1997) following the general refinement procedure outlined in Wenk et al. (2014). An example of MAUD refinement is shown in Fig. 2. Graphite peaks become more visible as pressure increases (e.g., Fig. 2b at 2θ values 6.0, 8.2, 13.4, and 14.6°). This is due to the closure of the window carved into the heater as the experiment proceeds. We exclude these regions in addition to the 2θ ranges where platinum is overlapping during the refinement process.

Diffraction background was fit using polynomial functions. Structural parameters of $NaCoF_3$ were obtained from Shirako et al. (2012), and cell parameters and B factors were further refined using the data. Crystallite size and microstrains were refined using the Popa line-broadening size–strain model (Popa, 1998).

Differential stress in $NaCoF_3$ was fit using a model that relies on the elastic theory of Singh et al. (1998), which assumes isotropic elastic properties and fits a value for the differential stress according to the displacement of peak positions with orientations. In the model of Singh et al. (1998), the average lattice strain across the sample is proportional to stress using $t = 6G\langle Q(hkl)\rangle$, where G is the shear modulus of the polycrystal sample and $\langle Q(hkl)\rangle$ is the average lattice strain across the sample. The MAUD fit requires an input value of the shear modulus, which is unknown for $NaCoF_3$ perovskite and post-perovskite at high temperature. In view of that limitation we use a constant value of $G = 44$ GPa, extracted from first-principles calculations on a cubic $NaCoF_3$ perovskite at zero pressure and temperature (Chenine et al., 2018). The t/G values are then recalculated from the fitted t and the fixed G values. Do note, however, the G value used when refining t in MAUD has no impact on the final t/G ratio. Also note that MAUD allows for extraction of individual $Q(hkl)$ for each diffraction peak, but the quality of our data and the number of overlapping peaks for perovskite and post-perovskite structures do not allow us to do so.

Table 1. Image number, pressure (P), temperature (T), lattice parameters, normalized stress, and crystallite size (CS) measured in the experiment. Numbers in parenthesis for temperatures are uncertainties on the last digits, determined from the difference in readings of both thermocouples. Errors are estimated to be 0.07 and 0.1 Å^3 for perovskite and post-perovskite unit cell volumes, respectively, 0.002 Å for unit cell parameters, 0.0002 for normalized stresses, and approximately 200 Å^3 for crystallite sizes. $NaCoF_3$ perovskite cell parameters are displayed in the Pbnm space group.

Image	P (GPa)	T (K)	Pt	$NaCoF_3$					
			a (Å)	Phase	a (Å)	b (Å)	c (Å)	t/G	CS (Å)
3	3.4	301 (0)	3.907	Pv	5.297	5.580	7.694	0.028	277
7	4.0	423 (4)	3.906	Pv	5.293	5.570	7.681	0.039	286
12	3.7	507 (15)	3.907	Pv	5.305	5.560	7.678	0.039	249
17	1.1	767 (7)	3.920	Pv	5.392	5.588	7.774	0.029	272
38	1.1	868 (9)	3.918	Pv	5.363	5.553	7.720	0.010	465
46	4.2	866 (10)	3.907	Pv	5.302	5.526	7.653	0.022	475
52	7.3	866 (10)	3.893	Pv	5.227	5.503	7.592	0.037	428
57	9.0	865 (10)	3.886	Pv	5.162	5.488	7.547	0.041	388
66	13.4	861 (10)	3.868	Pv	5.034	5.468	7.469	0.049	337
69	14.8	861 (10)	3.863	Pv	4.995	5.467	7.444	0.051	231
73	18.1	929 (7)	3.852	Pv	4.921	5.456	7.391	0.054	143
77	20.1	997 (10)	3.844	Pv	4.852	5.485	7.339	0.048	104
79	26.1	1013 (14)	3.824	pPv	2.894	9.030	6.974	0.016	87
83	27.5	1006 (18)	3.819	pPv	2.884	9.022	6.950	0.018	100
86	28.5	1004 (19)	3.816	pPv	2.872	9.014	6.944	0.018	107
87	29.1	1003 (20)	3.814	pPv	2.868	9.012	6.935	0.018	171
88	29.6	1003 (20)	3.813	pPv	2.867	9.008	6.930	0.020	359

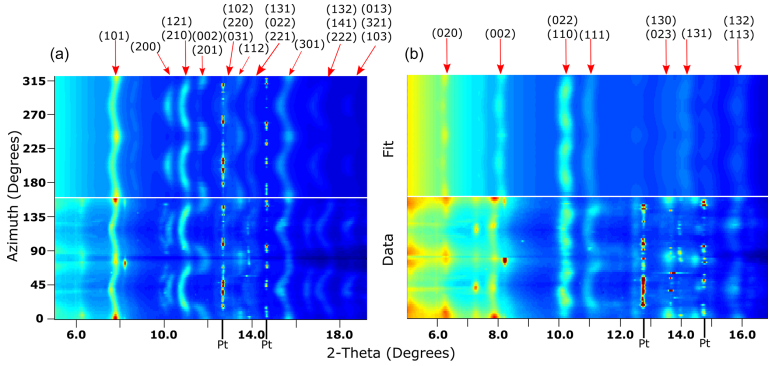

Figure 2. (a) Unrolled diffraction image of $NaCoF_3$ perovskite at 20.1 GPa and 997 K, immediately before transformation to post-perovskite. Below: measured diffraction (labeled data). Above: diffraction image recalculated by MAUD (labeled fit). Diffraction peaks of perovskite are labeled by their Miller indices, and platinum peaks are indicated by Pt. **(b)** Diffraction and fit for post-perovskite phase at 26.1 GPa and 1013 K. In both **(a)** and **(b)** diffraction lines vary in position and intensity, revealing texture and stress development due to compression. Graphite peaks from the heater are present at 6.0, 8.2, 13.4, and 14.6° 2θ. These diffraction peaks, becoming more visible as the experiment proceeds, show no strain and were ignored if necessary during the refinement process.

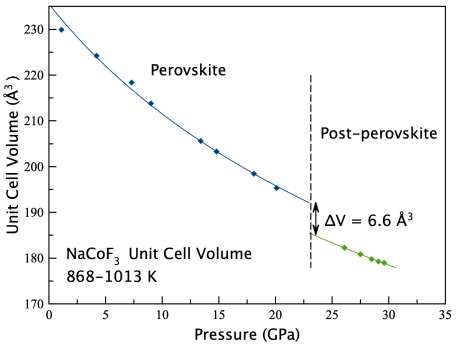

Figure 3. Unit cell volumes of $NaCoF_3$ perovskite and post-perovskite plotted vs. pressure. Lines are second-order Birch–Murnaghan equation of state, fit for each phase assuming constant temperature and used to illustrate compression behavior vs. experimental values.

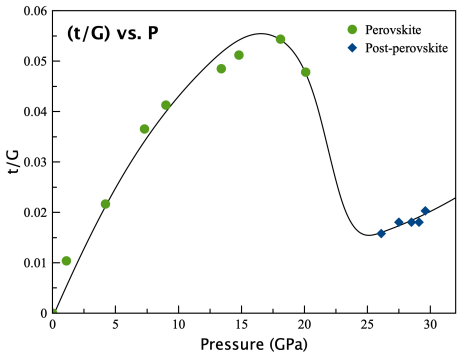

Figure 4. Normalized stress t/G in $NaCoF_3$ perovskite (green circles) and post-perovskite (blue diamonds) as a function of pressure. The solid line is a visual guide through the experimental data. The perovskite to post-perovskite transition occurs between 20.1 and 26.1 GPa.

Orientation distribution functions (ODFs) were calculated using the entropy Williams–Matthies–Imhof–Vinel (E-WIMV) algorithm which accounts for incomplete and arbitrary pole coverage. The ODF is a probability distribution function to find an orientation, which is normalized over the entire sample. An ODF with a multiple of random distribution (mrd) of 1 indicates a random orientation. Values greater or smaller than 1 indicate preferred orientation within an aggregate of grains, which we refer to as texture. Compression in the diamond anvil cell imposes a symmetry along the compression direction, set as the z axis in MAUD. Therefore, we impose a fiber symmetry and use an ODF resolution of 15°.

3 Results

$NaCoF_3$ crystallizes in the perovskite structure at ambient conditions. We observe a transformation to post-perovskite between 20.1 and 26.1 GPa at temperatures of $\approx$ 1000 K.

Unit cell volumes of $NaCoF_3$ in perovskite and post-perovskite are shown in Fig. 3 and the corresponding unit cell parameters in Table 1. In this study, we use the Pbnm space group for the orthorhombic setting of the perovskite phase. MAUD does report errors for each of the fitted parameters; however, these values underestimate the true physical error of the measurement. Hence, errors for unit cell volumes, unit cell parameters, normalized stress, and crystallite size have been estimated by running multiple series of MAUD refinements from different starting values. The error values reported in the caption of Table 1 are the maximum variation of each quantity. We observe a smooth decrease in unit cell volume with pressure.

We used the program EosFit (Gonzalez-Platas et al., 2016) to fit a second-order Birch–Murnaghan equation of state trend for perovskite between 1.1 GPa and 868 K and 20.1 GPa and 997 K and for all post-perovskite data. Considering the small ranges in temperature for the measurements, temperature effects were ignored. The resulting bulk modulus for perovskite and post-perovskite in the 868–1013 K range are 74.9 and 85.9 GPa, respectively. Based on Fig. 3, the drop of volume at the perovskite to post-perovskite transition is estimated to be 6.6 Å^3

Since the pressure and temperature effect on shear modulus is unknown for $NaCoF_3$, we report stresses in terms of normalized stress t/G. This quantity is a more appropriate representation of stress, does not require the extrapolation of G, and has been used in past studies to compare materials to each other (Duffy, 2007; Miyagi et al., 2009; Dorfman et al., 2015). As pressure increases from 1.1 to 18.1 GPa at temperatures between 868 and 929 K, normalized stress in $NaCoF_3$ perovskite increases from 0.010 to 0.054 (Fig. 4). Before the onset of transformation to post-perovskite, we observe a decrease in normalized stress to 0.048 at 997 K. This decrease in stress is likely due to relaxation as the transition is initiated. The t/G value drops to 0.016 as post-perovskite is formed at 26.1 GPa and 1013 K. Upon further compression to 29.6 GPa at 1003 K, t/G in post-perovskite increases to 0.020.

Texture development during the experiment is shown as inverse pole figures of the compression direction (Fig. 5). In the perovskite phase we observe a weak maximum at 100 (2.2 mrd) after the closure of the sample chamber (Fig. 5a). As compression of $NaCoF_3$ continues the maximum at 100 strengthens to an mrd value of 4.2 at 7.3 GPa (Fig. 5b). Upon

further compression to 13.4 GPa, a weak secondary maximum appears at 001 (Fig. 5c). This texture weakens before transitioning to post-perovskite at 26.1 GPa (Fig. 5f). This is likely a feature of the transformation. In all cases, there is a clear minimum at 010 in the perovskite phase.

At 26.1 GPa $NaCoF_3$ has transformed to a post-perovskite structure, and a weak preferred orientation can be observed at 010 (Fig. 5f). This texture strengthens upon compression to 29.6 GPa with mrd values never exceeding 3. Additionally, a clear minimum at 001 develops upon compression of the post-perovskite phase, as well as a small shift of 010 towards 001 (Fig. 5g).

4 Plastic deformation of $NaCoF_3$

4.1 Compression textures in $NaCoF_3$ perovskite

Texture evolution is indicative of ongoing plastic deformation and most likely dislocation glide or twinning. Other deformation mechanisms including dislocation climb or diffusion could be active during deformation; however, these mechanisms would not result in strong deformation textures like those observed in our experiments. In earth sciences, deformation textures in perovskite-structured materials are motivated because the most abundant mineral in the Earth's lower mantle is bridgmanite; $(Mg,Fe)SiO_3$ in the perovskite structure (Tschauner et al., 2014). Numerous studies have hence addressed the deformation textures and mechanisms in bridgmanite (e.g., Wang et al., 1992; Merkel et al., 2003; Wenk et al., 2004a; Cordier et al., 2004; Wenk et al., 2006; Ferré et al., 2007; Mainprice et al., 2008; Miyagi and Wenk, 2016; Kraych et al., 2016; Boioli et al., 2017). In addition, other studies implement structural analogue compositions such as $CaIrO_3$ (Niwa et al., 2007), $NaMgF_3$ (Kaercher et al., 2016), and $CaGeO_3$ (Wang et al., 2013) as lower pressures and temperatures are required to generate a compression texture, and data are easier to interpret. Furthermore, compression textures in $NaCoF_3$ have not been investigated before, which only allows us to compare them to other analogues such as the ones mentioned above. It is important to note, however, that not all perovskite-structured materials behave in the same manner during plastic deformation.

Here, we measure compression textures in $NaCoF_3$ between 1.1 and 29.6 GPa at temperatures between 767 and 1013 K. We observe a 100 compression texture very early in the compression (Fig. 5a) which strengthens with further compression to 18.1 GPa (Fig. 5d). This increase of the 100 texture maximum is accompanied by a decrease in intensity at 010. At 13.4 GPa, we observe the appearance of a secondary maximum at 001. The 100 maximum induced by the first stage of compression compares favorably with experiments on bridgmanite (Merkel et al., 2003; Wenk et al., 2004b; Miyagi and Wenk, 2016) in which it was assigned to a likely contribution of {110} mechanical twinning as identified in early transmission electron microscope (TEM) studies (Wang et al., 1992). This same 100 texture maximum was also observed in compressed $NaMgF_3$ (Kaercher et al., 2016). The secondary 001 maximum observed later in compression was also observed in D-DIA deformation experiments on $NaMgF_3$ (Kaercher et al., 2016) and was reported in the study of Miyagi and Wenk (2016) on bridgmanite at pressures below 55 GPa in which it was assigned to slip along (001).

Based on texture measurements, $NaCoF_3$ is a good analogue for constraining the plasticity of bridgmanite as both maxima at 100 and 001 are observed in both phases in compression experiments. The interpretation of which deformation mechanisms are responsible for experimental texture, however, requires a comparison with polycrystal plasticity simulations. This allows the most relevant deformation mechanism controlling microstructures in the experiment to be extracted and will be described in Sect. 4.3.

4.2 Compression textures in $NaCoF_3$ post-perovskite

Texture in post-perovskite can arise from phase transformations (Okada et al., 2010; Miyagi et al., 2010, 2011; Dobson et al., 2013; Miyagi and Wenk, 2016) or plastic deformation (Merkel et al., 2006, 2007; Yamazaki et al., 2006; Niwa et al., 2007; Miyajima and Walte, 2009; Hunt et al., 2016). Here, we measure textures in $NaCoF_3$ post-perovskite between 26.1 and 29.6 GPa at $\approx$ 1000 K. Post-perovskite is compressed over a restricted pressure range ($\approx$ 4 GPa), little texture evolution is observed, and textures are interpreted to arise primarily from transformation. There is a clear effect of transformation textures vs. deformation textures, and our observed texture mostly results from the phase transformation; thus interpretation based on deformation mechanisms will be biased. For this reason, we will focus on the analysis of the perovskite to post-perovskite transformation in Sect. 5.

4.3 Plastic deformation mechanism in perovskite

Texture development depends on a number of factors including deformation geometry, total strain, starting texture, and plastic deformation mechanism activity. Interpretations can be made by using a visco-plastic self-consistent (VPSC) model, which simulates the plastic deformation of polycrystalline aggregates depending on deformation mechanisms and loading conditions (Wenk, 1999). VPSC modeling has been used in the past to investigate deformation of perovskites at lower-mantle conditions (Mainprice et al., 2008; Miyagi and Wenk, 2016; Kaercher et al., 2016). Based on these publications, we test the following deformation mechanisms, (100)[010], (100)[001], (100)$\langle$011$\rangle$, (010)[100], (010)$\langle$101$\rangle$, (001)[100], (001)$\langle$110$\rangle$, {111}$\langle$110$\rangle$, and {110}$\langle$1$\bar{1}$0$\rangle$ twins, in order to generate the best fit texture observed in our experiments (Fig. 5). The final models used are shown in Table 2 and will be described below.

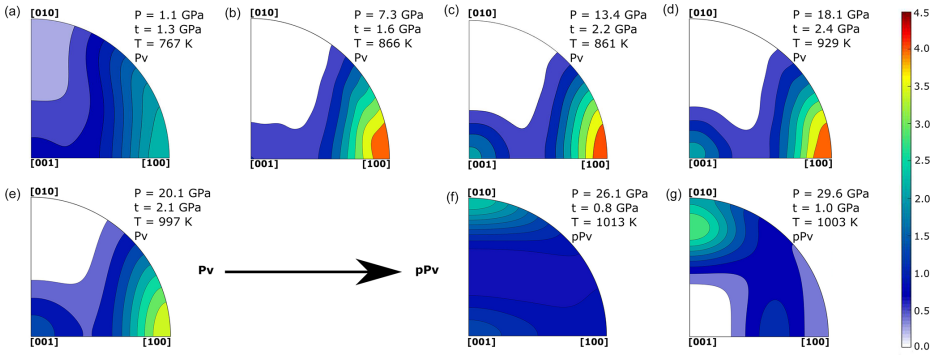

Figure 5. Inverse pole figures in the compression direction of $NaCoF_3$ at various stages of compression. **(a, b, c, d, e)** Perovskite structure (Pbmn setting). **(f, g)** Post-perovskite structure. Equal area projection. Color scale in multiples of random distribution (mrd). Values of t reported in the figure assume constant shear modulus value of G = 44 GPa.

Table 2. CRSS, start activity, and end activity of slip systems from VPSC calculations for perovskite. Sample compression is modeled in two stages. See text for details.

Slip system	Stage 1 (25 % strain)			Stage 2 (40 % strain)		
	CRSS	Start activity	End activity	CRSS	Start activity	End activity
(100)[010]	3	9.9 %	10.8 %	5	8.4 %	5.1 %
(100)[001]	2	10.2 %	17.8 %	5	0.7 %	1.0 %
(100)⟨011⟩	2	32.3 %	44.3 %	5	5.8 %	4.3 %
(010)[100]	5	2.1 %	2.3 %	5	8.4 %	5.1 %
(010)⟨101⟩	5	11.5 %	6.8 %	5	3.3 %	2.0 %
(001)[100]	5	0.7 %	1.1 %	6	0.4 %	1.0 %
(001)[010]	5	7.5 %	3.7 %	6	0.0 %	0.0 %
(001)⟨110⟩	5	7.5 %	5.2 %	1	69.5 %	79.7 %
{111}⟨110⟩	30	1.4 %	7.4 %	30	3.4 %	2.4 %
{110}⟨1$\bar{1}$0⟩ twin	2	17.0 %	0.5 %	25	0.0 %	0.0 %

The critical resolved shear stress (CRSS) values reported in this paper are only relative values to one another. Due to the absence of single crystal elastic information on $NaCoF_3$, we lack the elasticity information required to model deformation textures using an elasto-visco-plastic self-consistent (E-VPSC) model which would take into account elastic properties and absolute shear stresses. As a result, we use the visco-plastic self-consistent (VPSC) approach which does not include any effect of elasticity in which we adjust relative CRSS values to best match our observed textures. Starting from a set of 3000 random orientations (Fig. 6a), we can successfully generate a strong 100 texture while depleting 010 and maintaining orientations at 001, as measured at 7.3 GPa (Fig. 5b), by applying 25 % strain in axial compression with dominant slip on (100) and a significant contribution of {110} twins (Fig. 6c). It is necessary to include {110} twins in order to deplete the 010 direction while maintaining orientations at 001. Indeed, dominant slip on (100) only results in the depletion of both 010 and 001 (Kaercher et al., 2016) and is not consistent with our experimental results.

We were then unable to obtain orientations on the secondary 001 maximum while preserving the initial 100 texture as measured in the experiment above 13.4 GPa (Fig. 5c). Among the proposed deformation mechanisms, slip on (001) can indeed move orientations from 100 to 001, but such simulations will generate a slow movement of orientations from 100 to 001, as shown in the second stage simulations (Fig. 6d and e). This is not observed in the experiments for which the 001 maximum increases in the absence of intermediate orientations between 100 and 001. Twinning is an efficient mode for inducing fast grain reorientations without producing a gradual texture shift. The fast reorientation of grains from 100 to 001 hence alludes to a potential contribution of an unknown twinning mode. Despite all our attempts, we were

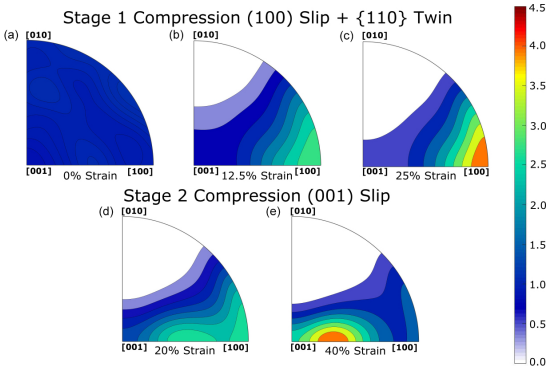

Figure 6. Inverse pole figures **(a, b, c)** of first stage compression in VPSC simulation starting from a random texture at 0 % strain to 25 % strain dominated by slip along (100) planes with significant contribution of {110} twins. Second stage of deformation **(d, e)** starting from **(c)**, allowing 20 % and 40 % strain with deformation dominated by (001) slip.

unable to characterize the observed 001 maximum based on twinning laws reported for perovskites.

5 Transformation of perovskite to post-perovskite in $NaCoF_3$

Many questions have arisen regarding the transformation of perovskite to post-perovskite, including the transformation mechanism itself (Tsuchiya et al., 2004; Oganov et al., 2005; Dobson et al., 2013), its effect on lattice preferred orientations (Okada et al., 2010; Miyagi et al., 2011), stress (Hunt et al., 2009; Dobson et al., 2012), and anisotropy in the Earth's lower mantle (Dobson et al., 2013; Walker et al., 2018b).

5.1 Pressure

Transformation of $NaCoF_3$ perovskite to post-perovskite takes place between 20.1 and 26.1 GPa. The broad pressure range of conversion reported can be explained by significant peak overlap between perovskite and post-perovskite obscuring the phase transition. We observed the phase transition at higher pressures than Dobson et al. (2011) and Yusa et al. (2012), who observe the transition from perovskite to post-perovskite at 18 GPa and 973 K and 14.5 GPa at 1173 K, respectively. This could be an effect of either stress or kinetics. During our experiment we do not allow as much time at the transition pressure as Dobson et al. (2011) who induced the transformation in a multi-anvil press. Additionally, Yusa et al. (2012) observe disproportionation phases after laser heating above 21 GPa at 1100 K that we do not. This could potentially be explained by the overall lower temperatures in our experiment.

5.2 Stress

With the transition of perovskite to post-perovskite we measure a drop of normalized stress from 0.054 to 0.016 (a factor of 3). In comparison, studies by Hunt et al. (2009) and Dobson et al. (2012) indicate post-perovskite deforms 5 to 10 times faster than perovskite when using analogues $NaCoF_3$ and $CaIrO_3$ based on strain rate measurements. Additionally, numerical simulations of diffusion in $MgSiO_3$ by Ammann et al. (2010) predicted a significantly weaker post-perovskite phase. The observed normalized strength drop in $NaCoF_3$ upon its transformation to post-perovskite is likely a result of transformation plasticity or transient weakening. In the absence of known values for elastic properties of $NaCoF_3$ under high P/T, we are unable to report actual differential stress values. Despite this limitation, overall our results are consistent with a weakening of materials at the perovskite to post-perovskite transition.

5.3 Mechanism

Phase transformations change crystal structures but also induce a change in texture of materials. Transformations can be diffusionless in nature, meaning the atoms within the material move in a homogeneous fashion or they can be reconstructive in nature and move by means of long-range diffusion. Diffusionless transformations involve orientation relationships between the parent and daughter phase and are sometimes referred to as martensitic (Christian et al., 1995). Diffusive transformations, on the other hand, do not imply orientation relationships between the parent and daughter phase.

Early predictions by Tsuchiya et al. (2004) indicate that the perovskite to post-perovskite transformation should lead

to orientation relationships. They determine that $[1\bar{1}0]$, [110], and [001] of Pbnm perovskite correspond to [100], [010], and [001], respectively, in Cmcm post-perovskite. In parallel, based on metadynamics, the simulations of Oganov et al. (2005) predict a less cooperative mechanism with stacking faults producing shear and fragments of post-perovskite structures. Experimentally, Dobson et al. (2013) studied the perovskite to post-perovskite transition in $NaNiF_3$ based on high-pressure experiments and electron microscopy on the recovered samples. They indicate that the *c* axis of the perovskite phase is preserved during the transformation to post-perovskite. In addition, they observed that the post-perovskite *hh*0 vector in reciprocal space is parallel to [010] in perovskite.

Here, we test these three different transformation models. The orientation relationships of Tsuchiya et al. (2004), starting from $NaCoF_3$ perovskite at 20.1 GPa, result in a transformation texture with diffuse weak maximums between 010 and 100 (Fig. 7c). The model proposed by Oganov et al. (2005) is not consistent with our data because orientation relationships are only considered along the *c* direction. We clearly observe a 010 texture in post-perovskite, implying there are additional orientation relationships than that along the *c* direction. When using the orientations relationships in Dobson et al. (2013), the simulated post-perovskite texture matches that measured experimentally (Fig. 7d). In both the experimental and simulated textures, we observe a maximum at 010. Moreover, the strength of the texture is consistent between experiments and simulations.

Based on the above reasoning, we can conclude that the transformation from perovskite to post-perovskite in $NaCoF_3$ involves orientation relationships and hence falls within the group of displacive phase transformations. Furthermore, these relationships fit the model of Dobson et al. (2013), based on experiments performed on $NaNiF_3$. This supports the idea that this mechanism could apply to natural perovskite phases.

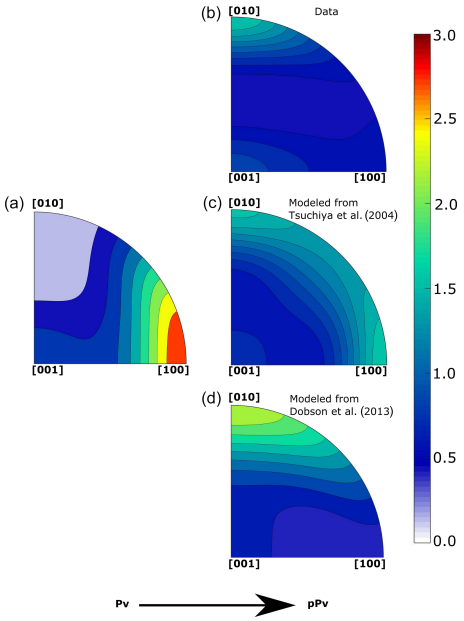

Figure 7. **(a)** Perovskite texture at 20.1 GPa immediately before transformation to post-perovskite. **(b)** Post-perovskite texture at 26.1 GPa after transformation from experimental measurements. **(c)** Modeled transformation texture of post-perovskite using orientation relationships from Tsuchiya et al. (2004). **(d)** Modeled transformation texture of post-perovskite using orientation relationships from Dobson et al. (2013).

6 Conclusion

This paper presented experimental results of $NaCoF_3$ compressed inside a resistive-heated radial diffraction DAC at pressures of 1.1 to 29.6 GPa and temperatures between 300 and 1013 K. A phase transformation from $NaCoF_3$ perovskite to post- perovskite was observed between 20.1 and 26.1 GPa.

Deformation of $NaCoF_3$ perovskite initially results in a strong 100 maximum when the sample is at 7.3 GPa. VPSC simulations show that this texture is formed by slip along (100) paired with important contributions from {110} twins. Later in the deformation process we observe a weak secondary 001 maximum appearing at 13.4 GPa. These deformation textures are similar to those of $NaMgF_3$ shown in Kaercher et al. (2016). We attempt to model this secondary maximum; however, we are unable to recreate it without shifting the original 100 maximum. Such fast grain reorientation could be explained by a twinning mode different from known perovskite twinning modes (Wang et al., 1992). Direct comparisons to $MgSiO_3$ deformation textures are made difficult because of the effect of starting material on the $MgSiO_3$ transformation textures (Miyagi and Wenk, 2016). Nevertheless, both the 100 and 001 compression textures observed in $NaCoF_3$ have been observed in natural compositions (Merkel et al., 2003; Wenk et al., 2004b; Miyagi and Wenk, 2016; Couper et al., 2020). $NaCoF_3$ hence appears as a good analogue for plasticity studies relevant for the Earth's mantle.

The phase transition from perovskite to post-perovskite results in a normalized strength drop from 0.054 to 0.016 (a factor of 3), which is likely a result of transformation plasticity or transient weakening. Transformation of $NaCoF_3$ perovskite to post-perovskite is martensitic in nature as demonstrated by the existence of orientation relationships between

both phases. The orientation relationships proposed by Dobson et al. (2013) can successfully reproduce our data.

Perovskite analogues continue to provide valuable insight to the behavior of materials at extreme pressures and temperatures relevant for planetary mantles. For Earth's mantle materials, it is important to understand the effect of temperature on deformation mechanisms which may be different from what is observed at 300 K. Analogues such as $NaCoF_3$ allow for studies at lower pressures. It would be interesting to study the effect of temperatures at these lower pressures to constrain the effect of temperature on the plasticity of perovskite phases. Further studies on analogues might also include the investigation of post-perovskite deformation textures in $NaCoF_3$ and other analogues, as well as potential post-post-perovskite phases (Crichton et al., 2016; Umemoto and Wentzcovitch, 2019). A general understanding of plasticity in perovskite and post-perovskite will help with improving the interpretation of seismic models in terms of mantle dynamics such as heat transfer through convection.

Code and data availability. The data were processed using MAUD (http://maud.radiographema.eu, Lutterotti et al., 1997) and MTEX (https://mtex-toolbox.github.io, Bachmann et al., 2010) which are open source and freely available. VPSC modeling was performed using the Los Alamos visco-plastic self-consistent code available from Ricardo A. Lebensohn and Carlos N. Tomé. Maud and VPSC input files are available on Zenodo using the following link: https://doi.org/10.5281/zenodo.5513910 (Gay et al., 2021).

Author contributions. LM and SM designed the project. LM, SM, CL, SC, and HPL conducted the experiment. DPD provided the sample. JPG and SM processed and interpreted the data. JPG and SM wrote the paper with comments from LM, SC, DPD, and HPL.

Competing interests. The contact author has declared that neither they nor their co-authors have any competing interests

Disclaimer. Publisher's note: Copernicus Publications remains neutral with regard to jurisdictional claims in published maps and institutional affiliations.

Special issue statement. This article is part of the special issue "Probing the Earth: experiments and mineral physics at mantle depths". It is a result of the 17th International Symposium on Experimental Mineralogy, Petrology and Geochemistry, Potsdam, Germany, 21–24 June 2020.

Acknowledgements. The Chevreul Institute is thanked for its help in the development of this work through the ARCHI-CM project supported by the "Ministère de l'Enseignement Supérieur de la Recherche et de l'Innovation", the region "Hauts-de-France", the ERDF program of the European Union, and the "Métropole Européenne de Lille". This research was carried out at the P02.2 beamline of the PETRA III synchrotron at DESY, a member of the Helmholtz Association (HGF). The authors would also like to thank Feng Lin for assistance with VPSC modeling.

Financial support. This research has been supported by the Association Nationale de la Recherche et de la Technologie (TIMEleSS, grant no. ANR-17-CE31-0025) and the Deutsche Forschungsgemeinschaft (grant nos. TH 1530/18-1, SA 2585/3-1, and SP1216/8-1). It was also supported by the bilateral PROCOPE-PPP program (grant nos. PHC 40555PC and DAAD 57390184). Christopher Langrand also received support from a fellowship of the Université de Lille and the Région Hauts-de-France. The research leading to this result has been supported by the EU Framework Programme for Research and Innovation HORIZON 2020 (CALIPSOplus (grant no. 730872)).

Review statement. This paper was edited by Max Wilke and reviewed by two anonymous referees.

References

Ammann, M. W., Brodholt, J. P., Wookey, J., and Dobson, D. P.: First-principles constraints on diffusion in lower-mantle minerals and a weak D″ layer, Nature, 465, 462–465, https://doi.org/10.1038/nature09052, 2010.

Bachmann, F., Hielscher, R., and Schaeben, H.: Solid State Phenomena, Texture Analysis with MTEX – Free and Open Source Software Toolbox, 160, 63–68, https://doi.org/10.4028/www.scientific.net/SSP.160.63 (last access 21 September 2021) 2010 (code available at: https://mtex-toolbox.github.io, last access: 21 September 2021).

Beghein, C., Trampert, J., and van Heijst, H. J.: Radial anisotropy in seismic reference models of the mantle, J. Geophys. Res.-Sol. Ea., 111, B02303, https://doi.org/10.1029/2005JB003728, 2006.

Boioli, F., Carrez, P., Cordier, P., Devincre, B., Gouriet, K., Hirel, P., Kraych, A., and Ritterbex, S.: Pure climb creep mechanism drives flow in Earth's lower mantle, Science Advances, 3, 1–7, https://doi.org/10.1126/sciadv.1601958, 2017.

Carrez, P., Ferré, D., and Cordier, P.: Implications for plastic flow in the deep mantle from modelling dislocations in $MgSiO_3$ minerals, Nature, 446, 68–70, https://doi.org/10.1038/nature05593, 2007.

Carrez, P., Goryaeva, A. M., and Cordier, P.: Prediction of Mechanical Twinning in Magnesium Silicate Post-Perovskite, Sci. Rep., 7, 17640, https://doi.org/10.1038/s41598-017-18018-1, 2017.

Chen, G., Liebermann, R. C., and Weidner, D. J.: Elasticity of single-crystal MgO to 8 Gigapascals and 1600 Kelvin, Science, 280, 1913–1916, https://doi.org/10.1126/science.280.5371.1913, 1998.

Chenine, D., Aziz, Z., Benstaali, W., Bouadjemi, B., Youb, O., Lantri, T., Abbar, B., and Bentata, S.: Theoretical Investigation of Half-Metallic Ferromagnetism in Sodium-Based Fluoroperovskite $NaXF_3$ (X = V, Co), J. Supercond. Nov. Magn., 31, 285–295, https://doi.org/10.1007/s10948-017-4204-4, 2018.

Christian, J. W., Olson, G. B., and Cohen, M.: Classification of Displacive Transformations: What is a Martensitic Transformation?, J. Phys. IV France, 05, C8-3–C8-10, https://doi.org/10.1051/jp4:1995801, 1995.

Čížková, H., Čadek, O., Matyska, C., and Yuen, D. A.: Implications of post-perovskite transport properties for core-mantle dynamics, Phys. Earth Planet. In., 180, 235–243, https://doi.org/10.1016/j.pepi.2009.08.008, 2010.

Cobden, L., Thomas, C., and Trampert, J.: The earth's heterogeneous mantle: A geophysical, geodynamical, and geochemical perspective, Springer International Publishing Switzerland, Cham, Switzerland, https://doi.org/10.1007/978-3-319-15627-9_13, 2015.

Cordier, P., Ungár, T., Zsoldos, L., and Tichy, G.: Dislocation creep in $MgSiO_3$ perovskite at conditions of the Earth's uppermost lower mantle, Nature, 428, 837–840, https://doi.org/10.1038/nature02472, 2004.

Couper, S., Speziale, S., Marquardt, H., Liermann, H. P., and Miyagi, L.: Does Heterogeneous Strain Act as a Control on Seismic Anisotropy in Earth's Lower Mantle?, Front. Earth Sci., 8, 540449, https://doi.org/10.3389/feart.2020.540449, 2020.

Crichton, W., Bernal, F., Guignard, J., Hanfland, M., and Margadonna, S.: Observation of Sb_2S_3-type post-post-perovskite in $NaFeF_3$. Implications for ABX_3 and A_2X_3 systems at ultrahigh pressure, Mineral. Mag., 80, 659–674, 2016.

Dobson, D. P., Hunt, S. A., Lindsay-Scott, A., and Wood, I. G.: Towards better analogues for $MgSiO_3$ post-perovskite: $NaCoF_3$ and $NaNiF_3$, two new recoverable fluoride post-perovskites, Phys. Earth Planet. In., 189, 171–175, https://doi.org/10.1016/j.pepi.2011.08.010, 2011.

Dobson, D. P., McCormack, R., Hunt, S. A., Ammann, M. W., Weidner, D., Li, L., and Wang, L.: The relative strength of perovskite and post-perovskite $NaCoF_3$, Mineral. Mag., 76, 925–932, https://doi.org/10.1180/minmag.2012.076.4.09, 2012.

Dobson, D. P., Miyajima, N., Nestola, F., Alvaro, M., Casati, N., Liebske, C., Wood, I. G., and Walker, A. M.: Strong inheritance of texture between perovskite and post-perovskite in the D″ layer, Nat. Geosci., 6, 575–578, https://doi.org/10.1038/ngeo1844, 2013.

Dorfman, S. M., Shieh, S. R., and Duffy, T. S.: Strength and texture of Pt compressed to 63 GPa, J. Appl. Phys., 117, 065901, https://doi.org/10.1063/1.4907866, 2015.

Duffy, T. S.: Strength of materials under static loading in the diamond anvil cell, AIP Conf. Proc., 955, 639–644, https://doi.org/10.1063/1.2833175, 2007.

Ferré, D., Carrez, P., and Cordier, P.: First principles determination of dislocations properties of $MgSiO_3$ perovskite at 30 GPa based on the Peierls-Nabarro model, Phys. Earth Planet. In., 163, 283–291, https://doi.org/10.1016/j.pepi.2007.05.011, 2007.

Ferreira, A. M., Faccenda, M., Sturgeon, W., Chang, S. J., and Schardong, L.: Ubiquitous lower-mantle anisotropy beneath subduction zones, Nat. Geosci., 12, 301–306, https://doi.org/10.1038/s41561-019-0325-7, 2019.

Garnero, E. J., Maupin, V., Lay, T., and Fouch, M. J.: Variable azimuthal anisotropy in earth's lowermost mantle, Science, 306, 259–261, https://doi.org/10.1126/science.1103411, 2004.

Gay, J. P., Miyagi, L., Couper, S., Langrand, C., Dobson, D. P., Liermann, H.-P., and Merkel, S.: Data for deformation and transformation of NaCoF3 perovskite and post-perovskite up to 30 GPa and 1013 K, Zenodo [data set], https://doi.org/10.5281/zenodo.5513910, 2021.

Girard, J., Amulele, G., Farla, R., Mohiuddin, A., and Karato, S. I.: Shear deformation of bridgmanite and magnesiowüstite aggregates at lower mantle conditions, Science, 351, 144–147, https://doi.org/10.1126/science.aad3113, 2016.

Gonzalez-Platas, J., Alvaro, M., Nestola, F., and Angel, R.: EosFit7-GUI: A new graphical user interface for equation of state calculations, analyses and teaching, J. Appl. Crystallogr., 49, 1377–1382, https://doi.org/10.1107/S1600576716008050, 2016.

Hernlund, J. W., Thomas, C., and Tackley, P. J.: A doubling of the post-perovskite, Nature, 434, 882–886, https://doi.org/10.1038/nature03472, 2005.

Hunt, S. A., Weidner, D. J., Li, L., Wang, L., Walte, N. P., Brodholt, J. P., and Dobson, D. P.: Weakening of calcium iridate during its transformation from perovskite to post-perovskite, Nat. Geosci., 2, 794–797, https://doi.org/10.1038/ngeo663, 2009.

Hunt, S. A., Walker, A. M., and Mariani, E.: In-situ measurement of texture development rate in $CaIrO_3$ post-perovskite, Phys. Earth Planet. In., 257, 91–104, https://doi.org/10.1016/j.pepi.2016.05.007, 2016.

Immoor, J., Marquardt, H., Miyagi, L., Speziale, S., Merkel, S., Schwark, I., Ehnes, A., and Liermann, H.-P.: An improved setup for radial diffraction experiments at high pressures and high temperatures in a resistive graphite-heated diamond anvil cell, Rev. Sci. Instrum., 91, 045121, https://doi.org/10.1063/1.5143293, 2020.

Kaercher, P., Miyagi, L., Kanitpanyacharoen, W., Zepeda-Alarcon, E., Wang, Y., Parkinson, D., Lebensohn, R. A., De Carlo, F., and Wenk, H. R.: Two-phase deformation of lower mantle mineral analogs, Earth Planet. Sc. Lett., 456, 134–145, https://doi.org/10.1016/j.epsl.2016.09.030, 2016.

Koelemeijer, P., Schuberth, B. S., Davies, D. R., Deuss, A., and Ritsema, J.: Constraints on the presence of post-perovskite in Earth's lowermost mantle from tomographic-geodynamic model comparisons, Earth Planet. Sc. Lett., 494, 226–238, https://doi.org/10.1016/j.epsl.2018.04.056, 2018.

Kraych, A., Carrez, P., and Cordier, P.: On dislocation glide in $MgSiO_3$ bridgmanite at high-pressure and high-temperature, Earth Planet. Sc. Lett., 452, 60–68, https://doi.org/10.1016/j.epsl.2016.07.035, 2016.

Liermann, H.-P., Merkel, S., Miyagi, L., Wenk, H.-R., Shen, G., Cynn, H., and Evans, W. J.: Experimental method for in situ determination of material textures at simultaneous high pressure and high temperature by means of radial diffraction in the diamond anvil cell, Rev. Sci. Instrum., 80, 104501, https://doi.org/10.1063/1.3236365, 2009.

Liermann, H.-P., Konôpková, Z., Morgenroth, W., Glazyrin, K., Bednarcik, J., McBride, E. E., Petitgirard, S., Delitz, J. T., Wendt, M., Bican, Y., Ehnes, A., Schwark, I., Rothkirch, A., Tischer, M., Heuer, J., Schulte-Schrepping, H., Kracht, T., and Franz, H.: The Extreme Conditions Beamline P02.2 and the Extreme Conditions Science Infrastructure at PETRA III, J. Synchrotron Radiat., 22, 908–924, https://doi.org/10.1107/S1600577515005937, 2015.

Lutterotti, L., Matthies, S., Wenk, H. R., Schultz, A. S., and Richardson, J. W.: Combined texture and structure analysis of deformed limestone from time-of-flight neutron diffraction spectra, J. Appl. Phys., 81, 594–600, https://doi.org/10.1063/1.364220,

1997 (data available at: http://maud.radiographema.eu, last access: 17 September 2021).

Mainprice, D., Barruol, G., Isma, W. B., Mainprice, D., Barruol, G., Isma, W. B., Mainprice, D., Barruol, G., and Isma, W. B.: The Seismic anisotropy of the Earth's mantle: From single crystal to polycrystal, vol. 117, American Geophysical Union, Washington D.C., USA, https://doi.org/10.1029/GM117, 2000.

Mainprice, D., Tommasi, A., Ferré, D., Carrez, P., and Cordier, P.: Predicted glide systems and crystal preferred orientations of polycrystalline silicate Mg-Perovskite at high pressure: Implications for the seismic anisotropy in the lower mantle, Earth Planet. Sc. Lett., 271, 135–144, https://doi.org/10.1016/j.epsl.2008.03.058, 2008.

McCormack, R., Dobson, D. P., Walte, N. P., Miyajima, N., Taniguchi, T., and Wood, I. G.: The development of shape- and crystallographic-preferred orientation in $CaPtO_3$ post-perovskite deformed in pure shear, Am. Mineral., 96, 1630–1635, https://doi.org/10.2138/am.2011.3881, 2011.

Merkel, S., Wenk, H. R., Badro, J., Montagnac, G., Gillet, P., Mao, H. K., and Hemley, R. J.: Deformation of $(Mg_{0.9},Fe_{0.1})SiO_3$ Perovskite aggregates up to 32 GPa, Earth Planet. Sc. Lett., 209, 351–360, https://doi.org/10.1016/S0012-821X(03)00098-0, 2003.

Merkel, S., Kubo, A., Miyagi, L., Speziale, S., Duffy, T. S., Mao, H. K., and Wenk, H. R.: Plastic deformation of MgGeO3 post-perovskite at lower mantle pressures, Science, 311, 644–646, https://doi.org/10.1126/science.1121808, 2006.

Merkel, S., McNamara, A. K., Kubo, A., Speziale, S., Miyagi, L., Meng, Y., Duffy, T. S., and Wenk, H. R.: Deformation of $(Mg,Fe)SiO_3$ post-perovskite and D″ anisotropy, Science, 316, 1729–1732, https://doi.org/10.1126/science.1140609, 2007.

Metsue, A., Carrez, P., Mainprice, D., and Cordier, P.: Numerical modelling of dislocations and deformation mechanisms in $CaIrO_3$ and $MgGeO_3$ post-perovskites – Comparison with $MgSiO_3$ post-perovskite, Phys. Earth Planet. In., 174, 165–173, https://doi.org/10.1016/j.pepi.2008.04.003, 2009.

Miyagi, L. and Wenk, H. R.: Texture development and slip systems in bridgmanite and bridgmanite + ferropericlase aggregates, Phys. Chem. Miner., 43, 597–613, https://doi.org/10.1007/s00269-016-0820-y, 2016.

Miyagi, L., Nishiyama, N., Wang, Y., Kubo, A., West, D. V., Cava, R. J., Duffy, T. S., and Wenk, H. R.: Deformation and texture development in $CaIrO_3$ post-perovskite phase up to 6 GPa and 1300 K, Earth Planet. Sc. Lett., 268, 515–525, https://doi.org/10.1016/j.epsl.2008.02.005, 2008.

Miyagi, L., Merkel, S., Yagi, T., Sata, N., Ohishi, Y., and Wenk, H. R.: Diamond anvil cell deformation of $CaSiO_3$ perovskite up to 49 GPa, Phys. Earth Planet. In., 174, 159–164, https://doi.org/10.1016/j.pepi.2008.05.018, 2009.

Miyagi, L., Kanitpanyacharoen, W., Kaercher, P., Lee, K. K., and Wenk, H. R.: Slip systems in $MgSiO_3$ post-perovskite: Implications for D'' anisotropy, Science, 329, 1639–1641, https://doi.org/10.1126/science.1192465, 2010.

Miyagi, L., Kanitpanyacharoen, W., Stackhouse, S., Militzer, B., and Wenk, H. R.: The enigma of post-perovskite anisotropy: Deformation versus transformation textures, Phys. Chem. Miner., 38, 665–678, https://doi.org/10.1007/s00269-011-0439-y, 2011.

Miyagi, L., Kanitpanyacharoen, W., Raju, S. V., Kaercher, P., Knight, J., MacDowell, A., Wenk, H. R., Williams, Q., and Alarcon, E. Z.: Combined resistive and laser heating technique for in situ radial X-ray diffraction in the diamond anvil cell at high pressure and temperature, Rev. Sci. Instrum., 84, 025118, https://doi.org/10.1063/1.4793398, 2013.

Miyajima, N. and Walte, N.: Burgers vector determination in deformed perovskite and post-perovskite of $CaIrO_3$ using thickness fringes in weak-beam dark-field images, Ultramicroscopy, 109, 683–692, https://doi.org/10.1016/j.ultramic.2009.01.010, 2009.

Murakami, M., Hirose, K., Kawamura, K., Sata, N., and Ohishi, Y.: Post-Perovskite Phase Transition in $MgSiO_3$, Science, 304, 855–858, https://doi.org/10.1126/science.1095932, 2004.

Nakagawa, T. and Tackley, P. J.: Effects of low-viscosity post-perovskite on thermo-chemical mantle convection in a 3-D spherical shell, Geophys. Res. Lett., 38, L04309, https://doi.org/10.1029/2010GL046494, 2011.

Niwa, K., Yagi, T., Ohgushi, K., Merkel, S., Miyajima, N., and Kikegawa, T.: Lattice preferred orientation in $CaIrO_3$ perovskite and post-perovskite formed by plastic deformation under pressure, Phys. Chem. Miner., 34, 679–686, https://doi.org/10.1007/s00269-007-0182-6, 2007.

Nowacki, A., Wookey, J., and Kendall, J. M.: Deformation of the lowermost mantle from seismic anisotropy, Nature, 467, 1091–1094, https://doi.org/10.1038/nature09507, 2010.

Nowacki, A., Walker, A. M., Wookey, J., and Kendall, J. M.: Evaluating post-perovskite as a cause of D″ anisotropy in regions of palaeosubduction, Geophys. J. Int., 192, 1085–1090, https://doi.org/10.1093/gji/ggs068, 2013.

Oganov, A. R. and Ono, S.: Theoretical and experimental evidence for a post-perovskite phase of $MgSiO_3$ in Earth's D″ layer, Nature, 430, 445–448, https://doi.org/10.1038/nature02701, 2004.

Oganov, A. R., Martoňák, R., Laio, A., Raiteri, P., and Parrinello, M.: Anisotropy of earth's D″ layer and stacking faults in the $MgSiO_3$ post-perovskite phase, Nature, 438, 1142–1144, https://doi.org/10.1038/nature04439, 2005.

Okada, T., Yagi, T., Niwa, K., and Kikegawa, T.: Lattice-preferred orientations in post-perovskite-type $MgGeO_3$ formed by transformations from different pre-phases, Phys. Earth Planet. In., 180, 195–202, https://doi.org/10.1016/j.pepi.2009.08.002, 2010.

Panning, M. and Romanowicz, B.: A three-dimensional radially anisotropic model of shear velocity in the whole mantle, Geophys. J. Int., 167, 361–379, https://doi.org/10.1111/j.1365-246X.2006.03100.x, 2006.

Pisconti, A., Thomas, C., and Wookey, J.: Discriminating Between Causes of D″ Anisotropy Using Reflections and Splitting Measurements for a Single Path, J. Geophys. Res.-Sol. Ea., 124, 4811–4830, https://doi.org/10.1029/2018JB016993, 2019.

Popa, N. C.: The (hkl) Dependence of Diffraction-Line Broadening Caused by Strain and Size for all Laue Groups in Rietveld Refinement, J. Appl. Crystallogr., 31, 176–180, https://doi.org/10.1107/S0021889897009795, 1998.

Romanowicz, B. and Wenk, H. R.: Anisotropy in the deep Earth, Phys. Earth Planet. In., 269, 58–90, https://doi.org/10.1016/j.pepi.2017.05.005, 2017.

Savage, M. S.: Seismic anisotropy and mantle deformation: What have we learned from shear wave splitting?, Rev. Geophys., 37, 65–106, https://doi.org/10.1029/98RG02075, 1999.

Shirako, Y., Shi, Y. G., Aimi, A., Mori, D., Kojitani, H., Yamaura, K., Inaguma, Y., and Akaogi, M.: High-pressure stability relations, crystal structures, and physical properties of perovskite and

post-perovskite of $NaNiF_3$, J. Solid State Chem., 191, 167–174, https://doi.org/10.1016/j.jssc.2012.03.004, 2012.

Singh, A. K., Balasingh, C., Mao, H. K., Hemley, R. J., and Shu, J.: Analysis of lattice strains measured under nonhydrostatic pressure, J. Appl. Phys., 83, 7567–7575, https://doi.org/10.1063/1.367872, 1998.

Tackley, P. J.: Dynamics and evolution of the deep mantle resulting from thermal, chemical, phase and melting effects, Earth-Sci. Rev., 110, 1–25, https://doi.org/10.1016/j.earscirev.2011.10.001, 2012.

Tschauner, O., Chi, M., Beckett, J. R., Prescher, C., Prakapenka, V. B., and Rossman, G. R.: Discovery of bridgmanite, the most abundant mineral in Earth, in a shocked meteorite, Science, 346, 1100–1102, https://doi.org/10.1126/science.1259369, 2014.

Tsuchiya, T., Tsuchiya, J., Umemoto, K., and Wentzcovitch, R. M.: Phase transition in $MgSiO_3$ perovskite in the earth's lower mantle, Earth Planet. Sci. Lett., 224, 241–248, https://doi.org/10.1016/j.epsl.2004.05.017, 2004.

Tsujino, N., Nishihara, Y., Yamazaki, D., Seto, Y., Higo, Y., and Takahashi, E.: Mantle dynamics inferred from the crystallographic preferred orientation of bridgmanite, Nature, 539, 81–84, https://doi.org/10.1038/nature19777, 2016.

Umemoto, K. and Wentzcovitch, R. M.: Ab initio exploration of post-PPV transitions in low-pressure analogs of $MgSiO_3$, Physical Review Materials, 3, 25–28, https://doi.org/10.1103/PhysRevMaterials.3.123601, 2019.

Walker, A. M., Dobson, D. P., Wookey, J., Nowacki, A., and Forte, A. M.: The anisotropic signal of topotaxy during phase transitions in D″, Phys. Earth Planet. In., 276, 159–171, https://doi.org/10.1016/j.pepi.2017.05.013, 2018a.

Walker, A. M., Dobson, D. P., Wookey, J., Nowacki, A., and Forte, A. M.: The anisotropic signal of topotaxy during phase transitions in D″, Phys. Earth Planet. In., 276, 159–171, https://doi.org/10.1016/j.pepi.2017.05.013, 2018b.

Walte, N. P., Heidelbach, F., Miyajima, N., Frost, D. J., Rubie, D. C., and Dobson, D. P.: Transformation textures in post-perovskite: Understanding mantle flow in the D″ layer of the earth, Geophys. Res. Lett., 36, 3–7, https://doi.org/10.1029/2008GL036840, 2009.

Wang, Y., Guyot, F., and Liebermann, R. C.: Electron microscopy of (Mg, Fe)SiO_3 perovskite: evidence for structural phase transitions and implications for the lower mantle, J. Geophys. Res., 97, 327–347, https://doi.org/10.1029/92jb00870, 1992.

Wang, Y., Hilairet, N., Nishiyama, N., Yahata, N., Tsuchiya, T., Morard, G., and Fiquet, G.: High-pressure, high-temperature deformation of $CaGeO_3$ (perovskite)±MgO aggregates: Implications for multiphase rheology of the lower mantle, Geochem. Geophys. Geosy., 14, 3389–3408, https://doi.org/10.1002/ggge.20200, 2013.

Wenk, H. R.: A voyage through the deformed Earth with the self-consistent model, Model. Simul. Mater. Sc., 7, 699, http://stacks.iop.org/0965-0393/7/i=5/a=304 (last access: 13 March 2019), 1999.

Wenk, H. R., Lonardeli, I., Pehl, J., Devine, J., Prakapenka, V., Shen, G., and Mao, H. K.: In situ observation of texture development in olivine, ringwoodite, magnesiowüstite and silicate perovskite at high pressure, Earth Planet. Sc. Lett., 226, 507–519, https://doi.org/10.1016/j.epsl.2004.07.033, 2004a.

Wenk, H. R., Lonardeli, I., Pehl, J., Devine, J., Prakapenka, V., Shen, G., and Mao, H. K.: In situ observation of texture development in olivine, ringwoodite, magnesiowüstite and silicate perovskite at high pressure, Earth Planet. Sc. Lett., 226, 507–519, https://doi.org/10.1016/j.epsl.2004.07.033, 2004b.

Wenk, H. R., Lonardelli, I., Merkel, S., Miyagi, L., Pehl, J., Speziale, S., and Tommaseo, C. E.: Deformation textures produced in diamond anvil experiments, analysed in radial diffraction geometry, Journal of Physics Condensed Matter, 18, S933–S947, https://doi.org/10.1088/0953-8984/18/25/S02, 2006.

Wenk, H. R., Lutterotti, L., Kaercher, P., Kanitpanyacharoen, W., Miyagi, L., and Vasin, R.: Rietveld texture analysis from synchrotron diffraction images. II. Complex multiphase materials and diamond anvil cell experiments, Powder Diffraction, 29, 220–232, https://doi.org/10.1017/S0885715614000360, 2014.

Wookey, J. and Kendall, J. M.: Seismic Anisotropy of Post-Perovskite and the Lowermost Mantle, 174, 171–189, available at: https://agupubs.onlinelibrary.wiley.com/doi/10.1029/174GM13 (last access: 23 July 2021), 2007.

Wookey, J., Kendall, J. M., and Barruol, G.: Mid-mantle deformation inferred from seismic anisotropy, Nature, 415, 777–780, https://doi.org/10.1038/415777a, 2002.

Yamazaki, D. and Karato, S. I.: Lattice-Preferred Orientation of Lower Mantle Materials and Seismic Anisotropy in the D″ Layer, Washington DC American Geophysical Union Geophysical Monograph Series, pp. 69–78, available at: https://agupubs.onlinelibrary.wiley.com/doi/10.1029/174GM07 (last access: 29 July 2021), 2007.

Yamazaki, D., Yoshino, T., Ohfuji, H., Ando, J.-i., and Yoneda, A.: Origin of seismic anisotropy in the D″ layer inferred from shear deformation experiments on post-perovskite phase, Earth Planet. Sc. Lett., 252, 372–378, https://doi.org/10.1016/j.epsl.2006.10.004, 2006.

Yusa, H., Shirako, Y., Akaogi, M., Kojitani, H., Hirao, N., Ohishi, Y., and Kikegawwa, T.: Perovskite-to-Postperovskite Transitions in $NaNiF_3$ and $NaCoF_3$ and Disproportionation of $NaCoF_3$ Postperovskite under High Pressure and High Temperature, Inorg. Chem., 51, 6559–6566, https://doi.org/10.1021/ic300118d, 2012.

Zha, C. S., Mibe, K., Bassett, W. A., Tschauner, O., Mao, H. K., and Hemley, R. J.: P-V-T equation of state of platinum to 80 GPa and 1900 K from internal resistive heating/x-ray diffraction measurements, J. Appl. Phys., 103, 054908, https://doi.org/10.1063/1.2844358, 2008.

Chapter 4

Transformation Microstructures in Pyrolite and Implications for Anisotropy Below the '660' Discontinuity

This section has been submitted to Earth and Planetary Science Letters in August 2022 in a slightly different form. Section is a combination of the main draft and supplementary materials.

4.1 Introduction

The '660' discontinuity serves as a boundary between the transition zone and lower mantle at approximately 660 km depth within the Earth's mantle. This discontinuity has been observed in several seismological studies by using a variety of reflected and transmitted waveforms [Xu et al., 2003, Deuss et al., 2006, Deuss, 2009]; however, some waveforms, including underside P-wave reflections and long period PP precursors, are less successful at detecting reflections at relevant depths [Day and Deuss, 2013, Waszek et al., 2021]. SS and P'P' precursors have been more successful in detecting an apparent sharp boundary, less that 2 km thick, at the '660' [Xu et al., 2003, Deuss, 2009]. These seismic observations occur both regionally [Wang and Niu, 2010, Jenkins et al., 2016] and globally [Shearer, 2000, Andrews and Deuss, 2008] within the mantle.

The 660 km discontinuity is also believed to be the result of mineralogical phase transitions in pyrolite [Ringwood, 1991], which is believed to be relevant model composition for the Earth's mantle [Faccenda and Zilio, 2017]. Phase transitions of pyrope garnet

during experimental diamond anvil cell experiments at conditions relevant to the '660' led to the discovery of (Mg,Fe)SiO_3 perovskite [gun Liu, 1974]; which was later discovered in nature in the Tenham L6 chondrite and formally named bridgmanite [Tschauner et al., 2014]. Bridgmanite alone comprises approximately 80% of the lower mantle by volume [Ishii et al., 2011, Wang et al., 2015], making it an important phase to investigate when determining how mineralogical microstructures impact phenomena such as seismic anisotropy. Deformation experiments on bridgmanite have been conducted in the past to explore texture development [Merkel et al., 2003, Miyagi and Wenk, 2016, Tsujino et al., 2016], strain weakening [Girard et al., 2016], and dislocation microstructures [Cordier et al., 2004, Miyajima et al., 2009]. However, there are no documented in-situ experiments that investigate transformation microstructures, including grain statistics, immediately before and after the '660' transition in polycrystalline pyrolite samples.

Seismic anisotropy, the directional dependence of seismic wave velocity, has been observed within the Earth's interior and can bring further information on processes at those depths [Long and Becker, 2010]. Anisotropy can be detected using multiple approaches. Surface waves in upper mantle regimes provides large-scale information on azimuthal anisotropy [Beller and Chevrot, 2020]; however shear wave splitting is more commonly used due to the straight forward measurement process [Long and Becker, 2010]; although such measurements may lack vertical resolution. Seismic anisotropy within the deep mantle, however, is widely debated, as it is observed locally below '660' in some studies [Wookey et al., 2002, Ferreira et al., 2019, Agrawal et al., 2020, Montagner et al., 2021], but is absent in other more global models [Meade et al., 1995, Panning and Romanowicz, 2006a, Panning et al., 2010]. The study of seismic anisotropy is largely motivated by providing constraints on deformation within the Earth's interior and interpreting mantle flow processes, but questions remain on its microscopic origin around the '660' discontinuity.

In this study, a series of laser heated diamond anvil cell (DAC) experiments were performed on polycrystalline samples of pyrolite using high energy X-rays from a synchrotron source. Multigrain X-ray diffraction (MGC) is employed in order to track the orientation of grains at pressures and temperatures relevant to the conditions both above and below the 660 km discontinuity. More specifically, we report on experimental textures obtained

before and after the transformation from (ringwoodite + garnet) to (bridgmanite + Ca-perovskite + ferropericlase). Also note that Ca-perovskite was renamed to davemaoite recently [Tschauner et al., 2021] and we will use this nomenclature in the paper. Our measurements demonstrate that strong transformation textures can be formed in bridgmanite due to the compressive stress applied to the sample. These textures are then employed to model P and S-wave anisotropy within a pyrolitic mantle in the vicinity of the '660' discontinuity. We show that our predictions of anisotropy are consistent with observations and could be used to understand the stress geometry within the pyrolitic portion of a subducting slab. Experimental procedures and a brief overview of data processing techniques will be also discussed.

4.2 Methods and Data Analysis

4.2.1 Sample Preparation

We use sintered polycrystalline pyrolite samples as our starting material. Single crystals of natural San-Carlos olivine, pyrope, enstatite, and diopside were ground to a powder by hand with ethanol. The mixed powders were then loaded into a boron-nitride capsule and inserted into a piston-cylinder press to sinter the samples at 2 GPa and 1000 °C for 30 minutes. The product of the sintering is a polycrystalline aggregate with heterogeneous grain size, ranging between < 1 μm and 15 μm. The sintered material was then cut into disks with a diamond wire saw and then polished by hand on both sides using a series of silicon diamond polishing papers until it reached a thickness of $\sim 10\mu$m Finally, the sample was coated on both side with 500 nm of platinum using a GATAN 682 Precision Etching and Coating System (PECS) and then cut into 20 μm diameter disks using a laser cutting machine at the Institut de minéralogie, de physique des matériaux et de cosmochimie in Paris, Sorbonne Université.

4.2.2 Diamond Anvil Cell

To perform these experiments at the relevant pressure and temperature conditions of the 660 km discontinuity, a remote controlled membrane driven laser heated diamond anvil cell (DAC) was used. The seats and external housing of the assembly have a wide angle window, which allows for image collection at rotation angles $\Delta\omega = \pm 28^\circ$ during multi-grain

crystallography (MGC) data collection. We used diamonds with a culet size of 250 μm diameter along with a rhenium gasket, indented to a thickness between 25 μm and 30 μm. A hole 1/3 the diameter of the diamond culet was drilled in the center of the intended gasket using a motorized electric discharge machine or laser cutting machine to serve as a sample chamber. The sintered disks of pyrolite were loaded in a controlled argon gas atmosphere between layers of KCl that served both as thermal insulation for laser heating and as a pressure calibrant. Platinum flakes were also loaded into the gasket to be used as pressure calibrant, but were not used in order to keep the X-ray beam focused on the same part of the sample through the X-ray diffraction data collection during the whole experiment.

4.2.3 High Pressure/Temperature XRD Experiments

All experiments were performed at the Extreme Conditions beamline P02.2 at PETRA III (DESY, Hamburg). A schematic of the beamline set up is shown in Figure 4.1. We used a monochromatic X-ray beam with a wavelength of 0.2898 Å, and beam dimensions of 1.4 μm (V) $\times$ 1.9 μm (H) FWHM, and a Perkin-Elmer XRD 1621 flat panel detector with 2048 $\times$ 2048 pixels and a 0.2×0.2 mm^2 pixel size. A CeO_2 powder standard from the National Institute of Standards and Technology (NIST; 674b) was used to calibrate the detector tilt, beam center, and calculate the sample to detector distance (551.262 mm). Double-sided laser heating was carried out using a Yb-fiber laser to reach the necessary temperatures as installed by default on the beamline and temperatures were determined using spectroradiometry described by Konôpková et al. [2021].

Compression and heating of the sample are conducted simultaneously to monitor in situ the transformations in pyrolite at the conditions of the '660'. Pressures and occurrence of the corresponding phases are identified during the experiment using powder diffraction images collected in situ at high P/T and analyzed in the software Dioptas [Prescher and Prakapenka, 2015]. The collection of MGC images allows us to observe the evolution of microstructures within the sample upon transformation by providing information on phases present and their associated textures, but requires quenching the sample to ambient temperature with the layout we used in this work. MGC image collections are taken as close to the transformation conditions as possible.

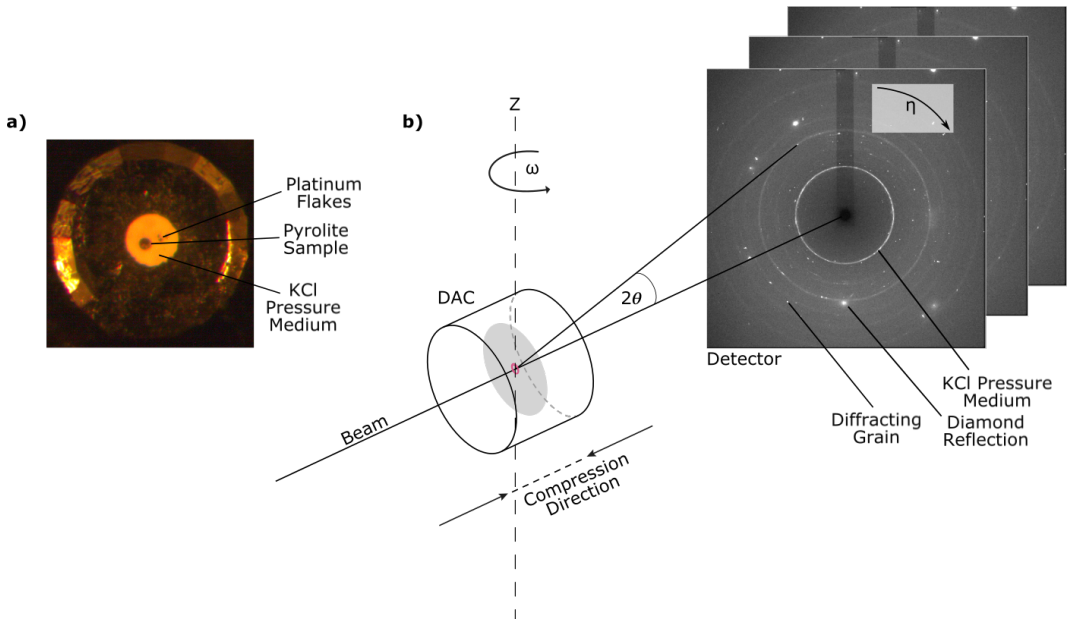

Figure 4.1: Experimental setup of multigrain X-ray diffraction at beamline P02.2 at PETRA III (DESY, Hamburg). a) Image of the sample sandwiched between KCl pressure medium along with platinum flakes taken from an optical microscope. b) Overall view of the DAC assembly with X-ray beam passing through the sample in the axial direction. The 2D Perkin-Elmer detector collects diffraction images every 0.5° as the assembly is rotated from −28° to 28° in ω. Actual diffraction images are shown in the insert.

The first series of MGC images are collected when ringwoodite and garnet form in the DAC at pressures between 18 and 19 GPa at temperatures between 1600 and 1900 K. Once, for instance, ringwoodite and garnet are observed in the powder diffraction pattern, the sample is quenched to ambient T by turning off the laser heating system and a multigrain X-ray diffraction image is taken. Acquisition of the image series happens by rotating the DAC in ω by 0.5° steps from −28° to 28° with collection times of 1 second per image, resulting in a total of 112 images for each MGC scan. After the MGC image collection, the sample is again heated between 1500 and 2000 K and then compressed at high temperature until pressures reach $\sim$ 24 GPa. Once bridgmanite is identified in the powder diffraction pattern, the sample is again quenched and MGC images are collected.

A total of three separate runs were performed: Pyr02, Pyr05, and Pyr07. Each sample was a separate experiment, with multigrain XRD images collected before and after the transformation to the bridgmanite + davemaoite + ferropericlase assemblage (Figure 4.2). Pressure during the experiment is tracked using powder diffraction images and the thermal equation of state of KCl from Tateno et al. [2019]. Temperature in KCl is ill-defined

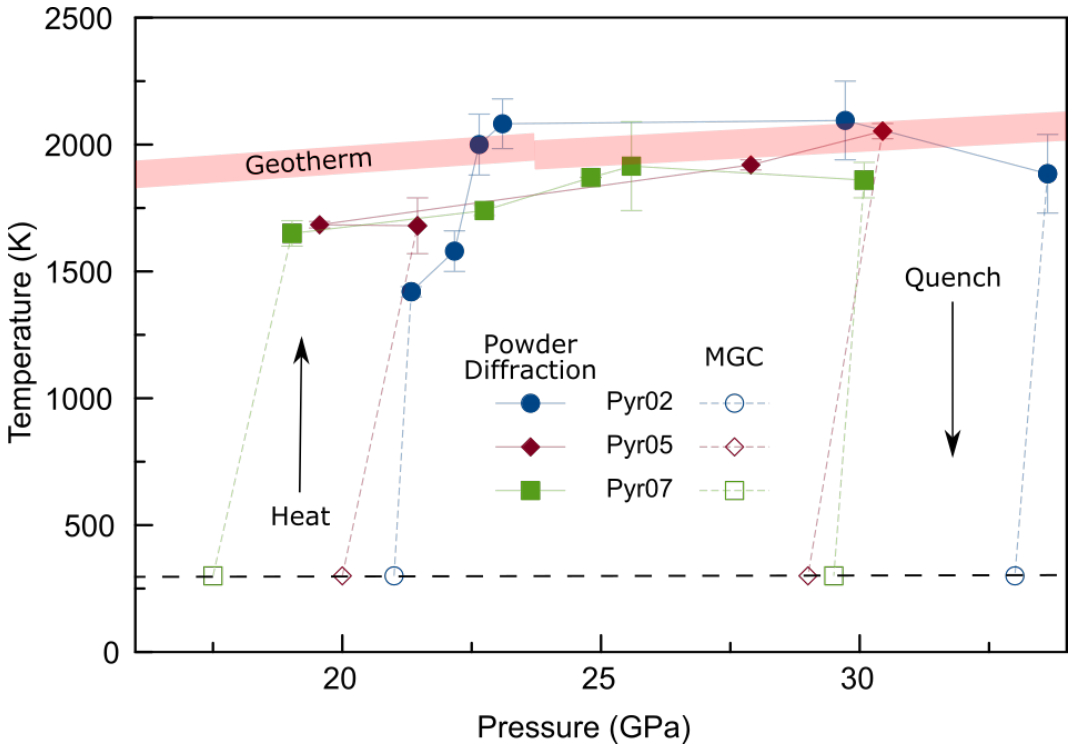

Figure 4.2: Pressure vs. temperature path for three experimental runs Pyr02, Pyr05, and Pyr07. Multigrain images are acquired at 300 K. Open markers are where MCG diffraction data was collected with filled markers indicating where powder diffraction images were taken. Dotted potion of lines along the P/T path denote when the sample is being heated or quenched. Errors in temperature are reported as the deviation from the average values between the upstream and downstream recorded temperature. Black dashed line is a visual aid marking 300 K. Red shaded area marks the geotherm from Katsura et al. [2010]. Pressures in KCl, estimated from the equation of state of Tateno et al. [2019], pressures reported during laser heating are corrected to account for temperature (see text for details).

because of the temperature gradient between the room temperature diamond and the heated sample, as measured using spectroradiometry. We hence assign the temperature at the mid-point between the diamonds and sample to KCl.

In the three Pyr02, Pyr05, and Pyr07 runs, ringwoodite + garnet assemblages were characterized between 17.5 and 21 GPa at 300 K and then compressed and converted at mantle geotherm temperatures up to pressures between 29 and 33 GPa. Bridgmanite + davemaoite + ferropericlase assemblages were then characterized using MGC on the quench run-products (Figure 4.2).

4.2.4 Processing MGC Data

Analysis of the MGC data is performed using a series of software packages discussed below. Only a brief outline of the process will be provided and more information can be found in Rosa et al. [2015] as well as Langrand et al. [2017]. A MGC image collection relies on the measurement of diffraction images at multiple ω angles in order to obtain a comprehensive view of the sample grain orientations in three dimensions. The aim of the procedure is to link the diffraction spots observed in the diffraction images to individual grains within the sample and extract microstructural information such as the number of grains and their orientations. This step is performed using the open-source software package FABLE-3DXRD Which cn be found at `https://github.com/FABLE-MGC`. During the first step of the processing, images are cleaned by subtracting the median background from the pressure transmitting medium and masking diamond spots.

Figure 4.3a shows the extracted diffraction peaks in sample Pyr05, plotted along the azimuth against inverse d-spacing. Figure 4.3c is an example of what diffraction spectra in sample Pyr05 look like when the MGC images are averaged and integrated into a 2D pattern, as one would use in powder diffraction. Diffraction peaks with lower intensities are masked by the KCl pressure medium, making it difficult to identify peak locations of garnet, bridgmanite, davemamoite, and ferropericlase phases. Figure 4.3b, on the other hand, shows a histogram of the number of diffraction spots against inverse d-spacing. Peaks from all phases can be clearly identified. Unit-cell parameters of the mineral phases are then extracted using the software MAUD [Lutterotti et al., 1997]. Note the analysis of this spectrum is not a true Rietveld refinement because the data in the histogram is

a number of single grain peaks rather than a true peak intensity. It is, however, very efficient at detecting peak positions of phases that would otherwise be drowned out by the KCl pressure medium.

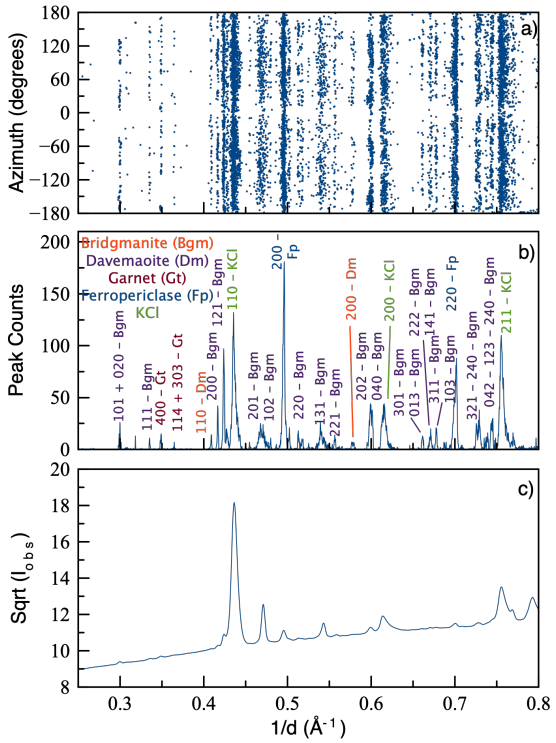

Figure 4.3: Experimental diffraction data from sample Pyr05 at 29 GPa. a) Extracted diffraction peaks from the 2D diffraction images plotted as a function of azimuth and inverse d-spacing. b) Histogram of the number of extracted single-grain diffraction peaks vs. 1/d. The corresponding phase and Laue indices of each diffraction line are indicated on the figure. c) Diffraction data in MAUD when using an average image of the MGC data collection. The signal is dominated by the pressure medium (KCl) and selected diffraction lines of bridgmanite.

After the peaks are extracted and the phases identified, we use ImageD11 to compute a list of g-vectors using the positions of diffraction peaks, refined unit cell parameters, and experimental conditions such as wavelength, sample to detector distance, and detector tilt. In order to avoid incorrectly assigning pressure medium g-vectors to sample grains, 2θ ranges that overlap with the pressure medium are excluded from the list.

Finally, we use GrainSpotter [Schmidt, 2014] and the list of g-vectors, to index grains within the sample by assigning g-vectors with matching orientations. To achieve this, GrainSpotter generates a series of randomly oriented grains and computes their corresponding g-vectors. GrainSpotter then tries to match each experimentally measured g-

vector to the generated theoretical g-vectors. A g-vector is assigned to a grain when the diffraction angles 2θ, η, and ω, shown in Figure 4.1, are within the defined tolerances from the theoretical values.

One difficulty arises from having multiple crystalline phases in the sample. This is remedied by running multiple subsequent GrainSpotter indexings for each individual phase, removing indexed g-vectors from the list of unassigned g-vectors at each step. Additionally, the number of indexed grains is improved by running multiple iterations of GrainSpotter with increasing tolerances. In the first iterations, tolerances are set to $\sigma_{2\theta} = 0.02°$, $\sigma_\eta = 1.0°$, and $\sigma_\omega = 2.0°$ for each phase. In the last iterations, tolerances are set to $\sigma_{2\theta} = 0.08°$, $\sigma_\eta = 2.0°$, and $\sigma_\omega = 3.0°$ for each phase. This results in the indexing of between 35 and 89% of the g-vectors, corresponding to between 44 and 736 sample grains (Table 4.1). Note that better indexing performance are obtained for samples including bridgmanite, davemaoite, and ferropericlase where between 83 and 89% of the g-vectors are assigned. The reason for the lower indexing performance on garnet + ringwoodite assemblages is unclear, but may be due to thee large number reflections in both the garnet and ringwoodite structures. Grain orientations from GrainSpotter are plotted as inverse pole figures (IPF) of the direction of compression using the MTEX toolbox [Bachmann et al., 2010, Mainprice et al., 2014]. We use MTEX to fit an orientation distribution function to the list of single grain orientations and plot the results as IPFs. Each dot on the IPF in Figure 4.4 represents a grain indexed, with color corresponding to the probability of a specific orientation, which is plotted using a scale of multiples of random distribution (m.r.d.).

4.2.5 Elasticity and Calculations of Seismic Anisotropy

Phase proportions in pyrolite, both before and after transformation, were calculated using the software package HeFESTo [Stixrude and Lithgow-Bertelloni, 2010] available at https://github.com/stixrude/HeFESToRepository. Above the '660', at conditions of 22 GPa and 1700 K, pyrolite is composed of 67% ringwoodite, 25% garnet, and 8% other minor phases by volume. Below the '660', at 27 GPa and 1900 K, pyrolite contains 77% bridgmanite, 17% ferropericlase, and 6% davemaoite by volume. Elastic constants for each phase are required in order to complete calculations of seismic velocities (Table 4.2).

In this work, garnet and ringwoodite are treated as isotropic materials, which is con-

sistent with measurements on single crystals in the pressure range of the mantle transition zone (MTZ) [Sinogeikin and Bass, 2000, Murakami et al., 2008, Zhou et al., 2022]. Studies report moderate elastic anisotropy of ferropericlase at the condition of the MTZ [Jackson et al., 2006, Yang et al., 2016, Fan et al., 2019, Immoor et al., 2022]. Additionally, in our experiments we observe no texture, therefore we also treat ferropericlase as an elastically isotropic material.

Both bridgmanite and davemaoite are elastically anisotropic at mid-mantle conditions [Kurnosov et al., 2018, Fu et al., 2019, Criniti et al., 2021, Li et al., 2006b] and will hence be treated to include the effect of anisotropy. Anisotropic elastic properties for textured polycrystals, pyrolite assemblage, and the corresponding wave velocities and anisotropy are then calculated using experimental texture data with MTEX and will be described later.

4.3 Results

4.3.1 Transformation Microstructures in Pyrolite

Grain Indexing Statistics

Grains are indexed before and after the phase transformation takes place in our experiments. Before the transition, we index ringwoodite and garnet phases simultaneously, which results in between 107 and 120 indexed grains between the two phases. After the transition we see a marked increase in the amount of grains indexed for phases bridgmanite, davemaoite, and ferropericlase. Here we are able to index between 508 and 736 grains amongst the three phases. Our indexing strategy leads to between 35 and 89% of all relevant g-vectors assigned to individual grains. For instance, 84% of the relevant g-vectors in Figure 4.3 have been assigned.

Table 4.1 shows grain indexing statistics for ringwoodite, garnet, bridgmanite, davemaoite, and ferropericlase in the three experimental runs. The number of grains indexed for each phase, number of diffraction peaks assigned to each grain, and the percentage of total g-vectors assigned to grains for each indexing are provided. In sample Pyr02, the first indexing includes the phases garnet and ringwoodite, at 21 GPa, with 95 grains of garnet and 232 grains of ringwoodite indexed. In the garnet phase, more peaks are assigned per grain due to the multiplicity, which is a result of crystal structure. During this

Table 4.1: Indexing statistics from GrainSpotter for garnet, ringwoodite, bridgmanite, davemaoite, and ferropericlase phases in runs Pyr02, Pyr05, and Pyr07. Pressures, number of grains indexed, average number of diffraction peaks assigned to grains, and percentage of g-vectors assigned to grains for each indexing are shown.

Exp.	Phase	P (GPa)	Gr. Ind.	Peaks per Gr.	Assigned Gve (%)
Pyr02	Garnet	21.0	95	88	78
	Ringwoodite		232	24	
	Bridgmanite	33.0	495	21	89
	Davemaoite		208	9	
	Ferropericlase		33	9	
Pyr05	Garnet	20.0	22	85	58
	Ringwoodite		89	22	
	Bridgmanite	29.0	334	23	84
	Davemaoite		54	8	
	Ferropericlase		230	9	
Pyr07	Garnet	17.5	13	91	35
	Ringwoodite		31	21	
	Bridgmanite	29.5	270	22	83
	Davemaoite		182	9	
	Ferropericlase		56	9	

first indexing, 78% of g-vectors are assigned to grains within the sample. In the second indexing of sample Pyr02, bridgmanite, davemaoite, and ferropericlase are included, at a pressure of 33 GPa, with 495, 208, and 33 grains indexed respectively. For this indexing 89% of g-vectors are assigned to grains within the sample. During the indexing of garnet and ringwoodite phases in sample Pyr05 at 20 GPa, 22 grains of garnet and 89 grains of ringwoodite are found. For this indexing 58% of the total g-vectors are assigned to grains. After transformation, another indexing is ran at 29 GPa where we find 334 grains of bridgmanite, 54 grains of davemaoite, and 230 grains of ferropericlase. For this indexing 84% of g-vectors are assigned to grains. For the last sample, Pyr07, phases of garnet and ringwoodite are indexed at 17.5 GPa, and yield 13 and 31 grains respectively. Only 35% of the g-vectors are assigned to grains within the sample. After transformation, however, 83% of the g-vectors are assigned to grains in the sample with 270 bridgmanite grains, 182 davemaoite grains, and 56 ferropericlase grains found.

Experimental Textures in Pyrolite Phases

Figure 4.4 shows grain orientations of ringwoodite and garnet before transformation; and bridgmanite, davemaoite, and ferropericlase after the transformation. In all samples, ringwoodite displays a 001 compression texture with m.r.d. values between 1.7 and 2.8. The

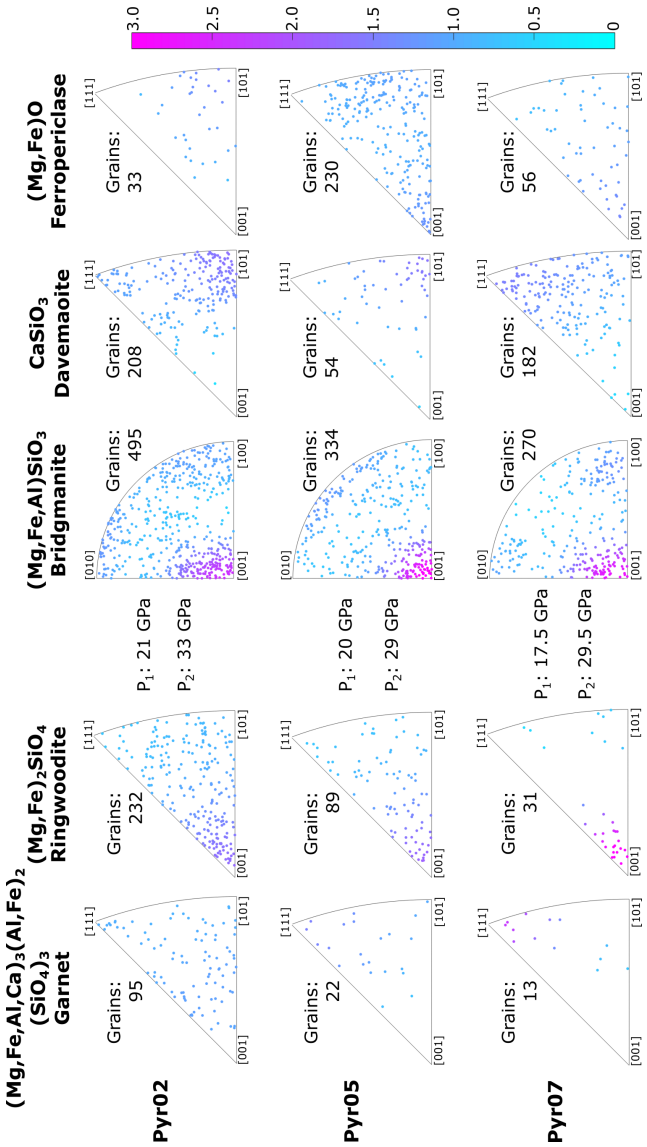

Figure 4.4: Inverse pole figures of the compression direction for samples Pyr02, Pyr05, and Pyr07 showing individual grain orientations of $Mg_3Al_2(SiO_4)_3$ garnet and $(Mg,Fe)_2SiO_4$ ringwoodite before transformation and $(Mg,Fe)SiO_3$ bridgmanite, $CaSiO_3$ davemaoite, and (Mg,Fe)O ferropericalse after complete transformation in a pyrolitic composition. Equal area projection. Grains are colored according to an orientation distribution fitted for each phase and color scale in multiples of random distribution (m.r.d.). P_1 indicates the pressure before transformation and P_2 the pressure after transformation. The number of indexed grains is indicated above each inverse pole figure.

Table 4.2: Density and elasticity of mineral phases and pyrolite. Densities, phase proportions, and isotropic elastic properties for ringwoodite, garnet, and ferropericlase were calculated using Hefesto [Stixrude and Lithgow-Bertelloni, 2010]. Anisotropic single-crystal elastic moduli for bridgmanite and davemaoite are from the study of Luo et al. [2021] and Li et al. [2006b], respectively. Polycrystal elastic properties are calculated here (see text for details).

	Material	ρ (g/cm^3)	C_{11}	C_{12}	C_{13}	C_{22}	C_{33}	C_{44}	C_{55}	C_{66}
Above '660'	Random Gt polycrystal	3.9297	382	169	169	382	382	106	106	106
22 GPa	Random Rw polycrystal	4.002	417	169	169	417	417	124	124	124
1700 K	Un-textured pyrolite	3.9823	407	169	169	407	407	119	119	119
Below '660' 27 GPa 1900 K	Single-crystal Bm	4.4930	540	200	189	611	548	209	178	161
	Textured Bm polycrystal	4.4930	564	196	208	560	564	185	178	185
	Single-crystal Dm	4.4646	423	217	217	423	423	201	201	201
	Textured Dm polycrystal	4.4646	500	171	186	515	500	143	157	143
	Random Fp polycrystal	4.4296	399	142	142	399	399	129	129	129
	Textured pyrolite	4.4806	528	184	194	526	528	172	167	172

garnet phase, however, is randomly oriented in all samples. After the transformation, bridgmanite exhibits strong preferred orientation in 001 along the compression axis with m.r.d. values between 2.7 and 3. Transformation textures in davemoaite varies between the three experimental runs. In samples Pyr02 and Pyr05, weak 101 orientations can be observed. Whereas in sample Pyr07, the orientations are more diffuse, with the majority of grains oriented in 111. M.r.d. values of the davemaoite phase across all three samples are the same; with maximum values of 1.6. Finally, ferropericlase exhibits a random texture throughout all three samples.

4.3.2 Seismic Wave Velocities Above and Below the '660' Discontinuity

Seismic Wave Velocity Calculations

Single-crystal elastic constants for bridgmanite and davemaoite were interpolated to 1900 K and 27 GPa from the results of [Luo et al., 2021] and [Li et al., 2006b]. The corresponding velocities in the single crystal are shown in Figure 4.5 as upper hemisphere projections. Maximum S-wave splitting in bridgmanite is 12.95% (0.83 km/s) for waves traveling along [010]. The mean P-wave velocity is 11.22 km/s and ranges from 10.94 km/s parallel [100] to 11.68 km/s along [010], which leads to 6.65% P-wave anisotropy. Maximum S-wave splitting in davemaoite is 33.16% (1.91 km/s) for waves traveling along ⟨110⟩. The mean P-wave velocity is 10.64 km/s and ranges from 9.74 km/s parallel to ⟨100⟩ to 11.14 km/s along ⟨111⟩, which leads to 13.2% P-wave anisotropy.

In order to evaluate the polycrystal elastic tensors and wave velocities for bridgmanite and davemaoite, we first use MTEX to generate a model texture matching the results of our experimental data (Figure 4.5) and the expected symmetry. Our experiments are conducted in uniaxial compression, that should result in a fiber symmetry along the compression axis. Considering there are only on the order of 50-500 grains in our measurements, potential artifacts that hide this expected fiber symmetry can arise. For bridgmanite we create a 001 texture aligned with compression and for davemaoite we average two separate orientations at 101 and 111, based on the two different transformation textures observed in run Pyr02 and Pyr07.

Polycrystal anisotropy plots of bridgmanite and davemaoite are also shown in Figure 4.5. Maximum S-wave splitting in the bridgmanite polycrystal is 2.05% (0.13 km/s) for waves traveling perpendicular to compression. Fast S-waves are vertically polarized where splitting is maximum. Mean P-wave velocity is 11.20 km/s and ranges from 11.17 km/s for waves traveling parallel to compression to 11.21 km/s at approximately 45° to compression, resulting in 0.41% P-wave anisotropy. Maximum S-wave splitting in the davemaoite polycrystal is 6.33% (0.38 km/s) for waves traveling approximately 45° to compression with a secondary maximum perpendicular to compression. Fast S-waves are horizontally polarized perpendicular to compression and vertical 45° to compression, where splitting is maximum. Mean P-wave velocity is 10.50 km/s and ranges from 10.38 km/s for waves traveling approximately 45° to compression to 10.76 km/s parallel to compression, resulting in 3.63% P-wave anisotropy.

Anisotropy in a Compressed Pyrolite Polycrystal Before and After Transformation

As mentioned in section 2.5, garnet and ringwoodite phases are both seismically isotropic in V_P and V_S at 22 GPa and 1700 K. Ferropericalse is also assumed to be elastically isotropic at 27 GPa and 1900 K based on the lack of texture in our experimental data. Nevertheless, they contribute to seismic velocities in the pyrolite polycrystal. We use MTEX and the phase proportions in section 2.5 to compute the velocities in a pyrolite polycrystal both above and below the '660'.

For the pyrolite polycrystal above '660' (Figure 4.6), there is zero anisotropy in V_S

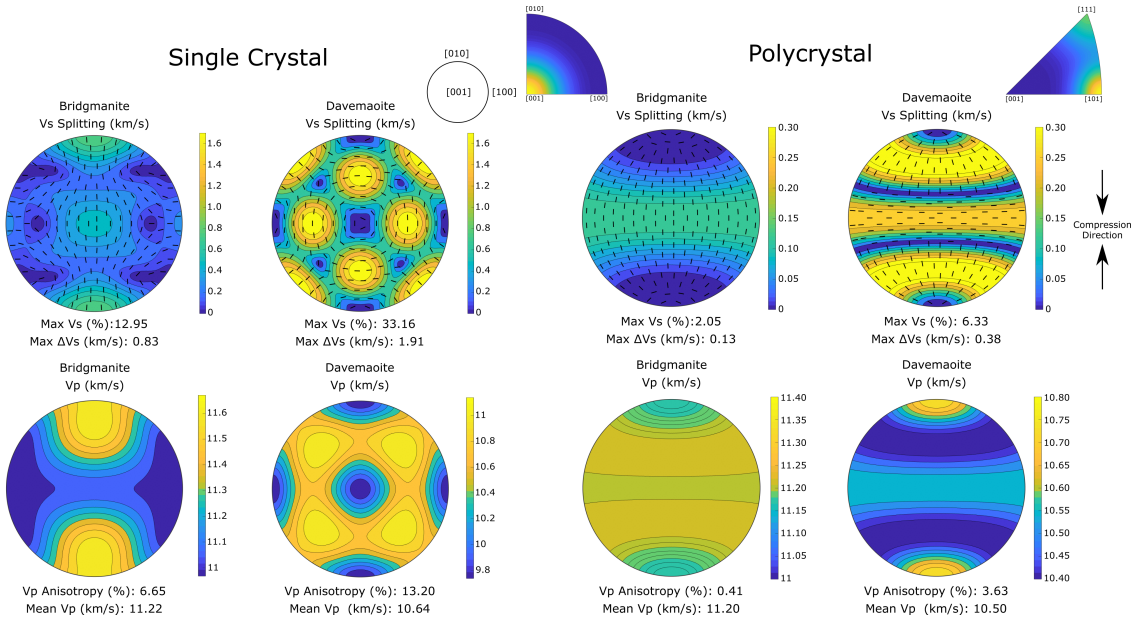

Figure 4.5: Seismic velocities in single (left column) and polycrystals (right column) of bridgmanite and davemaoite at 27 GPa and 1900 K. Both V_S splitting and V_P anisotropy are plotted in units of km/s. Black tick marks in V_S splitting plots indicate the fast wave polarization direction. Single crystal elastic constants and densities are from Table 4.2. Textures used to model polycrystal properties are shown as inverse pole figures of the compression direction in the insets. Direction of compression for polycrystal velocities plot is shown in the figure.

and V_P with mean P-wave velocity of 10.08 km/s. For the pyrolite polycrystal below the transition, however, maximum S-wave splitting is 1.28% (0.08 km/s) for waves traveling perpendicular to compression. S-waves are vertically polarized where splitting is maximum. For P-waves, mean velocity is 10.83 km/s, ranging between 10.82 km/s for waves traveling parallel to compression to 10.84 km/s for waves traveling perpendicular to compression, resulting in 0.17% P-wave azimuthal anisotropy.

4.4 Discussion

4.4.1 Pre-transformation Textures

At mantle conditions above the 660 km discontinuity, ringwoodite and garnet make up approximately 93% by volume of phases within pyrolite samples at pressures and temperatures of 22 GPa and 1700 K respectively, as calculated by HeFESTo. Ringwoodite is 67% by volume of the total, making it the dominant phase. When comparing ringwoodite textures between samples, all three display preferred orientation in 001, where (001) planes align perpendicular to the compression axis; however, the texture strength in sample Pyr07

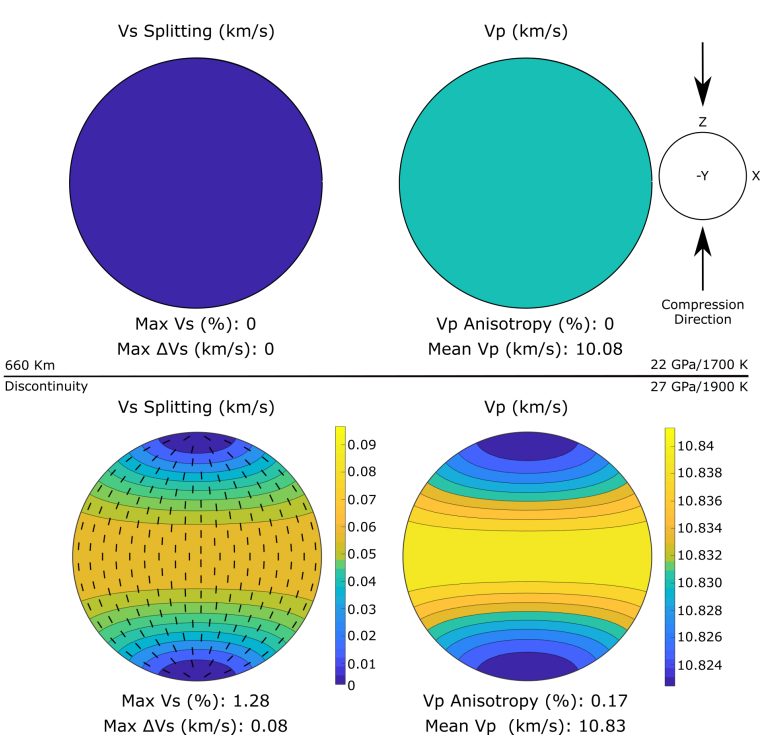

Figure 4.6: Seismic velocities in pyrolite at conditions above and below the 660 km discontinuity. Both V_S splitting and V_P anisotropy are plotted in units of km/s. Black tick marks in V_S anisotropy plots indicate the fast shear wave polarization direction. Plots are oriented so that compression is in the vertical direction.

is much stronger, with a m.r.d. value of 3 in Figure 4.4. It is likely that the stronger texture observed in sample Pyr07 is a result of only 31 indexed grains compared to 232 in Pyr02 and 89 in Pyr05. This can lead to an overestimation of intensity in the orientation distribution function. With a larger number of grains, orientations are distributed amongst more grains resulting in lower texture strengths. Therefore, we conclude the stronger texture in sample Pyr07 is due to the low number of grains and not representative of the true texture strength. The difference in amount of ringwoodite grains indexed between the Pyr02, Pyr05, and Pyr07 is probably a result of grain size differences in each sample, which would lead to a different number of indexed grains.

Past DAC and D-DIA experiments have reported 101 compression textures in ringwoodite [Wenk et al., 2004b, 2005]; however, in a study by Miyagi and Wenk [2016] ringwoodite displays a maximum in 101 with a weaker maximum in 001 orientations before the transformation to (bridgmanite + ferropericlase). Although we do not observe the same 101

textures in the ringwoodite phase of our experiments, DAC experiments in Wenk et al. [2004b] and D-DIA experiments in Wenk et al. [2005] were conducted at room temperature. Additionally, none of these experiments use a pyrolitic starting material.

The garnet phase of our pyrolite accounts for 25% by volume of the phases at pre-transformation conditions. Across all three samples garnet remains isotropic in texture (Figure 4.4). Recent radial diffraction experiments investigating texture development in garnet report weak texture in (001) orientations perpendicular to compression at ambient temperatures [Vennari et al., 2021]. Other studies on the plasticity of garnet have been conducted and found the resistance to plastic flow in garnet to be significantly higher than in other mantle minerals [Karato et al., 1995], while others argue garnet to actually be weaker than other mantle phases such as ringwoodite within the transition zone [Kavner, 2007]. Our explanation for the lack of texture development in garnet during compression is simply due to the weak deformation textures in garnet and the fact that we did not apply much strain in this sample.

4.4.2 Post-transformation Textures

The three dominant phases in pyrolite after transformation at the '660' are bridgmanite, davemaoite, and ferropericlase. Bridgmanite makes up 77% by volume of pyrolite at conditions of 27 GPa and 1900 K as reported by HeFESTo. Bridgmanite exhibits texture in (001) planes (Pbnm setting) perpendicular to the compression axis with m.r.d. values up to 3. Few studies have investigated transformation textures in bridgmanite; however, our results compare well with textures observed in radial diffraction experiments by Miyagi and Wenk [2016], where bridgmanite transformed from enstatite displays 001 texture at 31 GPa. Transformation from pure olivine to (bridgmanite + ferropericlase), however, results in a diffuse maximum spread between 001 and 100 orientations at 33 GPa as seen in figure 3b of Miyagi and Wenk [2016]. Another study by Wenk et al. [2006], also shows a difference in bridgmanite transformation textures depending on the pre-transformation phase. Bridgmanite transformed from olivine in a DAC, reveals 100 orientations perpendicular to compression at 25 GPa; however, when bridgmanite is transformed from enstatite at 44 GPa there is a strong maximum in 001 orientations. Additionally, in the same study, Wenk et al. [2006] observes an intermediate maximum in 101 orientations when

bridgmanite is transformed from pure ringwoodite at 43 GPa.

Experimental transformation textures of bridgmanite are unrelated to known slip systems. Past multianvil deformation studies have documented (100) slip in [001] in pure bridgmanite at conditions of the uppermost lower mantle [Tsujino et al., 2016]. At higher pressure, but below 55 GPa, the dominant slip plane is reported to be (100) resulting in a 100 deformation texture at 300 K [Merkel et al., 2003, Miyagi and Wenk, 2016]. X-ray diffraction analysis of dislocations by Cordier et al. [2004] on recovered bridgmanite samples, deformed in the multianvil press, report slip in (001)[100] and (001)[010]. Few of these previous results on deformation and slip systems in bridgmanite would result in preferred orientation of (001) planes perpendicular to compression as observed here. In addition, we applied very little strain in the sample post phase transformation. We hence conclude that our measured experimental textures are a result of oriented growth under stress rather than deformation.

Davemaoite also exhibits transformation textures in 101 and 111 orientations pyrolite. The strongest of these textures is observed in sample Pyr02 where (101) planes orient perpendicular to compression. This same texture is found in sample Pyr05, however, significantly less grains are indexed; 208 grains in Pyr02 versus 54 grains in Pyr05. Sample Pyr07 displays a different texture with 111 planes oriented perpendicular to the compressive axis. Textures in these experiments differ from deformation textures reported in radial diffraction DAC experiments by [Miyagi et al., 2009, Immoor et al., 2022], who report a 100 texture in deformed pure $CaSiO_3$. Again, our experiment are measuring transformation textures in a pyrolitic assemblage and could differ from deformation experiments in a pure phase.

4.4.3 Implications for Anisotropy in Subducting Slabs

It is believed that subducting slabs in the mantle collide with a more viscous layer around 660 km depth, which would initially apply a compressive stress on the slab [Wookey et al., 2002, Mao and Zhong, 2018]. Compositionally, the top outermost portion of the slab is made up of a thin layer of mid-ocean ridge basalt with an underlying layer of harzburgite; however, the majority of the slab is pyrolitic in nature [Faccenda and Zilio, 2017]. Therefore, we can consider that our transformation experiments on pyrolite at mantle P/T under

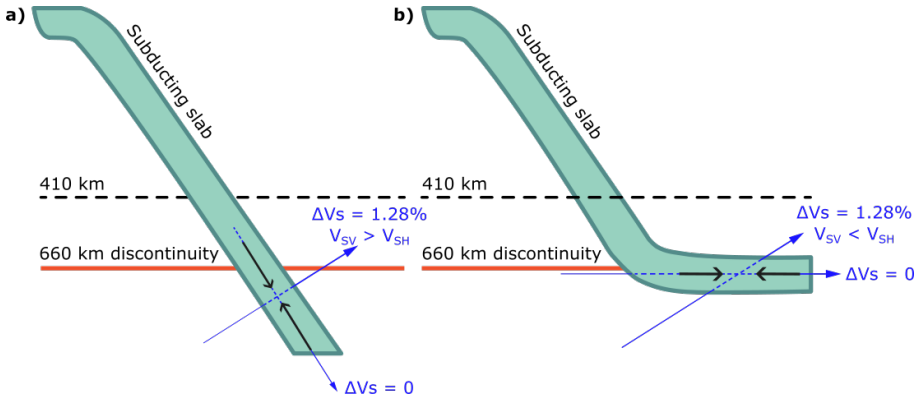

Figure 4.7: Scenarios for anisotropy in a subducting slab below the '660'. Blue arrows denote shear wave propagation directions with corresponding splitting values. Black arrows indicate compression direction. a) Subducting slab impinging on the more viscous upper-lower mantle below 660 km depth. b) Subducting slab bending along the 660 km discontinuity creating a horizontal compressive stress.

compressive stresses are relevant for observations of anisotropy inside subducting slabs.

Our model does not predict anisotropy above the 660 discontinuity. Below 660 km depth, seismic observations report that anisotropy is weak in comparison to shallower depths [Montagner and Kennett, 1996, Ohuchi et al., 2011], where olivine, the dominant mineral in the upper mantle, exhibits significant crystallographic preferred orientation and anisotropy. Nevertheless, anisotropy has been observed below the '660' in studies using surface waves [Yuan and Beghein, 2013, Montagner et al., 2021], body waves [Wookey et al., 2002, Agrawal et al., 2020], and seismic tomography [Ferreira et al., 2019]. Where exactly anisotropy is observed, however, remains largely debated with some literature suggesting it is developed mostly around rigid subducting slabs due to high induced strain in the surrounding hot mantle [Ferreira et al., 2019] and others arguing anisotropy is strongest within the slabs where they are most contorted; as the surrounding mantle is largely isotropic [Agrawal et al., 2020]. In the discussion below we will try to construct a model to understand these observations and show how our data can help reconcile these observations.

For a vertically compressive stress, we predict that S-waves will show no splitting for waves traveling parallel to compression and 1.28% splitting in waves traveling perpendicular compression (Figure 4.6). Some observations suggest average anisotropy values of 3% just below the '660' assuming anisotropy is confined to a 100 km layer [Wookey et al., 2002]; however, in another study by Yuan and Beghein [2013], the root mean square model amplitude at 800 km depth has approximately 1% anisotropy. This is comparable to

observations of radial anisotropy within the deep upper mantle in Beghein et al. [2006] and Panning and Romanowicz [2006a]. Additionally, Montagner et al. [2021], observe fast vertically polarized S-waves ($V_{SV} > V_{SH}$) at 800 km depth below western America, central Africa, and central Asia using surface-wave overtone datasets to generate 3D anisotropy models. In a separate study, Visser et al. [2008] created a 3D model of velocity and radial anisotropy that resulted in $V_{SV} > V_{SH}$ with 1-2% amplitude below the MTZ. Both the results of Visser et al. [2008] and Montagner et al. [2021] are consistent with the scenario proposed in Figure 4.7a, where a "vertical" compressive stress is generated within the slab as it passes through the '660' and impinges on the more viscous surrounding mantle material. In this scenario $V_{SV} > V_{SH}$ for S-waves traveling in near horizontal direction, with no splitting in V_S for waves traveling parallel to the slab.

In contrast, the study of Wookey et al. [2002] observes horizontally polarized shear waves leading vertically polarized shear waves, albeit with larger values of V_S anisotropy. Agrawal et al. [2020] reports maximum splitting within the slab for nearly vertically propagating waves. These two are not compatible with a vertical compressive stress geometry. These observations could be remedied by considering a scenario where a horizontal compressive force is generated within the slab as it bends and travels along the '660', as shown in Figure 4.7b. In this scenario $V_{SV} < V_{SH}$ for S-waves traveling perpendicular to the horizontal slab, with no splitting in V_S for waves traveling parallel to the slab. Other studies investigating anisotropy deeper within the mantle (660-1000 km) suggest fast horizontally polarized waves ($V_{SV} < V_{SH}$) imaged near subducting slabs below 660 km depth [Ferreira et al., 2019] which is consistent with Figure 4.7b. For such reports of deep mantle anisotropy, however, deformation textures resulting from slab subduction should also be taken into account as the microstructural imprint of phase transformation is likely to be erased or modified by further deformation.

4.5 Conclusions

In this chapter we presented the results of phase transformation experiments at the pressure and temperature conditions of the 660 km discontinuity on pyrolite. Compression was carried out in a laser-heated DAC at pressures ranging from 17.5 to 33 GPa and tem-

peratures between 1500 and 2000 K; implementing multigrain X-ray diffraction to study the sample. We successfully observe the phase transition from (ringwoodite + garnet) to (bridgmanite + davemaoite + ferropericlase) in all three samples along with the associated microstructures.

Multigrain data processing techniques resulted in the assignment of single crystal diffraction peaks to individual grains within the sample. Our indexing capability ranges from 508 to 736 grains post transformation in a multiphase material. Prior to transformation, garnet is isotropic and ringwoodite is weakly textured with 001 planes oriented perpendicular to the compressive stress. After the transformation is induced, bridgmanite displays strong texture in 001 across all experiments as a result of oriented growth under stress. Davemaoite is moderately textured with 101 orientations in one experiment, and 111 orientations in another. Ferropericlase remains largely untextured in all experiments.

Using single grain elastic constants, calculated at pressures and temperatures relevant to the MTZ, and our measured microstructures we computed P and S-wave anisotropy in a pyrolitic polycrystal both above and below the 660 discontinuity. Our models predict no anisotropy in V_S and V_P above the '660.' Below the '660' S-wave splitting is 1.28% (0.08 km/s) for waves traveling perpendicular to compression and null for waves traveling parallel. P-wave velocities range from 10.82 km/s for waves traveling parallel to compression to 10.84 km/s for waves traveling perpendicular to compression, resulting in 0.17% azimuthal P-wave anisotropy. Our predicted amplitudes of anisotropy below the '660' in our models are consistent with observations by Beghein et al. [2006], Panning and Romanowicz [2006a], Visser et al. [2008], Yuan and Beghein [2013]. Our prediction for fast S-wave polarization depends on compression geometry with $V_{SV} > V_{SH}$ for a vertically compressed subducting slab and $V_{SH} > V_{SV}$ for a horizontally compressed slab.

Seismic anisotropy observed below the '660' is still a much debated topic. Here we show that bridgmanite within a pyrolitic material can develop strong textures when formed under stress. Based on these experimental observations, we can then attribute the bulk of anisotropy below the '660' to bridgmanite oriented growth and establish how anisotropy can be used to map stress within a subducting slab in those regions. This study also demonstrates the relevance of high pressure and high temperature multigrain crystallog-

raphy in the diamond anvil cell for understanding mantle processes. Future work using this technique would prove useful in understanding anisotropy deeper in the mantle, where further plastic deformation would play an important role, which will be discussed in the following chapter.

Chapter 5

Anisotropy and Microstructures Induced by Deformation of Pyrolite in the Upper and Lower Mantle

5.1 Introduction

Pyrolite, a mantle rock containing a mixture of olivine, pyroxene, clinopyroxene, and garnet [Ringwood, 1962a], is generally considered the average composition of the Earth's upper mantle [Irifune and Ringwood, 1987]. Below 660 km depth, however, this mineral assemblage consists predominately of (Mg,Fe)SiO_3 bridgmanite, $CaSiO_3$ davemaoite, and (Mg,Fe)O ferropericlase [Murakami et al., 2007, Komabayashi et al., 2010, Wang et al., 2015]. Under high pressure and temperature conditions, bridgmanite and davemaoite develop crystallographic preferred orientations (CPO) that could be responsible for observations of seismic anisotropy below the mantle transition zone (MTZ) [Wookey et al., 2002, Ferreira et al., 2019]. Our ability to interpret these seismic observations, however, rely on understanding texture development and active slip systems at these conditions assuming that it is indeed the controlling deformation mechanism. The development of texture requires the deformation, preferably at mantle pressures and temperatures. Mineral physicist use an array of experimental devices to perform in-situ deformation experiments at relevant pressures and temperatures, including the diamond anvil cell (DAC), the multi-anvil press, and the rotational Drickamer apparatus paired with high energy x-rays from a synchrotron source. While the deformation behavior of bridgmanite [Merkel et al., 2003,

Wenk et al., 2004b, Cordier et al., 2004, Miyagi and Wenk, 2016, Tsujino et al., 2016], davemaoite [Miyagi et al., 2009, Immoor et al., 2022], and ferropericlase [Merkel et al., 2002, Miyagi and Wenk, 2016, Immoor et al., 2018] have been investigated under high pressures and temperatures in the past, few have performed these types of experiments on polycrystalline pyrolite samples. Results of deformation experiments are also used to study plasticity of mantle minerals [Cordier et al., 2004, Miyajima et al., 2009, Miyagi et al., 2010]. Insights on deformation mechanisms are gleaned from this information and applied to numerical models, allowing for studies on the effect of chemistry and strain rate of bridgmanite [Carrez et al., 2007, Ferré et al., 2007, Mainprice et al., 2008, Boioli et al., 2017, Carrez et al., 2017] that otherwise cannot be directly measured using present day experimental techniques.

While it has been stated that observations of seismic anisotropy below the 660 km discontinuity ('660') is a result of texture in bridgmanite, anisotropic anomalies are largely confined to depths between 660-1200 km [Ferreira et al., 2019]. Although dislocation glide can be seen as responsible for observed textures, and hence seismic anisotropy within the deep mantle [Miyagi and Wenk, 2016], other deformation processes may be at play at greater depths that do not produce such textures [Meade et al., 1995]. Seismic observations within the lower mantle appear to be largely isotropic [Meade et al., 1995, Chang et al., 2014] with observations of anisotropic structures heavily relying on corrections of crustal anisotropy [Panning et al., 2010]. It is debated whether dislocation creep is active in the lower mantle; however, with some suggesting it may be present [Ferreira et al., 2019] while others cite diffusion creep [Karato and Li, 1992] or dislocation climb [Cordier et al., 2004, Boioli et al., 2017] to be the dominant deformation mechanism. If diffusion creep is the dominant deformation mechanism at depths greater than 1200 km, one would expect little to no seismic anisotropy as diffusion creep is unlikely to produce any CPO [Karato, 1988]. In order to provide constraints on deformation and mantle flow processes, high pressure and temperature experiments must be conducted to observe texture forming processes in pyrolitic materials.

In the previous chapter we discuss textures that resulted from phase transformations in pyrolite. Here, we implement the same multigrain x-ray diffraction (MGC) techniques

to observe the development of texture beyond 660 km depth on 3 polycrystalline pyrolite samples. These textures are then used to model plasticity in bridgmanite at pressures up to 108 GPa, or depths of 2400 km, using Visco-Plastic Self-Consistent modeling (VPSC). These models can then be applied to mantle convection scenarios that take into account texture evolution and differences in elastic anisotropy with pressure and temperature.

5.2 Methods and Data Analysis

Methods and data analysis implemented in this section are outlined in the previous chapter *Transformation Microstructures in Pyrolite and Implications for Anisotropy Below the '660' Discontinuity*. Any changes in the experimental set-up will be discussed below. Two pyrolite samples, Pyr05 and Pyr07, are those of the previous section. An additional pyrolite sample of identical composition, Pyr01, was ran during a separate series of experiments and will also be discussed in this chapter.

5.2.1 High Pressure/Temperature XRD Experiments

The following experiments were performed at the Extreme Conditions beamline P02.2 at PETRA III (DESY, Hamburg). Beamline conditions for samples Pyr05 and Pyr07 are identical to those in the previous chapter. Sample Pyr01, however, was ran at a later date using a monochromatic x-ray beam with a wavelength of 0.2904 Å and beam dimension of 1.2 μm (V) x 1.9 μm (H) FWHM. The same Perkin-Elmer XRD 1621 flat panel detector is used with 2048 x 2048 pixels and a 0.2 x 0.2 mm pixel size. A CeO_2 powder standard from the National Institute of Standards and Technology (NIST; 674b) was used to calibrate the detector tilt, beam center, and calculate the sample to detector distance (403.3228 Å). Double-sided laser heating was carried out using a Yb-fiber laser to reach the necessary temperatures as installed by default on the beamline [Liermann et al., 2015].

Our objective during these experiments is to observe the evolution of texture during deformation in pyrolite in-situ at conditions beyond the '660'. MGC images are collected, providing information on the phases present and their associated textures. Multigrain image collections are taken every 5-10 GPa pressure increase in samples Pyr05 and Pyr07 and every 10-20 GPa in sample Pyr01. We use phases diagrams from Ishii et al. [2018] as a reference for targeting pressures and temperatures during the experiments. Pressures

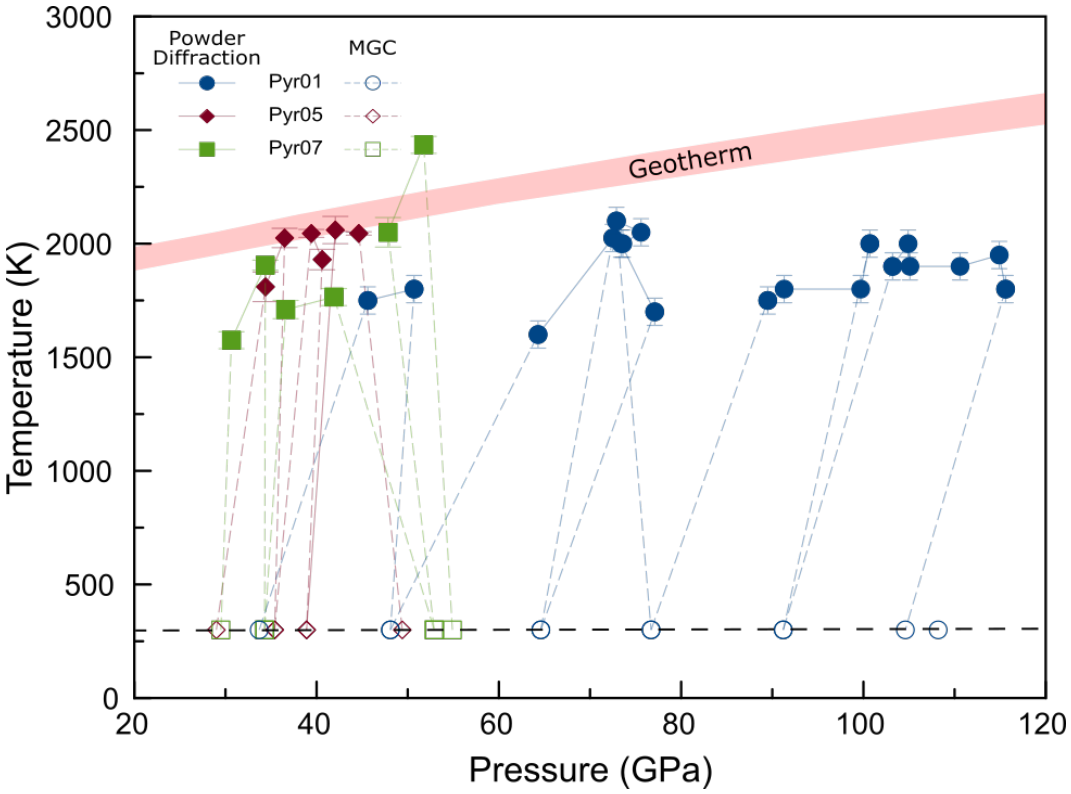

Figure 5.1: Pressure vs. temperature for three experimental runs Pyr05, and Pyr07. Multigrain image collections are acquired at 300 K. Open markers are where MCG diffraction data was collected with filled markers indicating where powder diffraction images were taken. Dotted potion of lines along the P/T path denote when the sample is being heated or quenched. Errors in temperature for runs Pry05 and Pyr07 are simply the deviation from the average values between the upstream and downstream recorded temperature. Errors in temperature for run Pyr01 are set to ±60 K. Black dashed line is a visual aid marking 300 K. Red shaded area marks the geotherm from Katsura et al. [2010]. Pressures in KCl (runs Pyr05 and Pyr07) and MgO (run Pyr01), estimated from the cell parameters of Tateno et al. [2019] and Speziale et al. [2001], respectively are reported during laser heating and corrected to account for temperature.

and occurrence of the corresponding phases are identified during the experiment using powder XRD and the computer software Dioptas [Prescher and Prakapenka, 2015]. The starting point of these deformation experiments is after the phase transformation where ringwoodite and garnet decompose to form bridgmanite + davemaoite + ferropericlase which occurs at $\sim$ 24 GPa at 1800 K. Experimental pressure and temperature path of runs Pyr01, Pyr05, and Pyr07 are shown in Figure 5.1. Images are collected using the same method as previously described by rotating the DAC in ω by 0.5° steps from $-28°$ to 28° with collection times of 1 second per image, resulting in a total of 112 images for each MGC scan. Samples are quenched before MGC images are collected.

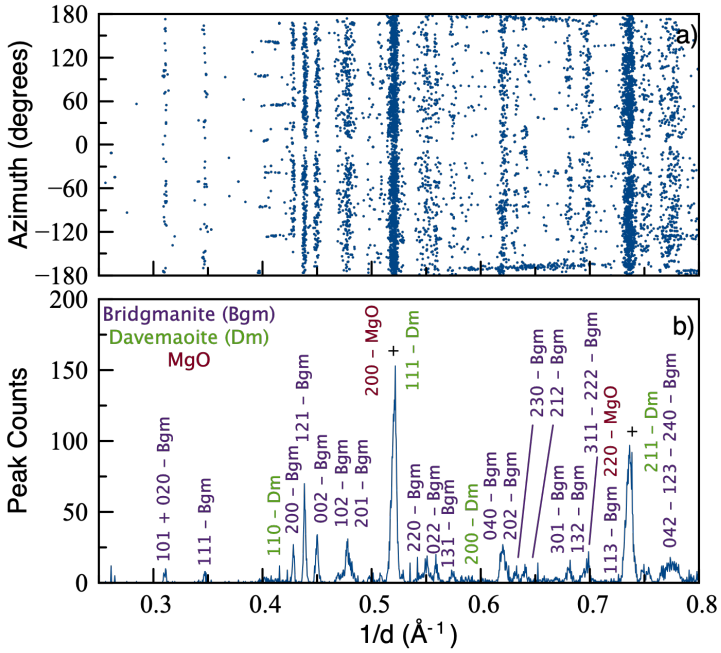

Figure 5.2: Experimental diffraction data from sample Pyr01 at 77 GPa. a) Diffraction peaks extracted from the 2D diffraction images plotted as a function of azimuth and inverse d-spacing. b) Histogram of the number of extracted single-grain diffraction peaks vs. $1/d$. The corresponding phase and Laue indices of each diffraction line are indicated on the figure.

Figure 5.2a shows the extracted diffraction peaks in sample Pyr01, plotted along the azimuth against inverse d-spacing. Figure 5.2b shows a histogram of the number of diffraction spots in counts which allows peaks from all phases to be clearly identified. Unit-cell parameters of the mineral phases are extracted using the software MAUD [Lutterotti et al., 1997]; however, the analysis of this spectrum is not a true Reitveld refinement because the

data in the histogram is the number of single-grain peaks rather than a true peak intensity. Nevertheless, it is efficient at detecting peak positions of phases that would otherwise be drowned out by the MgO pressure medium (as shown in 4.3 in the previous chapter).

5.3 Deformation Microstructures in Pyrolite up to a Megabar

5.3.1 Grain Indexing Statistics

Tables 5.1,5.2, and 5.3 show grain indexing statistics for bridgmanite, davemaoite, and ferropericlase in the 3 experimental runs. The number of grains indexed for each phase, number of diffraction peaks assigned to each grain, and the percentage of total g-vectors assigned to grains for each indexing are provided. In experimental run Pyr01, only bridgmanite and davemaoite are indexed, as MgO was used as a pressure medium in this experiment. For the other 2 runs, Pyr05 and Pyr07, bridgmanite and davemaoite are indexed in addition to ferropericalse as KCl was used as the pressure medium in these experiments. Assigned g-vectors in run Pyr01 are less than those in the other two runs due to larger strains on the sample at higher pressures.

Table 5.1: Indexing statistics from GrainSpotter for bridgmanite and davemaoite in run Pyr01. Pressures, number of grains indexed, amount of diffraction peaks assigned to grains, and percentage of g-vectors assigned to grains for each indexing are shown. MgO used as pressure transmitting medium and hence was not included in our grain indexings. Pressures are determined using the equation of state of MgO in Speziale et al. [2001].

Exp.	Phase	P (GPa)	Gr. Ind.	Peaks per Gr.	Assigned Gve (%)
Pyr01	Bridgmanite	34	165	25	77
	Davemaoite		6	8	
	Bridgmanite	48	122	21	76
	Davemaoite		174	8	
	Bridgmanite	65	107	20	67
	Davemaoite		4	8	
	Bridgmanite	77	157	20	68.5
	Davemaoite		0	0	
	Bridgmanite	91	130	20	60
	Davemaoite		31	8	
	Bridgmanite	105	194	20	70
	Davemaoite		21	8	
	Bridgmanite	108	220	20	71
	Davemaoite		74	8	

Table 5.2: Indexing statistics from GrainSpotter for bridgmanite, davemaoite, and ferropericlase phases in run Pyr05. Pressures, number of grains indexed, amount of diffraction peaks assigned to grains, and percentage of g-vectors assigned to grains for each indexing are shown. Pressures are determined using the equation of state of KCl in Tateno et al. [2019].

Exp.	Phase	P (GPa)	Gr. Ind.	Peaks per Gr.	Assigned Gve (%)
Pyr05	Bridgmanite	29	334	23	84
	Davemaoite		54	8	
	Ferropericlase		272	9	
	Bridgmanite	35	241	24	84
	Davemaoite		36	8	
	Ferropericlase		144	9	
	Bridgmanite	39	273	22	79
	Davemaoite		124	8	
	Ferropericlase		20	8	
	Bridgmanite	50	160	21	63
	Davemaoite		22	8	
	Ferropericlase		2	8	

Table 5.3: Indexing statistics from GrainSpotter for bridgmanite, davemaoite, and ferropericlase phases in run Pyr07. Pressures, number of grains indexed, amount of diffraction peaks assigned to grains, and percentage of g-vectors assigned to grains for each indexing are shown. Pressures are determined using the equation of state of KCl in Tateno et al. [2019].

Exp.	Phase	P (GPa)	Gr. Ind.	Peaks per Gr.	Assigned Gve (%)
Pyr07	Bridgmanite	29.5	270	22	83
	Davemaoite		182	9	
	Ferropericlase		56	9	
	Bridgmanite	34.0	442	23	86
	Davemaoite		140	9	
	Ferropericlase		62	9	
	Bridgmanite	53.0	316	22	74
	Davemaoite		100	9	
	Ferropericlase		26	8	
	Bridgmanite	55.0	207	22	76
	Davemaoite		105	9	
	Ferropericlase		14	8	
	Bridgmanite	57.5	137	22	70
	Davemaoite		65	9	
	Ferropericlase		9	9	

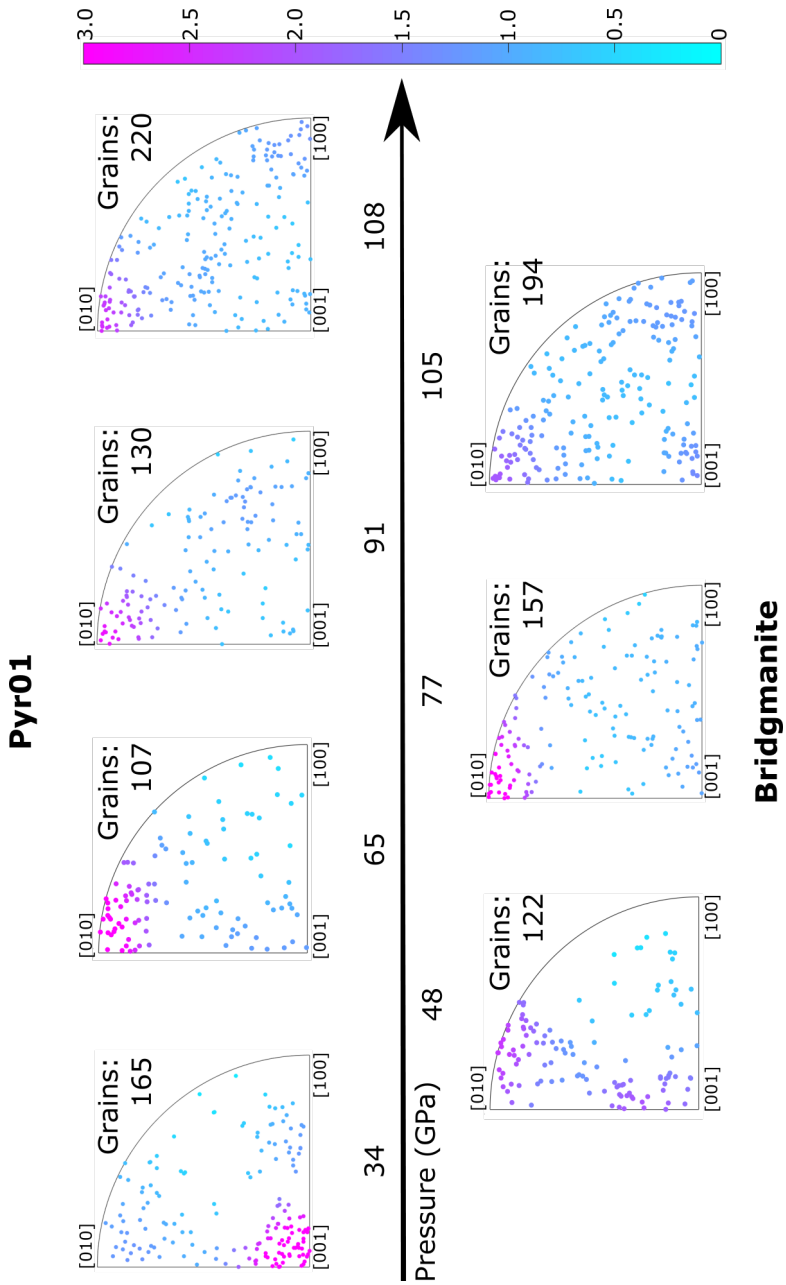

Figure 5.3: Inverse pole figures of the compression direction for sample Pyr01, showing individual grain orientations of bridgmanite in pyrolite at various pressures. Equal area projection. Grains are colored according to an orientation distribution fitted to the grain orientations and color scale in multiples of random distribution (m.r.d.). The number of indexed grains is indicated above each inverse pole figure.

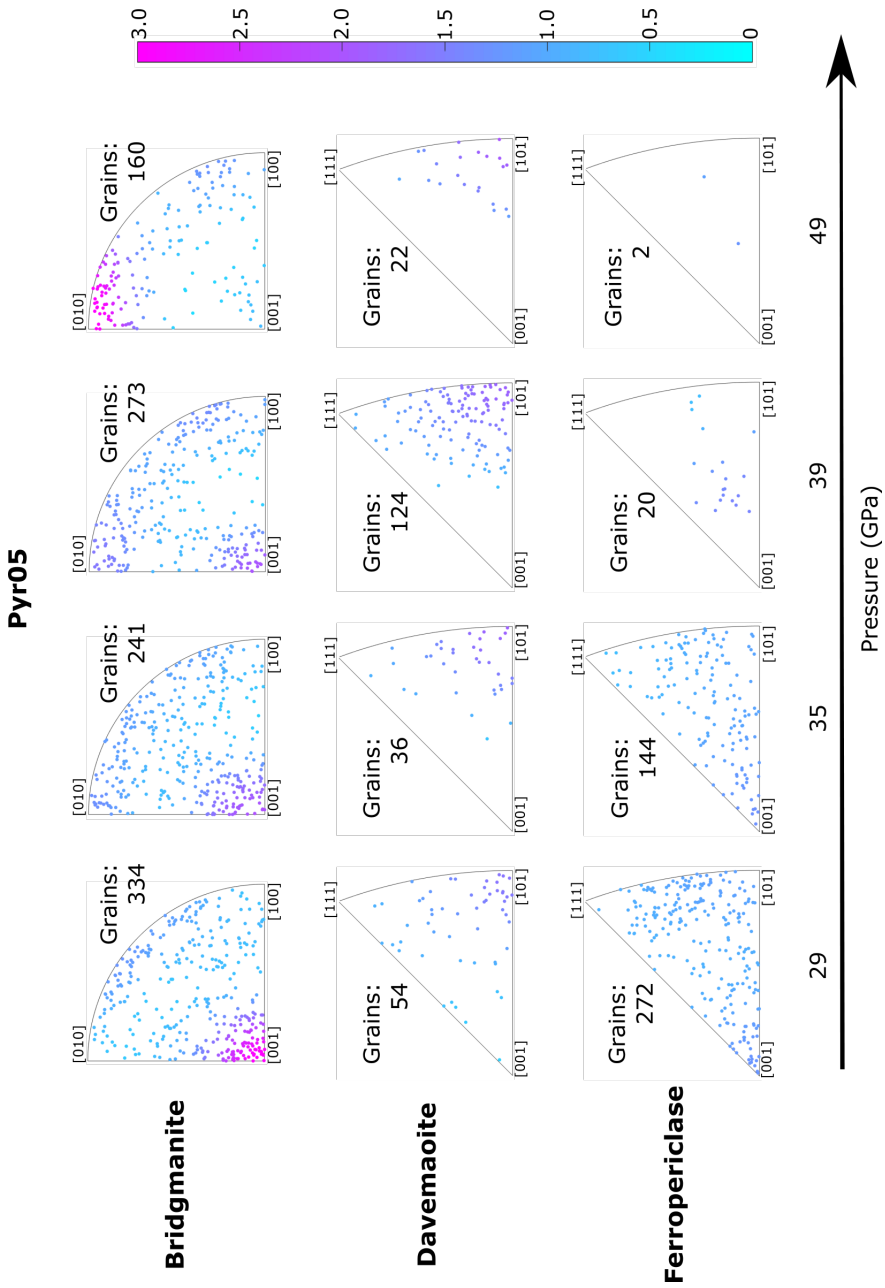

Figure 5.4: Inverse pole figures of the compression direction for sample Pyr05, showing individual grain orientations of bridgmanite, davemaoite, and ferropericlase in a pyrolitic composition at various pressures. Equal area projection. Grains are colored according to an orientation distribution fitted for each phase and color scale in multiples of random distribution (m.r.d.). The number of indexed grains is indicated above each inverse pole figure.

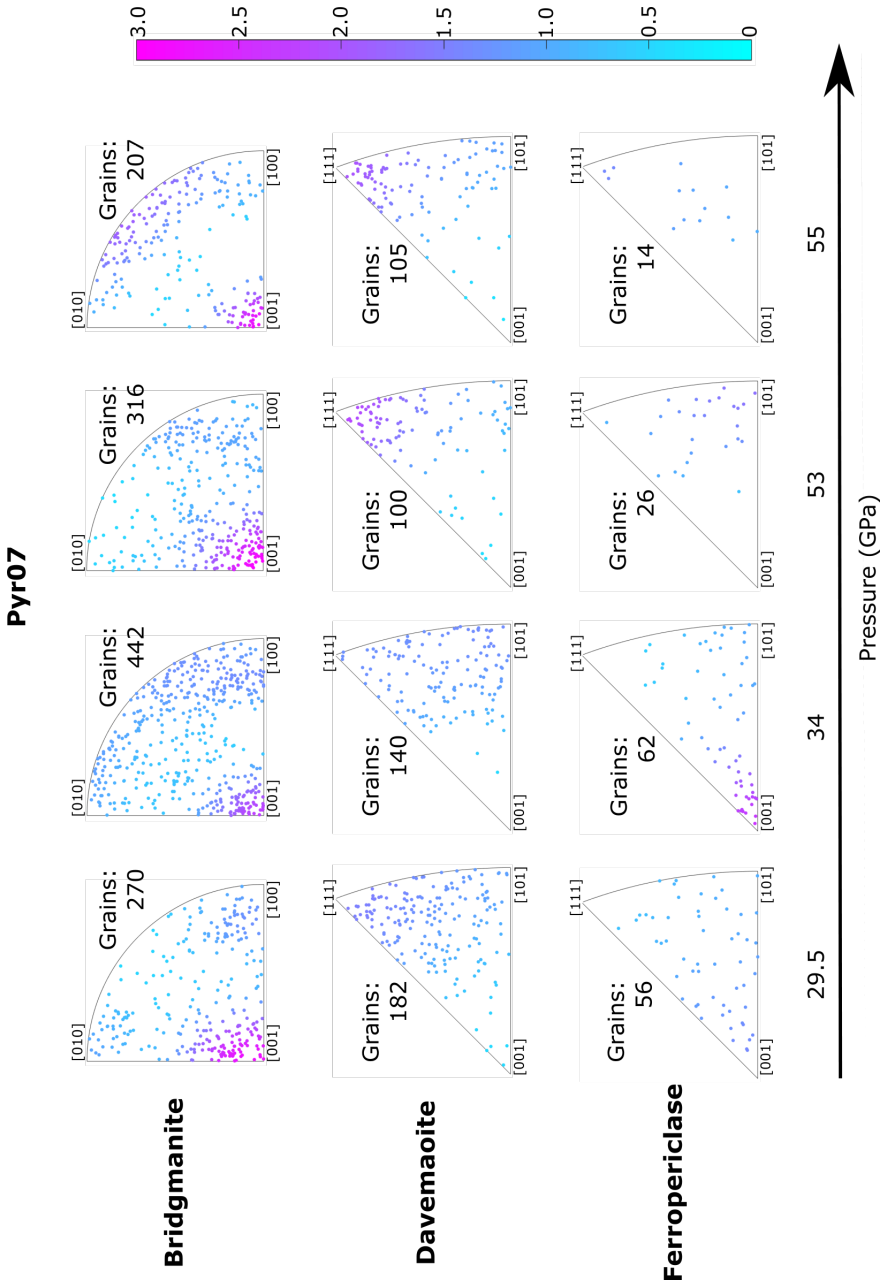

Figure 5.5: Inverse pole figures of the compression direction for sample Pyr07, showing individual grain orientations of bridgmanite, davemaoite, and ferropericlase in a pyrolitic composition at various pressures. Equal area projection. Grains are colored according to an orientation distribution fitted for each phase and color scale in multiples of random distribution (m.r.d.). The number of indexed grains is indicated above each inverse pole figure.

5.3.2 Experimental Deformation Textures in Pyrolite

A total of 3 separate samples were analyzed using synchroton x-ray diffraction; Pyr01, Pyr05, and Pyr07. Each sample was a separate experimental run, with MGC images collected at various pressures. Bridgmanite in all 3 runs displays a strong 001 texture, m.r.d. of 3, upon transformation. As pressures increase the 001 texture in Pyr05 and Pyr07 begin to weaken with (100) planes in run Pyr07 beginning to orient perpendicular to compression at 34 GPa. As compression continues in run Pyr07 the 001 maximum remains present, although a girdle forms between 100 and 010 by the end of the experiment at 55 GPa. In run Pyr05 we also observe a slight girdle between 100 and 010 with weak maxima at pressures between 35 and 39 GPa although occurring at lower pressures than in run Pyr07. At 49 GPa, in run Pyr05, planes are oriented perpendicular to 010 with no maximum at 001. Experimental run Pyr01 begins at 34 GPa with a strong maximum in 001 orientations, which weakens with compression to 48 GPa and gains a secondary maximum at 010; both with m.r.d. of 2.1. At 65 GPa the maximum at 001 is gone, leaving a strong preferred orientation of (010) planes perpendicular to compression; m.r.d. of 3.0. Texture remains largely unchanged until 105 GPa where the 010 maximum begins to weaken with m.r.d. values dropping to 2.0. The last multigrain acquisition is taken at 108 GPa with (010) planes oriented perpendicular to compression.

In experimental runs Pyr05 and Pyr07 davemaoite and ferropericlase were also indexed. In run Pyr05 davemaoite displays a 101 maximum throughout compression with m.r.d. values between 1.7 and 2.0. Davemaoite in run Pyr07, however, shows maximums in 111 orientations with m.r.d. values ranging just above 1.0 to 2.2. Ferropericalse remains randomly oriented in both runs during compression with the exception of run Pyr07 at 34 GPa. Davemaoite was not plotted for sample Pyr01 due to the low number of grains indexed in the multigrain images. This is due to the weaker intensity of davemaoite diffraction peaks compared to the surrounding phases, which lead to instances of peak overlap (Figure 5.2).

Table 5.4: CRSS and slip system activity in bridgmanite modeled using VPSC. Two stages of compression are performed in order to recreate the textures observed in the experimental data.

	Stage 1		Stage 2	
Slip System	CRSS	Activity (%)	CRSS	Activity (%)
(100)[010]	2	18.0	4	0.6
(100)[001]	1	34.7	4	9.0
(100)⟨011⟩	3	7.0	5	5.9
(010)[100]	4	2.2	1	36.9
(010)[001]	2	11.3	1	34.4
(010)⟨101⟩	3	9.4	4	1.4
(001)[100]	2	4.3	5	14.6
(001)[010]	2	11.3	3	1.3
(001)⟨110⟩	5	1.2	5	4.3
{111}⟨110⟩	30	1.6	30	1.6

5.4 Plasticity of Bridgmanite

Texture development depends on a number of factors including deformation geometry, total strain, starting texture, and plastic deformation mechanisms. While the deformation geometry is known in a DAC experiment, inferring the active deformation mechanism is less straightforward. In order to interpret our experimental textures, we implement VPSC modeling to simulate the deformation of polycrystalline bridgmanite. We then compare the results, using experimental textures to constrain the deformation mechanism, in order to identify the slip systems responsible for plastic behavior of our sample. Details on VPSC modeling have been outlined in the section on methods.

5.4.1 VPSC Modeling

To construct these models, a critical resolved shear stress (CRSS) must be assigned to each slip system. The CRSS is a threshold value of stress, upon when exceeded, the plane can slide in a given direction. These stresses can be calculated in a single crystal by relating the orientation of the plane and direction relative to the direction of maximum stress. In a polycrystal, however, all of the grains and their respective orientations must be taken into consideration, which requires us to test multiple possible CRSS values on a series of chosen slip planes and directions. The values are assigned by the user and are only relative values to one another, however this is enough to simulate the experimental texture.

A literature review on slip systems in bridgmanite is provided in the Introduction of

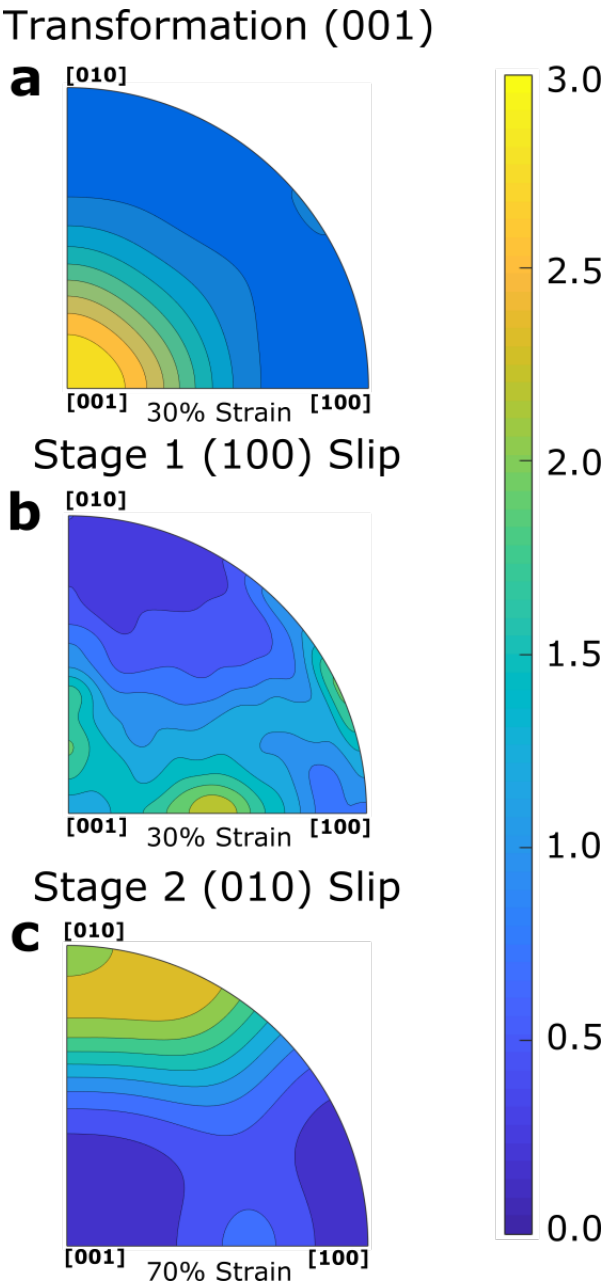

Figure 5.6: Inverse pole figures (a, b, c) of axial compression in VPSC simulation. Starting from transformation texture (a) applying 30% axial strain and allowing dominant slip on (100) planes generates (Fig. 5.6b). Second stage of deformation (c) starting from (Fig. 5.6b), allowing 70% strain with dominant slip along (010) planes.

the thesis. Here we test the following deformation mechanisms in bridgmanite, (100)[010], (100)[001], (100)⟨011⟩, (010)[100], (010)[001], (010)⟨101⟩, (001)[100], (001)[010], (001)⟨110⟩, and {111}⟨110⟩, based on our experimental results and the results of others in literature [Mainprice et al., 2008, Miyagi and Wenk, 2016, Couper et al., 2020, Kasemer et al., 2020]. The final models that most accurately replicate our experimental results are shown in Table 5.4 with corresponding CRSS values and slip activity.

Compression in bridgmanite was carried out in 2 stages in order to produce the observed textures in our experiments. Starting from a 001 transformation texture, we allow slip along (100)[010] and (100)[001] at 30% strain to deplete 001 orientations while generating a weak 100 texture, shown in Figure 5.6. Additionally, we observe the formation of a weak girdle between 100 and 010. In the second stage, we allow slip along (010)⟨101⟩, (010)[100], and (010)[001] to produce a concentrated 010 texture when strained to 70%.

5.5 Discussion

5.5.1 Textures of Pyrolitic Phases

At condition below the '660' there are 3 major mineral phases within our samples; bridgmanite, davemaoite, and ferropericlase. First, we will discuss the differences in texture between our experimental runs, followed by a comparison of what is found in literature for each of the 3 phases.

5.5.2 Bridgmanite

We identify 3 regimes of texture development in these experiments: 001 transformation textures, a reorientation to 100 with deformation, and then a shift to 010 orientations. Comparing the texture evolution of bridgmanite between the samples reveals some key differences however. While all samples display a strong maximum in 001 at the beginning of deformation, this maximum only remains in Pyr07 by the end of the experiment at 55 GPa. A possible explanation for this is simply that this sample was not subjected to sufficient deformation to completely reorient all of the grains. It is not until 49 GPa in run Pyr05 and 65 GPa in run Pyr01 that the 001 maximum disappears. We do see a gradual shift to 100 orientations in bridgmanite, which can first be observed at 34 GPa, throughout the compression in Pyr05, leading to a somewhat weak maximum in 100 at 39 GPa. Texture

in bridgmanite, where 100 planes are oriented perpendicular to compression, has been documented in past experiments including bridgmanite + ferropericlase transformed from olivine at 61 GPa and ringwoodite at 51 GPa [Miyagi and Wenk, 2016], in pure bridgmanite [Merkel et al., 2003], and when transformed from olivine at 25 GPa [Wenk et al., 2004b].

A deformation texture not observed in past deformation experiments of bridgmanite however, is the orientation of 010 planes seen in experimental runs Pyr01 and Pyr05 at 49 and 65 GPa respectively. The difference in these 2 runs, however, is the formation of a girdle between 100 and 010 in Pyr05 before a strong maximum in 010 orientations. In run Pyr01, orientations go from 001 straight to 010, with 001 orientations absents at 65 GPa. This girdle is also observed in sample Pyr07 at 55 GPa, although orientations in Pyr07 never completely reorient to 010. We reason that pressure increase in Pyr01 is less gradual, allowing for faster reorientation of bridgmanite grains, explaining the absence of an intermediate 100 texture.

5.5.3 Davemaoite

Davemaoite, in the cubic structure $Pb\bar{3}m$, was only indexed in runs Pyr05 and Pyr07. In sample Pyr05 davemaoite displays moderate texture in 101 orientations throughout the entire experiment. Sample Pyr07, however, shows comparatively stronger 111 orientations at 53 and 55 GPa. Past deformation experiments in the DAC have lead to observations of 001 orientations in davemaoite at pressures between 25.5 and 49.3 GPa with no change in strength [Miyagi et al., 2009]. The study by Immoor et al. [2022] reports texture in 001 planes perpendicular to compression with texture strength increasing from 31.1 to 52.5 GPa at 1150 K. This is inconsistent with both of our experimental runs; however, it is important to note that experiments carried out in Miyagi et al. [2006, 2009], Immoor et al. [2022] where performed on pure $CaSiO_3$ wollastonite and ignore the interaction with bridgmanite and ferropericlase.

There is a distinct difference in preferred orientations in $CaSiO_3$ between runs Pyr05 and Pyr07 despite being deformed over similar pressure ranges. We propose 2 separate reasons for this. First, is the effect of strain on the sample, which leads to changes in grain shape during compression and hence how grains align themselves [Kocks et al., 2000]. Strain can be distributed differently across the sample in each run leading to the possibility

of different textures. Second, is the effect of the surrounding phases on davemaoite. The strength of the surrounding material will largely impact how a crystal may deform and orient itself [Kaercher et al., 2016, and references within].

5.5.4 Ferropericlase

Ferropericlase in both runs, Pyr05 and Pyr07, does not display texture during compression with the exception of run Pyr07 at 34 GPa, where a moderate 001 texture is observed. The amount of grains indexed is low, ranging from 14 to 56 grains. As previously discussed about ringwoodite in Chapter 4, the texture observed in ferropericlase is likely a result of an overestimation of intensity in the orientation distribution function due to the overall lower amount of grains indexed.

Past resistive heated DAC experiments on ferropericlase by Immoor et al. [2018], conducted between 20-80 GPa and 1400 K, have reported strong textures in 001 and 101 orientations. In contrast, other experiments in the DAC on bridgmanite + ferropericlase aggregates have shown little to no texture in the ferropericlase phase [Miyagi and Wenk, 2016] when compressed between 33-61 GPa. These results align with what we observe in our experiments leading to the conclusion that coexisting phases have an impact of the resulting texture during deformation.

5.5.5 Plastic Behavior of Bridgmanite

Understanding the plastic behavior of bridgmanite is largely motivated by the fact that $(Mg,Fe)SiO_3$ in the perovskite structure makes up 80% of the Earth's lower mantle by volume [Hirose, 2002, Murakami et al., 2007, Ishii et al., 2011, Wang et al., 2015]. Additionally, texture development resulting from mantle convection has resulted in past observations of seismic anisotropy [Wookey et al., 2002, Beghein et al., 2006, Long and Silver, 2008, Ferreira et al., 2019] and hence is important for the interpretation of deep mantle processes. Texture evolution is generated through plastic deformation caused by dislocation glide and/or twinning within the crystal. Other processes including diffusion creep or dislocation climb may also be active, but neither result in the development of strong texture.

While many studies have investigated deformation textures and mechanisms in bridgmanite [e.g. Wang et al., 1992, Merkel et al., 2003, Wenk et al., 2004a, Cordier et al.,

2004, Wenk et al., 2006, Ferré et al., 2007, Mainprice et al., 2008, Miyagi and Wenk, 2016, Kraych et al., 2016, Boioli et al., 2017], and others taking into consideration multiple phases [Girard et al., 2016, Kaercher et al., 2016], none have studied the deformation behavior of bridgmanite within a pyrolitic material. Here, we will discuss deformation mechanisms in bridgmanite based on modeled textures using VPSC. Texture in davemaoite does not evolve with deformation and ferropericlase remains isotropic through out the experiments. Adding these phases will not impact the results of our VPSC models. Hence, we only consider the plastic deformation of bridgmanite and try to understand how to generate our experimental textures.

5.5.6 Modelling Deformation Mechanism of Bridgmanite

Below 50 GPa

The first stage of axial compression in our models requires dominant slip activity (34.7%) on (100)[001] with minor contributions (11.3%) from (010)[100] and (110) [010], in order to deplete orientations in 001 and generate gradual migration of orientations to 100. VPSC modeling has been used in the past to investigate deformation of perovskites at lower mantle conditions [Mainprice et al., 2008, Miyagi and Wenk, 2016, Kaercher et al., 2016]. VPSC simulations in Miyagi and Wenk [2016] determine [100], [010], and ⟨110⟩ on (001) planes to be the most active at pressures below 55 GPa, which is in agreement with first principal calculations in Ferré et al. [2007], who suggest the (001)[100] slip system as the easiest to activate in bridgmanite, owing to dislocation glide. Shear deformation experiments in Tsujino et al. [2016], however, report 100 deformation textures, also observed in our experiments, that are compatible with dominant slip on (100)[001]. Furthermore, using the Peierls-Nabarro model in addition to first-principle methods [Mainprice et al., 2008] finds (100)[010] to be the most active slip system at all pressures in $MgSiO_3$ bridgmanite. It is possible that the (001) slip assigned by Miyagi and Wenk [2016] could be an effect of transformation rather than deformation, as we observe strong 001 textures in bridgmanite upon transformation.

Above 50 GPa

In our experiments, we observe 010 textures at pressures greater than 50 GPa, which requires slip along (010) planes and little to no activity (0.6%) in (100)[010]. This is contrary to what Mainprice et al. [2008] models at pressures above 30 GPa. Modeling of dislocations in $MgSiO_3$ bridgmanite, indicate (100)[010] edge dislocations are most mobile at pressures between 30 and 50 GPa, with Peierls stress increasing significantly at pressures beyond 60 GPa [Hirel et al., 2014]. Additionally, (100)[010] screw dislocations also have a large rate of increase in Peierls stress up to 50 GPa. In another study by Kraych et al. [2016], (010)[100] and (100)[010] dislocation glide in bridgmanite is modeled at 30 and 60 GPa. CRSS values of (100)[010] are much lower at 30 GPa and 2000 K than that of (010)[100]; however, when pressures increase to 60 GPa, CRSS values of (100)[010] becomes larger than that of (010)[100]. These results compare well to the slip system activities in our VPSC simulations, where we observe little to no slip activity in (100) planes when generating 010 orientations in bridgmanite and an increased activity of (010) slip with pressure.

Deformation Mechanism Summary

Based on our VPSC modeling results, we determine that there are 2 separate deformation mechanisms at play during uniaxial compression of bridgmanite. Below 50 GPa we model dominant slip of (100) planes in [001] which is responsible for the depletion of 001 orientations and gradual reorientation to 100. Above 50 GPa we model dominant slip of (010) in [100] and [001] in order to generate (010) orientations.

The gradual reorientation from 001 to 100 in bridgmanite of our VPSC models compare favorably to experimental observations in Miyagi and Wenk [2016]. Bridgmanite + ferropericlase, transformed from either olivine or ringwoodite, when deformed displays intermediate textures across 001 and 100 between 36 and 53 GPa. Dominant slip systems determined by VPSC simulations in their experiments were reported as [100], [010], and $\langle 110 \rangle$ on (001) planes at pressures below 55 GPa and (100) at pressures greater than 55 GPa. In contrast, we model 100 textures below 50 GPa which require large contributions of slip along (100) planes with only minor contributions (11.3%) along (010) and (001)

planes. This is due in part that 100 orientations in bridgmanite are not observed in Miyagi and Wenk [2016] until above 55 GPa in their experiments, which could be attributed to compression at ambient temperatures. Textures from shear deformation experiments in a study by Tsujino et al. [2016] are compatible with dominant slip on (100)[001] at 25 GPa and 1872 K however.

Although, first-principal calculations of Mainprice et al. [2008] agree with our results below 50 GPa, they are not compatible with our observations of 010 textures in bridgmanite at high pressures. Slip system modeling in bridgmanite by Hirel et al. [2014] and Kraych et al. [2016] are in agreement with one another, in which (100) dislocations are easier to activate at pressures below 50 GPa; however, Kraych et al. [2016] observes a shift in dominant slip plane from (100) to (010) once pressures exceed 60 GPa. This supports the results of our VPSC modeling based on observed 010 experimental deformation textures in bridgmanite, where slip along (010) planes is dominant above 50 GPa. Nzogang et al. [2018] observes (010) dislocations in recovered bridgmanite, deformed at 27 GPa and 2130 K, using orientation mapping in the TEM. They conclude the observed dislocations are a result of (010)[100] slip. Although twinning is observed in Nzogang et al. [2018], they determine it is not pervasive enough to be considered a significant deformation mechanism in bridgmanite. Twinning was also considered in the VPSC modeling of Miyagi and Wenk [2016]; however, the textures generated are much stronger than their experimental textures and hence were not included in our simulations.

5.6 Implications for the Earth's Lower Mantle

Most anisotropy within the lower mantle is attributed to texture caused by the progressive deformation of pyrolite through the convective mantle flow. Whether or not there is anisotropy in the lower mantle is still highly debated. Here, we model a slab that penetrates the '660' and descends to depths of 2600 km and calculate how much anisotropy is produced in the process. This work is a starting collaboration done with John Keith Magali who is a postdoc working in the TIMEleSS project, combining his expertise on numerical modeling of anisotropy in the mantle and our experimental results. All results presented below are preliminary and will be updated with improvements to the models.

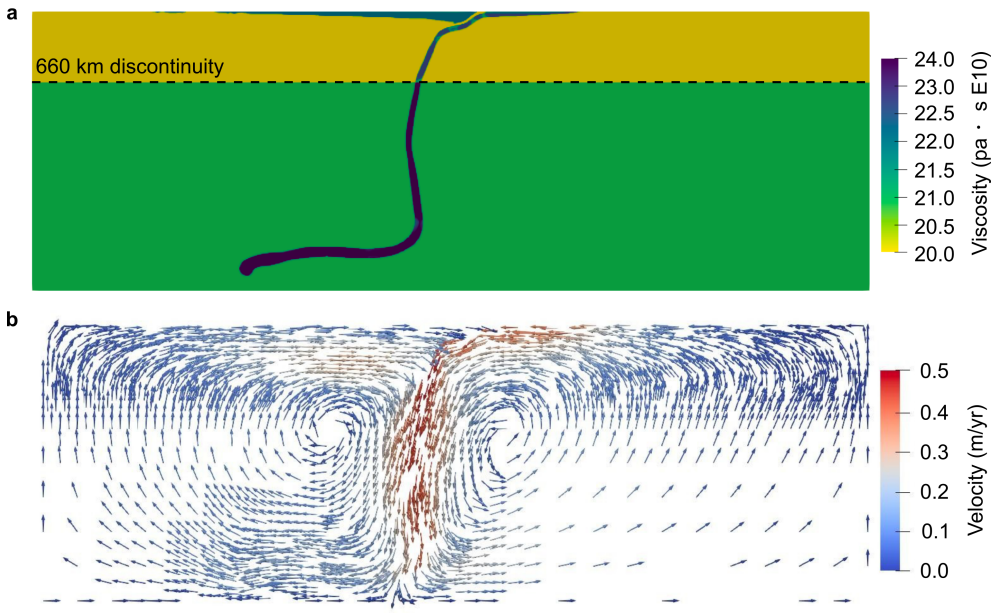

Figure 5.7: a) Effective viscosity η in the mantle. The dashed line illustrates the viscosity contrast between the transition zone and lower mantle. b) Resulting velocity field resulting from a slab stagnating at 2600 km.

5.6.1 Global Mantle Model

Two dimensional models of compositionally driven subduction were computed using the software Aspect [Kronbichler et al., 2012], which solves for the incomprehensibility, momentum, and energy equations in the Cartesian domain. Model dimensions are 7800 $\times$ 2600 km and with the help of adaptive mesh refinements, spatial resolutions vary from 5 km $\times$ 5 km across the slab and regions with large viscosity contrasts up to 325 km $\times$ 325 km far from the said regions. The mantle rheology used in this model is viscoplastic, where dislocation creep, diffusion creep, and plastic yielding are harmonically averaged. To allow for the decent of the slab into the lower mantle, we impose a viscosity contrast at the '660' by a factor of 10; although we acknowledge this contrast can be larger [e.g. Quinteros et al., 2010]. Figure 5.7 shows the effective viscosity and velocity of the flow in the mantle at 72 million years (Ma).

Coupling geodynamic models with tomographic images through texture evolution in bridgmanite requires the VPSC calculations performed in the previous section. From the 72 Ma state of the mantle, flow lines have been traced backwards in time until 80 percent strain accumulation has been reached. At each time step along the flow line a local velocity gradient tensor is estimated. These velocity gradients are then used as an input for VPSC

to calculate how much strain is accrued in 3000 bridgmanite grains. We restrict our VPSC calculations to a domain of 1200-6500 km horizontally and 660-2600 km vertically to avoid boundary effects. We use the 001 transformation texture in bridgmanite as the starting texture for the slab immediately below 660 km, whereas the bridgmanite aggregates in the surrounding mantle are initially randomly oriented. Using the active slip systems deduced from the experiment we are able to compute the resulting texture at each point in space. For instance, above 2000 km we impose dominant (100) slip within the slab, whereas below this depth (010) slip is dominant. The latter scenario is analogous to experiments in Pyr01, where we observe 001 compression textures reorient to 010 in bridgmanite at lower mantle pressures (Figure 5.3).

To obtain the full elastic tensor (i.e. tensor of elasticity with 21 independent coefficients), we use a Voigt-Reuss-Hill averaging scheme given the single crystal elastic constants of bridgmanite that vary with pressure and at a constant temperature of 1900 K. Oftentimes it is easier to interpret the elastic tensor using conventional elastic decomposition methods. Here we decompose the full elastic tensor into a vertically-transverse isotropic medium (VTI) using the method of Montagner and Nataf [1986]. In this way, we can determine the strength of S-wave anisotropy ξ (i.e. dependence of speeds to polarization orientation for horizontally propagating S-waves), and the P-wave anisotropy ϕ (i.e. ratio between the speeds of horizontally and vertically-propagating P-waves).

5.6.2 Results

Immediately below the '660' our S-wave anisotropy models (i.e. $\xi = \frac{V_{SH}^2}{V_{SV}^2}$) show faster vertically polarized shear waves (V_{SV}) than horizontally polarized shear waves (V_{SH}) for horizontally traveling waves (Figure 5.8a). The surrounding mantle at the same depths also displays V_{SV} leading V_{SH} ($V_{SV} > V_{SH}$), although not as strong as within the slab. The surrounding mantle far from the slab, however, shows $V_{SH} > V_{SV}$. With increasing pressures, the S-wave radial anisotropy varies in the surrounding mantle whereas it approximately stays the same within the slab. Overall, V_{SV} continues to lead V_{SH} above 2250 km. Beneath this depth however, we observe a shift in trend of ξ (i.e. $V_{SH} > V_{SV}$) within the slab. In this area the slab begins to bend and travel horizontally along the D" layer. The surrounding mantle, on the other hand, exhibits prominent $V_{SV} > V_{SH}$ below

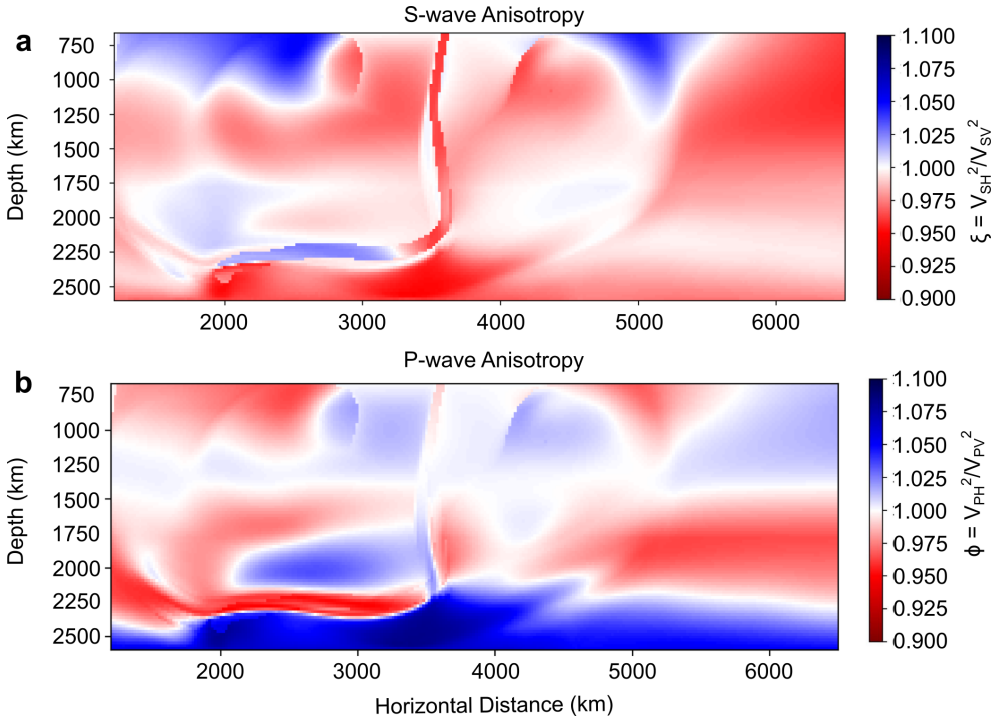

Figure 5.8: a) S-wave anisotropy (ξ) in the mantle defined as the ratio $\xi = \frac{V_{SH}^2}{V_{SV}^2}$ where V_{SH} and V_{SV} are horizontally and vertically polarized S-waves, respectively, for horizontally propagating S-waves. In the slab dominant slip in bridgmanite changes from 001 to 100 between 700 and 2000 km depth. b) P-wave anisotropy (ϕ) in the mantle defined as the ratio $\phi = \frac{V_{PH}^2}{V_{PV}^2}$ where V_{PH} and V_{PV} are horizontally and vertically propagating P-waves, respectively.

2250 km.

P-wave anisotropy ($\phi = \frac{V_{PH}^2}{V_{PV}^2}$) within the subducting slab immediately below the '660' is slightly anisotropic with vertically propagating waves (V_{PV}) traveling faster than horizontally propagating waves (V_{PH}) (Figure 5.8b). The surrounding mantle in this same area displays weak anisotropy with $V_{PH} > V_{PV}$. With increasing depth (between 1000 and 1500 km) the slab appears to have weaker P-wave anisotropy with V_{PV} slightly leading V_{PH}. Across the same depth range, we observe no considerable change in the surrounding mantle. Below 1500 km however, both the surrounding mantle and the slab become more anisotropic with depth, with an apparent switch in P-wave anisotropy patterns in both regions. As soon as the slab bends and travels horizontally along the D" layer, the P-wave anisotropy within the slab again reverts back to $V_{PV} > V_{PH}$. The surrounding mantle beneath the slab shows strong amplitudes of P-wave radial anisotropy with $V_{PH} > V_{PV}$.

In order to illustrate how the P-wave radial anisotropy structure would appear as a tomographic image, we perform a tomographic filtering technique that involves a homogenization of an elastic medium with no scale separation such as the Earth. Even with a homogeneous distribution of source-station pairs, seismic tomography only outputs a smooth version of the Earth due to finite-frequency seismic data. Because of this, tomographic filtering is essential for our anisotropic models to be compatible with existing tomographic models. Here we use the Fast-Fourier Homogenization algorithm developed by Capdeville et al. [2015]. In this method, small-scale spatial variations in the elastic medium are removed based on a minimum wavelength λ_h of the observed wavefield, and are instead replaced with effective properties. Thus homogenization can be viewed as the best possible image one would recover from seismic tomography assuming perfect data coverage [Capdeville and Métivier, 2018]. As a demonstration, we choose a homogenization wavelength $\lambda_h = 300$ km corresponding to the wavelength of long period P-waves sampling the lower mantle (Figure 5.9). Upon homogenization, we observe how the small-scale features in the original P-wave anisotropy model have been smoothed out. For instance, it is now difficult for us to delineate the subducting slab in Figure 5.9. We anticipate that selecting a homogenization wavelength shorter than the thickness of the slab would recover its small-scale features. Nevertheless, the general patterns of P-wave radial anisotropy in

our mantle model is preserved.

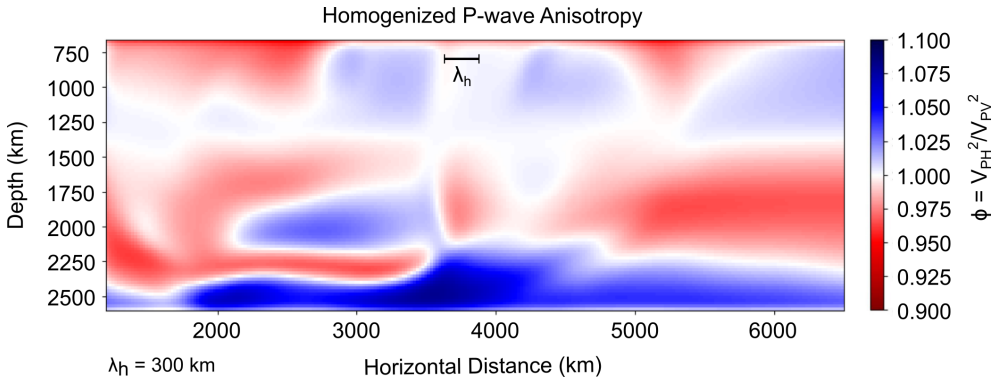

Figure 5.9: Homogenized P-wave anisotropy in the mantle. We use the non-periodic homogenization of Capdeville et al. [2015] to spatially average the set of elastic tensors obtained from VPSC modeling. Homogenization can be viewed as the best possible image one could retrieve from seismic tomography assuming perfect ray-path coverage [Capdeville and Métivier, 2018]. Here we use a homogenization wavelength $\lambda_h = 300$ km corresponding to the wavelength of P-waves sampling the lower mantle.

5.6.3 Discussion

In our geodynamic models, the slab geometry is subvertical as it penetrates the '660'. S-wave anisotropy is large in this region with $V_{SV} > V_{SH}$, which we attribute to strong 001 transformation textures in bridgmanite (Figure 5.8a). We do not see a change in this pattern until depths of 2250 km as the slab impinges and bends along the D" layer. As the slab migrates horizontally along this boundary, we now observe $V_{SH} > V_{SV}$. We also see a shift in the fast propagation direction in P-waves within the slab as it subducts. This could be a result of a change in the dominant slip systems of bridgmanite above 50 GPa. The study of Ferreira et al. [2019] does not consider texture in a subducting slab as, it is implied that texture development is impeded in a cold and highly viscous material.

In the lower mantle, Sturgeon et al. [2019] and Ferreira et al. [2019] only consider a single dominant slip system in their texture calculations of bridgmanite. Here we expanded upon their work by implementing pressure dependent slip systems of bridgmanite where we have demonstrated, how P-wave anisotropy increases with depth in the lower mantle. For instance, 100 orientations in bridgmanite are weak in comparison to the 010 orientations that are eventually generated at pressures beyond 50 GPa (Figure 5.4). This may provide a potential explanation as to why P-wave anisotropy increases below 1900 km depth in the

average lower mantle as observed by de Wit and Trampert [2015]. Note, however, that inconsistencies remain as we do not observe the stronger $V_{SH} > V_{SV}$ in the slab as is seen in the study of Ferreira et al. [2019].

We lay the groundwork of providing transformation and deformation textures observed in our experiments that can potentially be upscaled to lower mantle conditions. Being at the proof of concept stage, these models have their own set of limitations: i) A steady state assumption is made when back tracing flow stream lines. One must be cautious when making interpretations of anisotropy such as convergent margins [Faccenda and Capitanio, 2012], or in our case adjacent to regions where slab bending occurs. ii) Viscosity does not take into consideration temperature. iii) We assume that all of the deformation in bridgmanite is accommodated by the entire velocity gradient field, which would overestimate anisotropy. iv) We only consider deformation of a single phase (bridgmanite). v) The elastic constants of bridgmanite are calculated at varying pressures, but constant temperature (1900 K). Nevertheless we demonstrate how modeled textures from experimental observations in deformation experiments might be used to interpret seismic anisotropy from real geodynamic scenarios in the lower mantle.

5.7 Conclusion

In this chapter we presented the results of deformation experiments at the pressure and temperature conditions ranging from the 660 km discontinuity down to a depth of 1400 km on pyrolite. Compression was carried out in a laser-heated DAC at pressures ranging from 29 to 108 GPa and temperatures between 1500 and 2000 K; implementing multigrain X-ray diffraction to study the sample. We successfully observe deformation of (bridgmanite + davemaoite + ferropericlase) in all three samples along with the associated microstructures.

Multigrain data processing techniques resulted in the assignment of single crystal diffraction peaks to individual grains within the sample. We are able to index between 107 and 442 grains in bridgmanite, 4 to 182 grains of davemaoite, and 2 to 272 grains of ferropericlase in a multiphase material. At the beginning of deformation, bridgmanite displays a strong 001 texture that weakens and slowly shifts to orientations in 100. As pressure increases beyond ∼50 GPa, bridgmanite reorients to a 010 texture. Davemaoite

is only moderately textured with 101 orientations in one experiment, and 111 orientations in another. Ferropericlase remains largely untextured in all experiments.

Using our experimental textures, we implement VPSC to model potential slip systems responsible to the texture evolution seen in bridgmanite. We separate deformation into two stages, with 30% strain applied in compression for the first stage and 70% strain applied in the second. Starting from a 001 transformation texture, we find that (100)[001] is the dominant active slip system with minor contributions from (010)[001] and (001)[010]. During the second stage of compression, dominant slip is nearly evenly distributed between (010)[100] and (010)[001]. This is consistent with experimental observations observations in Miyagi and Wenk [2016] where they also observe a gradual shift from 001 to 100 orientations between 36 and 53 GPa for cold compressed bridgmanite. It is also consistent with the simple shear deformation experiments of Tsujino et al. [2016] with dominant slip on (100)[001] at 25 GPa and 1872 K.

First-principal calculations of Mainprice et al. [2008] agree with our results below 50 GPa. Slip system modeling in bridgmanite by Hirel et al. [2014], Kraych et al. [2016] find (100) dislocations are easiest to activate at pressures below 50 GPa and Kraych et al. [2016] observes a shift in dominant slip plane from (100) to (010) once pressures exceed 60 GPa. This is in agreement with the results of our experiments and VPSC modeling above 50 GPa, where slip along (010) planes is the dominant.

In this work we demonstrate that texture evolves from 100 to 010 orientations in bridgmanite within a pyrolitic material when deformed at lower mantle pressures and temperatures. Observations of seismic anisotropy are largely absent in the Earth's lower mantle, however. To address this we implement our VPSC calculations to model anisotropy within a subducting slab at lower mantle conditions. Within the subducting slab, we observe a change in S-wave radial anisotropy from $V_{SV} > V_{SH}$ to $V_{SH} > V_{SV}$ when the slab bends along the D" layer. P and S-wave radial anisotropy models show no clear correlations with mantle deformation and flow patterns. Additionally, anisotropy is weak in our models and does not correlate with flow, which may explain why anisotropy is not often observed in the lower mantle. Here, we have demonstrated a promising method, if only a starting point, to implement experimental results in anisotropy models. In the future, the development of

such integrated model, implementing results of experimental deformation experiments and numerical models of mantle, will help the interpretation of seismic signals and how they can be used to constrain flow and dynamic processes in the deep mantle.

Chapter 6

Transformation and Deformation Microstructures in Bridgmanite formed from Majoritic Garnet

6.1 Introduction

Subducting oceanic slabs are chemically stratified, containing a 6–7 km thick crust with enriched mid-ocean ridge basalt (MORB) composition, overlying a 5–20 km thick depleted harzburgitic layer, and deeper pyrolitic layer [Ringwood, 1982, Faccenda and Zilio, 2017]. Phase transformations and physical properties such as wave velocities in these compositions have been investigated experimentally in the past in order to determine which composition best matches observed seismic velocity profiles [Ita and Stixrude, 1992]. Calculations of seismic anisotropy will be directly impacted by the bulk composition of the material due to the elastic properties and preferential orientations of the phases it contains. We demonstrated an example of this in Chapter 4 where we calculate anisotropy both above an below the 660 km seismic discontinuity.

Up until this point, this thesis has focused on perovskite/post-perovskite analogues, phase transformations in pyrolite at conditions of the 660 km discontinuity ('660'), and the subsequent deformation of pyrolite at conditions corresponding to depths of 2400 km. In this chapter, we will try to understand the effect of aluminum on transformation and deformation microstructures starting from a pyrolitic garnet composition, pyrolite-minus-olivine, by performing deformation experiments in the laser-heated DAC combined with multigrain X-ray diffraction techniques. Many studies have been conducted in the past that aim to address the impact aluminum may have on the physical properties of bridgmanite

including the effect of elasticity [Nishiyama et al., 2007, Fu et al., 2019], phase transformation kinetics [Lessing et al., 2022], thermal conductivity [Okuda et al., 2017], electrical conductivity [Yoshino et al., 2008], compressibility and spin state of iron [Brodholt, 2000, Ballaran et al., 2012, Okuda et al., 2020], cation substitution [Fukui et al., 2016, Huang et al., 2021, Nakatsuka et al., 2021], aluminum solubility [Liu et al., 2021], and seismic anisotropy [Fukui et al., 2016, Fu et al., 2019]. This raises the question of the impact aluminum might have on observed microstructures presented in the previous chapters. More specifically, we aim to address whether or not the transformation and deformation textures in bridgmanite and $CaSiO_3$ davemaoite differ from those observed in our experiments on pyrolite.

6.2 Methods

Methods and data analysis implemented in this section are outlined in the previous two chapters. Any changes in the experimental set-up will be discussed below. Sample preparation of the pyrolite-minus-olivine samples are described in detail in the Methods chapter. Two pyrolite-minus-olivine samples, Pyr-Ol-1 and Pyr-Ol-2, were analyzed at the Extreme Conditions beamline P02.2 at PETRA III (DESY, Hamburg) using the same beamline setup from the muligrain X-ray diffraction experiments presented in the previous two chapters.

The first experiment, sample Pyr-Ol-1, was ran using an incident monochromatic X-ray beam focused to 1.9 μm x 1.9 μm paired with a PerkinElmer XRD 1621 detector with 200 μm x 200 μm pixel size. A CeO_2 standard from the National Institute of Standards and Technology (NIST; 674b) was used for calibration in order to correct for detector tilt, beam center, and calculate a sample to detector distance of 404.5133 mm. The wavelength for this experiment was fixed at 0.2891 Å. In the second experiment, sample Pyr-Ol-2, an incident monochromatic X-ray beam focused to 1.2 μm x 1.9 μm paired with a PerkinElmer XRD 1621 detector with 200 μm x 200 μm pixel size. A CeO_2 standard from the National Institute of Standards and Technology (NIST; 674b) was used for calibration and calculate a sample to detector distance of 403.4252 mm. The wavelength for this experiment was fixed at 0.2904 Å. Double-sided laser heating was carried out during compression using a

Yb-fiber laser to reach the necessary temperatures as installed by default on the beamline [Liermann et al., 2015].

The goal of these experiments is to observe transformation and deformation textures in bridgmanite and $CaSiO_3$ davemaoite at conditions of the '660' when starting from a pyrolitic garnet. Multigrain image collections are taken upon transformation to bridgmanite and then every 2-5 GPa up to 40 GPa. Experimental pressure and temperature path of Pyr-Ol-2 are shown in Figure 6.1. Images are collected using the same method as previously described by rotating the diamond anvil cell (DAC) in ω by 0.5° steps from $-28°$ to 28° with collection times of 1 second per image, resulting in a total of 112 images for each MGC scan. Samples are quenched before MGC images are collected. Unit-cell parameters of the mineral phases are again extracted using the software MAUD [Lutterotti et al., 1997] using the histogram method described in the previous chapters.

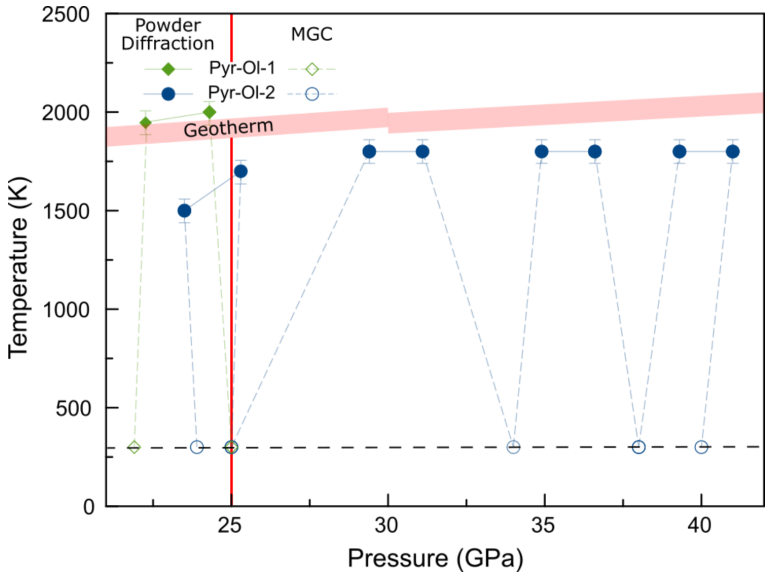

Figure 6.1: Pressure vs. temperature for samples Pyr-Ol-1 and Pyr-Ol-2. Multigrain image collections are acquired at 300 K. Open markers are where MCG diffraction data was collected with filled markers indicating where powder diffraction images were taken. Dotted potion of lines along the P/T path denote when the sample is being heated or quenched. Errors in temperature are set to ±60 K. Black dashed line is a visual aid marking 300 K. Red shaded area marks the geotherm from [Katsura et al., 2010]. Pressures in KCl and MgO are estimated from the equations of state of [Tateno et al., 2019] and [Speziale et al., 2001], respectively. We first observe the transformation to bridgmanite at 25 GPa in both samples as marked by the vertical red line.

6.3 Deformation Microstructures in pyrolite-minus-olivine

6.3.1 Grain Indexing Statistics

Table 6.1 shows grain indexing statistics for bridgmanite and davemaoite in experimental runs Pyr-Ol-1 and Pyr-Ol-2. The number of grains indexed for each phase, number of diffraction peaks assigned to each grain, and the percentage of total g-vectors assigned to grains for each indexing are provided. Our indexing capabilities for these experiments are similar to those in our previous work on pyrolite. Similar 2θ ranges, i.e. 8.2° to 8.3°, 11.6° to 11.7°, were filtered in order to avoid incorrectly assigning pressure medium g-vectors to sample grains.

Table 6.1: Indexing statistics from GrainSpotter for bridgmanite and davemaoite in run Pyr-Ol-1 and Pyr-Ol-2. Pressures, number of grains indexed, amount of diffraction peaks assigned to grains, and percentage of g-vectors assigned to grains for each indexing are shown. KCl used as pressure transmitting medium in run Pyr-Ol-1 and MgO used as pressure transmitting medium in run Pyr-Ol-2. Pressures are determined using the equation of state of KCl and MgO in Tateno et al. [2019] and Speziale et al. [2001], respectively.

Exp.	Phase	P (GPa)	Gr. Ind.	Peaks per Gr.	Assigned Gve (%)
Pyr-Ol-1	Bridgmanite	25	434	25	88
	Davemaoite		235	10	
Pyr-Ol-2	Bridgmanite	25	220	23	80
	Davemaoite		96	8	
	Bridgmanite	34	240	24	85
	Davemaoite		136	8	
	Bridgmanite	38	212	23	83
	Davemaoite		171	8	
	Bridgmanite	40	144	21	67
	Davemaoite		142	9	

6.3.2 Experimental Deformation Textures

Two samples were analyzed using synchroton x-ray diffraction; Pyr-Ol-1 and Pyr-Ol-2. Each sample was a separate experimental run, with MGC images collected at various pressures. Here we will focus on textures from the experiment on sample Pyr-Ol-2 (Figure 6.2), as the experiment on sample Pyr-Ol-1 was ended after the observation of the transformation to bridgmanite. Bridgmanite again displays a strong 001 texture, m.r.d. of 3, upon transformation in addition to a weak 010 maximum at 25 GPa. With further compression the 001 maximum weakens significantly and we observe the appearance of 100 orientations, m.r.d. of ∼1.9, at 34 GPa. As pressures increase to 40 GPa, we are left with only 001 and

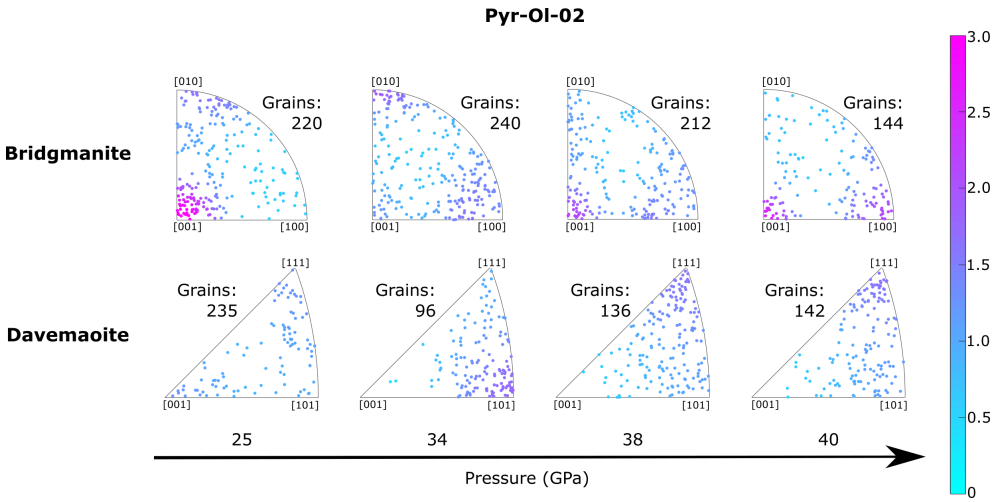

Figure 6.2: Inverse pole figures of the compression direction for sample Pyr-Ol-2, showing individual grain orientations of bridgmanite and davemaoite in a pyrolitic garnet composition at various pressures. Equal area projection. Grains are colored according to an orientation distribution fitted for each phase and color scale in multiples of random distribution (m.r.d.). The number of indexed grains is indicated above each inverse pole figure.

100 orientations. Davemaoite, on the other hand, does not display an initial transformation texture. With further compression to 34 GPa, however, we observe same dominant 101 orientations as in sample Pyr05. Textures in davemaoite shift to 111 at 38 GPa and remain as such until the end of the experiment with no change in strength.

6.3.3 Bridgmanite Unit Cell Parameters

Figure 6.3 details the unit cell volumes of bridgmanite in all of our experimental runs. Bridgmanite in all of the samples fit a similar trend in unit cell parameters with the increase of pressure. Furthermore, we add trend lines that represent the equation of state for two separate compositions: 13% iron-rich pyrolite [Wolf et al., 2015] and aluminum-bearing pyrolite [Nishiyama et al., 2007]. Regardless of composition, both equations of state show no significant difference in the elastic properties of bridgmanite. In addition, our unit cell volumes for both a pyrolitic or aluminum-rich bridgmanite are consistent with both these equations of state. Implications of this will be covered in the Discussion section of this chapter.

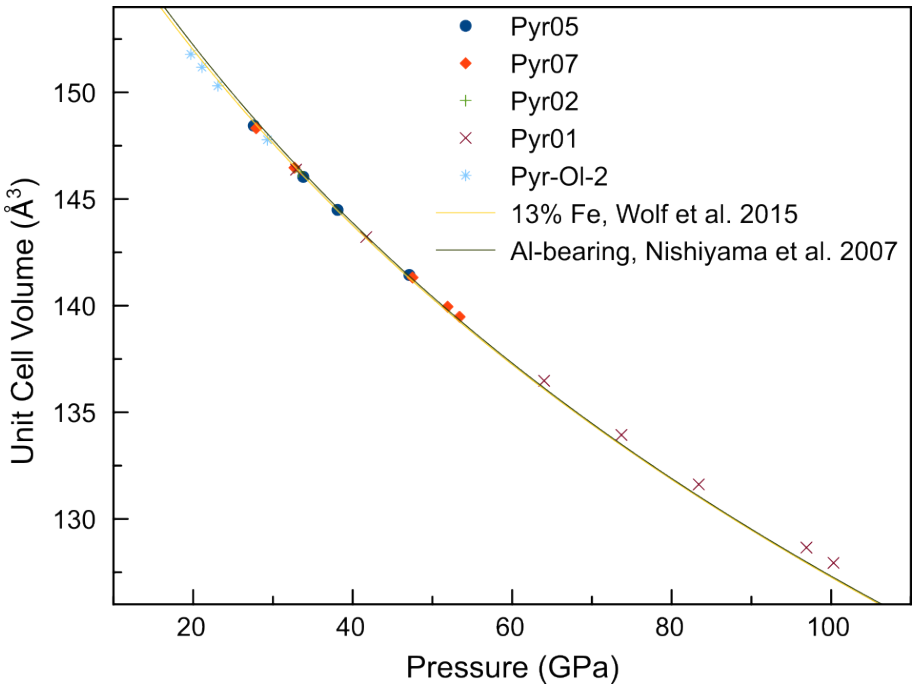

Figure 6.3: Unit cell volumes of bridgmanite in pyrolitic and pyrolitic garnet compositions used in multigrain X-ray diffraction indexings plotted vs. pressure. Lines are Vinet equation of state for 13% Fe bridgmanite [Wolf et al., 2015] and third-order Birch–Murnaghan equation of state for aluminum bearing bridgmanite [Nishiyama et al., 2007] at 300 K and used to illustrate compression behavior vs. experimental values.

6.4 Discussion

Textures in both bridgmanite and davemaoite resemble those in our previous experiments on pyrolite with only minor differences. Upon transformation to bridgmanite, we observe a strong 001 transformation texture along with weak orientations in 010. Above 34 GPa in Pyr-Ol-02, orientations in 001 become weaker and we observe the appearance of a weak 100 texture, which are present from 34 to 40 GPa (Figure 6.2). This shift in texture with deformation from 001 at 25 GPa to 100 orientations at 38 GPa in bridgmanite formed from pyrolite-minus-olivine is consistent with textures observed in our pyrolite experiments, both in strength and pressure occurrence. Based on these observations, one could expect similar active glide planes in bridgmanite under plastic deformation and little change in anisotropic properties based on texture alone. For these reasons, we do not see an effect of composition on the plasticity of bridgmanite and hence do not model active slip systems or anisotropy in pyrolite-minus-olivine. Furthermore, we observe 010 textures in bridgmanite in our pyrolite samples at pressures above 50 GPa that are not observed during these

experiments. We reason that the absence of these 010 orientations is due to the fact we never reached large enough pressure to reorient the grains. Nevertheless, one could expect, based on the consistencies between our pyrolite and pyrolite-minus-olivine composition samples, that grain might reorient as pressures exceed 50 GPa.

Davemaoite is very consistent with our other experiments on pyrolite in both texture and strength. Although we do not observe texture immediately after the transformation, we do observe 101 orientations at 34 GPa which compares favorably with both sample Pyr05 and Pyr07. Furthermore, we see 111 orientations in pyrolite-minus-olivine, which are also observed in sample Pyr07 at 53 and 55 GPa. The change in orientations here is again attributed to the effect of strain on the sample, which can lead to changes in grain shape during compression and hence how grains align themselves. Strain can be distributed differently across the sample, so it is possible with further heating during compression strains could have redistributed, hence account for the shift in texture.

It has long been debated how aluminum might impact the physical properties of bridgmanite at lower mantle conditions, as well as observations of seismic anisotropy. In Figure 6.3, we can see there is a negligible difference in composition on the impact of elastic properties in bridgmanite. Here we argue, based on our experimental results and the equations of state presented in Wolf et al. [2015] and Nishiyama et al. [2007], that the presence or lack of aluminium in a pyrolitic system would not greatly impact observations of seismic anisotropy in the mantle. While temperature may have an impact on microstructures present in the mantle and hence observations of anisotropy, one could argue that the values of P and S-wave anisotropy within a subducting slab and the surrounding material would be similar.

6.5 Conclusion

In this chapter, we perform deformation experiments in the laser-heated DAC on a modified composition of pyrolite that does not contain olivine (pyrolite-minus-olivine) i.e. pyrolitic garnet. Experiments were carried out at pressures ranging from 25 to 40 GPa and temperatures of ∼1800 K. We present an extreme case, where the model composition of pyrolite is rich in aluminum, in order to determine if aluminum would have an impact

on transformation and deformation microstructures within our sample. Multigrain data processing techniques resulted in the assignment of single crystal diffraction peaks to individual grains within the sample. We are able to index between 144 and 434 grains in bridgmanite and 96 to 235 grains of davemaoite in a multiphase material. We find that the 001 transformation textures observed in pyrolite-minus-olivine after transformation to bridgmanite are the same as those seen during our experiments on pyrolite. This indicates that the mechanism for grain growth in bridgmanite under stress after transformation is only weakly sensitive to the staring composition. Additionally, we observe 100 orientations with further deformation to pressures up to 40 GPa, indicating that the plastic behavior of bridgmanite is identical in both pyrolite and pyrolite-minus-olivine compositions. Furthermore, davemaoite does not display texture upon transformation in these experiments. With deformation, however, we see the appearance of 101 orientations that end up reorienting to orientations in 111. These textures also compares well with those seen in our experiments on pyrolite in the previous chapters. As the textures observed in these experiments are similar in both strength and pressure occurrence, we did not model active slip systems or anisotropy in bridgmanite formed in a composition of pyrolite-minus-olivine. We do suggest, however, that observation of seismic anisotropy, both within and outside of a subducting slab, will not be effected due to aluminum in the system.

Overall, we find that the incorporation of aluminum in a pyrolitic composition does not have a considerable impact of the physical properties of bridgmanite or davemaoite. Although, in this chapter we only compare orientations in bridgmanite and davemaoite to those observed in the previous chapters, further work could be done investigating the effect of aluminum on stress or strength of bridgmanite, which we do not address here. Additionally, experiments where deformation is carried out to higher pressures would answer remaining questions on what textures are present in aluminum enriched bridgmanite at lower mantle conditions.

General Conclusion

In this thesis we investigate microstructures in mantle minerals and the deformation mechanisms for which they are associated with. We use this information to make improved interpretations of seismic anisotropy observed in the Earth's upper and lower mantle. In order to predict which deformation mechanisms are active in these regions of the Earth, we perform deformation experiments that allow us to observe the development of microstructures at the relevant pressures and temperatures. These deformation mechanisms are then used to model seismic anisotropy in the mantle and be compared to observations.

A phase transformation in the bridgmanite analogue $NaCoF_3$ from the perovskite to post-perovskite structure takes place between 20.1 and 26.1 GPa in a resistive-heated diamond anvil cell. This transformation results in both deformation textures in perovskite and transformation textures in post-perovskite. Initial deformation of perovskite results in strong 100 orientations at 7.3 GPa, with a weak secondary 001 maximum appearing at 13.4 GPa. Visco-plastic self-consistent (VPSC) simulations were used to determine that orientations in 100 are a result of slip along (100) paired with important contributions from {110} twins. We determine $NaCoF_3$ is a good analogue for plasticity studies relevant for the Earth's mantle as both 100 and 001 textures have been observed in natural compositions. Note, however, that the slip system in (010) we identify in bridgmanite at pressures above 50 GPa is not observed in NaCoF3 which is stable over a more reduced pressure range. Transformation from perovskite to post-perovskite structure in $NaCoF_3$ involves orientation relationships, determined by simulating a post-perovskite texture that matches our experimental results, where the vector $hh0$ (normal to (110) in post-perovskite) is parallel to [010] in perovskite and [001] in post-perovskite is parallel to [001] in perovskite.

The phase transformation from (ringwoodite + garnet) to (bridgmanite + davemaoite + ferropericlase) was observed in four pyrolitic samples using multigrain X-ray diffraction

in a laser-heated diamond anvil cell (DAC). Compression was carried out between 17.5 and 108 GPa at temperatures between 1500 and 2000 K. Indexing capabilities of these multiphase systems ranges between 107 to 736 grains post transformation depending on the sample. Prior to the transformation, ringwoodite displays a weak texture with 001 planes oriented perpendicular to the compressive stress, while no texture is observed in the garnet phase. Post transformation, bridgmanite displays strong transformation texture in 001 across all experiments as a result of oriented growth under stress. Davemaoite is moderately textured with both 101 and 111 orientations depending on the experiment. Ferropericlase remains largely untextured in all experiments. Further deformation of the sample results in the weakening of 001 orientations and a slow shift to orientations in 100 below 50 GPa. As pressure increases beyond ∼50 GPa, however, bridgmanite reorients to a 010 texture. Davemaoite is only moderately textured with 101 orientations in one experiment, and 111 orientations in another. Ferropericlase remains largely untextured in all experiments.

In order to determine the deformation mechanisms at play, we use VPSC to model our experimental textures in bridgmanite. We separate deformation into two stages, with 30% strain applied in compression for the first stage and 70% strain applied in the second. Starting from a 001 transformation texture, we find that (100)[001] is the dominant active slip system with minor contributions from (010)[001] and (001)[010]. During the second stage of compression, dominant slip is nearly evenly distributed between (010)[100] and (010)[001]. These simulations are not only able to reproduce the texture evolution of bridgmanite observed in our experiments, but also match textures observed in other deformation experiments where (100) slip is most active below 50 GPa and (010) slip active at pressures above 50 GPa.

Using single crystal elastic constants, calculated at pressures and temperatures relevant to mantle transition zone and lower mantle pressures and temperatures, we are able to calculate seismic anisotropy corresponding to the microstructures observed in our deformation experiments. We first consider the case of a near vertical subducting slab under compressive stresses penetrating the 660 km discontinuity ('660'). Above this boundary, our models predict no anisotropy in S and P-wave anisotropy. Below, however, S-wave

splitting is 1.28% (0.08 km/s) for waves travelling perpendicular to compression and null for waves travelling parallel. P-wave azimuthal anisotropy is 0.17% in the same region. Additionally, we implement our VPSC calculations into large scale models of mantle flow to model anisotropy within a subducting slab and the surrounding mantle at lower mantle conditions. Within the subducting slab, we observe a change in S-wave radial anisotropy from vertically polarized shear waves leading horizontally polarized waves ($V_{SV} > V_{SH}$) to horizontally polarized shear wave leading vertically polarized waves ($V_{SH} > V_{SV}$) when the slab bends above the D" layer. In the surrounding mantle, our models predict $V_{SV} > V_{SH}$ at all depths surrounding the slab. Although our implementation of experimental results in anisotropy models are only a starting point, the development of an integrated model will help the interpretation of seismic signals and how they can be used to constrain flow and dynamic processes in the deep mantle.

In closing, we determined the mechanisms of high pressure and temperature transformation and deformation in bridgmanite, while also covering the geophysical implications of our experimental results. Deformation experiments have not been performed at such pressures and temperatures. Moreover, it is the first time that the plastic behaviour of bridgmanite has been studied within a pyrolitic composition, which is more representative of the mantle than experiments on pure bridgmanite or bridgmanite and ferropericlase assemblages that have been used in previous studies. We provide new mineralogical data on analogue and pyrolitic materials within the Earth's mantle. Results of the pyrolite experiments can be further used to improve interpretations of seismological observations, although future work is needed to address remaining questions. The effects of grain size on deformation after the phase transformation have not yet been investigated in a pyrolitic composition. Furthermore, when modeling plastic deformation in the lower mantle, we only consider a bridgmanite aggregate (as it makes up the majority of the lower mantle) even though there are other phases within the pyrolite polycrystal that exhibit deformation textures. We also have a poor understanding on the impact of strain rate, as compression experiments cannot realistically be carried out at strain rates of the Earth. Additionally, there is no evaluation of the stress levels in our samples. Multigrain crystallography should allow us to map out grain by gain stain and stress distributions, but we were not able to

evaluate those methods and their reliability within the time frame of this PhD. Finally, we are missing postmortem analysis using SEM and TEM techniques which, most likely would have brought a wealth of information on the microstructures at the micron and sub-micron scale. This work continues to build upon the foundation of integrating experimental mineral physics with seismological studies, with the goal of constraining deformation and mantle dynamics in a planet we call Earth.

List of Figures

List of Tables

Bibliography

S. Agrawal, C. M. Eakin, D. E. Portner, E. E. Rodriguez, and S. L. Beck. The deformational journey of the nazca slab from seismic anisotropy. Geophysical Research Letters, 47:1–9, 2020. ISSN 19448007. doi: 10.1029/2020GL087398.

J. Amodeo, P. Carrez, and P. Cordier. Modelling the effect of pressure on the critical shear stress of MgO single crystals. Philosophical Magazine, 92:1523–1541, 4 2012. ISSN 1478-6435. doi: 10.1080/14786435.2011.652689.

O. L. Anderson, D. G. Isaak, and S. Yamamoto. Anharmonicity and the equation of state for gold. Journal of Applied Physics, 65:1534–1543, 1989. ISSN 00218979. doi: 10.1063/1.342969.

D. Andrault and G. Fiquet. Synchrotron radiation and laser heating in a diamond anvil cell. Review of Scientific Instruments, 72:1283–1288, 2001. ISSN 00346748. doi: 10.1063/1.1343866.

D. Andrault, G. Fiquet, J.-P. Itié, P. Richet, P. Gillet, D. Häusermann, and M. Hanfland. Thermal pressure in the laser-heated diamond-anvil cell: An x-ray diffraction study. European Journal of Mineralogy, 10:931–940, 1998. ISSN 0935-1221. doi: 10.1127/ejm/10/5/0931.

D. Andrault, N. Bolfan-Casanova, and N. Guignot. Equation of state of lower mantle (Al,Fe)-$MgSiO_3$ perovskite. Earth and Planetary Science Letters, 193:501–508, 2001. ISSN 0012821X. doi: 10.1016/S0012-821X(01)00506-4.

J. Andrews and A. Deuss. Detailed nature of the 660 km region of the mantle from global receiver function data. Journal of Geophysical Research: Solid Earth, 113:1–12, 2008. ISSN 21699356. doi: 10.1029/2007JB005111.

R. J. Angel. Equations of state. Reviews in Mineralogy and Geochemistry, 41:35–59, 2000. ISSN 1529-6466. doi: 10.2138/rmg.2000.41.2.

R. J. Angel, M. Alvaro, and F. Nestola. 40 years of mineral elasticity: a critical review and a new parameterisation of equations of state for mantle olivines and diamond inclusions. Physics and Chemistry of Minerals, 45:95–113, 2018. ISSN 14322021. doi: 10.1007/s00269-017-0900-7.

F. Bachmann, R. Hielscher, and H. Schaeben. Texture analysis with MTEX- Free and open source software toolbox. volume 160, pages 63–68, 2010. ISBN 3908451787. doi: 10.4028/www.scientific.net/SSP.160.63.

T. B. Ballaran, A. Kurnosov, K. Glazyrin, D. J. Frost, M. Merlini, M. Hanfland, and R. Caracas. Effect of chemistry on the compressibility of silicate perovskite in the lower mantle. Earth and Planetary Science Letters, 333-334:181–190, 2012. ISSN 0012821X. doi: 10.1016/j.epsl.2012.03.029. URL http://dx.doi.org/10.1016/j.epsl.2012.03.029.

C. Beghein, J. Trampert, and H. J. van Heijst. Radial anisotropy in seismic reference models of the mantle. Journal of Geophysical Research: Solid Earth, 111:1–9, 2006. ISSN 21699356. doi: 10.1029/2005JB003728.

S. Beller and S. Chevrot. Probing depth and lateral variations of upper-mantle seismic anisotropy from full-waveform inversion of teleseismic body-waves. Geophysical Journal International, 222:352–387, 2020. ISSN 1365246X. doi: 10.1093/GJI/GGAA069.

M. I. Billen. Modeling the dynamics of subducting slabs. Annual Review of Earth and Planetary Sciences, 36:325–356, 2008. ISSN 0084-6597. doi: 10.1146/annurev.earth.36.031207.124129.

F. Birch. Elasticity and Constitution of the Earth's Interior. Journal of Geophysical Research, 57:227–286, 1952.

R. Boehler, M. Ross, and D. B. Boercker. High-pressure melting curves of alkali halides. Physical Review B - Condensed Matter and Materials Physics, 53:556–563, 1996. ISSN 1550235X. doi: 10.1103/PhysRevB.53.556.

R. Boehler, M. Ross, D. B. Boercker, and Y. Yamazaki. Melting of LiF and NaCl to 1 Mbar: Systematics of Ionic Solids at Extreme Conditions. Physical Review Letters, 78: 4589–4592, 1997. ISSN 10797114. doi: 10.1103/PhysRevLett.78.4589.

F. Boioli, P. Carrez, P. Cordier, B. Devincre, K. Gouriet, P. Hirel, A. Kraych, and S. Ritterbex. Pure climb creep mechanism drives flow in Earth's lower mantle. Science Advances, 3:1–7, 2017. doi: 10.1126/sciadv.1601958.

W. H. Bragg. X-rays and Crystals. Nature, 90:219–219, 10 1912. doi: 10.1038/090219a0.

J. P. Brodholt. Pressure-induced changes in the compression mechanism of aluminous perovskite in the Earth's mantle. Nature, 407:620–622, 10 2000. ISSN 0028-0836. doi: 10.1038/35036565.

Y. Capdeville and L. Métivier. Elastic full waveform inversion based on the homogenization method: theoretical framework and 2-D numerical illustrations. Geophysical Journal International, 213:1093–1112, 5 2018. ISSN 0956-540X. doi: 10.1093/gji/ggy039.

Y. Capdeville, M. Zhao, and P. Cupillard. Fast fourier homogenization for elastic wave propagation in complex media. Wave Motion, 54:170–186, 4 2015. ISSN 01652125. doi: 10.1016/j.wavemoti.2014.12.006.

P. Carrez, D. Ferré, and P. Cordier. Implications for plastic flow in the deep mantle from modelling dislocations in $MgSiO_3$ minerals. Nature, 446:68–70, 2007. ISSN 14764687. doi: 10.1038/nature05593.

P. Carrez, A. M. Goryaeva, and P. Cordier. Prediction of mechanical twinning in magnesium silicate post-perovskite. Scientific Reports, 7:1–9, 2017. ISSN 2045-2322. doi: 10.1038/s41598-017-18018-1.

B. C. Chandler, K. Yuan, M. Li, S. Cottaar, B. Romanowicz, C. N. Tomé, and H. R. Wenk. A refined approach to model anisotropy in the lowermost mantle. IOP Conference Series: Materials Science and Engineering, 375, 2018. ISSN 1757899X. doi: 10.1088/1757-899X/375/1/012002.

S. J. Chang, A. M. Ferreira, J. Ritsema, H. J. V. Heijst, and J. H. Woodhouse. Global radially anisotropic mantle structure from multiple datasets: A review, current challenges, and outlook. Tectonophysics, 617:1–19, 2014. ISSN 00401951. doi: 10.1016/j.tecto.2014.01.033.

G. Chen, R. C. Liebermann, and D. J. Weidner. Elasticity of single-crystal MgO to 8 gigapascals and 1600 kelvin. Science, 280:1913–1916, 1998. ISSN 00368075. doi: 10.1126/science.280.5371.1913.

W. P. Chen and M. R. Brudzinski. Seismic anisotropy in the mantle transition zone beneath Fiji-Tonga. Geophysical Research Letters, 30, 7 2003. ISSN 00948276. doi: 10.1029/2002GL016330.

D. Chenine, Z. Aziz, W. Benstaali, B. Bouadjemi, O. Youb, T. Lantri, B. Abbar, and S. Bentata. Theoretical Investigation of Half-Metallic Ferromagnetism in Sodium-Based Fluoro-perovskite $NaXF_3$ (X = V, Co). Journal of Superconductivity and Novel Magnetism, 31:285–295, 2018. ISSN 15571947. doi: 10.1007/s10948-017-4204-4.

J. W. Christian, G. B. Olson, and M. Cohen. Classification of displacive transformations: What is a martensitic transformation? Le Journal de Physique IV, 05:C8–3–C8–10, 1995. ISSN 1155-4339. doi: 10.1051/jp4:1995801.

P. Cordier, T. Ungár, L. Zsoldos, and G. Tichy. Dislocation creep in $MgSiO_3$ perovskite at conditions of the Earth's uppermost lower mantle. Nature, 428:837–840, 2004. doi: 10.1038/nature02472.

S. Couper, S. Speziale, H. Marquardt, H. P. Liermann, and L. Miyagi. Does Heterogeneous Strain Act as a Control on Seismic Anisotropy in Earth's Lower Mantle? Frontiers in Earth Science, 8:1–20, 2020. ISSN 22966463. doi: 10.3389/feart.2020.540449.

S. Crampin. A review of wave motion in anisotropic and cracked elastic-media. Wave Motion, 3:343–391, 10 1981. ISSN 01652125. doi: 10.1016/0165-2125(81)90026-3.

G. Criniti, A. Kurnosov, T. B. Ballaran, and D. J. Frost. Single-Crystal Elasticity of $MgSiO_3$ Bridgmanite to Mid-Lower Mantle Pressure. Journal of Geophysical Research: Solid Earth, 126, 2021. ISSN 21699356. doi: 10.1029/2020JB020967.

F. Datchi, R. LeToullec, and P. Loubeyre. Improved calibration of the SrB_4O_7:Sm_2 + optical pressure gauge: Advantages at very high pressures and high temperatures. Journal of Applied Physics, 81:3333–3339, 1997. ISSN 00218979. doi: 10.1063/1.365025.

E. A. Day and A. Deuss. Reconciling PP and P'P' precursor observations of a complex 660 km seismic discontinuity. Geophysical Journal International, 194:834–838, 2013. ISSN 0956540X. doi: 10.1093/gji/ggt122.

R. de Wit and J. Trampert. Robust constraints on average radial lower mantle anisotropy and consequences for composition and texture. Earth and Planetary Science Letters, 429:101–109, 11 2015. ISSN 0012821X. doi: 10.1016/j.epsl.2015.07.057.

A. Deuss. Global observations of mantle discontinuities using SS and PP precursors. Surveys in Geophysics, 30:301–326, 2009. ISSN 01693298. doi: 10.1007/s10712-009-9078-y.

A. Deuss, S. A. Redfern, K. Chambers, and J. H. Woodhouse. The nature of the 660-kilometer discontinuity in Earth's mantle from global seismic observations of PP precursors. Science, 311:198–201, 2006. ISSN 00368075. doi: 10.1126/science.1120020.

A. Dewaele, P. Loubeyre, and M. Mezouar. Equations of state of six metals above 94 GPa. Physical Review B - Condensed Matter and Materials Physics, 70:1–8, 2004. ISSN 01631829. doi: 10.1103/PhysRevB.70.094112.

A. Dewaele, A. B. Belonoshko, G. Garbarino, F. Occelli, P. Bouvier, M. Hanfland, and M. Mezouar. High-pressure-high-temperature equation of state of KCl and KBr. Physical Review B - Condensed Matter and Materials Physics, 85, 2012. ISSN 10980121. doi: 10.1103/PhysRevB.85.214105.

D. P. Dobson, S. A. Hunt, A. Lindsay-Scott, and I. G. Wood. Towards better analogues for $MgSiO_3$ post-perovskite: $NaCoF_3$ and $NaNiF_3$, two new recoverable fluoride post-perovskites. Physics of the Earth and Planetary Interiors, 189:171–175, 2011. ISSN 00319201. doi: 10.1016/j.pepi.2011.08.010.

D. P. Dobson, R. McCormack, S. A. Hunt, M. W. Ammann, D. Weidner, L. Li, and

L. Wang. The relative strength of perovskite and post-perovskite $NaCoF_3$. Mineralogical Magazine, 76:925–932, 2012. ISSN 0026-461X. doi: 10.1180/minmag.2012.076.4.09.

D. P. Dobson, N. Miyajima, F. Nestola, M. Alvaro, N. Casati, C. Liebske, I. G. Wood, and A. M. Walker. Strong inheritance of texture between perovskite and post-perovskite in the D" layer. Nature Geoscience, 6(7):575–578, jul 2013. ISSN 1752-0894. doi: 10.1038/ngeo1844.

S. M. Dorfman, S. R. Shieh, and T. S. Duffy. Strength and texture of Pt compressed to 63 GPa. Journal of Applied Physics, 117, 2015. ISSN 10897550. doi: 10.1063/1.4907866.

L. Dubrovinsky, N. Dubrovinskaia, E. Bykova, M. Bykov, V. Prakapenka, C. Prescher, K. Glazyrin, H. P. Liermann, M. Hanfland, M. Ekholm, Q. Feng, L. V. Pourovskii, M. I. Katsnelson, J. M. Wills, and I. A. Abrikosov. The most incompressible metal osmium at static pressures above 750 gigapascals. Nature, 525:226–229, 2015. ISSN 14764687. doi: 10.1038/nature14681.

T. S. Duffy. Strength of materials under static loading in the diamond anvil cell. AIP Conference Proceedings, 955:639–644, 2007. ISSN 0094243X. doi: 10.1063/1.2833175.

A. M. Dziewonski and D. L. Anderson. Preliminary reference earth model. Physics of the Earth and Planetary Interiors, 25:297–356, 1981.

M. Faccenda and F. A. Capitanio. Development of mantle seismic anisotropy during subduction-induced 3-D flow. Geophysical Research Letters, 39, 6 2012. ISSN 00948276. doi: 10.1029/2012GL051988.

M. Faccenda and L. D. Zilio. The role of solid–solid phase transitions in mantle convection. Lithos, 268-271:198–224, 1 2017. ISSN 00244937. doi: 10.1016/j.lithos.2016.11.007.

D. Fan, S. Fu, J. Yang, S. N. Tkachev, V. B. Prakapenka, and J. F. Lin. Elasticity of single-crystal periclase at high pressure and temperature: The effect of iron on the elasticity and seismic parameters of ferropericlase in the lower mantle. American Mineralogist, 104:262–275, 2019. ISSN 19453027. doi: 10.2138/am-2019-6656.

H. Fei, U. Faul, and T. Katsura. The grain growth kinetics of bridgmanite at the topmost lower mantle. Earth and Planetary Science Letters, 561:116820, 2021. ISSN 0012821X. doi: 10.1016/j.epsl.2021.116820.

Y. Fei, A. Ricolleau, M. Frank, K. Mibe, G. Shen, and V. Prakapenka. Toward an internally consistent pressure scale. Proceedings of the National Academy of Sciences of the United States of America, 104:9182–9186, 2007. ISSN 00278424. doi: 10.1073/pnas.0609013104.

A. M. Ferreira, M. Faccenda, W. Sturgeon, S. J. Chang, and L. Schardong. Ubiquitous lower-mantle anisotropy beneath subduction zones. Nature Geoscience, 12(4):301–306, 2019. ISSN 17520908. doi: 10.1038/s41561-019-0325-7.

D. Ferré, P. Carrez, and P. Cordier. First principles determination of dislocations properties of $MgSiO_3$ perovskite at 30 GPa based on the Peierls-Nabarro model. Physics of the Earth and Planetary Interiors, 163:283–291, 2007. ISSN 00319201. doi: 10.1016/j.pepi.2007.05.011.

D. J. Frost. The upper mantle and transition zone. Elements, 4:171–176, 2008. ISSN 18115209. doi: 10.2113/GSELEMENTS.4.3.171.

S. Fu, J. Yang, N. Tsujino, T. Okuchi, N. Purevjav, and J. F. Lin. Single-crystal elasticity of (Al,Fe)-bearing bridgmanite and seismic shear wave radial anisotropy at the topmost lower mantle. Earth and Planetary Science Letters, 518:116–126, 2019. ISSN 0012821X. doi: 10.1016/j.epsl.2019.04.023.

H. Fukui, A. Yoneda, A. Nakatsuka, N. Tsujino, S. Kamada, E. Ohtani, A. Shatskiy, N. Hirao, S. Tsutsui, H. Uchiyama, and A. Q. Baron. Effect of cation substitution on bridgmanite elasticity: A key to interpret seismic anomalies in the lower mantle. Scientific Reports, 6:1–10, 2016. ISSN 20452322. doi: 10.1038/srep33337.

E. J. Garnero and A. K. McNamara. Structure and Dynamics of Earth's Lower Mantle. Science, 320:626–628, 4 2008. doi: 10.1126/science.1148028.

E. J. Garnero, V. Maupin, T. Lay, and M. J. Fouch. Variable azimuthal anisotropy in Earth's lowermost mantle. Science, 306:259–261, 2004. ISSN 00368075. doi: 10.1126/science.1103411.

E. J. Garnero, A. K. McNamara, and S.-H. Shim. Continent-sized anomalous zones with low seismic velocity at the base of Earth's mantle. Nature Geoscience, 9:481–489, 7 2016. ISSN 1752-0894. doi: 10.1038/ngeo2733.

J. P. Gay, L. Miyagi, S. Couper, C. Langrand, D. P. Dobson, H.-P. Liermann, and S. Merkel. Deformation of $NaCoF_3$ perovskite and post-perovskite up to 30 GPa and 1013 K: implications for plastic deformation and transformation mechanism. European Journal of Mineralogy, 33:591–603, 2021. doi: 10.5194/ejm-33-591-2021.

J. Girard, G. Amulele, R. Farla, A. Mohiuddin, and S. I. Karato. Shear deformation of bridgmanite and magnesiowüstite aggregates at lower mantle conditions. Science, 351: 144–147, 2016. ISSN 10959203. doi: 10.1126/science.aad3113.

J. Gonzalez-Platas, M. Alvaro, F. Nestola, and R. Angel. Eosfit7-gui: A new graphical user interface for equation of state calculations, analyses and teaching. Journal of Applied Crystallography, 49:1377–1382, 2016. ISSN 16005767. doi: 10.1107/S1600576716008050.

A. M. Goryaeva, P. Carrez, and P. Cordier. Modeling defects and plasticity in $MgSiO_3$ post-perovskite: Part 1—generalized stacking faults. Physics and Chemistry of Minerals, 42:781–792, 11 2015a. ISSN 14322021. doi: 10.1007/s00269-015-0762-9.

A. M. Goryaeva, P. Carrez, and P. Cordier. Modeling defects and plasticity in $MgSiO_3$ post-perovskite: Part 2—screw and edge [100] dislocations. Physics and Chemistry of Minerals, 42:793–803, 11 2015b. ISSN 14322021. doi: 10.1007/s00269-015-0763-8.

A. M. Goryaeva, P. Carrez, and P. Cordier. Modeling defects and plasticity in $MgSiO_3$ post-perovskite: Part 3—Screw and edge [001] dislocations. Physics and Chemistry of Minerals, 44:521–533, 7 2017. ISSN 14322021. doi: 10.1007/s00269-017-0879-0.

D. H. Green and A. E. Ringwood. Mineral assemblages in a model mantle composition. Journal of Geophysical Research, 68:937–945, 1963. doi: 10.1029/jz068i003p00937.

L. gun Liu. Silicate perovskite from phase transformations of pyrope-garnet at high pressure and temperature. Geophysical Research Letters, 1:277–280, 1974.

J. W. Hernlund, C. Thomas, and P. J. Tackley. A doubling of the post-perovskite. Nature, 434(April):882–886, 2005. doi: 10.1038/nature03472.

P. Hirel, A. Kraych, P. Carrez, and P. Cordier. Atomic core structure and mobility of [100](010) and [010](100) dislocations in $MgSiO_3$ perovskite. Acta Materialia, 79:117–125, 2014. ISSN 13596454. doi: 10.1016/j.actamat.2014.07.001.

K. Hirose. Phase transitions in pyrolitic mantle around 670-km depth: Implications for upwelling of plumes from the lower mantle. Journal of Geophysical Research: Solid Earth, 107:ECV 3–1–ECV 3–13, 2002. ISSN 2169-9356. doi: 10.1029/2001jb000597.

K. Hirose, Y. Nagaya, S. Merkel, and Y. Ohishi. Deformation of $MnGeO_3$ post-perovskite at lower mantle pressure and temperature. Geophysical Research Letters, 37:1–5, 2010. ISSN 00948276. doi: 10.1029/2010GL044977.

N. C. Holmes, J. A. Moriarty, G. R. Gathers, and W. J. Nellis. The equation of state of platinum to 660 GPa (6.6 Mbar). Journal of Applied Physics, 66:2962–2967, 1989. ISSN 00218979. doi: 10.1063/1.344177.

Q. Huang, N. Schmerr, L. Waszek, and C. Beghein. Constraints on seismic anisotropy in the mantle transition zone from long-period ss precursors. Journal of Geophysical Research: Solid Earth, 124:6779–6800, 2019. ISSN 21699356. doi: 10.1029/2019JB017307.

R. Huang, T. B. Ballaran, C. A. McCammon, N. Miyajima, and D. J. Frost. The Effect of Fe-Al Substitution on the Crystal Structure of $MgSiO_3$ Bridgmanite. Journal of Geophysical Research: Solid Earth, 126, 9 2021. ISSN 2169-9313. doi: 10.1029/2021JB021936.

S. A. Hunt, D. J. Weidner, L. Li, L. Wang, N. P. Walte, J. P. Brodholt, and D. P. Dobson. Weakening of calcium iridate during its transformation from perovskite to post-perovskite. Nature Geoscience, 2:794–797, 2009. ISSN 17520894. doi: 10.1038/ngeo663.

S. A. Hunt, A. M. Walker, and E. Mariani. In-situ measurement of texture development rate in $CaIrO_3$ post-perovskite. Physics of the Earth and Planetary Interiors, 257:91–104, 2016. ISSN 00319201. doi: 10.1016/j.pepi.2016.05.007.

J. Immoor, H. Marquardt, L. Miyagi, F. Lin, S. Speziale, S. Merkel, J. Buchen, A. Kurnosov, and H. P. Liermann. Evidence for {100}⟨011⟩ slip in ferropericlase in Earth's lower mantle from high-pressure/high-temperature experiments. Earth and Planetary Science Letters, 489:251–257, 2018. ISSN 0012821X. doi: 10.1016/j.epsl.2018.02.045.

J. Immoor, H. Marquardt, L. Miyagi, S. Speziale, S. Merkel, I. Schwark, A. Ehnes, and H.-P. Liermann. An improved setup for radial diffraction experiments at high pressures and high temperatures in a resistive graphite-heated diamond anvil cell. Review of Scientific Instruments, 91:045121, 2020. ISSN 0034-6748. doi: 10.1063/1.5143293.

J. Immoor, L. Miyagi, H.-P. Liermann, S. Speziale, K. Schulze, J. Buchen, A. Kurnosov, and H. Marquardt. Weak cubic $CaSiO_3$ perovskite in the Earth's mantle. Nature, 603: 276–279, 2022. ISSN 0028-0836. doi: 10.1038/s41586-021-04378-2.

T. Irifune. An experimental investigation of the pyroxene-garnet transformation in a pyrolite composition and its bearing on the constitution of the mantle. Physics of the Earth and Planetary Interiors, 45:324–336, 1987. ISSN 00319201. doi: 10.1016/0031-9201(87)90040-9.

T. Irifune and A. E. Ringwood. Phase transformations in primitive MORB and pyrolite compositions to 25 GPa and some geophysical implications. Terra Scientific Publishing Company, 1987. doi: 10.1029/gm039p0231.

T. Ishii, H. Kojitani, and M. Akaogi. Post-spinel transitions in pyrolite and Mg_2SiO_4 and akimotoite-perovskite transition in $MgSiO_3$: Precise comparison by high-pressure high-temperature experiments with multi-sample cell technique. Earth and Planetary Science Letters, 309:185–197, 2011. ISSN 0012821X. doi: 10.1016/j.epsl.2011.06.023.

T. Ishii, H. Kojitani, and M. Akaogi. Phase relations and mineral chemistry in pyrolitic mantle at 1600–2200 °C under pressures up to the uppermost lower mantle: Phase transitions around the 660-km discontinuity and dynamics of upwelling hot plumes. Physics of the Earth and Planetary Interiors, 274(April 2017):127–137, 2018. ISSN 00319201. doi: 10.1016/j.pepi.2017.10.005.

J. Ita and L. Stixrude. Petrology, elasticity, and composition of the mantle transition zone. Journal of Geophysical Research, 97:6849–6866, 1992. ISSN 01480227. doi: 10.1029/92JB00068.

J. M. Jackson, S. V. Sinogeikin, S. D. Jacobsen, H. J. Reichmann, S. J. Mackwell, and J. D. Bass. Single-crystal elasticity and sound velocities of $(Mg_{0.94}Fe_{0.06})O$ ferropericlase to 20 GPa. Journal of Geophysical Research: Solid Earth, 111:1–8, 2006. ISSN 21699356. doi: 10.1029/2005JB004052.

A. Jayaraman. Diamond anvil cell and high-pressure physical investigations. Reviews of Modern Physics, 55:65–108, 1983. ISSN 00346861. doi: 10.1103/RevModPhys.55.65.

J. Jenkins, S. Cottaar, R. S. White, and A. Deuss. Depressed mantle discontinuities beneath iceland: Evidence of a garnet controlled 660 km discontinuity? Earth and Planetary Science Letters, 433:159–168, 2016. ISSN 0012821X. doi: 10.1016/j.epsl.2015.10.053.

H. Jung, W. Mo, and H. W. Green. Upper mantle seismic anisotropy resulting from pressure-induced slip transition in olivine. Nature Geoscience, 2:73–77, 1 2009. ISSN 17520894. doi: 10.1038/ngeo389.

P. Kaercher, L. Miyagi, W. Kanitpanyacharoen, E. Zepeda-Alarcon, Y. Wang, D. Parkinson, R. A. Lebensohn, F. D. Carlo, and H. R. Wenk. Two-phase deformation of lower mantle mineral analogs. Earth and Planetary Science Letters, 456:134–145, 2016. ISSN 0012821X. doi: 10.1016/j.epsl.2016.09.030.

S. Karato. The role of recrystallization in the preferred orientation of olivine. Physics of the Earth and Planetary Interiors, 51:107–122, 1988. ISSN 00319201. doi: 10.1016/0031-9201(88)90029-5.

S. Karato and P. Li. Diffusion creep in perovskite: Implications for the rheology of the lower mantle. Science, 255:1238–1240, 1992.

S. I. Karato, Z. Wang, B. Liu, and K. Fujino. Plastic deformation of garnets: systematics and implications for the rheology of the mantle transition zone. Earth and Planetary Science Letters, 130:13–30, 1995. ISSN 0012821X. doi: 10.1016/0012-821X(94)00255-W.

M. Kasemer, E. Zepeda-Alarcon, R. Carson, P. Dawson, and H. R. Wenk. Deformation heterogeneity and intragrain lattice misorientation in high strength contrast, dual-phase bridgmanite/periclase. Acta Materialia, 189:284–298, 2020. ISSN 13596454. doi: 10.1016/j.actamat.2020.02.061.

T. Katsura, A. Yoneda, D. Yamazaki, T. Yoshino, E. Ito, D. Suetsugu, C. Bina, T. Inoue, D. Wiens, and M. Jellinek. Adiabatic temperature profile in the mantle. Physics of the Earth and Planetary Interiors, 183:212–218, 2010. ISSN 00319201. doi: 10.1016/j.pepi.2010.07.001.

A. Kavner. Garnet yield strength at high pressures and implications for upper mantle and transition zone rheology. Journal of Geophysical Research: Solid Earth, 112:1–9, 2007. ISSN 21699356. doi: 10.1029/2007JB004931.

T. Kawazoe, T. Ohuchi, Y. Nishihara, N. Nishiyama, K. Fujino, and T. Irifune. Seismic anisotropy in the mantle transition zone induced by shear deformation of wadsleyite. Physics of the Earth and Planetary Interiors, 216:91–98, 3 2013. ISSN 00319201. doi: 10.1016/j.pepi.2012.12.005.

S. Klotz, J.-C. Chervin, P. Munsch, and G. L. Marchand. Hydrostatic limits of 11 pressure transmitting media. Journal of Physics D: Applied Physics, 42:1–7, 4 2009. ISSN 0022-3727. doi: 10.1088/0022-3727/42/7/075413.

U. Kocks, C. N. Tomé, and H.-R. Wenk. Plasticity Modeling in Minerals and Rocks, 2000.

P. Koelemeijer, B. S. Schuberth, D. R. Davies, A. Deuss, and J. Ritsema. Constraints on the presence of post-perovskite in Earth's lowermost mantle from tomographic-geodynamic model comparisons. Earth and Planetary Science Letters, 494:226–238, 2018. ISSN 0012821X. doi: 10.1016/j.epsl.2018.04.056.

T. Komabayashi, K. Hirose, N. Sata, Y. Ohishi, and L. S. Dubrovinsky. Phase transition in $CaSiO_3$ perovskite. Earth and Planetary Science Letters, 260:564–569, 2007. ISSN 0012821X. doi: 10.1016/j.epsl.2007.06.015.

T. Komabayashi, K. Hirose, Y. Nagaya, E. Sugimura, and Y. Ohishi. High-temperature compression of ferropericlase and the effect of temperature on iron spin transition.

Earth and Planetary Science Letters, 297:691–699, 2010. ISSN 0012821X. doi: 10.1016/j.epsl.2010.07.025.

Z. Konôpková, W. Morgenroth, R. Husband, N. Giordano, A. Pakhomova, O. Gutowski, M. Wendt, K. Glazyrin, A. Ehnes, J. T. Delitz, A. F. Goncharov, V. B. Prakapenka, and H. P. Liermann. Laser heating system at the Extreme Conditions Beamline, P02.2, PETRA III. Journal of Synchrotron Radiation, 28:1747–1757, 11 2021. ISSN 16005775. doi: 10.1107/S1600577521009231.

A. Kraych, P. Carrez, and P. Cordier. On dislocation glide in $MgSiO_3$ bridgmanite at high-pressure and high-temperature. Earth and Planetary Science Letters, 452:60–68, 2016. ISSN 0012821X. doi: 10.1016/j.epsl2016.07.035.

M. Kronbichler, T. Heister, and W. Bangerth. High accuracy mantle convection simulation through modern numerical methods. Geophysical Journal International, 191:12–29, 2012. doi: 10.1111/j.1365-246X.2012.05609.x.

A. Kurnosov, H. Marquardt, D. J. Frost, T. B. Ballaran, and L. Ziberna. Elasticity of lower-mantle bridgmanite. Nature, 564:E18–E26, 2018. ISSN 14764687. doi: 10.1038/s41586-018-0741-7.

C. Langrand, N. Hilairet, C. Nisr, M. Roskosz, G. Ribárik, G. B. Vaughan, and S. Merkel. Reliability of multigrain indexing for orthorhombic polycrystals above 1 Mbar: Application to $MgSiO_3$ post-perovskite. Journal of Applied Crystallography, 50:120–130, 2017. ISSN 16005767. doi: 10.1107/S1600576716018057.

V. Lekic, S. Cottaar, A. Dziewonski, and B. Romanowicz. Cluster analysis of global lower mantle tomography: A new class of structure and implications for chemical heterogeneity. Earth and Planetary Science Letters, 357-358:68–77, 12 2012. ISSN 0012821X. doi: 10.1016/j.epsl.2012.09.014.

S. Lessing, D. P. Dobson, S. Rost, L. Cobden, and C. Thomas. Kinetic effects on the 660-km-phase transition in mantle upstreams and seismological implications. Geophysical Journal International, 231:877–893, 7 2022. ISSN 0956-540X. doi: 10.1093/gji/ggac196.

L. Li, D. J. Weidner, J. Brodholt, D. Alfè, and G. D. Price. Elasticity of Mg_2SiO_4 ringwoodite at mantle conditions. Physics of the Earth and Planetary Interiors, 157:181–187, 2006a. ISSN 00319201. doi: 10.1016/j.pepi.2006.04.002.

L. Li, D. J. Weidner, J. Brodholt, D. Alfè, G. D. Price, R. Caracas, and R. Wentzcovitch. Elasticity of $CaSiO_3$ perovskite at high pressure and high temperature. Physics of the Earth and Planetary Interiors, 155:249–259, 2006b. ISSN 00319201. doi: 10.1016/j.pepi.2005.12.006.

H.-P. Liermann, S. Merkel, L. Miyagi, H.-R. Wenk, G. Shen, H. Cynn, and W. J. Evans. Experimental method for in situ determination of material textures at simultaneous high pressure and high temperature by means of radial diffraction in the diamond anvil cell. Review of Scientific Instruments, 80:1–8, 10 2009. ISSN 0034-6748. doi: 10.1063/1.3236365.

H. P. Liermann, Z. Konôpková, W. Morgenroth, K. Glazyrin, J. Bednarčik, E. E. McBride, S. Petitgirard, J. T. Delitz, M. Wendt, Y. Bican, A. Ehnes, I. Schwark, A. Rothkirch, M. Tischer, J. Heuer, H. Schulte-Schrepping, T. Kracht, and H. Franz. The extreme conditions beamline p02.2 and the extreme conditions science infrastructure at petra iii. Journal of Synchrotron Radiation, 22:908–924, 2015. ISSN 16005775. doi: 10.1107/S1600577515005937.

J.-F. Lin, S. Speziale, Z. Mao, and H. Marquardt. Effects of the electronic spin transitions of iron in lower mantle minerals: Implications for deep mantle geophysics and geochemistry. Reviews of Geophysics, 51:244–275, 4 2013. ISSN 87551209. doi: 10.1002/rog.20010.

Z. Liu, R. Liu, Y. Shang, F. Shen, L. Chen, X. Hou, M. Yao, T. Cui, B. Liu, and T. Katsura. Aluminum solubility in bridgmanite up to 3000 k at the top lower mantle. Geoscience Frontiers, 12:929–935, 2021. ISSN 16749871. doi: 10.1016/j.gsf.2020.04.009.

M. D. Long. Constraints on subduction geodynamics from seismic anisotropy. Reviews of Geophysics, 51:76–112, 3 2013. ISSN 19449208. doi: 10.1002/rog.20008.

M. D. Long and T. W. Becker. Mantle dynamics and seismic anisotropy. Earth

and Planetary Science Letters, 297:341–354, 2010. ISSN 0012821X. doi: 10.1016/j.epsl.2010.06.036.

M. D. Long and P. G. Silver. The subduction zone flow field from seismic anisotropy: A global view. Science, 319:315–318, 1 2008. ISSN 0036-8075. doi: 10.1126/science.1150809.

C. Luo, X. Deng, W. Wang, G. Shukla, Z. Wu, and R. M. Wentzcovitch. cij: A python code for quasiharmonic thermoelasticity. Computer Physics Communications, 267:108067, 2021. ISSN 00104655. doi: 10.1016/j.cpc.2021.108067.

L. Lutterotti, S. Matthies, H. R. Wenk, A. S. Schultz, and J. W. Richardson. Combined texture and structure analysis of deformed limestone from time-of-flight neutron diffraction spectra. Journal of Applied Physics, 81:594–600, 1997. ISSN 00218979. doi: 10.1063/1.364220.

C. Lynner and M. D. Long. Heterogeneous seismic anisotropy in the transition zone and uppermost lower mantle: Evidence from South America, Izu-Bonin and Japan. Geophysical Journal International, 201:1545–1552, 2015. ISSN 1365246X. doi: 10.1093/gji/ggv099.

D. Mainprice. Seismic anisotropy of the deep earth from a mineral and rock physics perspective. In G. Schubert, editor, Treatise on Geophysics (Second Edition), pages 487–538. Elsevier, Oxford, second edition edition, 2015. ISBN 978-0-444-53803-1. doi: https://doi.org/10.1016/B978-0-444-53802-4.00044-0.

D. Mainprice, G. Barruol, W. B. Isma, D. Mainprice, G. Barruol, W. B. Isma, D. Mainprice, G. Barruol, and W. B. Isma. The Seismic anisotropy of the Earth's mantle: From single crystal to polycrystal, volume 117. 2000. ISBN 9780875909752. doi: 10.1029/GM117.

D. Mainprice, A. Tommasi, D. Ferré, P. Carrez, and P. Cordier. Predicted glide systems and crystal preferred orientations of polycrystalline silicate mg-perovskite at high pressure: Implications for the seismic anisotropy in the lower mantle. Earth and Planetary Science Letters, 271:135–144, 2008. ISSN 0012821X. doi: 10.1016/j.epsl.2008.03.058.

D. Mainprice, F. Bachmann, R. Hielscher, and H. Schaeben. Descriptive tools for the analysis of texture projects with large datasets using mtex: Strength, symmetry and

components. Geological Society Special Publication, 409:251–271, 2014. ISSN 03058719. doi: 10.1144/SP409.8.

H. K. Mao, J. Xu, and P. M. Bell. Calibration of the ruby pressure gauge to 800 kbar under quasi-hydrostatic conditions. Journal of Geophysical Research, 91:4673–4676, 1986. ISSN 0148-0227. doi: 10.1029/jb091ib05p04673.

W. Mao and S. Zhong. Slab stagnation due to a reduced viscosity layer beneath the mantle transition zone. Nature Geoscience, 11:876–881, 2018. ISSN 17520908. doi: 10.1038/s41561-018-0225-2.

A. K. McNamara, E. J. Garnero, and S. Rost. Tracking deep mantle reservoirs with ultra-low velocity zones. Earth and Planetary Science Letters, 299:1–9, 10 2010. ISSN 0012821X. doi: 10.1016/j.epsl.2010.07.042.

C. Meade, P. G. Silver, and S. Kaneshima. Laboratory and seismological observations of lower mantle isotropy. Geophysical Research Letters, 22:1293–1296, 1995. ISSN 19448007. doi: 10.1029/95GL01091.

S. Merkel, R. J. Hemley, and H. K. Mao. finite-element modeling of diamond deformation at multimegabar pressures. Applied Physics Letters, pages 656–658. ISSN 00036951. doi: 10.1063/1.123031.

S. Merkel, H. R. Wenk, J. Shu, G. Shen, P. Gillet, H. kwang Mao, and R. J. Hemley. Deformation of polycrystalline MgO at pressures of the lower mantle. Journal of Geophysical Research: Solid Earth, 107:ECV 3–1–ECV 3–17, 2002. ISSN 0148-0227. doi: 10.1029/2001jb000920.

S. Merkel, H. R. Wenk, J. Badro, G. Montagnac, P. Gillet, H. K. Mao, and R. J. Hemley. Deformation of $(Mg_{0.9},Fe_{0.1})SiO_3$ Perovskite aggregates up to 32 GPa. Earth and Planetary Science Letters, 209:351–360, 2003. ISSN 0012821X. doi: 10.1016/S0012-821X(03)00098-0.

S. Merkel, H. R. Wenk, P. Gillet, H. kwang Mao, and R. J. Hemley. Deformation of polycrystalline iron up to 30GPa and 1000K. Physics of the Earth and Planetary Interiors, 145:239–251, 2004. ISSN 00319201. doi: 10.1016/j.pepi.2004.04.001.

S. Merkel, A. Kubo, L. Miyagi, S. Speziale, T. S. Duffy, H. K. Mao, and H. R. Wenk. Plastic deformation of $MgGeO_3$ post-perovskite at lower mantle pressures. Science, 311: 644–646, 2006. ISSN 00368075. doi: 10.1126/science.1121808.

S. Merkel, A. K. McNamara, A. Kubo, S. Speziale, L. Miyagi, Y. Meng, T. S. Duffy, and H. R. Wenk. Deformation of $(Mg,Fe)SiO_3$ post-perovskite and D anisotropy. Science, 316:1729–1732, 2007. ISSN 10959203. doi: 10.1126/science.1140609.

A. Metsue, P. Carrez, D. Mainprice, and P. Cordier. Numerical modelling of dislocations and deformation mechanisms in $CaIrO_3$ and $MgGeO_3$ post-perovskites-Comparison with $MgSiO_3$ post-perovskite. Physics of the Earth and Planetary Interiors, 174:165–173, 5 2009. ISSN 00319201. doi: 10.1016/j.pepi.2008.04.003.

L. Miyagi and H. R. Wenk. Texture development and slip systems in bridgmanite and bridgmanite + ferropericlase aggregates. Physics and Chemistry of Minerals, 43:597–613, 2016. ISSN 14322021. doi: 10.1007/s00269-016-0820-y.

L. Miyagi, S. Merkel, T. Yagi, N. Sata, Y. Ohishi, and H. R. Wenk. Quantitative Rietveld texture analysis of $CaSiO_3$ perovskite deformed in a diamond anvil cell. Journal of Physics Condensed Matter, 18, 2006. ISSN 09538984. doi: 10.1088/0953-8984/18/25/S07.

L. Miyagi, S. Merkel, T. Yagi, N. Sata, Y. Ohishi, and H. R. Wenk. Diamond anvil cell deformation of $CaSiO_3$ perovskite up to 49 GPa. Physics of the Earth and Planetary Interiors, 174:159–164, 2009. ISSN 00319201. doi: 10.1016/j.pepi.2008.05.018.

L. Miyagi, W. Kanitpanyacharoen, P. Kaercher, K. K. Lee, and H. R. Wenk. Slip systems in $MgSiO_3$ post-perovskite: Implications for D anisotropy. Science, 329:1639–1641, 2010. ISSN 00368075. doi: 10.1126/science.1192465.

L. Miyagi, W. Kanitpanyacharoen, S. Stackhouse, B. Militzer, and H. R. Wenk. The enigma of post-perovskite anisotropy: Deformation versus transformation textures. Physics and Chemistry of Minerals, 38:665–678, 2011. ISSN 03421791. doi: 10.1007/s00269-011-0439-y.

L. Miyagi, W. Kanitpanyacharoen, S. V. Raju, P. Kaercher, J. Knight, A. MacDowell, H. R. Wenk, Q. Williams, and E. Z. Alarcon. Combined resistive and laser heating technique for in situ radial x-ray diffraction in the diamond anvil cell at high pressure and temperature. Review of Scientific Instruments, 84, 2013. ISSN 00346748. doi: 10.1063/1.4793398.

N. Miyajima and N. Walte. Burgers vector determination in deformed perovskite and post-perovskite of $CaIrO_3$ using thickness fringes in weak-beam dark-field images. Ultramicroscopy, 109:683–692, 2009. ISSN 03043991. doi: 10.1016/j.ultramic.2009.01.010.

N. Miyajima, T. Yagi, and M. Ichihara. Dislocation microstructures of $MgSiO_3$ perovskite at a high pressure and temperature condition. Physics of the Earth and Planetary Interiors, 174:153–158, 2009. ISSN 00319201. doi: 10.1016/j.pepi.2008.04.004.

J. P. Montagner and B. L. Kennett. How to reconcile body-wave and normal-mode reference earth models. Geophysical Journal International, 125:229–248, 1996. ISSN 0956540X. doi: 10.1111/j.1365-246X.1996.tb06548.x.

J. P. Montagner and H. C. Nataf. A simple method for inverting the azimuthal anisotropy of surface waves. Journal of Geophysical Research, 91:511–520, 1986. ISSN 01480227. doi: 10.1029/JB091iB01p00511.

J. P. Montagner, G. Burgos, Y. Capdeville, E. Beucler, and A. Mocquet. The mantle transition zone dynamics as revealed through seismic anisotropy. Tectonophysics, 821: 229133, 2021. ISSN 00401951. doi: 10.1016/j.tecto.2021.229133.

M. Murakami, K. Hirose, K. Kawamura, N. Sata, and Y. Ohishi. Post-Perovskite Phase Transition in $MgSiO_3$. Science, 304(5672):855–858, 2004. ISSN 00368075. doi: 10.1126/science.1095932.

M. Murakami, S. V. Sinogeikin, J. D. Bass, N. Sata, Y. Ohishi, and K. Hirose. Sound velocity of $MgSiO_3$ post-perovskite phase: A constraint on the D discontinuity. Earth and Planetary Science Letters, 259:18–23, 2007. ISSN 0012821X. doi: 10.1016/j.epsl.2007.04.015.

M. Murakami, S. V. Sinogeikin, K. Litasov, E. Ohtani, and J. D. Bass. Single-crystal elasticity of iron-bearing majorite to 26 GPa: Implications for seismic velocity structure of the mantle transition zone. Earth and Planetary Science Letters, 274:339–345, 2008. ISSN 0012821X. doi: 10.1016/j.epsl.2008.07.045.

A. Nakatsuka, H. Fukui, S. Kamada, N. Hirao, M. Ohkawa, K. Sugiyama, and T. Yoshino. Incorporation mechanism of fe and al into bridgmanite in a subducting mid-ocean ridge basalt and its crystal chemistry. Scientific Reports, 11:22839, 12 2021. ISSN 2045-2322. doi: 10.1038/s41598-021-00403-6.

Y. Nishihara, I. Aoki, E. Takahashi, K. N. Matsukage, and K. I. Funakoshi. Thermal equation of state of majorite with MORB composition. Physics of the Earth and Planetary Interiors, 148:73–84, 2005. ISSN 00319201. doi: 10.1016/j.pepi.2004.08.003.

N. Nishiyama, T. Yagi, S. Ono, H. Gotou, T. Harada, and T. Kikegawa. Effect of incorporation of iron and aluminum on the thermoelastic properties of magnesium silicate perovskite. Physics and Chemistry of Minerals, 34:131–143, 2007. ISSN 03421791. doi: 10.1007/s00269-006-0134-6.

K. Niwa, T. Yagi, K. Ohgushi, S. Merkel, N. Miyajima, and T. Kikegawa. Lattice preferred orientation in $CaIrO_3$ perovskite and post-perovskite formed by plastic deformation under pressure. Physics and Chemistry of Minerals, 34(9):679–686, 2007a. ISSN 14322021. doi: 10.1007/s00269-007-0182-6.

K. Niwa, T. Yagi, K. Ohgushi, S. Merkel, N. Miyajima, and T. Kikegawa. Lattice preferred orientation in $CaIrO_3$ perovskite and post-perovskite formed by plastic deformation under pressure. Physics and Chemistry of Minerals, 34:679–686, 2007b. ISSN 14322021. doi: 10.1007/s00269-007-0182-6.

A. Nowacki, A. M. Walker, J. Wookey, and J. M. Kendall. Evaluating post-perovskite as a cause of D" anisotropy in regions of palaeosubduction. Geophysical Journal International, 192:1085–1090, 2013. ISSN 1365246X. doi: 10.1093/gji/ggs068.

A. Nowacki, J.-M. Kendall, J. Wookey, and A. Pemberton. Mid-mantle anisotropy in

subduction zones and deep water transport. Geochemistry, Geophysics, Geosystems, 16: 764–784, 3 2015. ISSN 15252027. doi: 10.1002/2014GC005667.

B. C. Nzogang, J. Bouquerel, P. Cordier, A. Mussi, J. Girard, and S. Karato. Characterization by Scanning Precession Electron Diffraction of an Aggregate of Bridgmanite and Ferropericlase Deformed at HP-HT. Geochemistry, Geophysics, Geosystems, 19: 582–594, 2018. ISSN 15252027. doi: 10.1002/2017GC007244.

J. Oddershede, S. Schmidt, H. F. Poulsen, H. O. Sørensen, J. Wright, and W. Reimers. Determining grain resolved stresses in polycrystalline materials using three-dimensional x-ray diffraction. Journal of Applied Crystallography, 43:539–549, 2010. ISSN 0021-8898. doi: 10.1107/S0021889810012963.

A. R. Oganov and S. Ono. Theoretical and experimental evidence for a post-perovskite phase of mgsio$_{3}$ in earth's d layer. Nature, 430:445–448, 2004. ISSN 00280836. doi: 10.1038/nature02701.

A. R. Oganov, R. Martoňák, A. Laio, P. Raiteri, and M. Parrinello. Anisotropy of earth's D layer and stacking faults in the $MgSiO_3$ post-perovskite phase. Nature, 438:1142–1144, 2005. ISSN 14764687. doi: 10.1038/nature04439.

T. Ohuchi, T. Kawazoe, Y. Nishihara, N. Nishiyama, and T. Irifune. High pressure and temperature fabric transitions in olivine and variations in upper mantle seismic anisotropy. Earth and Planetary Science Letters, 304:55–63, 2011. ISSN 0012821X. doi: 10.1016/j.epsl.2011.01.015.

T. Okada, T. Yagi, K. Niwa, and T. Kikegawa. Lattice-preferred orientations in post-perovskite-type $MgGeO_3$ formed by transformations from different pre-phases. Physics of the Earth and Planetary Interiors, 180:195–202, 2010. ISSN 00319201. doi: 10.1016/j.pepi.2009.08.002.

Y. Okuda, K. Ohta, T. Yagi, R. Sinmyo, T. Wakamatsu, K. Hirose, and Y. Ohishi. The effect of iron and aluminum incorporation on lattice thermal conductivity of bridgmanite at the earth's lower mantle. Earth and Planetary Science Letters, 474:25–31, 2017.

ISSN 0012821X. doi: 10.1016/j.epsl.2017.06.022. URL http://dx.doi.org/10.1016/j.epsl.2017.06.022.

Y. Okuda, K. Ohta, R. Sinmyo, K. Hirose, and Y. Ohishi. Anomalous compressibility in (fe,al)-bearing bridgmanite: implications for the spin state of iron. Physics and Chemistry of Minerals, 47:1–14, 2020. ISSN 14322021. doi: 10.1007/s00269-020-01109-3. URL https://doi.org/10.1007/s00269-020-01109-3.

M. Panning and B. Romanowicz. A three-dimensional radially anisotropic model of shear velocity in the whole mantle. Geophysical Journal International, 167:361–379, 2006a. ISSN 0956540X. doi: 10.1111/j.1365-246X.2006.03100.x.

M. Panning and B. Romanowicz. A three-dimensional radially anisotropic model of shear velocity in the whole mantle. Geophysical Journal International, 167(1):361–379, 2006b. ISSN 0956540X. doi: 10.1111/j.1365-246X.2006.03100.x.

M. Panning, V. Lekić, and B. A. Romanowicz. Importance of crustal corrections in the development of a new global model of radial anisotropy. Journal of Geophysical Research: Solid Earth, 115:1–18, 2010. ISSN 21699356. doi: 10.1029/2010JB007520.

A. Pisconti, C. Thomas, and J. Wookey. Discriminating between causes of d anisotropy using reflections and splitting measurements for a single path. Journal of Geophysical Research: Solid Earth, 124:4811–4830, 2019. ISSN 21699356. doi: 10.1029/2018JB016993.

J.-P. Poirier. Creep of Crystals: High-Temperature Deformation Processes in Metals, Ceramics and Minerals. Cambridge Earth Science Series. Cambridge University Press, 1985. doi: 10.1017/CBO9780511564451.

C. Prescher and V. B. Prakapenka. Dioptas: A program for reduction of two-dimensional x-ray diffraction data and data exploration. High Pressure Research, 35:223–230, 2015. ISSN 14772299. doi: 10.1080/08957959.2015.1059835.

J. Quinteros, S. V. Sobolev, and A. A. Popov. Viscosity in transition zone and lower mantle: Implications for slab penetration. Geophysical Research Letters, 37:1–5, 5 2010. ISSN 00948276. doi: 10.1029/2010GL043140.

R. Reali, F. Boioli, K. Gouriet, P. Carrez, B. Devincre, and P. Cordier. Modeling plasticity of MgO by 2.5D dislocation dynamics simulations. Materials Science and Engineering: A, 690:52–61, 4 2017. ISSN 09215093. doi: 10.1016/j.msea.2017.02.092.

H. M. Rietveld. A profile refinement method for nuclear and magnetic structures. Journal of Applied Crystallography, 2(2):65–71, Jun 1969. doi: 10.1107/S0021889869006558.

A. Ringwood. Phase transformations and differentiation in subducted lithosphere: implications for mantle dynamics, basalt petrogenesis, and crustal evolution. The Journal of Geology, 90:611–643, 1982.

A. E. Ringwood. A model for the layered upper mantle. Journal of Geophysical Research, 67:857–867, 1962a. doi: https://doi.org/10.1029/JZ067i002p00857.

A. E. Ringwood. A model for the layered upper mantle, 2. Journal of Geophysical Research, 67:4473–4477, 3 1962b. doi: https://doi.org/10.1029/JZ067i011p04473.

A. E. Ringwood. Phase transformations and their bearing on the constitution and dynamics of the mantle. Geochimica et Cosmochimica Acta, 55:2083–2110, 1991. ISSN 00167037. doi: 10.1016/0016-7037(91)90090-R.

A. D. Rosa, N. Hilairet, S. Ghosh, G. Garbarino, J. Jacobs, J. P. Perrillat, G. Vaughan, and S. Merkel. In situ monitoring of phase transformation microstructures at earth's mantle pressure and temperature using multi-grain xrd. Journal of Applied Crystallography, 48:1346–1354, 2015. ISSN 16005767. doi: 10.1107/S1600576715012765.

S. Schmidt. Grainspotter: A fast and robust polycrystalline indexing algorithm. Journal of Applied Crystallography, 47:276–284, 2014. ISSN 00218898. doi: 10.1107/S1600576713030185.

P. M. Shearer. Upper mantle seismic discontinuities, 1 2000. ISSN 23288779.

A. K. Singh, C. Balasingh, H. K. Mao, R. J. Hemley, and J. Shu. Analysis of lattice strains measured under nonhydrostatic pressure. Journal of Applied Physics, 83:7567–7575, 1998. ISSN 00218979. doi: 10.1063/1.367872.

S. V. Sinogeikin and J. D. Bass. Single-crystal elasticity of pyrope and MgO to 20 GPa by Brillouin scattering in the diamond cell. Physics of the Earth and Planetary Interiors, 120:43–62, 2000. ISSN 00319201. doi: 10.1016/S0031-9201(00)00143-6.

S. Speziale, C.-S. Zha, T. S. Duffy, R. J. Hemley, and H. kwang Mao. Quasi-hydrostatic compression of magnesium oxide to 52 GPa: Implications for the pressure-volume-temperature equation of state. Journal of Geophysical Research: Solid Earth, 106: 515–528, 1 2001. ISSN 01480227. doi: 10.1029/2000JB900318.

L. Stixrude and C. Lithgow-Bertelloni. Thermodynamics of mantle minerals - ii. phase equilibria. Geophysical Journal International, 184:1180–1213, 2010. ISSN 0956540X. doi: 10.1111/j.1365-246X.2010.04890.x.

W. Sturgeon, A. M. Ferreira, M. Faccenda, S. J. Chang, and L. Schardong. On the origin of radial anisotropy near subducted slabs in the midmantle. Geochemistry, Geophysics, Geosystems, 20:5105–5125, 2019. ISSN 15252027. doi: 10.1029/2019GC008462.

H. O. Sørensen, S. Schmidt, J. P. Wright, G. B. Vaughan, S. Techert, E. F. Garman, J. Oddershede, J. Davaasambu, K. S. Paithankar, C. Gundlach, and H. F. Poulsen. Multigrain crystallography. Zeitschrift fur Kristallographie, 227:63–78, 2012. ISSN 00442968. doi: 10.1524/zkri.2012.1438.

M. Tarrida and P. Richet. Equation of State of $CaSiO_3$ Perovskite to 96 GPa. Geophysical Research Letters, 16:1351–1354, 1989.

S. Tateno, K. Hirose, T. Komabayashi, H. Ozawa, and Y. Ohishi. The structure of Fe-Ni alloy in Earth's inner core. Geophysical Research Letters, 39:1–4, 6 2012. ISSN 00948276. doi: 10.1029/2012GL052103.

S. Tateno, T. Komabayashi, K. Hirose, N. Hirao, and Y. Ohishi. Static compression of B2 KCl to 230 GPa and its P-V-T equation of state. American Mineralogist, 104:718–723, 2019.

A. Tommasi, M. Knoll, A. Vauchez, J. W. Signorelli, C. Thoraval, and R. Logé. Structural reactivation in plate tectonics controlled by olivine crystal anisotropy. Nature Geoscience, 2:423–427, 6 2009. ISSN 17520894. doi: 10.1038/ngeo528.

J. Trampert and H. J. van Heijst. Global azimuthal anisotropy in the transition zone. Science, 296:1297–1299, 5 2002. ISSN 0036-8075. doi: 10.1126/science.1070264.

O. Tschauner, M. Chi, J. R. Beckett, C. Prescher, V. B. Prakapenka, and G. R. Rossman. Discovery of bridgmanite, the most abundant mineral in earth, in a shocked meteorite. Science, 346:1100–1102, 2014. ISSN 10959203. doi: 10.1126/science.1259369.

O. Tschauner, S. Huang, S. Yang, M. Humayun, W. Liu, S. N. G. Corder, H. A. Bechtel, J. Tischler, and G. R. Rossman. Discovery of davemaoite, $CaSiO_3$-perovskite, as a mineral from the lower mantle. Science, 374:890–894, 2021. doi: 10.1126/science.abl8568.

T. Tsuchiya, J. Tsuchiya, K. Umemoto, and R. M. Wentzcovitch. Phase transition in $MgSiO_3$ perovskite in the Earth's lower mantle. Earth and Planetary Science Letters, 224:241–248, 2004. ISSN 0012821X. doi: 10.1016/j.epsl.2004.05.017.

N. Tsujino, Y. Nishihara, D. Yamazaki, Y. Seto, Y. Higo, and E. Takahashi. Mantle dynamics inferred from the crystallographic preferred orientation of bridgmanite. Nature, 539:81–84, 2016. ISSN 14764687. doi: 10.1038/nature19777.

N. Tsujino, D. Yamazaki, Y. Nishihara, T. Yoshino, Y. Higo, and Y. Tange. Viscosity of bridgmanite determined by in situ stress and strain measurements in uniaxial deformation experiments. Science Advances, 8:1821, 4 2022. ISSN 2375-2548. doi: 10.1126/sciadv.abm1821.

R. D. van Der Hilst, S. Widiyantoro, and E. R. Engdahl. Evidence for deep mantle circulation from global tomography. Nature, 386:578–584, 1997.

C. E. Vennari, F. Lin, M. Kunz, M. Akaogi, L. Miyagi, and Q. Williams. Deformation and strength of mantle relevant garnets: Implications for the subduction of basaltic-rich crust. American Mineralogist, 106:1045–1052, 2021. ISSN 19453027. doi: 10.2138/am-2021-7587.

P. Vinet, J. R. Smith, J. Ferrante, and J. H. Rose. Temperature effects on the universal equation of state of solids. Physical Review B, 35:1945–1953, 1987. ISSN 01631829. doi: 10.1103/PhysRevB.35.1945.

K. Visser, J. Trampert, S. Lebedev, and B. L. Kennett. Probability of radial anisotropy in the deep mantle. Earth and Planetary Science Letters, 270:241–250, 2008. ISSN 0012821X. doi: 10.1016/j.epsl.2008.03.041.

A. M. Walker, D. P. Dobson, J. Wookey, A. Nowacki, and A. M. Forte. The anisotropic signal of topotaxy during phase transitions in D. Physics of the Earth and Planetary Interiors, 276:159–171, 2018. ISSN 00319201. doi: 10.1016/j.pepi.2017.05.013.

D. Walker, L. M. Cranswick, P. K. Verma, S. M. Clark, and S. Buhre. Thermal equations of state for B1 and B2 KCl. American Mineralogist, 87:805–812, 2002. ISSN 0003004X. doi: 10.2138/am-2002-0701.

B. Wang and F. Niu. A broad 660 km discontinuity beneath northeast china revealed by dense regional seismic networks in china. Journal of Geophysical Research: Solid Earth, 115:1–12, 2010. ISSN 21699356. doi: 10.1029/2009JB006608.

X. Wang, T. Tsuchiya, and A. Hase. Computational support for a pyrolitic lower mantle containing ferric iron. Nature Geoscience, 8:556–559, 2015. ISSN 17520908. doi: 10.1038/ngeo2458.

Y. Wang, F. Guyot, and R. C. Liebermann. Electron microscopy of (Mg,Fe)SiO_3 perovskite: evidence for structural phase transitions and implications for the lower mantle. Journal of Geophysical Research, 97:327–347, 1992. ISSN 01480227. doi: 10.1029/92jb00870.

L. Waszek, B. Tauzin, N. C. Schmerr, M. D. Ballmer, and J. C. Afonso. A poorly mixed mantle transition zone and its thermal state inferred from seismic waves. Nature Geoscience, 14:949–955, 2021. ISSN 17520908. doi: 10.1038/s41561-021-00850-w.

D. J. Weidner. A mineral physics test of a pyrolite mantle. Geophysical Research Letters, 12:417–420, 1985.

H.-R. Wenk. A voyage through the deformed earth with the self-consistent model. Modelling and Simulation in Materials Science and Engineering, 7:699–722, 9 1999. ISSN 0965-0393. doi: 10.1088/0965-0393/7/5/304.

H. R. Wenk and P. V. Houtte. Texture and anisotropy, 8 2004. ISSN 00344885.

H. R. Wenk, I. Lonardeli, J. Pehl, J. Devine, V. Prakapenka, G. Shen, and H. K. Mao. In situ observation of texture development in olivine, ringwoodite, magnesiowüstite and silicate perovskite at high pressure. Earth and Planetary Science Letters, 226(3-4):507–519, 2004a. ISSN 0012821X. doi: 10.1016/j.epsl.2004.07.033.

H. R. Wenk, I. Lonardeli, J. Pehl, J. Devine, V. Prakapenka, G. Shen, and H. K. Mao. In situ observation of texture development in olivine, ringwoodite, magnesiowüstite and silicate perovskite at high pressure. Earth and Planetary Science Letters, 226:507–519, 2004b. ISSN 0012821X. doi: 10.1016/j.epsl.2004.07.033.

H. R. Wenk, G. Ischia, N. Nishiyama, Y. Wang, and T. Uchida. Texture development and deformation mechanisms in ringwoodite. Physics of the Earth and Planetary Interiors, 152:191–199, 2005. ISSN 00319201. doi: 10.1016/j.pepi.2005.06.008.

H. R. Wenk, I. Lonardelli, S. Merkel, L. Miyagi, J. Pehl, S. Speziale, and C. E. Tommaseo. Deformation textures produced in diamond anvil experiments, analysed in radial diffraction geometry. Journal of Physics Condensed Matter, 18:S933–S947, 2006. ISSN 09538984. doi: 10.1088/0953-8984/18/25/S02.

H. R. Wenk, L. Lutterotti, P. Kaercher, W. Kanitpanyacharoen, L. Miyagi, and R. Vasin. Rietveld texture analysis from synchrotron diffraction images. II. Complex multiphase materials and diamond anvil cell experiments. Powder Diffraction, 29(3):220–232, 2014. ISSN 19457413. doi: 10.1017/S0885715614000360.

A. S. Wolf, J. M. Jackson, P. Dera, V. B. Prakapenka, and W. E. T. Al. The thermal equation of state of (Mg,Fe)SiO_3 bridgmanite (perovskite) and implications for lower mantle structures. Journal of Geophysical Research, 2015. doi: 10.1002/2015JB012108.Received.

J. Wookey and J.-M. Kendall. Seismic anisotropy of post-perovskite and the lowermost mantle, 2007. ISSN 23288779.

J. Wookey, J. M. Kendall, and G. Barruol. Mid-mantle deformation inferred from seismic anisotropy. Nature, 415:777–780, 2002. ISSN 00280836. doi: 10.1038/415777a.

F. Xu, J. E. Vidale, and P. S. Earle. Survey of precursors to PP: Fine structure of mantle discontinuities. Journal of Geophysical Research: Solid Earth, 108:ETG 7–1–ETG 7–10, 2003. doi: 10.1029/2001jb000817.

F. Xu, D. Yamazaki, S. A. Hunt, N. Tsujino, Y. Higo, Y. Tange, K. Ohara, and D. P. Dobson. Deformation of post-spinel under the lower mantle conditions. Journal of Geophysical Research: Solid Earth, 127:1–12, 2022. ISSN 2169-9313. doi: 10.1029/2021jb023586.

D. Yamazaki, T. Kato, E. Ohtani, and M. Toriumi. Grain Growth Rates of $MgSiO_3$ Perovskite and Periclase Under Lower Mantle Conditions. Science, 274:2052–2055, 1996.

D. Yamazaki, T. Yoshino, H. Ohfuji, J. ichi Ando, and A. Yoneda. Origin of seismic anisotropy in the D layer inferred from shear deformation experiments on post-perovskite phase. Earth and Planetary Science Letters, 252:372–378, 2006. ISSN 0012821X. doi: 10.1016/j.epsl.2006.10.004.

J. Yang, J. F. Lin, S. D. Jacobsen, N. M. Seymour, S. N. Tkachev, and V. B. Prakapenka. Elasticity of ferropericlase and seismic heterogeneity in the Earth's lower mantle. Journal of Geophysical Research: Solid Earth, 121:8488–8500, 2016. ISSN 21699356. doi: 10.1002/2016JB013352.

M. Yoshida. Trench dynamics: Effects of dynamically migrating trench on subducting slab morphology and characteristics of subduction zones systems. Physics of the Earth and Planetary Interiors, 268:35–53, 7 2017. ISSN 00319201. doi: 10.1016/j.pepi.2017.05.004.

T. Yoshino, M. Nishi, T. Matsuzaki, D. Yamazaki, and T. Katsura. Electrical conductivity of majorite garnet and its implications for electrical structure in the mantle transition zone. Physics of the Earth and Planetary Interiors, 170:193–200, 11 2008. ISSN 00319201. doi: 10.1016/j.pepi.2008.04.009.

K. Yuan and C. Beghein. Seismic anisotropy changes across upper mantle phase transitions. Earth and Planetary Science Letters, 374:132–144, 2013. ISSN 0012821X. doi: 10.1016/j.epsl.2013.05.031.

D. Zahn. Nucleation mechanism and kinetics of the perovskite to post-perovskite transition of $MgSiO_3$ under extreme conditions. Chemical Physics Letters, 573:5–7, 6 2013. ISSN 00092614. doi: 10.1016/j.cplett.2013.04.058.

C. S. Zha, K. Mibe, W. A. Bassett, O. Tschauner, H. K. Mao, and R. J. Hemley. P-V-T equation of state of platinum to 80 GPa and 1900 K from internal resistive heating/x-ray diffraction measurements. Journal of Applied Physics, 103(5), 2008. ISSN 00218979. doi: 10.1063/1.2844358.

W. Y. Zhou, J. S. Zhang, Q. Huang, X. Lai, B. Chen, P. Dera, and B. Schmandt. High pressure-temperature single-crystal elasticity of ringwoodite: Implications for detecting the 520 discontinuity and metastable ringwoodite at depths greater than 660 km. Earth and Planetary Science Letters, 579:117359, 2022. ISSN 0012821X. doi: 10.1016/j.epsl.2021.117359.

Microstructures and anisotropy of pyrolite in the Earth's lower mantle: insights from high pressure/temperature deformation and phase transformation experiments

Plain Language Summary

The Earth's interior has been gradually cooling through heat exchange from the core to the surface, which leads to many of the physical processes observed on the surface of the planet including plate tectonics and the underlying mantle convection. Seismic observations provide a mean to observe structures within the Earth's interior through features such as anisotropy or the detection of boundaries through changes in wave velocity. At the rock scale, seismic waves are sensitive to microstructures (i.e. grain size, shape, and orientation) created by ongoing deformation or mineralogical transformations. Here, we implement experimental transformation and deformation experiments at the conditions of the upper and lower mantle on rocks in a pyrolitic composition. We quantify how these microstructures are developed and the deformation mechanisms that may be active in dominant mantle minerals such as bridgmanite, providing an avenue to constrain mantle processes from observations.

Keywords: Diamond anvil cell, high pressure, pyrolite, multigrain X-ray diffraction, texture, seismic anisotropy, deep earth, Earth's mantle

---

Microstructures et anisotropie de la pyrolite dans le manteau inférieur : expériences de déformation et de transformations de phase sous hautes pressions et températures

Résumé grand public

L'intérieur de la Terre se refroidit gâce aux échanges de chaleur du noyau vers la surface, ce qui se manifeste par des processus tels que la tectonique des plaques et la convection sous-jacente du manteau. Les observations sismiques (vitesses de propagation d'onde, anisotropie, ou discontinuités de vitesses) permettent de sonder les structures à l'intérieur de la Terre. À l'échelle de la roche, les ondes sismiques sont sensibles aux microstructures (la taille, la forme et l'orientation des grains) générées par la déformation ou les transformations minéralogiques. Ici, nous utilisons des expériences de transformation et de déformation aux conditions de pression et température du manteau sur une composition pyrolitique. Nous quantifions la façon dont ces microstructures se développent et les mécanismes de déformation sous-jacents dans des minéraux tels que la bridgmanite, fournissant ainsi les données nécessaires pour contraindre les processus mantelliques à partir des observations.

Mots clés: cellule diamant, hautes pressions, pyrolite, diffraction multigrains, texture, anisotropie sismique, terre profonde, manteau terrestre